Università degli Studi di Ferrara

Doctoral course in Physics

Cycle XXXVI

Photometry and astrometry with wide-field imagers

Coordinator: Prof. E. Luppi

Scientific-Disciplinary Sector: FIS/05

Candidate

M. Griggio

Supervisors

Dr. L. R. Bedin

Prof. P. Rosati

Year 2020/2024

Abstract

This thesis presents an effort to extend high-precision photometry and astrometry techniques developed for the Hubble Space Telescope to ground-based, wide-field detectors, enabling detailed investigations of stellar clusters. Building upon previous work focused on achieving precise astrometry with wide-field imagers, we develop new techniques to calibrate the geometric distortion by leveraging the absolute reference frame provided by *Gaia*, and software routines to process largely dithered mosaics. In the first chapter we introduce a new formalism to compute star cluster membership probabilities that include the parallax contribution, benefiting from the unprecedented precision of *Gaia* measurements. Subsequent chapters delve into observational studies of the open clusters M37 and M38, using data from Asiago Schmidt and CFHT telescopes, combined with the *Gaia* catalogue. These investigations include analyses of white dwarf members, proper motions beyond the *Gaia* limit, and main sequence broadening. We also apply our techniques to derive the geometric distortion correction for the NIRCam detector onboard *JWST*, which we then use in the study of low-mass members of the globular cluster 47 Tuc. Finally, in the last chapter, we present a new pipeline for reprocessing data from the *Vista Variables in the Via Lactea* survey to extend *Gaia* astrometry into dust-obscured regions of the Galactic plane.

Contents

1. Introduction

Photometry and astrometry play pivotal roles in advancing our understanding of astrophysics, and in particular in the study of star clusters, shedding light on fundamental aspects of stellar evolution and galactic dynamics (Frebel and Norris, 2015; Renzini and Buzzoni, 1986). A star cluster consists of a group of stars that are gravitationally bound and have formed from the same giant molecular cloud of gas and dust. They are divided into two main categories. Open clusters (OCs), typically composed of young stars, often less than a few hundred million years old, that populate the disk of a galaxy, such as the Milky Way. OCs are loosely bound, and their stars are relatively spread out. Over time, the gravitational interactions within the cluster and with the surrounding galactic environment can cause the cluster to disperse. Globular clusters (GCs), on the other hand, are dense, spherical collections of tens of thousands to millions of stars. GCs are old systems, often several billion years old, and are mostly found in the bulge and halo of a galaxy. Stars in GCs are tightly packed, and the gravitational field is strong, keeping the cluster bound over long periods.

The study of star clusters is crucial for the understanding of stellar evolution, because all the stars within a cluster are essentially at the same distance from the Sun and share similar age and composition: this uniformity makes them excellent laboratories to study the factors influencing the birth and the life cycle of stars. Additionally, the distribution and properties of star clusters in galaxies provide essential clues about the formation and evolution of galaxies themselves.

Photometric observations of a star cluster in two or more filters allow us to build colour-magnitude diagrams, which in turn enable us to determine the cluster age, distance and chemical composition by comparing the observed luminosities and colours of its member stars with those predicted by theoretical models. This information is crucial for the understanding of the cluster's formation history and evolution, as photometry is essentially very low resolution spectroscopy.

Astrometry, on the other hand, involves precise measurements of positions and motions of celestial objects. In the study of star clusters, astrometric data provide insights into clusters' dynamics, interactions, and overall structure within the Galaxy and, most importantly, allow us to isolate cluster members from field sources.

The combination of precise photometry and astrometry enables detailed comparisons with theoretical models of stellar evolution and dynamics, allowing us to gain valuable insights into the physical mechanisms governing the formation and interaction of stars. Over the past few decades, a substantial amount of high-quality data have been acquired, resulting in significant advancements in our comprehension of stellar astrophysics.

However, there are still many aspects of star clusters that are not fully understood. For example, the discovery of multiple populations in virtually all GCs has changed the idea that GCs are made up by simple stellar populations, i.e. stars born at the same time and with the same chemical composition. This phenomenon is observable spectroscopically (see, e.g., Carretta et al., 2011) and photometrically, e.g., in the color-magnitude diagrams in appropriate filters, where the appearance of split sequences is indicative of the presence of multiple populations with different chemical abundances (Piotto et al., 2015). This observational fact strongly challenges theoretical models of cluster formation and evolution, and represents one of the most astonishing discoveries in this field. While the presence of multiple populations in GCs is now established, its origin is still uncertain, and further investigations are needed to shed more light on this topic (Bastian and Lardo, 2018).

On the other side of the mass and age spectrum, young and less massive Galactic OCs do not exhibit split sequences, nor have shown sizable variations in the chemical abundances of their members, and are still believed to host simple stellar populations. This idea has recently been questioned after a signature of a possible, significant chemical spread has been discovered in the OC M37 (Griggio et al., 2022b). If confirmed, the possibility that also OCs host stars born with different chemical composition will make the phenomenon of multiple populations even more complex than what already is, as existing models and scenarios explaining the formation of multiple populations in GCs do not readily apply to OCs.

Another example where additional efforts are needed is the characterization of the lower end of the clusters' main sequence, which is still a poorly-explored region, as the detection of low mass, faint, and red sources in crowded environments is observationally challenging. Low-mass stars constitute the larger fraction of cluster's members, as implied by theoretical models of star formation, and their detection requires high angular resolution and high sensitivity in the infrared wavelengths. The characterization of the low-mass population in star clusters will help to further understand how stars form and evolve and to constrain the initial mass function, which is a fundamental parameter governing the process of star formation.

The detection of the main sequence knee in GCs, a phenomenon originating from the redistribution of stellar flux within the core due to opacity changes, offers a novel approach for age determination. This feature, observable exclusively in near-infrared wavelengths, allows to infer a cluster's age without prior knowledge of distance and reddening (Saracino et al., 2018).

Finally, the transition between hydrogen-burning stars and brown dwarfs (BDs) still has to be detected, and its observation in GCs would be crucial to test and calibrate metal-poor models of BDs' atmospheres, formation and evolution, and can also help us to learn more about the properties of exoplanets, as they are thought to have similar atmospheres and compositions of BDs (Dieball et al., 2019).

1.1 Astrometry in the Modern Era

Astrometry stands as one of the fundamental aspects of astronomy. From ancient civilizations charting the positions of stars across the night sky to contemporary space missions mapping the cosmos with unprecedented accuracy, astrometry has played a crucial role in our understanding of the universe. The replacement of photographic plates with charge-coupled devices (CCDs) in the 1980s revolutionized astrometry, allowing to significantly reduce the measurements uncertainties. In recent decades, advances in technology, space-based observatories and precision measurement techniques, further expanded the field of astrometry, enabling ground-breaking discoveries.

The first space mission dedicated to high-precision astrometry is the Hipparcos mission (van Leeuwen, 1997), launched by the European Space Agency in 1989. Hipparcos measured the positions, distances, and motions of over 100 000 stars in the Milky Way with unprecedented accuracy, refining our knowledge of the Galaxy and contributing to broader astronomical endeavors (e.g., it confirmed the predictions of General Relativity, Frœschlé et al., 1997). In addition, it paved the way for subsequent astrometric missions, such as *Gaia* (Gaia Collaboration et al., 2016a), which has continued and expanded upon the legacy of precise astrometry initiated by Hipparcos.

Among the ground-based efforts in the astrometry field, the United States Naval Observatory CCD Astrograph Catalog (UCAC) project (Zacharias et al., 2000), aimed to create an all-sky precise astrometric catalog using data from a CCD astrograph. This ambitious project sought to provide accurate positions and proper motions for millions of stars across the celestial sphere. By employing advanced CCD technology and sophisticated data analysis techniques, UCAC significantly improved upon previous astrometric catalogs, reducing positional uncertainties. The catalog generated by the UCAC project has been invaluable for various astronomical investigations, including studies of stellar dynamics, Galactic structure, and the properties of celestial objects.

1.1.1 The *Gaia* mission

In the latest years the *Gaia* mission has contributed to further enhance the field of astrometry by providing an all-sky, absolute reference frame, supported by its unprecedented levels of precision and accuracy in measuring the positions, distances and motions of stars in the Galaxy.

Launched by the European Space Agency in 2013, the *Gaia* satellite has been meticulously surveying the sky, observing over a billion stars multiple times with extraordinary accuracy. One of the most significant contributions of *Gaia* is its ability to measure stellar parallaxes (and thus distances) with unparalleled precision, allowing astronomers to create a three-dimensional map of the Milky Way. *Gaia* data have greatly improved the accuracy of distance measurements compared to previous surveys, leading to a more precise understanding of the distribution and structure of stars in our galaxy. Additionally, it has provided highly accurate measurements of stellar motions that allow us to study the chemo-dynamical properties of the Milky Way (Helmi et al., 2018), the kinematics of its GCs (Vasiliev, 2019), and to discover new star clusters (see, e.g., Cantat-Gaudin and Anders, 2020; Cantat-Gaudin et al., 2018a).

Gaia DR1, released on September 13, 2016, marks the initial data release from the *Gaia* mission, covering observations spanning 14 months up to September 2015. This release provides essential data, including positions and magnitudes in a single photometric band for approximately 1.1 billion stars solely from *Gaia* observations. Moreover, it offers positions, parallaxes, and proper motions for over 2 million stars by combining *Gaia* and Tycho-2 data for common objects. Additionally, *Gaia* DR1 includes light curves and attributes for about 3000 variable stars, along with positions and magnitudes for over 2000 extragalactic sources essential for defining the celestial reference frame.

The second data release (DR2, Gaia Collaboration et al., 2018), published on April 2018, is derived from observations spanning 22 months from July 2014, to May 2016. This comprehensive release contains positions, parallaxes, and proper motions for approximately 1.3 billion stars, along with the positions of an extra 300 million stars within the G-magnitude range 3–20. It further includes $G_{\rm BP}$ and $G_{\rm RP}$ photometric data for around 1.1 billion stars and single-color photometry for an additional 400 million stars. Moreover, *Gaia* DR2 provides median radial velocities for approximately 7 million stars, spanning G-magnitudes 4 to 13.

The third data release, based on 34 months of observations, has been divided into two part to prioritize the release of readily available data. The initial portion, Early Data Release 3 (EDR3 Gaia Collaboration et al., 2021), was made public on December 3, 2020, while the complete DR3 (Gaia Collaboration et al., 2023) was published on 13 June 2022. This release features enhanced astrometry, Solar System data, variability information and several astrophysical parameters. Coordinates in DR3 are referenced to a new version of the Gaia celestial reference frame (*Gaia*–CRF3), established on observations of 1 614 173 extragalactic sources.

The availability of a comprehensive all-sky, absolute reference system has a significant influence, particularly given its potential to serve as a reference to anchor observations made with other telescopes, eliminating the necessity of a dedicated set of calibration observations. This versatility is exemplified by, e.g, Griggio et al. (2022a, 2023b), which demonstrate how the *Gaia* reference system can be effectively employed to calibrate the geometric distortion of ground-based instruments.

However, even though the *Gaia* telescope conducted observations across the entire sky, its data are limited to objects brighter than $G = 21$, and the astrometric precision for sources with $G \gtrsim 18$ is much worse than that of brighter sources. Its observations are also notably incomplete in dust-obscured and/or crowded regions, such as those found in the Galactic plane. Due to these factors, while *Gaia* has demonstrated unparalleled astrometric precision for nearby and relatively bright objects, its effectiveness is limited when it comes to studying faint objects like the low-mass members of star clusters or intrinsically red or dust-obscured sources.

1.1.2 Narrow-field astrometry: *HST* and *JWST*

Space-based telescopes, such as the *Hubble Space Telescope* (*HST*) and the recently launched *James Webb Space Telescope* (*JWST*), largely contribute to expanding the frontiers of astrometry, leading to breakthrough discoveries in several fields. Space-based telescopes have a number of advantages with respect to ground-based observatories. First, their location above Earth's atmosphere enables the acquisition of diffraction-limited images, achieving exceptional spatial resolution that is crucial for precise astrometry in crowded fields, and enabling the accurate measurement of stellar positions and the detection of faint objects. The absence of atmospheric effects translates into a point-spread function (PSF) that remains remarkably constant over time and that can therefore be modelled accurately. In addition, they are free from the differential-refraction effects that commonly afflict ground-based observations not captured at the zenith, and are not limited by the seasonal visibility of the targets. Finally, the weightless environment ensures that telescope flexure does not induce significant alterations in the distortion solution, allowing for a much more detailed modelling.

Anderson and King (2000) demonstrated that, with appropriate PSF modelling, it is possible to reach an astrometric precision of few milliarcseconds (mas) and an accuracy at the sub-mas level with *HST*'s Wide-Field Planetary Camera 2 (WFPC2). In the following years, similar techniques were applied to other *HST* cameras, enabling a series of works based on *HST* high-precision astrometry and photometry. For example, *HST* allowed for the analysis of the colour-magnitude diagram and luminosity function of GCs down to the hydrogen burning limit, e.g. in NGC 6397 (King et al., 1998; Richer et al., 2008) and in M4 (Bedin et al., 2001). It enabled the discovery of the phenomenon of multiple stellar populations in GCs (see, e.g., Bedin et al., 2004; Piotto et al., 2007) and the detailed study of the radial distribution of the multiple stellar populations in, e.g. ω Centauri (Bellini et al., 2009b). Using *HST*, Zivick et al. (2018) measured the Small Magellanic Cloud systemic proper motion, and Calamida et al. (2014) analysed the white dwarf cooling sequence of the Bulge. Thanks to *HST*'s exquisite photometric and astrometric capabilities, it has also been possible to investigate in details the properties of the white dwarf cooling sequence of several GCs, down to their end (e.g., Bedin et al., 2015; Bedin et al., 2005; Bellini et al., 2013).

Less than one year after launch, *JWST* showed that it can exceed also the level of precision of *HST*, thanks to an accurate modelling of the PSF (Nardiello et al., 2022) and of the geometric distortion (Griggio et al., 2023a; Libralato et al., 2023) of its cameras. *JWST*'s infrared sensitivity will allow us to study objects obscured by dust clouds or those emitting predominantly in the infrared spectrum. Probing these regions is especially useful for astrometric studies of star-forming regions, young stellar clusters and the low-mass objects populating a cluster's main-sequence near and below the hydrogen burning limit. In fact, *JWST*'s larger aperture compared to *HST* enables the observation of fainter and more distant objects: this is valuable for extending astrometric studies to a broader range of celestial bodies, such as the elusive brown dwarf population of star clusters (Nardiello et al., 2023a).

1.1.3 Astrometry with ground-based wide-field imagers

Despite all the benefits of astrometry from above the Earth's atmosphere, there are also some limitations that come with space telescopes. For instance, the limited bandwidth sets a threshold on the amount of data that can be collected by these instruments per hour. For this reason, the detectors are typically undersampled in order to get the maximum sky coverage for the limited number of pixels. This

Table 1.1: List of the instruments used in this thesis with their field of view. *HST* WFC3/UVIS has been included as reference.

Name	Telescope	Detectors	Pix. scale [$''$/px]	Field of view
CFH12K	CFHT	12	0.206	$42' \times 28'$
Asiago	Asiago Schmidt	1	0.868	$59' \times 59'$
Megaprime	CFHT	40	0.187	$1^\circ \times 1^\circ$
VIRCAM	VISTA	16	0.339	$1^\circ \times 1.2^\circ$
WFC3/UVIS	*HST*	2	0.039	$160'' \times 160''$
NIRCam	*JWST*	8	0.031	$260'' \times 130''$

fact introduces a significant complexity to the data analysis, and special care must be taken to derive accurate PSFs (Anderson and King, 2000), such that we can measure positions without biases. Ground-based instruments are not affected by these limitations. They can be made up of several detectors, and can afford to oversample the images, such that accuracy will not be affected. Moreover, they can observe large areas of the sky more efficiently, given the much larger field of view. This is particularly true for wide-field imagers as, e.g., the one mounted at the Asiago telescope used among other instruments in this thesis work, which has a field of view approximately 500 times greater than that of *HST*'s WFC3 detector (see Fig. 1.1 and Table 1.1).

Besides technical limitations, there are several investigations that, by their nature, are better suited to ground-based observations. The study of the outskirts of star clusters, for example, requires mapping large portions of the sky, without the need for high spatial resolution, as these regions are typically less densely populated with respect to cluster's core. In fact, to obtain a comprehensive understanding of cluster evolution, it is necessary to integrate surveys conducted within the cluster core with surveys covering the outer regions. Furthermore, close-by OCs, with few exceptions, are inherently sparse objects that do not fit well within the narrow field of view of the current space telescopes, and the majority of their members can be effectively observed from Earth.

Nonetheless, astrometry plays an essential role in these studies, providing a powerful tool to obtain a pure sample of cluster members decontaminated from field sources, as it does in many projects carried out from space. For this reason, it is of fundamental importance to develop tools to extract the best possible photometry and astrometry also from ground-based telescopes.

Anderson et al. (2006) applied the techniques developed to derive high-precision photometry and astrometry from *HST* images to data taken with the Wide Field

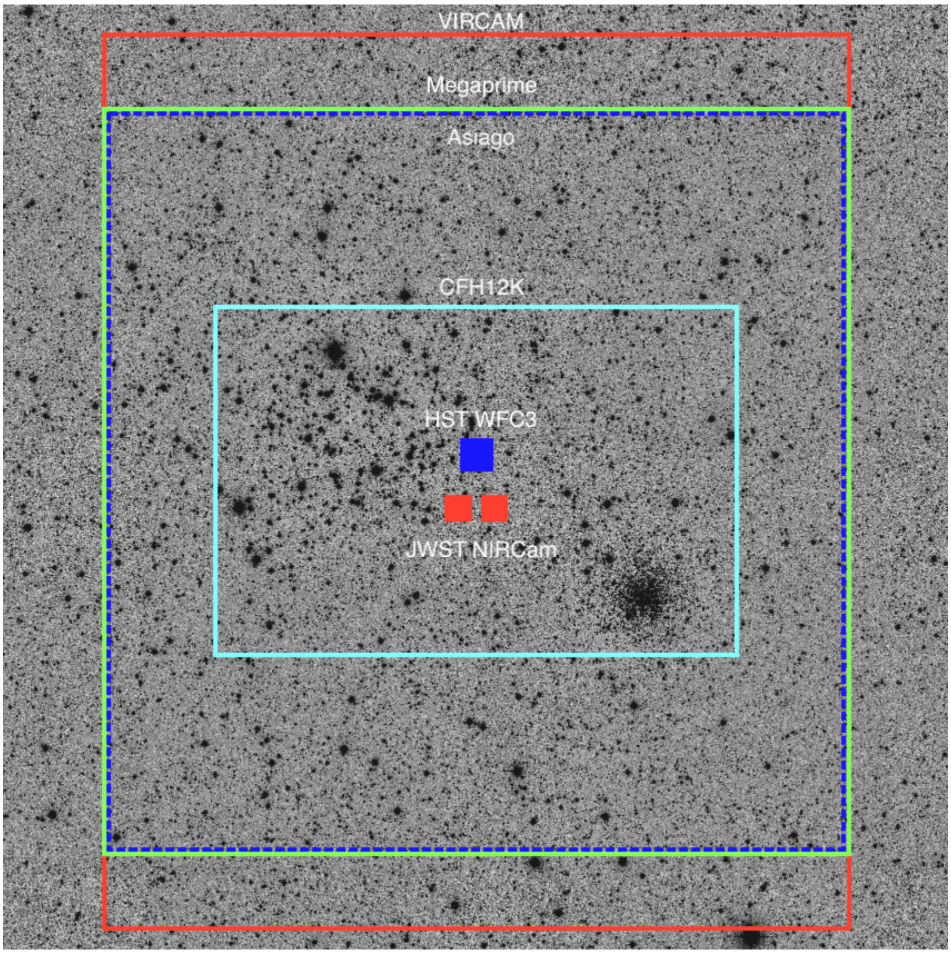

Figure 1.1: Comparison of the field of view of the wide-field imagers used in this thesis with those of *HST* WFC3 UVIS and *JWST* NIRCam, over an image of M35 and NGC 2158 captured with the Asiago Schmidt telescope. See also Table 1.1

Imager (WFI) mounted at ESO 2.2 m telescope at La Silla Observatory, located in the Atacama desert in Chile. The accurate PSF and the detailed modelling of the geometric distortion of the detector allowed them to obtain a precision of $\sim$7 mas in a sigle measurement, and they were able to separate cluster members from field sources in the GCs M4 and NGC 6397.

Following these promising results, several works were devoted to refine the techniques to derive high-precision astrometry from ground-based wide-field imagers. For instance, Bellini et al. (2010) presented for the first time a proper-motion-selected sample of white dwarfs of the old Galactic OC M67 down to the bottom end of the white dwarf cooling sequence. To derive proper motions, they coupled

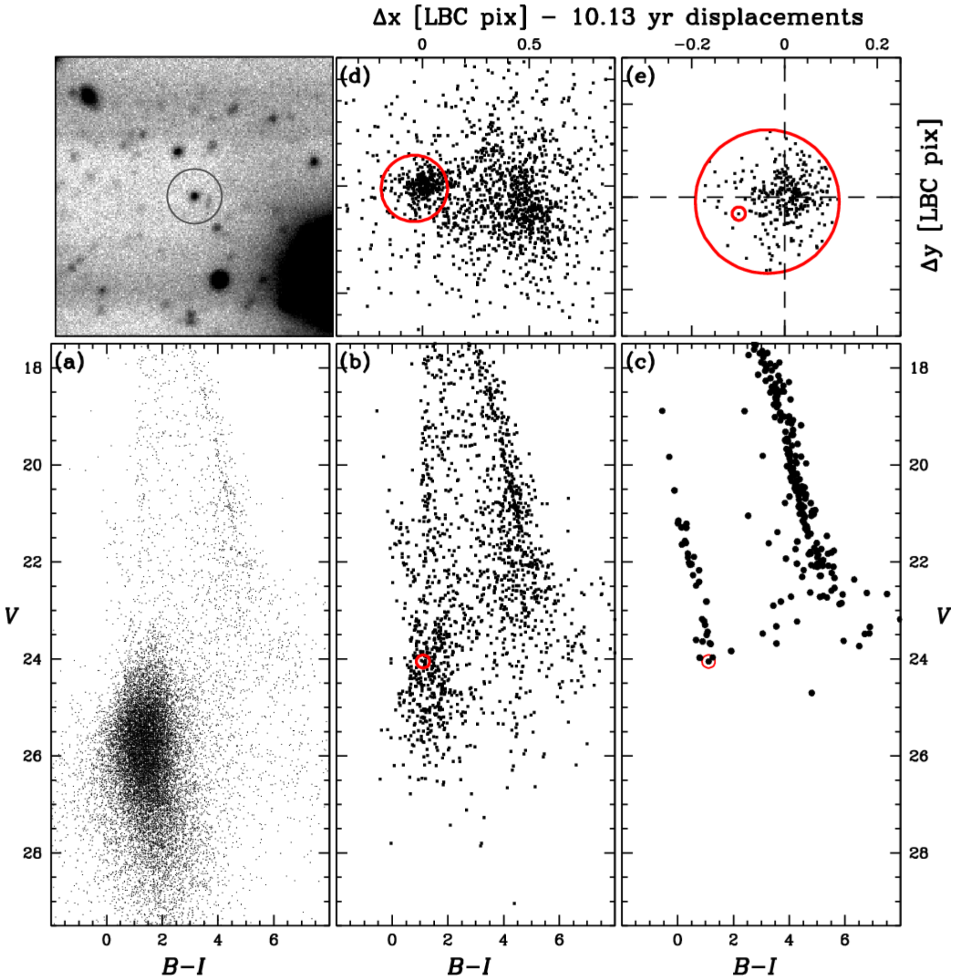

Figure 1.2: Example of proper motion decontamination for the OC M67 from Bellini et al. (2010). See the text for details.

observations of M67 taken with the Large Binocular Telescope with data taken ten years prior with the Canada-France-Hawaii Telescope (CFHT). As an example of proper-motion cluster-field decontamination, we reproduced Fig. 4 of Bellini et al. (2010) in Fig. 1.2. Panel (a) of Fig. 1.2 shows a B vs $(B-V)$ color-magnitude diagram for all the measured objects in the observed field; panel (b) shows only the objects for which proper motions were measured; panel (d) shows the vector-point diagram for the objects in panel (b). A red circle encompasses the most-likely cluster members. Finally, panel (c) and (e) show the color-magnitude and vector-point diagrams for the stars selected in this way, respectively. A small red circle in panels (b), (c) and (e) indicates the faintest proper-motion selected white dwarf, shown in a 30″-width cutout of the B-stacked image in the top left panel. This is a great example of investigation that is more suited to ground-based wide-field imagers, as the coverage of a single LBT pointing would require about 100 *HST* exposures.

Later on, Libralato et al. (2014) applied the same techniques to the near-infrared detector HAWK-I, a wide-field imager mounted at the UT4/VLT ESO 8 m telescope. They were able to achieve a single-image astrometric precision of about 3 mas for well-exposed stars, with systematic errors smaller than 0.1 mas. They combined the HAWK-I observations of the GC NGC 6656 with WFI archival data to derive proper motions and isolate member stars. This allowed the study of the radial distribution of sub-giant branch stars in the cluster's outer regions, complementing the observations of the cluster's core carried out with *HST* by Piotto et al. (2012), thus highlighting the synergies between ground- and space-based telescopes.

Both these works have shown that an accurate modelling of the geometric distortion is of fundamental importance in obtaining high-precision astrometry. Imaging distortion arises from several factors, such as misalignments of the optics of the telescope, inhomogeneities in the filters that result in different paths of the photons, detector defects and misalignments of the detectors themselves. It leads to systematic errors in the positions that can vary from few pixels to several tenths of pixels, depending on the severity, affecting the astrometric accuracy. Moreover, it can also affect photometry, as it alters the pixels' area on the sky.

Projection effects in large mosaics

In addition to the geometric distortion, Libralato et al. (2015) showed that, when dealing with largely dithered wide-field images, one must also take into account projection effects. The positions of stars measured in an astronomical image intrinsically lie on a plane tangent to the celestial sphere at the central point of the exposure (as in a gnomonic projection). Comparing positions measured in different exposures on different tangent planes introduces systematic errors. These errors are basically negligible for small dithers and small field of views. However, achieving high-precision astrometry with wide-field imagers requires to account for these projection effects.

Projecting equatorial coordinates (α, δ) onto the plane tangent to the celestial sphere at the point (α_0, δ_0) can be accomplished with the relations (see, e.g., Bedin and Fontanive, 2018)

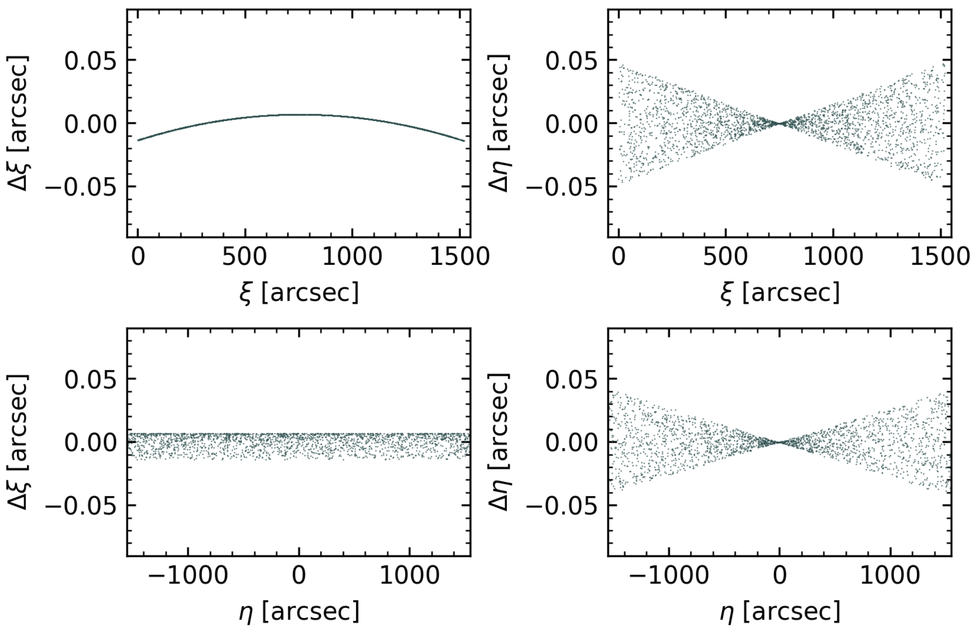

Figure 1.3: Positional residuals from the inter-comparison of positions lying in different tangent planes. See the text for details.

$$\begin{cases} \xi = \dfrac{\cos\delta\sin\left(\alpha-\alpha_\circ\right)}{\sin\delta_\circ\sin\delta+\cos\delta_\circ\cos\delta\cos\left(\alpha-\alpha_\circ\right)} \\ \eta = \dfrac{\cos\delta_\circ\sin\delta-\sin\delta_\circ\cos\delta\cos\left(\alpha-\alpha_\circ\right)}{\sin\delta_\circ\sin\delta+\cos\delta_\circ\cos\delta\cos\left(\alpha-\alpha_\circ\right)} \end{cases},$$

where (ξ,η) are the coordinates in the reference system on the tangent plane. The tangent points coordinates (α_0,δ_0) are mapped to $(\xi,\eta)=(0,0)$. The ξ- and η-axis are oriented as (α,δ), with ξ having the opposite direction with respect to α.

The relations to project tangent-plane coordinates back onto equatorial angles are given by

$$\begin{cases} \alpha = \alpha_\circ + \tan^{-1}\left(\dfrac{\xi}{\cos\delta_\circ - \eta\ \sin\delta_\circ}\right) \\ \delta = \tan^{-1}\left(\cos\left(\tan^{-1}\left(\dfrac{\xi}{\cos\delta_\circ-\eta\ \sin\delta_\circ}\right)\right)\dfrac{\sin\delta_\circ+\eta\cos\delta_\circ}{\cos\delta_\circ-\eta\sin\delta_\circ}\right) \end{cases}.$$

This projection does not preserve distances. To compare the positions measured in two dithered images, six-parameters linear transformations are usually employed, to transform the coordinates relative to one image into the reference frame of the other. For small dithers, these transformations are enough to absorb the projection effects.

However, this is not the case for largely dithered mosaics. To illustrate the effect we simulated a catalogue of (α, δ) positions. The simulated positions are around the center of the OC M37 ($\alpha = 88.074, \delta = +32.545$). We projected the equatorial angles onto two tangent planes with tangent points differing by 0.5 deg only in α, mimicking two images dithered only in one direction. Notice that wide-field mosaics can be dithered even more than 0.5 deg (see, e.g., Griggio et al., 2022a). Using a six-parameter linear transformation we transformed the coordinates of one tangent plane into the reference frame of the other one. Cross-matching the sources yields the positional residuals displayed in Fig. 1.3. The projection effects are similar to those of geometric distortion. The residuals shown in Fig. 1.3 are up to 50 mas, but depending on the dither they can be even larger. Assuming the pixel scale of the Megaprime detector – one of those used in this thesis – mounted at the focus of CFHT (0.187 arcsec per pixel, Table 1.1), these errors correspond to $\sim$0.2-0.3 pixels, which is much larger than the precision enabled by the geometric distortion solution.

1.2 The aim of this thesis

In this thesis, we carry out several investigations on star clusters with ground-based observations. We export the state-of-the-art techniques to obtain high-precision photometry and astrometry with *HST* to ground-based detectors, extending the efforts described in the previous sections to other wide-field imagers. In particular, we will show how, by exploiting the *Gaia* absolute reference frame, it is possible to derive an accurate geometric distortion solution without the need for a dedicated set of observations. We will also develop routines to account for projection effects in wide-field data.

In Chapter 2, we focus on the membership probability, a key quantity in the study of star clusters, that tells us how likely is a source to belong to the a cluster. We extend the formalism to compute the astrometric membership probability in order to include the contribution of the parallax, which is now available with unmatched precision for a large number of sources thanks to *Gaia*. In Chapter 3, we use observations of the OC M37 obtained with the Asiago Schmidt telescope to study its high-mass white dwarf members. In Chapter 4, we apply our techniques to observations of M37 acquired with the CFHT. We derive proper motions for sources well beyond the *Gaia* reach, coupling our dataset with observations taken in 1999. The data allow us to study in details its white dwarf cooling sequence down to its end. In Chapter 5, we couple the Asiago Schmidt photometry with the *Gaia* catalogue to investigate the unusual broadening of M37's main sequence. A similar analysis is carried out for the OC M38 in Chapter 6. In Chapter 7, we applied our techniques to derive the geometric distortion correction of the NIRCam detector onboard of *JWST*. We show how we are able to obtain a precision that exceeds that of the official pipeline solution. We also use publicly-available calibration data to showcase the astrometric capabilities of *JWST*. In Chapter 8 we use *JWST* data of the GC 47 Tuc to study its low mass members. In Chapter 9, we develop a new pipeline to reprocess the data from the *Vista Variables in the Via Lactea* survey, to exploit its multi-epoch observations of the Galactic bulge to extend the *Gaia* astrometry to dust-obscured regions where *Gaia* is severely limited. We conclude with Chapter 10, with a summary of the work and an overview of the future prospects.

2. Star cluster membership probability[1]

In this chapter, starting from the well-accepted relations in literature, we introduce a new formalism to compute the astrometric membership probabilities for sources in star clusters, and we provide an application to the case of the open cluster M37. The novelty of our approach is a refined –and magnitude-dependent– modelling of the parallax distribution of the field stars. We employ the here-derived list of members to estimate the cluster's mean systemic astrometric parameters, which are based on the most recent *Gaia*'s catalogue (EDR3).

2.1 Introduction

Star clusters represent one of our most important sources of knowledge of stellar formation and evolution: the measurements of their distance, age and chemical composition provide strong constraints on astrophysical models of stellar evolution. Star clusters consist of gravitationally bound stars which share the same distance and center of mass motion, and they appear as a stellar over-density in a region of the sky. In the studies of these objects one of the most crucial steps is the determination of the membership probability of the observed stars, to distinguish actual members of the cluster from field stars that lie in the same region but are not bound to the cluster.

Traditionally, the problem of estimating membership probabilities using the astrometric parameters of the sources has been treated with techniques that were developed in the pioneering work by Vasilevskis et al. (1958) and Sanders (1971). In their works the distribution of sources in the vector-point diagram (VPD) is modelled as a mixture of two Gaussian distributions, one for the cluster members and another one for the field sources. This method was further refined by the

[1]The content of this chapter has been published in Griggio and Bedin (2022).

contribution of several authors (see Balaguer-Núnez et al., 1998; Tian et al., 1998, and refs therein).

An additional improvement of this technique introduced by Kozhurina-Platais et al. (1995) foresees the partition of the data in brightness (a *sliding window* in magnitude) and spatial bins when deriving the parameters of the distributions. One of the advantages of using a "local sample" approach is that membership probabilities are not biased by possible differences in the shape of the field and cluster luminosity functions, or in proper motion accuracy for bright and faint stars.

In this work we discuss an improvement of the astrometric method exploiting the *Gaia* astrometry to increase the separation between cluster and field stars.

Including parallaxes provides additional information to estimate membership probabilities. While multiple publications since 1998 have taken into account Hipparcos (e.g. Baumgardt et al., 2000; Robichon et al., 1999), and later *Gaia* (e.g. Cantat-Gaudin et al., 2018b; Castro-Ginard et al., 2018; Gagné et al., 2018; Monteiro et al., 2020) parallaxes, none of these works introduced a proper formalism, with the only exception of Monteiro et al. (2020), which however made an over-simplification that will be discussed later.

This paper is organized as follows: in Section 2.2 we review the classical formalism used to compute the membership probability, in Section 2.3 we introduce the new term to account for the parallax distribution, while in Section 2.4 we compare the membership calculated with this new term and without it, taking the open cluster M37 as a test case. In Sections 2.5 and 2.6 we use the membership probability to select a list of cluster's members and we use them to derive a new estimate of the cluster's mean proper motion and parallax. We also publicly release a catalogue of all the sources with the membership probabilities. Finally, in Section 2.7 we provide a summary of this work.

2.2 Membership probability: the classical approach

In this section we will review the formalism "traditionally" employed to determine the membership probability of the i-th star using four out of its five astrometric parameters, namely its position (x_i, y_i) and its proper motion (μ_{x_i}, μ_{y_i}). We will follow the formulation from Tian et al. (1998) and Balaguer-Núnez et al. (1998).

In these works the cluster membership probability of the i-th star is calculated as

$$P_{\rm c}(i) = \frac{\Phi_{\rm c}(i)}{\Phi(i)}, \tag{2.1}$$

where $\Phi_{\rm c}$ is the cluster distribution function and Φ is the total distribution given by

$$\Phi = \Phi_{\rm c} + \Phi_{\rm f}, \tag{2.2}$$

with $\Phi_{\rm f}$ the distribution function of field stars. The distribution function of cluster (and field) stars is given by the contribution of two terms, i.e.,

$$\Phi_{\rm c/f} = n_{\rm c/f} \cdot \Phi^{v}_{\rm c/f} \cdot \Phi^{r}_{\rm c/f}, \tag{2.3}$$

in which Φ^v is the distribution function in the velocity space, Φ^r is the distribution function in the position space and n is the normalized number of stars ($n_{\rm c}+n_{\rm f} = 1$).

For the cluster velocity distribution they adopt an asymmetric 2D Gaussian in the form:

$$\begin{aligned}\Phi^{v}_{\rm c}(i) =& \frac{1}{2\pi(\sigma^2_{\mu_{x\rm c}} + \epsilon^2_{\mu_{x_i}})^{1/2}(\sigma^2_{\mu_{y\rm c}} + \epsilon^2_{\mu_{y_i}})^{1/2}} \\ & \exp\left\{-\frac{1}{2}\left[\frac{(\mu_{x_i} - \mu_{x\rm c})^2}{\sigma^2_{\mu_{x\rm c}} + \epsilon^2_{\mu_{x_i}}} + \frac{(\mu_{y_i} - \mu_{y\rm c})^2}{\sigma^2_{\mu_{y\rm c}} + \epsilon^2_{\mu_{y_i}}}\right]\right\},\end{aligned} \tag{2.4}$$

where (μ_{x_i}, μ_{y_i}) are the proper motions of the i-th star, $(\mu_{x\rm c}, \mu_{y\rm c})$ is the cluster proper motion center, $(\sigma_{\mu_{x\rm c}}, \sigma_{\mu_{y\rm c}})$ is the intrinsic proper motion dispersion of member stars and $(\epsilon_{\mu_{x_i}}, \epsilon_{\mu_{y_i}})$ are the observed errors of the proper motions of the i-th star. Similarly, for the field stars velocity distribution we have

$$\begin{aligned}\Phi^{v}_{\rm f}(i) =& \frac{1}{2\pi\,(1-\gamma^2)^{1/2}\,(\sigma^2_{\mu_{x\rm f}} + \epsilon^2_{\mu_{x_i}})^{1/2}(\sigma^2_{\mu_{y\rm f}} + \epsilon^2_{\mu_{y_i}})^{1/2}} \\ & \exp\left\{-\frac{1}{2\,(1-\gamma^2)}\left[\frac{(\mu_{x_i} - \mu_{x\rm f})^2}{\sigma^2_{\mu_{x\rm f}} + \epsilon^2_{\mu_{x_i}}}\right.\right. \\ & \left.\left. - \frac{2\gamma\,(\mu_{x_i} - \mu_{x\rm f})\,(\mu_{y_i} - \mu_{y\rm f})}{(\sigma^2_{\mu_{x\rm f}} + \epsilon^2_{\mu_{x_i}})^{1/2}(\sigma^2_{\mu_{y\rm f}} + \epsilon^2_{\mu_{y_i}})^{1/2}} + \frac{(\mu_{y_i} - \mu_{y\rm f})^2}{\sigma^2_{\mu_{y\rm f}} + \epsilon^2_{\mu_{y_i}}}\right]\right\},\end{aligned} \tag{2.5}$$

where (μ_{x_i}, μ_{y_i}) are the proper motions of the i-th star, γ is the correlation coefficient between μ_{x_i} and μ_{y_i}, $(\mu_{x\rm f}, \mu_{y\rm f})$ the field proper motion center, $(\epsilon_{\mu_{x_i}}, \epsilon_{\mu_{y_i}})$ the observed errors of the proper motions of the i-th star and $(\sigma_{\mu_{x\rm f}}, \sigma_{\mu_{y\rm f}})$ the field intrinsic proper motion dispersion.

For the spatial distribution of cluster members a simple (and sufficient for the purpose) approximation is to use a Gaussian profile:

$$\Phi_{\rm c}^{r}(i) = \frac{1}{2\pi r_{\rm c}^2} \exp\left\{ -\frac{1}{2} \left[\left(\frac{x_i - x_{\rm c}}{r_{\rm c}} \right)^2 + \left(\frac{y_i - y_{\rm c}}{r_{\rm c}} \right)^2 \right] \right\}, \tag{2.6}$$

in which (x_i, y_i) is the position of the i-th star, $(x_{\rm c}, y_{\rm c})$ the center of the cluster and $r_{\rm c}$ the characteristic radius. The field star spatial distribution is assumed to be flat:

$$\Phi_{\rm f}^{r}(i) = \frac{1}{\pi r_{\rm max}^2}, \tag{2.7}$$

where $r_{\rm max}$ is the radius of the portion of the sky under exam (assuming it has a circular shape).

This method to compute the membership probabilities was applied in a number of papers in the recent literature (see for example Bellini et al., 2009a; Nardiello et al., 2018b; Scalco et al., 2021; Yadav et al., 2008).

2.3 Including the parallax

The *Gaia* EDR3 (Gaia Collaboration et al., 2016a, 2021) catalogue is an unprecedented astronomical data set in terms of its size and astrometric precision and accuracy. In particular, it provides the full 5-parameter astrometric solution (positions, proper motions and parallaxes) and magnitudes in its three photometric bands (G, G_{BP}, G_{RP}) for more than 1.4 billion sources, with a limiting magnitude of about $G \approx 21$ and a bright limit of about $G \approx 3$. Thanks to the *Gaia* EDR3 exquisite astrometry we can extend the formalism presented in the previous section including a new term to take into account the parallax distribution. Particularly, the parallax uncertainties in the EDR3 are $0.02 - 0.03$ mas for $G < 15$, 0.07 mas at $G = 17$, 0.5 mas at $G = 20$ and 1.3 mas at $G = 21$ (Lindegren et al., 2021b). This unmatched level of precision allows us to include the parallax in the computation of the membership probability, thus achieving a more robust estimate for this fundamental quantity.

To account for the parallax distribution we rewrite Equation 2.3 as:

$$\Phi_{\rm c/f} = n_{\rm c/f} \cdot \Phi_{\rm c/f}^{\upsilon} \cdot \Phi_{\rm c/f}^{r} \cdot \Phi_{\rm c/f}^{\varpi}, \tag{2.8}$$

where $\Phi_{\rm c/f}^{\varpi}$ is the distribution function of the parallaxes for the cluster members and for the field stars.

We can assume that the parallaxes of cluster members are normally distributed, such that:

$$\Phi_{\rm c}^{\varpi}(i) = \frac{1}{\left(2\pi(\sigma_{\varpi_{\rm c}}^2 + \epsilon_{\varpi_i}^2)\right)^{1/2}} \exp\left\{-\frac{1}{2}\left(\frac{\varpi_i - \varpi_{\rm c}}{\sigma_{\varpi_{\rm c}}^2 + \epsilon_{\varpi_i}^2}\right)^2\right\}, \tag{2.9}$$

where $(\varpi_i, \varpi_{\rm c})$ are the parallax of the i-th star and of the cluster respectively, ϵ_{ϖ_i} are the observed errors of the parallax of the i-th star and $\sigma_{\varpi_{\rm c}}$ the cluster intrinsic parallax dispersion (in the case where the size of the cluster is not negligible compared to its distance).

However, modeling the distribution function of the parallaxes of field stars, $\Phi_{\rm f}^{\varpi}$, is more complicated: we are not observing an ensemble of stars all at the same distance, or at an average distance with a normal distribution around the mean. In the case of the parallaxes of the field we are rather observing the closest stars to the Sun and stars potentially well into the Galactic Halo. The exact distribution function of stars in the Galactic field in different directions and at the various magnitudes is hard to model, and to derive an accurate distribution is well beyond the purpose of this paper. For our purposes, it will be sufficient to adopt a simple approximation, analogous to what described in Eq. 2.5 for the proper motion distribution of field objects $\Phi_{\rm f}^{v}$ (which is a widely accepted approximation in literature). To reproduce the field stars' parallax distribution we adopted a sum of two Gaussian functions, which are assumed to model as well the measurement errors in the parallaxes. This choice let us reproduce very well the parallax at each magnitude bin without complicating too much our formalism. Therefore, we have:

$$\begin{aligned}\Phi_{\rm f}^{\varpi} = &\frac{A_1}{(2\pi\sigma_{1_{\rm f}}^2)^{1/2}} \exp\left\{-\frac{1}{2}\left(\frac{\varpi_i - \varpi_{1_{\rm f}}}{\sigma_{1_{\rm f}}^2}\right)^2\right\} \\ &+ \frac{A_2}{(2\pi\sigma_{2_{\rm f}}^2)^{1/2}} \exp\left\{-\frac{1}{2}\left(\frac{\varpi_i - \varpi_{2_{\rm f}}}{\sigma_{2_{\rm f}}^2}\right)^2\right\},\end{aligned} \tag{2.10}$$

where A_1, A_2, $\varpi_{1_{\rm f}}$, $\varpi_{2_{\rm f}}$, $\sigma_{1_{\rm f}}$ and $\sigma_{2_{\rm f}}$ are the parameters of the two Gaussian and ϖ_i the parallax of the i-th star. We verified that this simple model for the distribution of the parallaxes for field objects is a general valid approximation. To this aim, we downloaded portions of the *Gaia* EDR3 catalogue in various directions of the sky, to probe different parts of the Galactic field. The obtained *Gaia* EDR3 distributions of the parallaxes for field objects at various magnitudes were always represented – within the statistical sampling errors – by our simple model.

We note here that Monteiro et al. (2020) followed a method that is qualitatively similar to ours, but they do not use the sliding window approach and they adopted a single Gaussian model; while this assumption works well in the case of parallaxes dominated by errors (faint stars), it does not represents well the intrinsic parallax distribution of field stars when uncertainties are small. We show a detailed comparison of the two models in the next section.

2.4 Example: the case of M37

We considered the open cluster M37 (NGC 2099) as a test case for this new formalism for the computation of the membership probabilities. We downloaded a portion of the *Gaia* EDR3 catalogue centered on M37 ($\alpha_{\rm c} = 88.074$ deg, $\delta_{\rm c} = +32.545$ deg, Cantat-Gaudin and Anders, 2020, hereafter CG20) with a radius of 1.5 deg, and we computed the membership probability for each source both including and neglecting the contribution from the *Gaia* parallaxes. We adopted a sliding window in magnitude of 1.5 mag, which we found as a good compromise between having a good statistics at all magnitudes and considering sources with magnitude similar to the target star. As initial guess, we employed for the cluster's systemic proper motion[2] $(\mu_{x_{\rm c}}, \mu_{y_{\rm c}}) = (\mu_{\alpha_c}, \mu_{\delta_c}) = (1.924, -5.648,)$ mas/yr and for the systemic parallax $\varpi_{\rm c} = 0.666$ mas, which are the values given by CG20.

We started by estimating the intrinsic dispersion of the proper motions of the cluster, i.e. $\sigma_{\mu_{x_{\rm c}}}$ and $\sigma_{\mu_{y_{\rm c}}}$ of Eq. 2.4. We selected the members of M37 for which CG20 give their clustering score equal to one (the highest score), choosing only the sources with $G < 17$ (where the *Gaia* errors are of the order, 10^{-2} mas/yr). We σ-clipped the values at 3-σ around the median, and then we calculated the $68.27^{\rm th}$ percentile of the residuals from the median of μ_α and μ_δ, which we assumed as the observed dispersion. Subtracting in quadrature from the observed dispersion the median observational relative errors provided by *Gaia* EDR3 gives a reasonable estimate of the cluster intrinsic dispersion. We obtain $\sigma_{\mu_{x_{\rm c}}} = \sigma_{\mu_\alpha} = 137\,\mu$as and $\sigma_{\mu_{y_{\rm c}}} = \sigma_{\mu_\delta} = 138\,\mu$as. Note that at a corresponding distance of 1.5 kpc (for $\varpi = 0.666$ mas), these translate into transverse velocities of less than 1 km/s, which is a reasonable value for such an open cluster (e.g. seeCG20, and refs therein). The values for proper motions and estimated errors of individual sources in the Eq. 2.4 are taken straight from the *Gaia* EDR3 catalog, i.e.: $\mu_{x_i} = \mu_{\alpha_i}$, $\mu_{y_i} = \mu_{\delta_i}$, $\epsilon_{x_i} = \epsilon_{\mu_{\alpha_i}}$, and $\epsilon_{y_i} = \epsilon_{\mu_{\delta_i}}$.

The parameters $\mu_{x(y)_{\rm f}}$ and $\sigma_{\mu_{x(y)_{\rm f}}}$ of Eq. 2.5 have been estimated from the sources in the magnitude window of the star under exam. We adopted as $\mu_{x(y){\rm f}}$ the median values of the proper motion of field objects, and the $68.27^{\rm th}$ percentile of the residuals around these median as the observed dispersion: $\sigma^{\rm obs}_{\mu_{x(y)_{\rm f}}}$. We

[2] Where for conciseness in the notation we indicate $\mu_{\alpha\cos\delta_{\rm c}}$ with μ_{α_c}

then calculated the average observational error of the sources in the magnitude window, $\epsilon_{\mu_{x(y)_\mathrm{f}}}$, by clipping the errors at 3-σ and computing the median. This value is then used to calculate the intrinsic dispersion for field proper motion as: $\sigma^2_{\mu_{x(y)_\mathrm{f}}} = (\sigma^{\mathrm{obs}}_{\mu_{\mathrm{x(y)_f}}})^2 - \epsilon^2_{\mu_{x(y)_\mathrm{f}}}$, which are the ones to be used in Eq. 2.5. Again, for individual sources the values for proper motions and proper motion errors in the Eq. 2.5 are taken from the *Gaia* EDR3 catalog.

To deal with the spatial distribution, we projected the *Gaia* coordinates (α_i, δ_i) on the tangent plane (ξ, η), adopting the center of the cluster as tangent point $(\alpha_\mathrm{c}, \delta_\mathrm{c})$, employing standard relations (e.g., see Eq. 3 in Bedin and Fontanive, 2018). Therefore, the coordinates on the tangent plane became $x_i = \xi_i$ and $y_i = \eta_i$ in Eq. 2.6. The estimate of r_c of Eq. 2.6 have been performed from the stars in the magnitude bin of the target; we calculate r_x (r_y) as the 68.27$^{\mathrm{th}}$ percentile of the residuals from x_c (y_c), and we adopt as cluster radius in the magnitude bin $r_c^2 = r_x^2 + r_y^2$. This procedure allows us to account for the different distributions of the stars in each magnitude bin, which is a proxy for different mass-bins (at least along the Main Sequence). The parameter r_{max} of Eq. 2.7 is the radius of the *Gaia* EDR3 slice that we considered, i.e. $r_{\mathrm{max}} = 1.5\,\mathrm{deg}$.

The intrinsic dispersion of the parallaxes ($\sigma_{\varpi_\mathrm{c}}$ in Eq. 2.9) is negligible for M37 and it can be set equal to zero. Again, for this initial computation we adopt for the cluster average parallax the value from CG20, while the values of the parallax (ϖ_i) and parallax error (ϵ_{ϖ_i}) for individual sources are those given by the *Gaia* EDR3 catalog. In the next sections we will then derive our own estimates for the cluster mean proper motions and parallax, employing *Gaia* EDR3 instead of the DR2, and finally re-compute the updated membership probabilities.

For the distribution of parallaxes in the Galactic field we used Eq. 2.10, so we fitted the distribution in each magnitude window with a sum of two Gaussian functions. From the fit we obtain the $\tilde{\sigma}_{1(2)_\mathrm{f}}$ parameters, which contain also the contributions of errors in parallaxes at the considered magnitude. To account for the observational errors, we compute the quantity $\sigma'^2_{1(2)_\mathrm{f}} = \tilde{\sigma}^2_{1(2)_\mathrm{f}} - \bar{\epsilon}^2_{1(2)_\mathrm{f}}$, where $\bar{\epsilon}_{1(2)_\mathrm{f}}$ is the median error of the stars in the magnitude window that we are considering, calculated after performing a 3-σ clip. These are the values employed in Eq. 2.10, which are the sum in quadrature of intrinsic distributions and errors, $\sigma^2_{1(2)_\mathrm{f}} = \sigma'^2_{1(2)_\mathrm{f}} + \epsilon^2_{\varpi_i}$. We then used the *Gaia* EDR3 values for the parallax ϖ_i and parallax error ϵ_{ϖ_i}. In Figure 2.1 we show the distribution of the parallaxes in the M37 field of view, for different magnitude bins, where for comparison we show the fitted distribution of the parallaxes of cluster+field stars obtained in the case of a two-Gaussian model (solid line) and in the case of one-Gaussian model (dotted line).

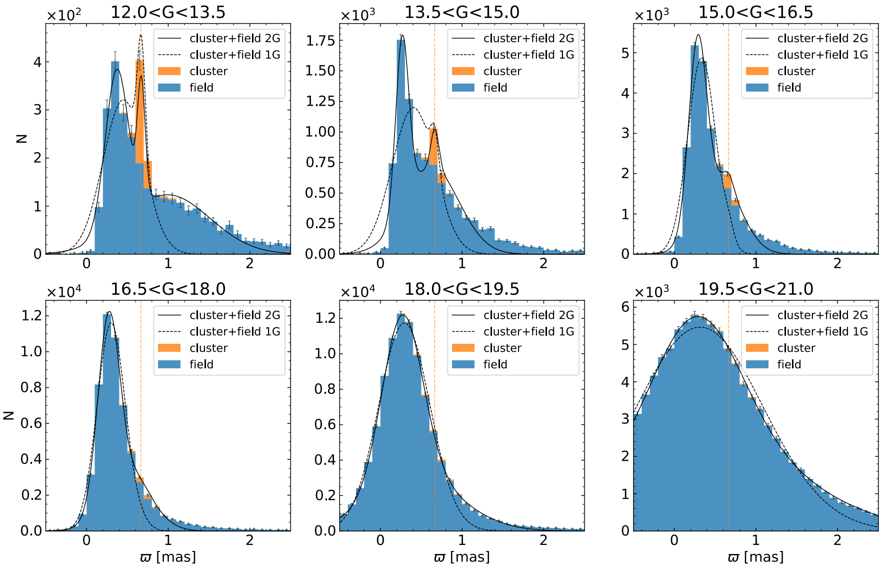

Figure 2.1: Parallax distribution in different magnitude bins in the M37 field of view. We plotted in orange the stars with parallax within 0.2 mas from the cluster's mean parallax and proper motions within a circle of 0.5 mas/yr in radius centered on the cluster's mean proper motions. Mean values were obtained from Cantat-Gaudin and Anders (2020). The solid black line represents the sum of the Gaussian of the cluster and the field modelled with two Gaussian functions, while the dashed black line is the same but using a single Gaussian to model the field's parallax distribution.

We finally computed the membership probability, hereafter P_ϖ, following Eq. 2.8, which includes the parallax, and we compared it with the membership probability calculated without including the parallax, i.e. P, computed according to Eq. 2.3. The results show that including the parallax term allow us to better separate the cluster members from the field stars, in particular at fainter magnitudes ($16 < G < 18$).

In the top panel of Figure 2.2 we show the membership probability calculated with the standard approach, without the parallax term, while on the bottom panel we show the results obtained including the parallax. In the left panels ($0\,\% < P < 95\,\%$) we can see that there are considerably less sources with magnitudes in the range $10 < G < 19$ within $25\,\% < P < 75\,\%$ if we account for the parallax distribution (372 sources in the top panel, 282 in the bottom), confirming that the discrimination between member and field stars is better.

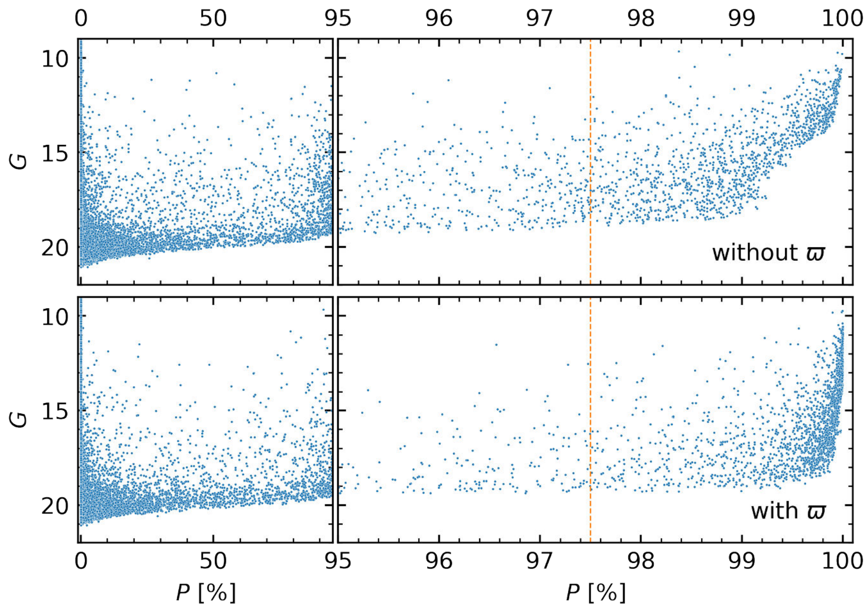

Figure 2.2: Comparison between the membership probability calculated without the parallax term (top) and accounting for the parallax of the sources (bottom); $P > 95\,\%$ are zoomed on the right panels. Vertical orange line indicates $P = 97.5\,\%$.

In Figure 2.3 (top) we plotted the maximum membership probability per magnitude bin versus the *Gaia* G magnitude. The blue and red lines represent the probability calculated with and without taking into account the parallax respectively. This plot shows us that very high membership probabilities extend deeper when considering the parallax contribution in the calculation (about 1 mag at $P_{\mathrm{max}} = 99\,\%$).

We then divided the sources in magnitude bins of 1 mag, and calculated the number of sources in each bin with $P > 97.5\,\%$. In Figure 2.3 (bottom) we plot the results: in blue we show the points obtained without accounting for the parallax, in red those obtained including the parallax in the membership calculation. It is clear that for $G \gtrsim 14$ we find more member stars if we use the parallax term. In total we found 1266 sources with $P \geq 97.5\,\%$, and 1824 sources with $P_{\varpi} \geq 97.5\,\%$ in the region $10 < G < 20$, where P_{ϖ} is the membership probability calculated with the formalism introduced in this work.

Figure 2.4 shows a comparison between CG20 and this work. In the left column we show all the sources in the catalog; in this figure we limit the sample only to sources within a radius of 0.3 deg (slightly more than the cluster radius given by

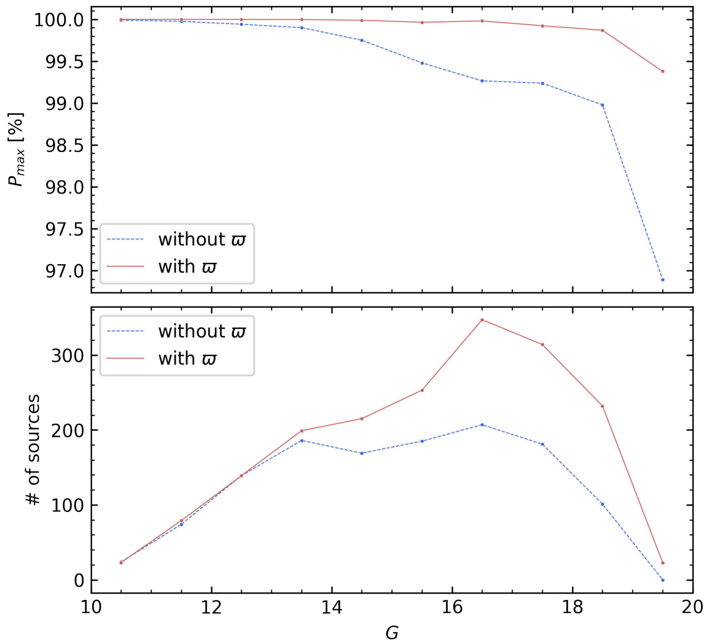

Figure 2.3: Top: maximum membership probability per magnitude bin. The dashed blue (solid red) line is the membership probability computed without (with) taking into account the parallax distribution. Bottom: number of sources per magnitude bin. The dashed blue (solid red) line is the number of sources with $P > 97.5\,\%$ ($P_\varpi > 97.5\,\%$).

Dias et al., 2002) from the center of the cluster, as the number of field objects beyond this limit would overwhelm the plot, making the comparisons less clear.

In the central column we show the stars with $P \geq 0.9$ (top panel) and with $P_\varpi \geq 90\,\%$ (bottom panel). The clustering score given by CG20 is provided only for stars brighter than $G = 18$ (black dashed line) and according to the authors is a proxy for cluster membership probability. However the Main Sequence of M37 clearly extends (and it is well populated) also to fainter magnitudes than that limit. In the common region analysed by both works ($G \leq 18$) we found about 200 extra sources with membership probability greater than 90%, with respect to those with clustering score greater than 0.9 by CG20. Nevertheless, the most interesting plots are shown in the right column, where we plotted the sources that did not pass the membership selection; in the top panel we highlighted in red the sources that did not pass the $P > 0.9$ selection in the middle-top panel, but that passed the $P > 90\%$ membership probability of the present work. Conversely, the stars in red in the bottom-right panel are those members according to $P > 0.9$ in

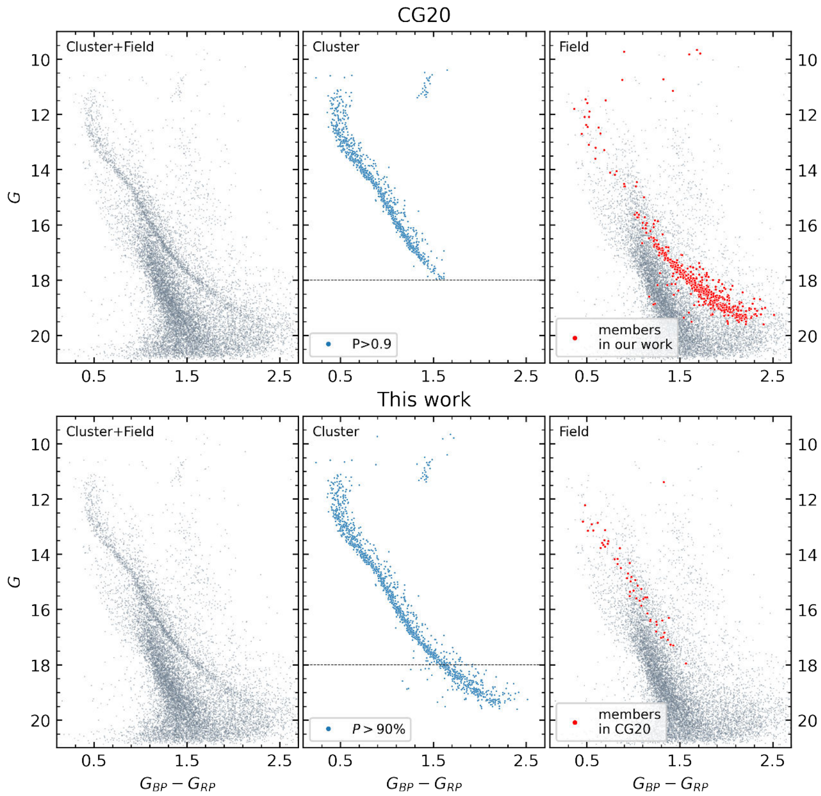

Figure 2.4: Color-magnitude diagram of the sources in M37 field of view: top panels show members identified by CG20, while bottom panels show the members selected in this work. Left: all the sources. Center: sources with $P \geq 0.9\,\%$ (top) and $P_\varpi \geq 90\,\%$ (bottom). Right: sources with $P < 0.9\,\%$ (top) and $P_\varpi < 90\,\%$ (bottom); in the top (bottom) panel we highlighted in red the sources that passed the membership cut in the bottom (top) row. See text for more details.

GC20, but not to the here derived $P > 90\%$. Apart from the obvious improvement of the present work in finding members beyond $G > 18$, we note a significant improvement in identifying members also in the magnitude range $16 < G < 18$.

2.5 Astrometric Parameters of M37

To derive the mean astrometric parameters of M37 from the EDR3 catalog, we first need to select the most probable cluster members. The selection procedure is illustrated in Figure 2.5. In the top-left panel we show the membership probability

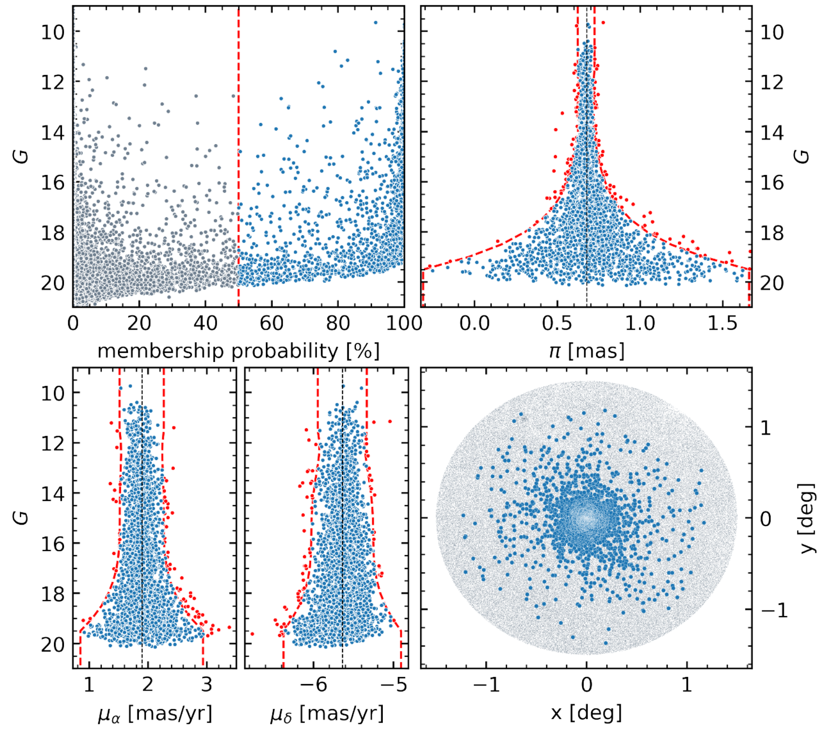

Figure 2.5: Members selection. Top left: membership probability for all the sources. We reject the stars with $P < 50\,\%$. Top right: G magnitude vs parallax. Here we reject the stars that fall outside the region delimited by the two red lines. The black dashed line represents the median parallax. Bottom left: proper motion of the sources vs their G magnitude. We kept the sources between the red dashed lines. The vertical black line is the median proper motion. Bottom right: spatial distribution of the sources. Blue markers are the selected members of M37.

plotted against the G band magnitude. We started by rejecting all the sources with membership probability lower than 50%. Among these sources we rejected those falling outside the area delimited by the two red dashed line on the top-right panel. To define these red lines we proceeded as follows: first we divided the stars into G-magnitude bins of 0.5, for each bin we calculated the 3σ-clipped median of the errors on the parallax given by the EDR3, and we took this median –multiplied by a factor of 2.5– as the maximum error for members at the given G-magnitude. We then define the red lines as a spline through these maxima. In the bottom-left panels we applied a similar cut, but we did not use the measurements errors on the proper motion from the *Gaia* catalogue as the errors are much smaller than the intrinsic proper motion dispersion of cluster members (especially at the brighter

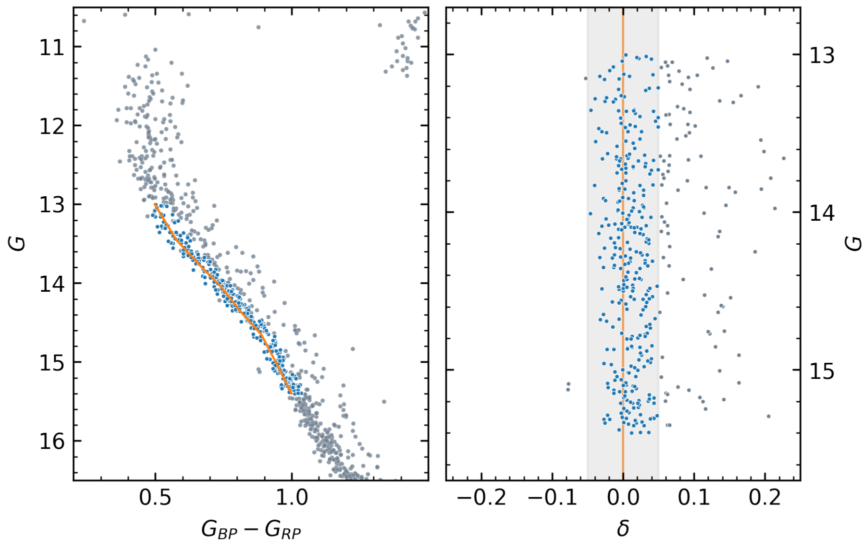

Figure 2.6: Left: color-magnitude diagram showing in blue the sources that we used to estimate the mean parameters of M37. Right: colour residuals from the fiducial for the stars in the selected sample; we used the sources in the shaded gray area which corresponds to 1σ.

magnitudes). Therefore, to define the widths of each bin we used instead the 68.27^{th} of the observed residuals from the median (defined after a 3σ-clipping), and again multiplied by a factor of 2.5. On the bottom-right panel we show the spatial distribution of the stars that passed all these four selections and which we then we consider as most probable members of M37.

We then further restrict this sample to the very best stars, requiring:

1. $P_{\varpi} > 99.5\,\%$, i.e., high confidence members;
2. magnitudes in all the three *Gaia* filters (no color trends);
3. $13 \leq G \leq 15.4$, were the astrometric calibration of the EDR3 catalogue provide homogeneous errors (cfr. Fabricius et al., 2021);
4. $\sigma_{\varpi}/\varpi < 0.1$, $\sigma_{\mu_\alpha}/\mu_\alpha < 0.1$ and $\sigma_{\mu_\delta}/\mu_\delta < 0.1$;
5. passing a number of quality cuts on the diagnostic parameters provided within the *Gaia* EDR3, as done by Soltis et al. (2021).

Specifically, these applied quality-parameters cuts are:

`astrometric_excess_ noise` < 1;

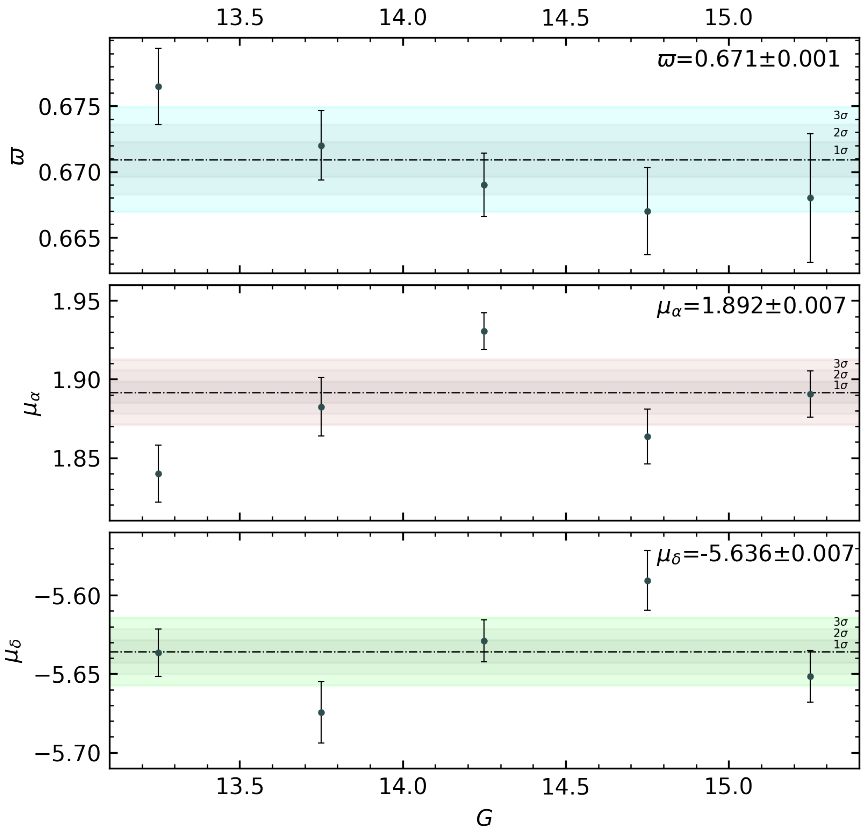

Figure 2.7: Mean values of the parallax (top) and proper motion components (middle and bottom) in each magnitude bin; the dash-dotted line is the overall weighted mean value, which is reported on the top right corner of each panel and in Table 2.1.

`astrometric_excess_noise_sig` $<= 10$;

`phot_bp_rp_excess_factor` < 1.6;

`phot_proc_mode` $= 0$;

`astrometric_gof_al` < 4.

After these selections we considered the color-magnitude diagram (CMD) of member stars (Figure 2.6, left panel) and applied a constraint in the G vs $(G_{BP} - G_{RP})$ plane to exclude the region of the CMD populated by high-mass ratio photometric binaries (real or blends) that may have lower precision astrometry. This is achieved as follows: we divided the sample into G-magnitude bins of 0.3 mag and we arbitrarily defined a specific colour for each bin as the 30^{th} percentile of the colour distribution of the stars in the bin. We then interpolated these points at any given G-mag with a spline. The fiducial line defined in this way follows the bluer envelope of the Main-Sequence, as shown in the left panel of Figure 2.6. We then calculated the colour residuals δ from the fiducial and discarded the sources with $|\delta| > 1\sigma$ (Figure 2.6, right panel).

With this tight selection of the very best measured and most likely members just defined for M37, we now proceed with our own derivation of the cluster mean astrometric parameters. We first compute the 3σ-clipped median of ϖ, μ_α and μ_δ for each G-bin of 0.5 mag, with σ defined as the 68.27^{th} percentile of the residuals around the median. The error associated with each bin is defined as $\epsilon_k = \sigma/\sqrt{(N-1)}$, with N the number of sources in the bin. The values for the mean parallax and proper motions are calculated as a weighted mean through all the bins, with $1/\epsilon_k^2$ as weight.

As the astrometric parameters for M37 are now better determined, thanks of the use of EDR3 (instead of being based on DR2 as in CG20) and the improved memberships, it makes more sense to use the newly determined cluster's mean parameters as starting values for our algorithm and to re-determine the membership probabilities. Therefore, we repeated the analysis just discussed to derive our final estimate of the mean proper motion and parallax of M37. The values of mean parallax and proper motions for each magnitude bin are plotted in Fig. 2.7, with the weighted mean through all the bins shown on the top right of each panel. These final values are also reported in Table 2.1. We point out that neglecting the last selection on the CMD (displayed in Figure 2.6) our estimates do not change significantly (less than 0.3σ).

Finally, Lindegren et al. (2021a) found that EDR3 parallaxes of sources identified as quasars are systematically offset from the expected distribution around zero by a few tens of microarcseconds. They give an attempt to account for this offset which depends non trivially on the magnitude, colour, and ecliptic latitude of the source. We used their `Python` code to correct the parallaxes of M37 members and then recomputed the mean value. However, as they point out in their work, this correction is still under development and has problems, which seems to be supported by the disagreement with the expected values of $\sim 20\,\mu$as (cfr. Figure 5 of Lindegren et al., 2021a). We report also in Table 2.1 this bias-corrected value, as ϖ^{L21}.

As a final note, while the absolute value of the parallax has not a direct effect on the membership probabilities, which is mostly a differential computation, it would

Table 2.1: M37 mean parallax and proper motion. The value of ϖ^{L21} is the parallax corrected for the bias as is Lindegren et al. (2021a).

Parameter	value	unit
ϖ	0.671 ± 0.001	mas
ϖ^{L21}	0.629 ± 0.001	mas
μ_α	1.892 ± 0.007	mas yr−1
μ_δ	-5.636 ± 0.007	mas yr−1

still be good to have an indication of the systematic error in the just derived parallax. Therefore, we can conservatively associate a maximal error of $|\varpi - \varpi^{\mathrm{L21}}| = 0.043$ mas, to the absolute parallax of M37 derived from *Gaia* EDR3: $0.671 \pm 0.001 \pm 0.043$ mas, i.e., corresponding to a distance of 1.5±0.1 kpc.

2.6 Catalogue of M37

As part of this work, we electronically release as Supporting Information on the Journal a catalogue containing the *Gaia* EDR3 `source ID` and P_ϖ (the membership probability calculated with the formalism presented in this work).

2.7 Summary

In this paper we presented a simple term, which involve parallaxes, to extend the classical method for computing cluster-membership probabilities based *only* on proper motions and spatial distributions. The proposed new formalism, therefore, takes into account the full-astrometric information to compute memberships. Although currently this method suite only data provided by the *Gaia* EDR3 catalog, in principle this formalism could be adopted also to future other 5-parameters high-precision astrometric catalogs, or possibly to extensions of the *Gaia* astrometry to fainter magnitudes exploiting superior instruments capabilities (e.g. using *Hubble Space Telescope* observations as in Bedin and Fontanive, 2018, 2020). We also note that employing relative instead of absolute parallaxes would not affect the membership probabilities as parallaxes enter only as a relative quantity in the calculations, nor would make any difference to add corrections for the systematic errors, such as those described in Lindegren et al. (2021a) for *Gaia* EDR3.

We successfully applied this formalism to the case of the close-by open cluster M37, and release the derived membership probabilities. Results show that the new term allow us to better separate cluster members from field stars at all the magnitudes. We finally used the here-derived list of members to give a new estimate of the astrometric parameters of the cluster.

Future improvements of the method might combine the photometric information. Indeed, especially on wide open clusters with sparse densities, or in their outskirts in general, field objects might survive even tights membership probability selections, incidentally having same distance and motion of the clusters. Other future works might also include a term that would take into account the velocity along the line-of-sight of the sources (commonly referred to as *radial velocities* in spectroscopy), when available. As *Gaia* radial velocities have not a great precision (200-300 $\mathrm{m\,s^{-1}}$ at best, up to 2.5 $\mathrm{km\,s^{-1}}$), nor they extend to sufficiently faint magnitudes (G in the range 4-13), we ignored this term in this paper, which is focused on the astrometric parameters only.

3. Astro-photometric study of M37[1]

In this chapter we present an astrometric and photometric wide-field study of the Galactic open star cluster M37 (NGC 2099). The studied field was observed with ground-based images covering a region of about four square degrees in the *Sloan*-like filters *ugi*. We exploited the *Gaia* catalogue to calibrate the geometric distortion of the large field mosaics, developing software routines that can be also applied to other wide-field instruments. The data are used to identify the hottest white dwarf (WD) member candidates of M37. Thanks to the *Gaia* EDR3 exquisite astrometry we identified seven such WD candidates, one of which, besides being a high-probability astrometric member, is the putative central star of a planetary nebula. To our knowledge, this is a unique object in an open cluster, and we have obtained follow-up low-resolution spectra that are used for a qualitative characterisation of this young WD. Finally, we publicly release a three-colour atlas and a catalogue of the sources in the field of view, which represents a complement of existing material.

3.1 Introduction

The vast majority of low- to intermediate-mass stars in the Galaxy end their lives as white dwarfs (WDs). Their nature of compact objects has served as an important test case for many areas of fundamental physics and stellar evolution theories. WDs in open clusters (OCs) represent a unique opportunity to study these objects in well characterised environments, as OCs usually have very well determined properties such as age, distance, metallicity and reddening.

M37, also known as NGC 2099, is a rich (with an estimated total mass of $\sim 1500\,M_\odot$ by Piskunov, A. E. et al., 2008), intermediate-age OC, with an angular size of about 1 deg (Griggio and Bedin, 2022). As revealed by Cordoni et al. (2018), this cluster exhibits an extended Main-Sequence (MS) Turn-Off, thus its precise age is still under debate; Mermilliod et al. (1996) gives an age of about

[1]The content of this chapter has been published in Griggio et al. (2022a)

400-500 Myr, compatible with the more recent estimate by Cordoni et al. (2018) that gives an age of 550 Myr. M37 is located in the Auriga constellation, at a distance of about 1.4 kpc (Griggio and Bedin, 2022; Kharchenko et al., 2005). It has been the object of several photometric studies (e.g., Kalirai et al., 2001b) as well as spectroscopic investigations (e.g., Pancino et al., 2010). Both photometric and spectroscopic analyses mostly agree on the metallicity of this cluster, which is around solar ([Fe/H] = 0.02-0.08, Casamiquela et al. (2019), Heiter et al. (2014) and Netopil et al. (2016)), and give a reddening estimate in the range 0.2-0.3 (e.g., Kang et al., 2007; Sarajedini et al., 2004). M37 has been long known to host quite a large population of WD candidates, consisting of ~ 50 stars that were identified via deep B- and V-band photometry down to $V = 23.5$ mag (Kalirai et al., 2001b) and were characterised through optical spectroscopy (Kalirai et al., 2005). More recently, spectroscopic follow-up have confirmed, rejected, or identified new cluster members (Cummings et al., 2015), including a very massive $\sim 1.28\,M_\odot$ object (Cummings et al., 2016). The WD census of this OC is not yet complete due to several reasons, like source crowding, dispersal of cluster members, unresolved binarity with MS companions; current estimates outnumber the WD candidates by a factor of 2-4 (Kalirai et al., 2001b; Richer et al., 2021). Despite their faintness, 10-15 confirmed WD members have been extensively studied for the characterisation of the initial-to-final-mass relation (IFMR), leading to an increasingly improved understanding of mass loss for low- to intermediate-mass stars (Catalán et al., 2008; Cummings et al., 2018; Ferrario et al., 2005; Salaris et al., 2009).

In this paper we employ observations of M37 collected at the Asiago Schmidt telescope[2] in the *Sloan*-like *ugi* filters to develop and test a procedure to calibrate the geometric distortion of the instrument, exploiting the *Gaia* Early Data Release 3 (EDR3, Gaia Collaboration et al., 2021) absolute reference system, which will be applied also to other wide-field imager mosaics.

By using the method of astrometric cluster membership presented in Griggio and Bedin (2022), we have identified seven new WD member candidates that are currently at the hot end of the WD cooling sequence, which has so far been overlooked by previous searches. These new candidates include the likely central star of a planetary nebula, for which we have also obtained two sets of follow-up spectra. We analyse their physical properties and further discuss their cluster membership.

In Sections 3.2 and 3.3 we describe the observations and the data reduction

[2] https://www.oapd.inaf.it/asiago/scientific-information-about-telescopes-research/telescopes-and-instrumentations/schmidt-6792

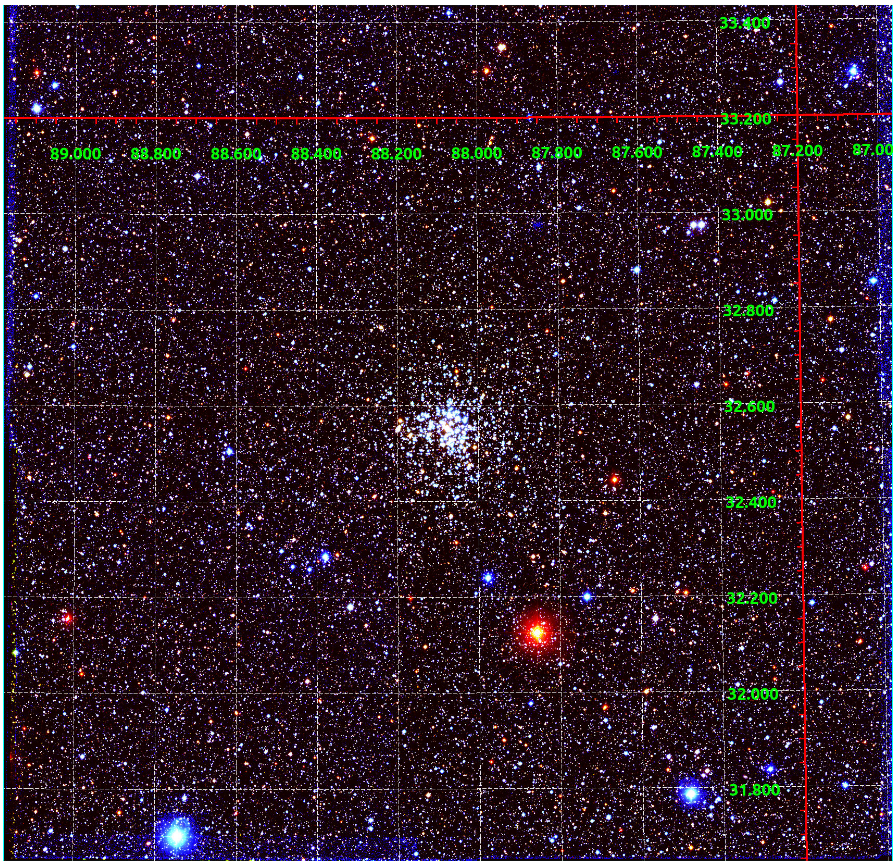

Figure 3.1: Stacked three-colour image (u,g,i) of the field of view, with superimposed a grid with equatorial ICRS coordinates.

routines. In Sections 3.4 and 3.5 we use the membership probability and the astrometric parameters to select cluster members, and we show the colour-magnitude diagrams in the *ugi* filters. The newly identified WD member candidates and the their spectral energy distribution analysis are presented in Section 3.6. Section 3.7 describes the catalogue that we publicly release.

3.2 Data set

The data were collected with the Schmidt 67/92 cm telescope in Asiago (Italy) between 2020 November, 8^{th} and 21^{st}. The telescope is equipped with a KAF-16803 CCD, with an active area of 4096×4096 pixels and a field of view (FOV) of $59 \times 59\,\mathrm{arcmin}^2$, that corresponds to a $\sim 0.87\,\mathrm{arcsec/px}$ scale. We collected a mosaic of about $2{\times}2\,\mathrm{deg}^2$, with a ~ 13 arcmin overlap. All the tiles of the mosaic

Table 3.1: Data set used in this work. All the observations were carried out in November 2020.

Filter	# of exp. $\times t_{\rm exp}$	Airmass (arcsec) (best-worst)	Seeing (arcsec) (best-worst)
i	$66 \times 240\,$s	1.03-1.72	1.51-3.22
	$22 \times 10\,$s	1.03-1.73	1.47-3.04
g	$66 \times 240\,$s	1.03-1.84	1.53-3.25
	$22 \times 10\,$s	1.03-1.85	1.52-3.05
u	$66 \times 240\,$s	1.04-1.97	1.55-2.40
	$23 \times 10\,$s	1.04-1.98	1.53-2.63

were dithered, and images collected in three filters, u-,g-, i-*Sloan*, for a total of 198 images (some of which were later discarded due to poor image quality) each with a 240 s exposure time. In addition, we collected a set of images with a 10 s exposure time to have a better estimation of the flux of very bright sources that are saturated in the 240 s data. Table 3.1 summarises the observation log.

The mosaic covers an area centred on M37. A stacked image in three-colour version is shown in Figure 3.1; a description on how the stack was produced will be given in Section 3.3.4.

3.3 Data reduction

The data have been corrected via standard calibrations (bias, dark, linearity and flat field). In addition, we accounted for the effects of geometric distortion on the pixels' area in different positions of the CCD, which result into wrong estimations of the flux. In particular, for each pixel we computed a correction factor as the ratio of the area of the distortion-corrected pixel (see 3.3.2) and the area of the raw pixel (by definition equal to unity).

3.3.1 Preliminary photometry

The first step was to perform a "preliminary" photometry (i.e. we extracted only the flux of the brighter stars down to a magnitude limit of $g \simeq 17$), which is then used to compute the transformations between the frames. To this extent we started by using a version of the software by Anderson et al. (2006) adapted to the Schmidt's images to derive a grid of empirical point spread functions (PSFs) for each image. To take into account the spatial variation of the PSF across the FOV,

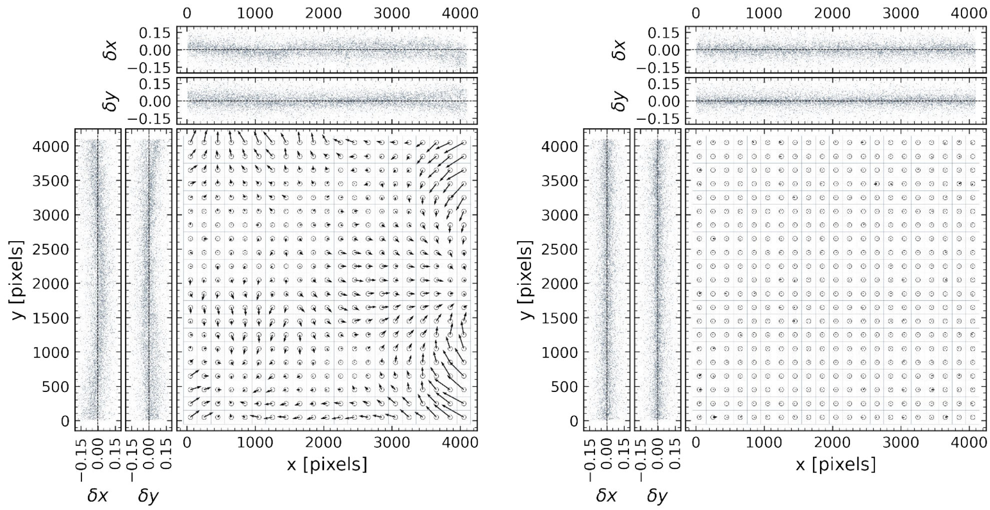

Figure 3.2: Distortion map for image `SC132788` before (left) and after (right) the distortion correction routine. The central panels represent the CCD coordinate system, with the arrows showing the magnitude and direction of the distortion on each point, corresponding to a 200×200 pixels box. The arrows have been multiplied by a factor 2500 for visualisation purposes. On the top and left panels we show a projection on the axes of the x and y components of the distortion.

the image is divided into 9×9 regions, and for each region, a PSF is empirically computed using bright, unsaturated and isolated stars. In this way, for each point on the image, a local empirical PSF can be derived by the bilinear interpolation of the 4 closest PSFs.

The grid of PSFs and the image are taken as inputs from a software (described in Anderson et al., 2006, and adapted to our detector) that finds and measures positions and fluxes of the sources in the image by using the local PSF. The routine goes through several iterations progressively finding and measuring fainter sources, until it reaches a threshold limit of 5σ above the sky background noise. The software outputs a catalogue (one for each image) containing positions and instrumental magnitudes of the stars.

3.3.2 Geometric distortion

To correct for field distortion, we exploited the *Gaia* EDR3 absolute reference frame. We cross-referenced the stars in our preliminary catalogues with the stars in the *Gaia* EDR3. We used bright, unsaturated sources to derive a general six parameter transformation between the reference frame of our catalogues to the

Gaia reference frame (projected onto the tangent plane of each exposure), and then we computed for each star in each catalogue the residuals between the transformed positions and those given by *Gaia*. We divided the residuals from all the catalogues in bins of 200×200 pixels, and for each bin we calculated the mean residual in x and y. The distortion correction routine uses this map of residuals to correct the position of each star via a bi-linear interpolation between the four nearest grid points. In Figure 3.2 we show an example of distortion map before and after the correction, left and right, respectively. In the figure we see the CCD divided into 21×21 bins, where the arrows represent the mean residual of each bin. Before applying the correction, in particular near the edges of the detector, the distortion goes up to 0.15 pixels, while after the correction have been applied the distortion is less than 0.05 pixels (about 40 mas).

3.3.3 The master frame

The next step is to put all our images into a common reference frame. This allows us to measure the same star in different exposures simultaneously, thus increasing the signal for fainter sources. The coordinate system on the CCD lies on the plane tangent to the celestial sphere at the central point of the FOV. Since our images have large dithers, each of the 2×2 fields lies in a significantly different tangent plane, as discussed also in Libralato et al. (2015) for a different detector.

In order to derive the coordinate transformations to put every image in the same tangent plane, we took advantage of the *Gaia* absolute reference frame. We started by cross-referencing the stars in our preliminary photometry catalogues with the *Gaia* EDR3, after correcting their positions for geometric distortions of the field. The *Gaia* coordinates were corrected for proper motions to be reported at the epoch of the observations, and then projected onto the tangent plane of each exposure using the procedure described in Bedin and Fontanive (2018). This allowed us to derive (for each frame) a global six-parameter transformation from the (X, Y) reference system of the CCD to the meta-coordinate system (ξ, η) of its tangent plane.

We then applied the inverse transformation to project back on the celestial sphere our positions, to have all our preliminary catalogues in spherical coordinates (α, δ). We then arbitrarily chose a point (α_0, δ_0) (the same for all the exposures) to project down again all the catalogues onto a common reference system (that now lies in the same tangent plane for every image): in particular we projected all the catalogues on the tangent plane of the image `SC132969` (archival name), and then applied the inverse transformation from the (ξ, η) coordinate system of the tangent plane to the (X, Y) system of the chosen catalogue.

After these steps we have all the catalogues lying in the same plane, in physical pixel coordinates (X, Y), with a mean pixel scale of 868 mas/px. For the sake of conciseness, in the following we will call "preliminary catalogues" the catalogues after the transformations to get them onto the same coordinate system.

To define the master frame we downloaded a portion of the *Gaia* EDR3 catalogue centred on M37 with a radius of 1.5 deg, we reported the positions of its stars to the observed epoch, we projected it down on the same tangent plane chosen in the previous step and we converted the meta-coordinates to pixel-coordinates by dividing by the pixel scale. For each filter (u, g, i) we compiled an average catalogue combining all the single preliminary catalogues and produced a list of the sources found in at least eight images, giving for each source the 3σ-clipped averaged position and magnitude. These averaged positions and magnitudes are then cross-referenced with the *Gaia* catalogue to obtain a final list of objects with *Gaia* positions and ugi-magnitudes. This list is then used as master frame: we compute the transformations between each preliminary catalogue to this reference system, which are then used as input in the next step.

3.3.4 Second-pass photometry

The second-pass photometry is performed by the software `KS2` (an evolution of the code presented in Anderson et al., 2008b) originally developed for HST images, modified to suit the Schmidt sensor and data taken with large dither patterns. Below we give a brief overview of the `KS2` software, which is described in detail by Bellini et al. (2017) and Nardiello et al. (2018b) (see also Scalco et al. (2021) for a more recent application).

The inputs of the `KS2` routine are: the images, the PSFs and the transformations derived from the preliminary photometry to find and measure the sources in all the exposures simultaneously. The star finding process goes through different iterations, moving progressively from the brightest to the faintest sources. The software takes as input also a list of bright stars from the preliminary photometry and construct weighted masks around them, which help to avoid PSF-related artefacts. In each iteration the program finds and measures the stars which fit the conditions specified for that iteration, and then subtracts them and proceeds with the next iteration.

`KS2` measures, in each image, the flux and position of the source using the appropriate local PSF. The star position and flux is determined by fitting the PSF to its 5×5 central pixels as in the preliminary photometry, but it computes the final position ad flux as an average between all the images, with the local sky value is computed from the surrounding pixels.

Saturated stars are not measured by KS2; their position and fluxes are recovered by the preliminary photometry and supplemented in the output. To properly measure the stars that were saturated in the 240 s exposures we used the 10 s images. We performed a second-pass photometry on the short exposures separately, with the zero point registered on the long exposures, and we cross-referenced the sources in the long and short catalogues. We then replaced the magnitudes of the saturated stars in the 240 s catalogue with those measured on the 10 s frames.

The major upgrade in the code is devoted to perform the projections illustrated in Sec. 3.3.3 on the images, to make the code suited to wide-field images taken with large dither patterns. The upgraded code takes as input a set of additional files that are needed to perform the transformations between the local and the master frames. The additional files are:

1. one file per image containing the coefficients for the six parameters of the most general linear transformation from the local (X, Y) to the (ξ, η) frame of the tangent plane;

2. one file per image containing the tangent point to each frame used for the projection on spherical coordinates;

3. one file that contains the (α_0, δ_0) point needed to project all the frames onto the same tangent plane;

4. one file that contains the parameters to transform the projected positions on the (X, Y) frame of the chosen image.

The KS2 software also outputs an image stack per filter that can be combined for display (as in Figure 3.1), although they are not suitable for extracting photometry (details on how the stack is produced are given in Anderson et al., 2008a). As part of this work, we also made publicly available these atlases of the astronomical scene in the three bands *ugi*.

3.3.5 Input-output corrections

In extracting photometry for faint stars, the flux is systematically overestimated when the central pixel of a star coincides with a local maximum of the background noise. This is a well known effect (sometimes referred to as “stellar migration”) that needs to be corrected for (see Bedin et al. (2009) for details). In order to asses the systematic errors, we performed an artificial-star (AS) test using the same procedure described in Anderson et al. (2008b). For each AS we chose a random position and u magnitude; the $g - i$ colour is then chosen such that the

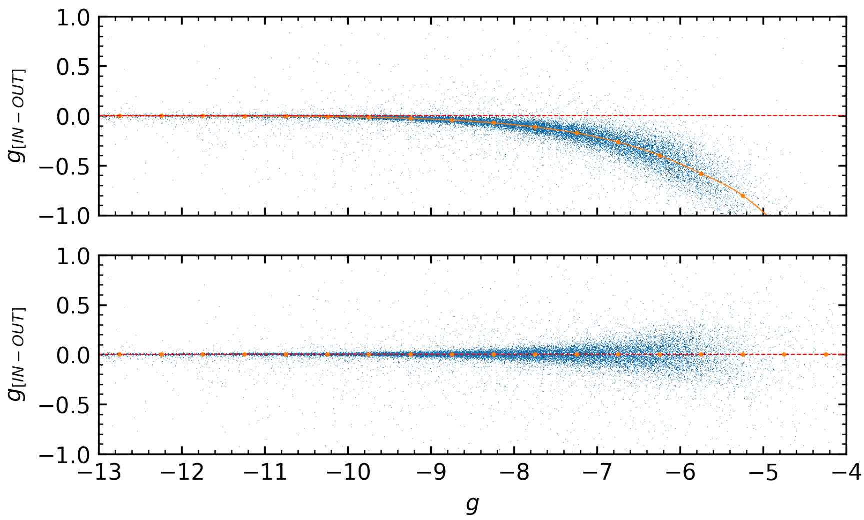

Figure 3.3: Correction of stellar migration for g-filter magnitudes. Top panel: difference between the inserted and the recovered magnitude. Orange dots are the mean residuals for each magnitude bin. The orange line is the interpolating quadratic spline. The dashed line indicates the null difference. Bottom panel: residuals after the correction. Orange dots are the mean residual for each magnitude bin. The dashed line indicates the null difference. Magnitudes on the x axis are instrumental.

star falls on the MS ridge-line (drawn by eye). The AS is added in each exposure at the specified position, in the form of an appropriately scaled PSF with Poisson noise. The software routines then operate blindly, finding and measuring all the stars. Examining the output we can determine the accuracy at each magnitude in recovering the AS. Figure 3.3 (top panel) shows the difference between the inserted and recovered magnitudes for ASs in the g filter, as function of the instrumental magnitude.

To account for these errors we derived a correction in the following way: we started dividing the ASs in bins of 0.5 magnitudes. We sigma-clipped each bin (at 2σ) around its median to remove outliers, and calculated the median as an estimator of the residual for that bin. We then interpolated the points with a quadratic spline as a function of the magnitude. We used this relation $m_{\mathrm{IN}} - m_{\mathrm{OUT}}$ versus m to correct the effects of the stellar migration on the magnitudes of the stars in our catalogue. In Figure 3.3 (bottom panel) we show the result of this procedure.

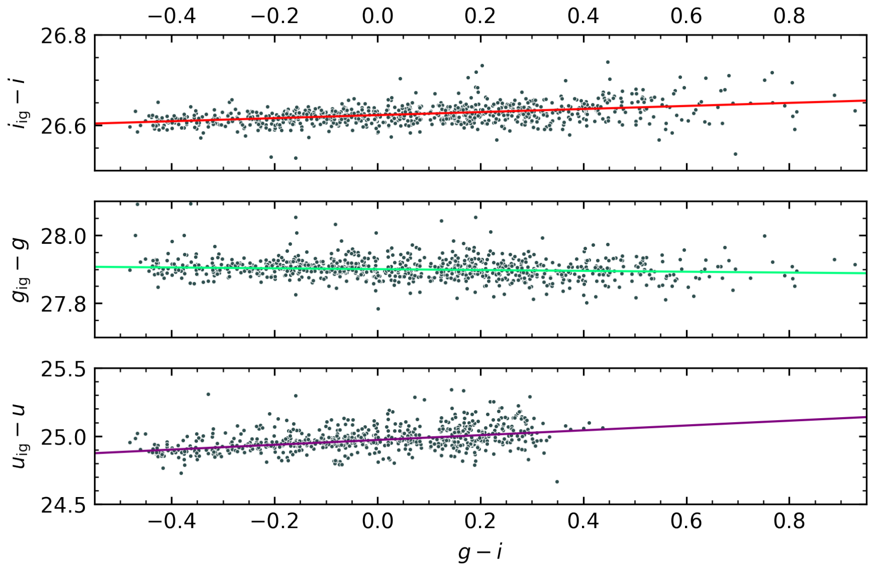

Figure 3.4: Calibration of the three filters (i, g, u): the coloured lines represent the linear fit.

3.3.6 Photometric calibration

Our instrumental magnitudes have been transformed into the Isaac Newton Telescope (INT) Galactic Plane Survey (IGAPS; Monguió et al., 2020) photometric system, that merges the INT Photometric Hα Survey (IPHAS; Drew et al., 2005) and the UV-Excess Survey (UVEX; Groot et al., 2009). We chose the IGAPS catalogue as a reference because, to our knowledge, it is the only one covering the M37 FOV in our three (u, g, i) filters, though its pass-bands are not exactly equal to ours. The IGAPS gri photometry is itself uniformly calibrated against the Pan-STARRS system (Chambers et al., 2016) with an internal accuracy of 0.02 mag (Monguió et al., 2020). The IGAPS U_{RGO} band is calibrated on a run-by-run basis across the M37 region.

We calibrated our photometry by using the relation $m_{\mathrm{IGAPS}} - m_{\mathrm{instr}}$ versus the colour index $(g-i)$ in our instrumental magnitudes, as illustrated in Figure 3.4. To obtain this relation we cross-matched our sources with the IGAPS catalogue. We considered the stars that were not saturated in both our exposures and IGAPS, and we linearly interpolated (for $m = i$, g, u) the $m_{\mathrm{IGAPS}} - m_{\mathrm{instr}}$ versus $g - i$ distribution. A first calibration has been performed using all the unsaturated stars in our catalogue, and after selecting the cluster members (see next section), in order to mitigate potential systematic effects, we further restricted the sample

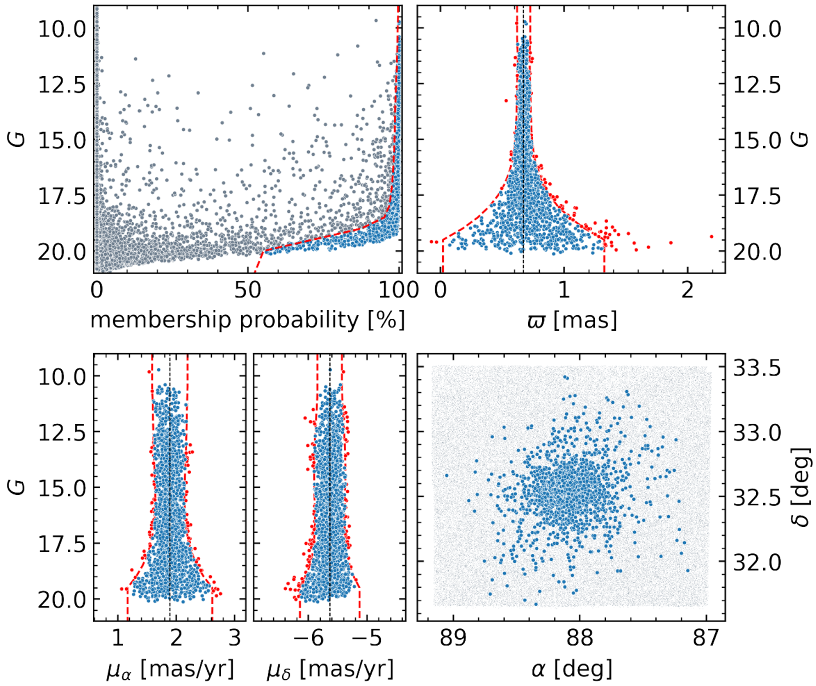

Figure 3.5: Members selection. Top left: membership probability for all the sources. We reject the stars that fall above the red line. Top right: G magnitude vs parallax. Here we reject the stars that fall outside the region delimited by the two red lines (blue dots). The black dashed line represents the median parallax. Bottom left: proper motions of the sources that passed the previous two cuts vs their G magnitude. We kept the sources between the red dashed lines (blue dots). Bottom right: spatial distribution of the sources. Blue dot are the selected members of M37.

to M37 members only. To transform the instrumental magnitudes we adopted the relation $m_{\mathrm{cal}} = m_{\mathrm{instr}} + a_0 + a_1 \times (g - i)$, where m_{cal} is our final magnitude calibrated with respect to IGAPS, and the coefficients are determined via a best fit approach. Higher order polynomials proved to be unnecessary.

3.4 Selection of cluster members

The selection of member stars have been performed using the membership probabilities derived from Griggio and Bedin (2022). To select highly-reliable cluster members we adopted the procedure that is displayed in Figure 3.5. In the top left panel, we show the membership probability plotted against the *Gaia*-G band

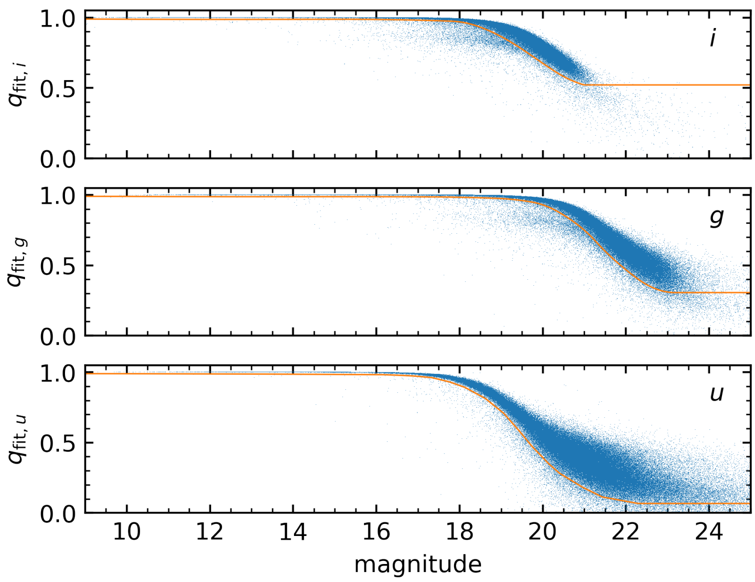

Figure 3.6: $q_{\rm fit}$ versus magnitude in each filter. We marked as good (`pho_sel_f`$= 1$, f $= u$, g, i) the stars that are above the orange line and 3σ above the sky.

magnitude. We applied a by-eye cut with the idea of selecting the bulk of sources with cluster membership at each magnitude. This cut is indicated by the dashed red curve, and we kept only the sources below that curve. This cut on the membership probabilities becomes less strict going towards fainter magnitudes as the measurement errors increase and members becomes less certain.

This sample has then been constrained on the parallax versus magnitude plane (top right panel). We divided the data into magnitude bins of 1 mag, and for each bin we calculated $\sigma_{\varpi,i} = 68.27^{\rm th}$ percentile of the residuals around cluster's parallax ϖ (given by Griggio and Bedin, 2022). We derived the red curves interpolating the points $\varpi \pm 2\sigma_{\varpi,i}$ with a spline. The last selection was performed on the proper motions versus G plane. We applied the same procedure as for the parallax to μ_α and μ_δ to derive the red curves. On the bottom right panel we show the spatial distribution of the stars that are selected as M37 members.

3.5 *Sloan* colour-magnitude diagrams

We first rejected sources with poor measurements, by applying a cut in the quality of fit ($q_{\rm fit}$) parameter, which is in the `KS2` output for each source. The $q_{\rm fit}$ measures how well a source is fitted by the PSF; a $q_{\rm fit} = 1$ indicates a perfect fit. The cuts

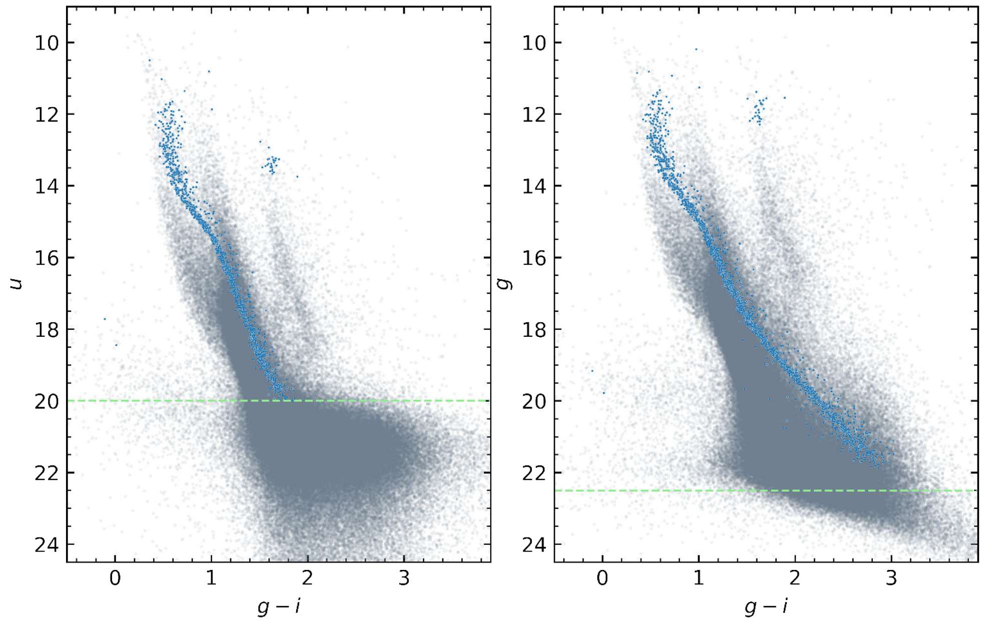

Figure 3.7: Colour-magnitude diagrams in *ugi* filters. Grey points represent the sources that passed the quality cuts in the considered filters of each CMD. Blue points are the sources that passed the members selection. The dashed green line represents the 3σ cut above the sky background level (in u and g respectively).

we performed are shown in Figure 3.6. In addition to these cuts, we selected the sources that are at least 3σ above the sky background. The sources that passed these selection criteria and are not saturated are flagged with `pho_sel_f` = 1 in our catalogue, with f = u, g, i. The additional flag `pho_sel` = 1 is for stars that passed the selection in all the three filters.

In Figure 3.7 we show a colour-magnitude diagram (CMD) of the selected sources in the FOV (in grey) of M37 and the cluster members as defined in previous Section (in blue). The dashed green line represents the 3σ cut above the sky background in the u and g filters.

3.6 White dwarf member candidates

M37 is known to host a few, faint white dwarf (WD) members, also including a very massive object of $\approx 1.3\,\mathrm{M}_\odot$ (Cummings et al., 2015, 2016). Given the current age of M37, the lightest WD members that could have formed through canonical single-star evolution are expected to have $\approx 0.7\,\mathrm{M}_\odot$. We focused our search for

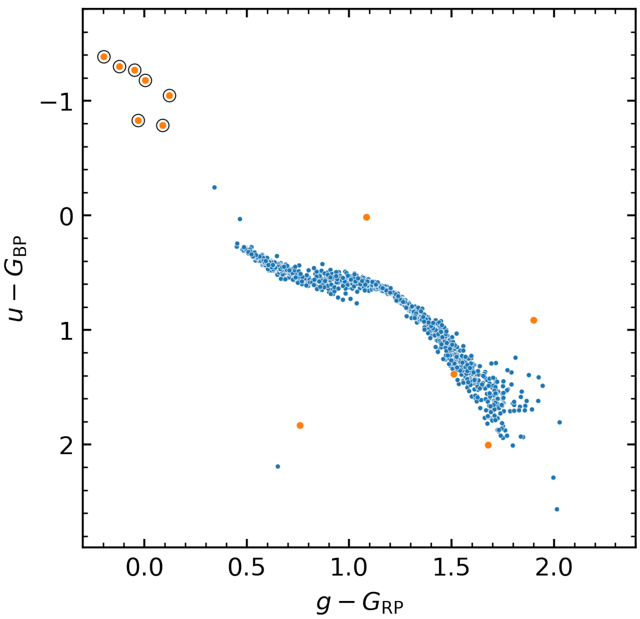

Figure 3.8: Two colour diagram of member stars. Blue points represent the cluster members. Orange dots indicate the sources that passed the selection described in the text. The orange dots encircled in black are those that we selected as WD member candidates.

WD candidates at the hot-end of their cooling sequence that, however, for M37 corresponds to a region of the CMD where the measurement errors of *Gaia* are the largest.

We restricted our search to sources with $G_{BP} > 18$ and $-0.5 < G_{BP} - G_{RP} < 0.5$ where we expect to find WDs that have just recently formed and have both the same distance and reddening of M37 ($d = 1.5 \pm 0.1$ kpc, Griggio and Bedin (2022); $E(B-V) = 0.26$, Cordoni et al. (2018)). We selected from this region the stars with proper motions and parallaxes that are compatible within 3σ with those of the cluster. To confirm the isolated WD nature of these objects we built a two-colour ($u - G_{BP}$, $g - G_{RP}$) diagram (Figure 3.8), in which we identify the stars that passed this selection with an orange dot. Seven of them possess the typical blue colours of isolated WDs. All the previously known WD members of M37 are fainter than our *Gaia*-based selection (Cummings et al., 2015, 2016, and references therein).

The astrometric and photometric properties of the seven WD candidates are shown in Figure 3.9 along with the other cluster members. Their relevant *Gaia* data are listed in Table 3.2. In Figure 3.12 we show the finding charts for WD2–7,

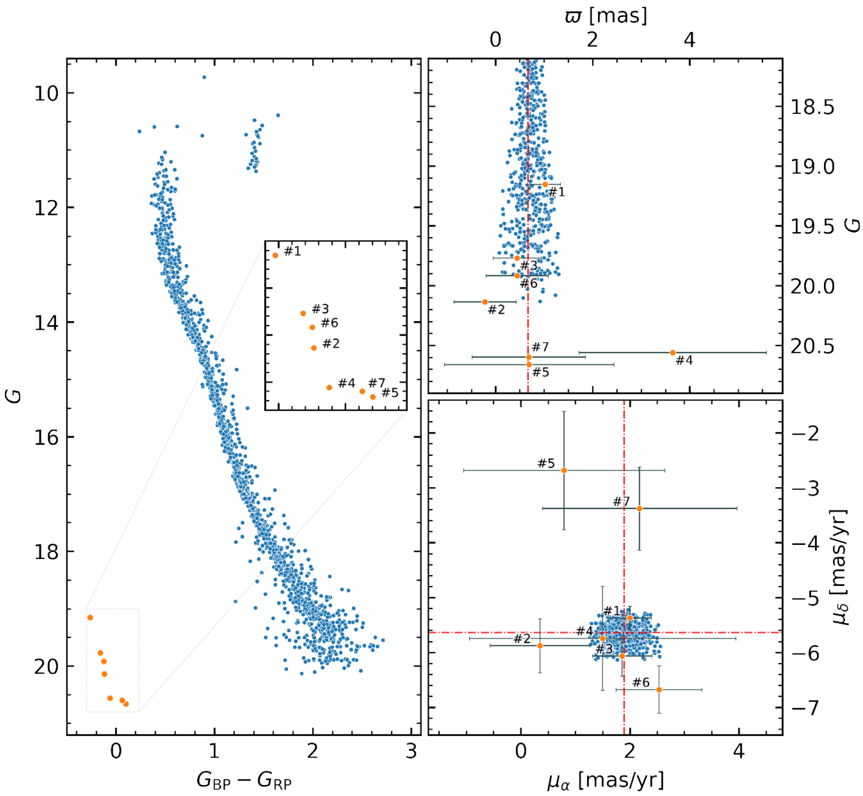

Figure 3.9: Left: CMD of M37 members in the *Gaia* pass-bands (blue). Orange dots are the WD member candidates identified in this work. Error bars for parallax and proper motions are given by *Gaia* EDR3 uncertainties. Top right: parallax vs *Gaia* G magnitude; the vertical red line represents the parallax of the cluster. Bottom right: Proper motion diagram; the red lines represent the absolute proper motion of the cluster.

while that of WD1 is shown in Figure 3.10 (right).

3.6.1 Spectroscopic follow-up of WD1

We collected optical spectra of the brightest candidate, WD1, with the Asiago Faint Object Spectrograph and Camera (AFOSC) mounted on the 1.82-m Copernico telescope operated by INAF-Osservatorio Astronomico di Padova atop of Mount Ekar, Asiago, Italy. We used the gr4 grating with both 2.5 and 1.69-wide slits, achieving a resolving power of $R = 219$ and 325 at the central wavelength of gr4 for the two setups, respectively. One single exposure of 3600-s were taken on November 10, 2021, under hazy sky conditions (slit 2.50 arcsec), while three

Table 3.2: Photometric and astrometric properties of the seven WD candidates.

#	*Gaia* EDR3 ID	G	$G_{\rm BP}$	$G_{\rm RP}$	g	u	i
WD1	3451205783698632704	19.154	19.100	19.362	19.164	17.716	19.271
WD2	3451182182857026048	20.137	20.038	20.156	20.160	18.859	19.923
WD3	3451201076423973120	19.769	19.746	19.904	19.781	18.448	19.768
WD4	3451167786125150592	20.560	20.492	20.552	20.641	19.707	20.762
WD5	3451200114340263296	20.660	20.642	20.540	20.662	19.596	20.457
WD6	3448258267902375296	19.917	19.957	20.081	20.050	19.130	20.171
WD7	3454340495645123584	20.599	20.643	20.580	20.531	19.375	20.134
	μ_α [mas/yr]		μ_δ [mas/yr]		ϖ [mas]		
WD1	2.003 ± 0.387		-5.371 ± 0.219		1.020 ± 0.315		
WD2	0.353 ± 0.916		-5.877 ± 0.490		-0.224 ± 0.640		
WD3	1.858 ± 0.550		-6.064 ± 0.368		0.444 ± 0.492		
WD4	1.500 ± 2.443		-5.743 ± 0.946		3.649 ± 1.932		
WD5	0.796 ± 1.845		-2.684 ± 1.076		0.688 ± 1.746		
WD6	2.534 ± 0.787		-6.675 ± 0.435		0.443 ± 0.643		
WD7	2.177 ± 1.786		-3.378 ± 0.755		0.682 ± 1.164		

exposures of 2700-s each were taken on January 12, 2022 under good sky conditions (slit 1.69 arcsec). The data were reduced with an `iraf` (Tody, 1986) based pipeline, i.e. `FOSCGUI`[3]. The average second-epoch spectrum signal-to-noise ratio (S/N) is around 15. A first look of the combined spectrum confirmed this star as a hot, likely hydrogen-deficient star.

We re-observed WD1 with the Device Optimized for the LOw RESolution (DOLORES, LRS in short) that is mounted on the Telescopio Nazionale Galileo (TNG) at the Observatorio del Roque de los Muchachos (Canary Islands, Spain). We took three exposures of 1800 seconds each on 2022-03-03, in service mode during Director Discretionary Time (program A44DDT3). We used the low-resolution blue grating (LR-B) with a 1-arcsec slit that enabled a dispersion of 2.8 Å/pixel and a resolution of 11 Å at 5577 Å. The observations were performed in dark time under good weather conditions and with a seeing well below 1 arcsec. The spectrophotometric standard Hiltner 600 was observed at the beginning of the night with the same slit width. The data were reduced, 1D optimally extracted and wavelength and flux calibrated by using standard reduction procedures with the

[3]FOSCGUI is a graphic user interface aimed at reducing spectrophotometric data and extracting spectroscopy of the focal reducer type spectrograph/camera FOSC. It was developed by E. Cappellaro. A package description can be found at http://sngroup.oapd.inaf.it/foscgui.html

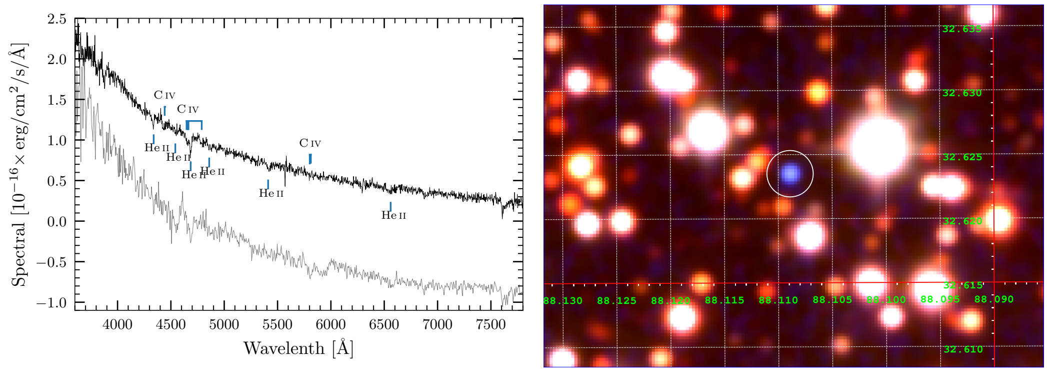

Figure 3.10: Left: The TNG/LRS spectrum (black) and the Asiago/AFOSC spectrum (gray). The latter is shifted vertically by a constant factor. We have labelled some of the most prominent He II and C IV lines. Right: Tri-chromatic stack finding-chart of WD1.

`starlink` (Currie et al., 2014), `pamela` (Marsh, 2014), and `molly` (Marsh, 2019) software packages. The average LRS spectrum of WD1 has S/N = 35 at 5500 Å. In Fig. 3.10, we show both the AFOSC and LRS spectra, labelling the most prominent absorption features of C IV at $\approx$ 4660 and 5801–5812 Å and the He II lines.

3.6.2 Physical parameters

In order to shed more light on the properties of the seven WD candidates, we performed model fits of their Spectral Energy Distributions (SED). We collected available photometry from the *Galaxy Evolution Explorer* (GALEX DR6+7; Bianchi et al., 2017), IGAPS (Monguió et al., 2020), PanSTARRS (Chambers et al., 2016), and the *Sloan* Digital Sky Survey (SDSS DR12; Alam et al., 2015). The SED fitting procedure allowed us to estimate the effective temperature ($T_{\rm eff}$), radius, mass, and cooling age of the candidate WDs via χ^2 minimisation of the difference among observed photometry and the appropriate synthetic magnitudes. The latter were computed from a grid of Koester (2010) models for hydrogen-dominated WD spectra (DA type), which we mapped on the La Plata cooling tracks (Althaus et al., 2013; Camisassa et al., 2016). We adopted the distance of M37 and the differential reddening estimated (following the procedure described in Bellini et al., 2017) from the cluster neighbours of each WD candidate as external priors in the SED fitting routine. The results of our SED fitting are shown in Fig. 3.13 for WD2–WD7. Their photometrically estimated physical parameters are listed in Table 3.3. The physical parameters of WD1 that could be obtained

Table 3.3: Physical parameters of six WD candidates obtained from the SED fitting analysis.

#	$T_{\rm eff}$ [K]	$R/\mathrm{R}_\odot$	$M/\mathrm{M}_\odot$	$\tau_{\rm cool}$ [Myr]
WD2	46900^{+20900}_{-14700}	$0.019^{+0.005}_{-0.003}$	$0.52^{+0.11}_{-0.10}$	$1.9^{+2.2}_{-1.5}$
WD3	64500^{+10000}_{-11700}	$0.020^{+0.002}_{-0.002}$	$0.57^{+0.05}_{-0.05}$	$0.7^{+0.8}_{-0.4}$
WD4	60800^{+12100}_{-10800}	$0.015^{+0.001}_{-0.001}$	$0.67^{+0.08}_{-0.07}$	$0.8^{+1.0}_{-0.4}$
WD5	41900^{+16000}_{-9800}	$0.017^{+0.003}_{-0.002}$	$0.56^{+0.12}_{-0.09}$	$3.4^{+3.8}_{-2.5}$
WD6	35000^{+4200}_{-2700}	$0.024^{+0.002}_{-0.002}$	$0.44^{+0.03}_{-0.06}$	$3.1^{+1.6}_{-1.6}$
WD7	21100^{+2300}_{-2100}	$0.027^{+0.002}_{-0.002}$	$0.33^{+0.03}_{-0.04}$	$7.4^{+20.2}_{-5.6}$

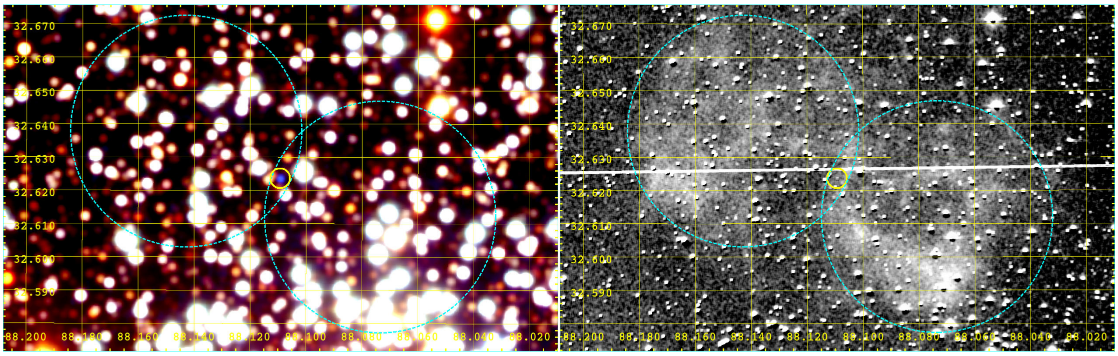

Figure 3.11: Left: RGB stack of the region around WD1, encircled in yellow. The putative locations of the two lobes of the PN are encircled in cyan. Right: Hα–r image of the same region, which highlights the nebula, taken from the HASH database (Parker et al., 2016).

from the SED fitting routine would not be reliable, because this star is confirmed not to have a hydrogen-dominated atmosphere (see next section). A spectroscopic follow-up of the most likely candidates (that is WD2, WD3, WD4, and WD5) remains necessary in order to independently confirm their cluster membership.

WD1

The LRS spectrum of WD1 confirms it as a hot, hydrogen-deficient WD that appears as an intermediate object between the PG 1159 and DO classes (Reindl et al., 2014; Werner and Herwig, 2006). The spectral resolution and S/N of the spectra in hand are not sufficient for performing a quantitative spectral analysis, but its $T_{\rm eff}$ is likely hotter than 60,000 K. This star was also identified by Chornay and Walton (2021) as the central star of a faint, bipolar planetary nebula (PN) (PN G177.5+03.1; Parker et al., 2016). From Fig. 3.11 a diameter $d = 460$ arcsec can be estimated (consider $d = 4 \times r$, with r being the radius of one lobe). Assuming furthermore a distance of 1.5 kpc (Griggio and Bedin, 2022), and an expansion velocity of 20 km/s, one can estimate the age of the PN to be 82 kyr. Such an old PNe can be expected for a star that has already entered the WD cooling sequence. The relation of this PN (shown in Figure 3.11) with WD1 needs further confirmation: additional follow-up observations are needed to better characterise the evolutionary status and cluster membership of WD1 (that appears as a high-probability astrometric member of this cluster, having passed the membership selection criteria), via quantitative spectral analysis. If its physical properties and radial velocities turn out to be also compatible with the expected parameters (a mass that is larger than $0.7\,M_\odot$, as well as a total age and mean radial velocity like those of the other M37 members) WD1 would represent a very rare (if not unique) central star of a planetary nebula (CSPN) that has passed all the tests of open cluster membership (Bond et al., 2020; Fragkou et al., 2019; Moni Bidin et al., 2014).

WD2, WD3 and WD5

For these three stars we have estimated photometric masses that are within 2 or 3-sigmas from the minimum allowed mass for single star evolution of $0.7\,M_\odot$. The estimated cooling ages are compatible with the total age of M37. In addition, WD3 passed the membership selection criteria.

WD4

This object is the most likely cluster member confirmed at the 1-σ level, as we obtain a $T_{\rm eff} = 60\,800^{+12\,100}_{-10800}$ K, a mass of $0.67 \pm 0.08\,M_\odot$, and a cooling age of $0.8^{+1.0}_{-0.4}$ Myr. If confirmed via spectroscopic follow-up, this WD could be one of the youngest evolved members of M37.

WD6 and WD7

Although they are likely very young, these two WD candidates have photometric estimates of radii and masses that are not compatible with their proposed membership to M37. In fact, masses lower than $0.5\,M_\odot$ are indicative of He-core WDs, originated from RGB stars with electron degenerate helium cores, that have lost their envelope before the onset of the helium flash. Given the age of this cluster, the presence of He-degenerate cores in the post-MS stars is very unlikely (theoretical isochrones predict post-MS stars with initial masses larger than $2.5\,M_\odot$). Therefore, we do not believe that these two WDs can belong to M37.

3.7 A new catalogue

With this paper we publicly release a catalogue of the region described in Section 3.2. The catalogue contains photometry of 210 907 sources in the *Sloan*-like filters u, g and i and *Gaia* EDR3 photometry and astrometry for the sources that are present also in the *Gaia* catalogue. The sources that are not detected by *Gaia* have the column `gid` set to zero. The value 999 is a placeholder for missing values (e.g., a source that has not been detected in the u filter has $u = 999$). The columns of the catalogue are described in Table 3.4. The catalogue and the stacked image are available at the following url: `https://web.oapd.inaf.it/bedin/files/PAPERs_eMATERIALs/M37_ugiSchmidt/`.

3.8 Conclusions

We reduced and analysed Schmidt images of the open cluster M37 combining our photometric catalogue with *Gaia* EDR3. We developed software tools to correct for the geometric distortion exploiting the *Gaia* reference system in the case of data from wide-field imagers collected with large-dithers. The set of routines that we developed for this specific instrument will be applied also to other wide-field imagers.

We have astrometrically and photometrically identified seven isolated WDs as candidate cluster members. We obtained follow-up low resolution spectra for one of them, confirming it as a hot, hydrogen-deficient (pre-) WD. This star was previously identified as the likely central star of a faint PN (Chornay and Walton, 2020). Further follow-up spectroscopy is needed to univocally confirm it as one rare example of CSPN belonging to a Galactic open cluster. By means of spectral energy distribution analysis, we suggest that four out of seven WD candidates are likely or very likely cluster members. Follow-up spectroscopy is also needed to confirm their cluster membership, eventually joining the already numerous family of degenerate stars found in this rich open cluster (Cummings et al., 2015, 2016).

We also publicly released a catalogue of 210 907 sources in a $\sim 2 \times 2\,\mathrm{deg}^2$ region centred on M37, complementing the already existing data from IGAPS.

Table 3.4: Description of the columns in our catalogue.

Column	**Description**
`gid`	*Gaia* EDR3 id of the source
`ra`	right ascension [deg]
`dec`	declination [deg]
`i`	magnitude in the i filter
`ei`	error on the i mag
`g`	magnitude in the g filter
`eg`	error on the g mag
`u`	magnitude in the u filter
`eu`	error on the u mag
`qi`	quality flag for i mag
`qg`	quality flag for g mag
`qu`	quality flag for u mag
`oi`	fraction of flux within the PSF aperture in i filter due to neighbours
`og`	fraction of flux within the PSF aperture in g filter due to neighbours
`ou`	fraction of flux within the PSF aperture in u filter due to neighbours
`pho_sel`	1 if source passed photometric cuts in all filters
`pho_sel_i`	1 if source passed photometric cuts in the i filter
`pho_sel_g`	1 if source passed photometric cuts in the g filter
`pho_sel_u`	1 if source passed photometric cuts in the u filter
`G`	magnitude in the *Gaia* EDR3 G filter
`eG`	error on the G mag
`Gbp`	magnitude in the *Gaia* EDR3 G_{BP} filter
`eGbp`	error on the G_{BP} mag
`Grp`	magnitude in the *Gaia* EDR3 G_{RP} filter
`eGrp`	error on the G_{RP} mag
`PI`	parallax [mas]
`ePI`	error on parallax [mas]
`muRa`	proper motion on ra [mas/yr]
`emuRa`	error on muRa [mas/yr]
`muDec`	proper motion on dec [mas/yr]
`emuDec`	error on muDec [mas/yr]
`P`	membership probability
`member`	1 for sources that passed our members selection

3.9 Additional figures

In this section we show the finding charts and the best fit results for the SED analysis of six WD candidates.

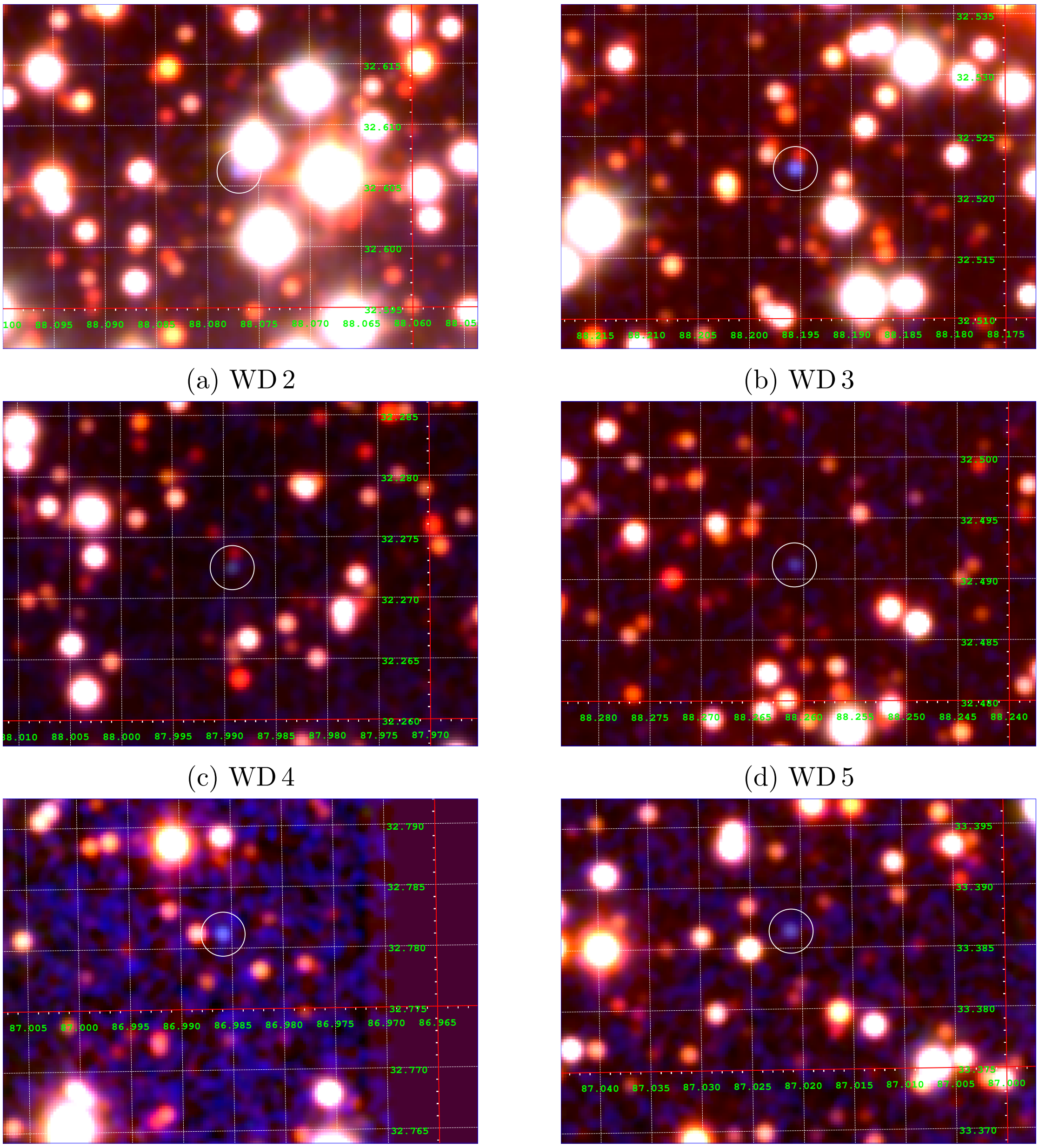

(a) WD 2

(b) WD 3

(c) WD 4

(d) WD 5

(e) WD 6

(f) WD 7

Figure 3.12: Finding charts of six WD candidates.

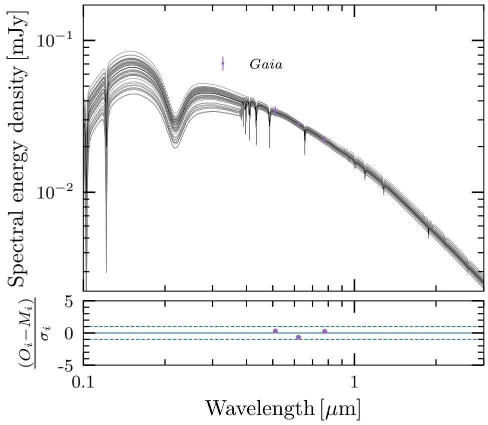

(a) WD 2

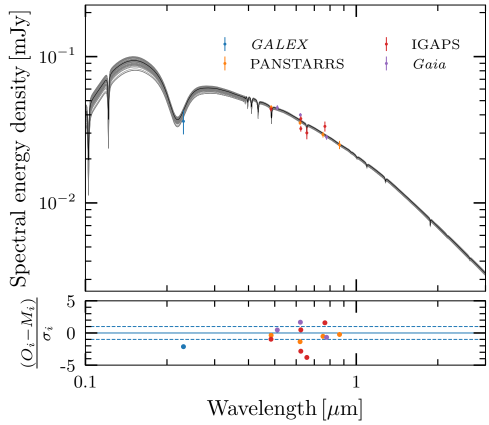

(b) WD 3

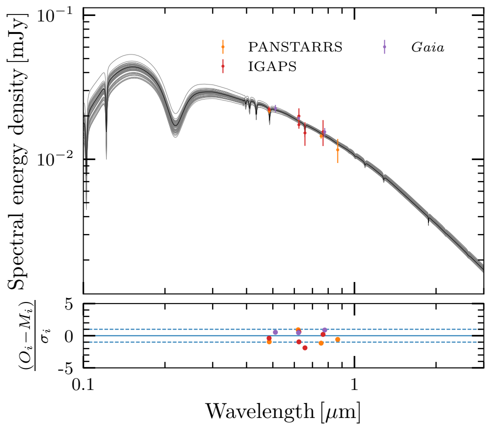

(c) WD 4

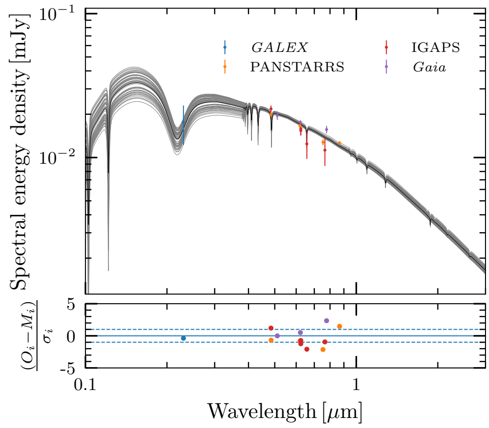

(d) WD 5

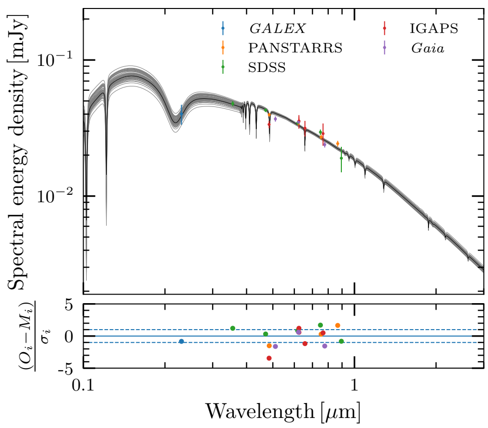

(e) WD 6

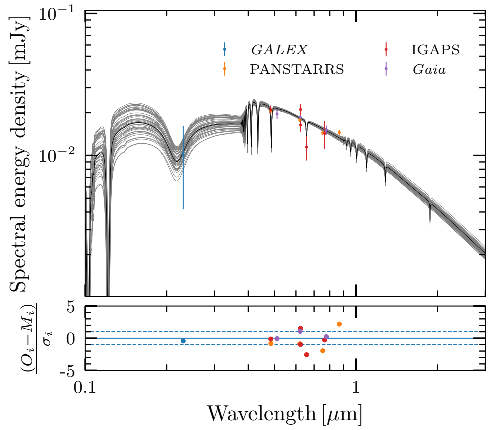

(f) WD 7

Figure 3.13: Best fit results for the SED analysis of six WD candidates. In each panel, the upper plot shows the best-fit model (black) and the models corresponding to the uncertainty range (grey). The bottom plots represent the residuals among the used photometry and the best-fit model.

4. The white dwarf sequence in M37[1]

In this chapter we use new observations from the Canada-France-Hawaii Telescope to study the white dwarf cooling sequence of the open cluster M37, a cluster that displays an extended main sequence turn-off and, according to a recent photometric analysis, also a spread of initial chemical composition. By taking advantage of a first epoch collected in 1999 with the same telescope, we have been able to calculate proper motions for sources as faint as $g \sim 26$ (about ~ 6 magnitudes fainter than the *Gaia* limit), allowing us to separate cluster members from field stars. This has enabled us to isolate a sample of the white dwarf population of M37, reaching the end of the cooling sequence (at $g \sim 23.5$). The here-derived atlas and calibrated catalogue of the sources in the field of view are publicly released as supplementary on-line material. Finally, we present an exhaustive comparison of the white dwarf luminosity function with theoretical models, which has allowed us to exclude the age-spread scenario as the main responsible for the extended turnoff seen in the cluster colour-magnitude-diagram.

4.1 Introduction

During the last few years the unprecedented quality of the photometric and astrometric data obtained with the *Gaia* spacecraft has greatly refined our knowledge of the Milky Way open clusters (OCs). The OC census has improved through the rejection of thousands of misidentified OCs in the literature and the discovery of several hundreds new confirmed OCs (see, e.g., Cantat-Gaudin et al., 2018a; Castro-Ginard et al., 2018, for some examples); moreover, the improved determination of stellar memberships and orbital parameters has provided us with a better characterisation of individual clusters.

In this respect, the analysis of the exquisite, high-precision *Gaia* colour-magnitude diagrams (CMDs) of *bona fide* members of selected OCs, has recently revealed the presence of extended main sequence (MS) turn off (TO) regions and broadened

[1]The content of this chapter has been published in Griggio et al. (2023b).

MSs, that cannot be originated by field contamination, binaries and differential reddening alone (see, e.g., Bastian et al., 2018; Cordoni et al., 2018; Griggio et al., 2022b; Marino et al., 2018b, and references therein). These features are similar to what is observed in the Magellanic where star clusters younger than about 2 Gyr display extended TO regions (see, e.g., Goudfrooij et al., 2014; Mackey and Broby Nielsen, 2007; Mackey et al., 2008; Piatti and Bastian, 2016, and references therein), and clusters younger than $\sim$600-700 Myr display also split MSs (see, e.g., Correnti et al., 2017; Li et al., 2017; Marino et al., 2018a, and references therein).

Whilst there is mounting evidence that rotation –as opposed to an age range among the cluster population– is the main culprit to explain these features in the CMD of both open OCs and Magellanic Cloud clusters (see, e.g., Bastian et al., 2018; Kamann et al., 2018, 2020, 2023, and references therein), our photometric analysis of the $\sim$500 Myr old OC M37 (NGC 2099) – with an extended TO and no split MS – has targeted a magnitude range populated by stars with convective envelopes, hence predicted to be in any case slow rotators, disclosing the presence of a sizeable initial chemical abundance spread, which may or may not be somehow related to the extended TO (Griggio et al., 2022b). We made use of synthetic stellar population and differential colour-colour diagrams using a combination of *Gaia* and *Sloan* photometry to show that the observed MS colour spread in the high-precision *Gaia* Early Data Release 3 (EDR3 Gaia Collaboration et al., 2021) CMD can only be reproduced by differential reddening and unresolved binaries plus either a metallicity spread Δ[Fe/H]$\sim$0.15, or a range of initial helium mass fractions $\Delta Y \sim 0.10$. As discussed in Griggio et al. (2022b), the existing spectroscopic (high- and medium resolution) measurements of the cluster stars' metallicity provide indications both in favour and against the existence of a [Fe/H] spread (in which case our results would point to a sizeable helium abundance spread), but a high-precision differential abundance analysis of a consistent sample of cluster stars is needed to address this issue spectroscopically.

It is worth noticing that the existence of chemical abundance spreads in low-mass clusters like OCs (M37 has an estimated mass of just 1 000–1 500 $M_\odot$, see Piskunov, A. E. et al., 2008) is unexpected and hard to explain, and has important implications not only for models of cluster formation and the test of stellar models on CMDs of OCs, but also for the technique of chemical tagging (Freeman and Bland-Hawthorn, 2002), based on the idea that clustering in chemical space can in principle associate individual field stars with their birth clusters, assumed chemically homogeneous. If OCs are commonly born with a sizeable internal [Fe/H] range, the suitability of this technique for field stars in the disk of the Milky Way is challenged.

In this paper, we present a new photometric analysis of M37's white dwarf

(WD) cooling sequence (CS), which improves upon earlier results by Kalirai et al. (2001b) in several ways. The area covered by our observations is over three times larger than Kalirai et al. (2001b), who also used the outer regions of their mosaic to estimate field stars contamination, which are however now known to host several members stars (Griggio et al., 2022a). For our field decontamination we have used a safer region much further away from the cluster core, and in addition we exploited their data to obtain proper motions with a time baseline of 23 years, which allowed us to determine a sample of WD members.

Taking advantage of this new data we have performed a theoretical analysis of the observed CS to seek for additional constraints on the origin of the cluster extended TO and its chemical abundance spread. The *present-day* low total mass of M37 seems to preclude the presence of multiple generations of stars and hence of an age spread according to the scenario presented by Goudfrooij et al. (2014), because the cluster should not be able to retain the ejecta of those first-generation stars that can provide material for further episodes of star formation (asymptotic giant branch stars, supernovae). However, the chemical composition spread we detected photometrically seems to suggest otherwise, hence it is important to derive independent constraints about the origin of the observed extended TO. The study of the WD cooling sequence and its consistency –or lack of– with ages inferred from the TO can provide us with these independent clues.

We also publicly release the catalogue with magnitudes and proper motions of the covered region, containing more than 120 000 sources.

The outline of the paper is as follows. Section 4.2 presents our new observations, the data reduction process, and the artificial star tests; Sections 4.3 and 4.4 present the observed WD CS and its theoretical analysis, respectively, and are followed by Section 4.5 with the conclusions.

4.2 Observations

The main data employed in this article was obtained with the MegaPrime camera at *CFHT*, between September 27th and 29th, 2022 (PI: Nardiello). The MegaPrime camera is composed of forty 2048×4612 pixels CCDs, with a pixel scale of ~ 0.187 arcsec/px. We collected a set of three images with an exposure time of 300 s, and three images of 5 s, both in the *Sloan* filters g and r. The observations in g were repeated twice, for a total of eighteen images, twelve in g and six in r. The data was dithered enough to cover the CCDs' gaps, with a total field of view of about 1.2×1.0 sq. degrees; a three-colour stacked image of the data is shown in Fig. 4.1.

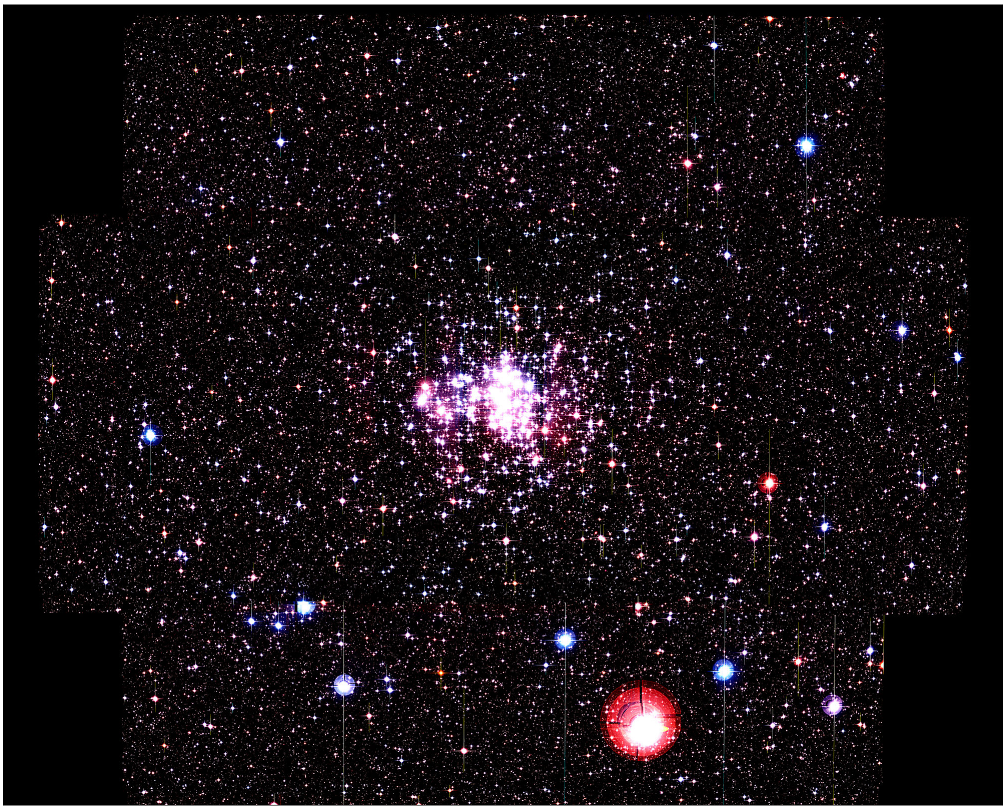

Figure 4.1: Three-colour view of the field of view. We used g as blue, r as red, and a combination of gr for the green colour.

Since the brightest members of M37 MS and all the red clump stars were saturated even in the short exposures, we collected a set of 50 dithered images with exposure times of 10 s in both g and r with the Asiago Schmidt telescope, to complete the photometry of the brighter part of the CMD. The Asiago Schmidt telescope has a $\sim$1 sq. degree field of view, and similar data collected with this instrument were described in Griggio et al. (2022a).

We also took advantage of an early epoch collected at *CFHT* (with the pioneering CHF12K camera, 12 CCDs, $\sim$0.206 arcsec/px, 42×28 sq. arcmin) in 1999 (PI: Fahlman, Kalirai et al., 2001a), to obtain proper motions. The CH12K was one of the first wide-field CCD camera to become operative, and these images were collected in the *Johnson B* and *V* filters. We used three images per filter, with an exposure time of 300 s.

A log of the observations is reported in Table 4.1.

Table 4.1: Summary of the observations.

Filter	Exp. time	N. of images	Avg. seeing
Megaprime			
g	300 s	6	0.55 arcsec
g	5 s	6	0.58 arcsec
r	300 s	3	0.56 arcsec
r	5 s	3	0.70 arcsec
Schmidt			
g	10 s	50	1.86 arcsec
r	10 s	50	1.97 arcsec
CFH12K			
B	300 s	3	0.79 arcsec
V	300 s	3	0.81 arcsec

4.2.1 Preliminary photometry

As a first step, we derived a 'preliminary photometry', i.e. we measured the flux and position of the brighter sources, that are then used as a starting point to correct for the geometric distortion and to compute the transformations between the different exposures. We treated each CCD of each exposure as an independent image; in the following we will use the terms 'exposure' and 'image' to refer to the image associated to the single CCD. Using a version of the software by Anderson et al. (2006) adapted to the *CFHT* data, we computed a 5×9 grid of empirical point spread functions (PSFs) for each image to take into account for the time variations; the grid is necessary to account for the spatial variation of the PSF across the CCD. Each PSF is derived empirically from bright, unsaturated and isolated stars, and to each point on the image we associated a local PSF by a bilinear interpolation of the four closest PSFs in the grid. We then used the software described in Anderson et al. (2006) to find and measure the position and flux of the sources in the images by using the local PSF. The software outputs a catalogue with positions and instrumental magnitudes of the sources for each exposure.

4.2.2 Geometric distortion

Given that one of our goals was to measure proper motions, we needed accurate positions in both epochs. To this purpose, we corrected the geometric distortion following the same approach for both the detectors CFH12K and MegaPrime (the procedure is similar to the one adopted in Griggio et al., 2022a).

We selected bright ($g_{\rm instr} < -10$), unsaturated sources from each catalogue derived by the preliminary photometry. We cross-identified the sources in our catalogues with the sources in the *Gaia* DR3 catalogues, projected onto the tangent plane of each image in its central pixel, after transforming the positions to the epoch of each observation. We then fitted the residuals between the *Gaia* positions and the positions measured in our images with a third-order polynomial, and applied the 75% of the correction. We then repeated the process, starting with the corrected positions of the previous iteration, reaching convergence after 30 iterations.

After the correction, the residuals' dispersion for bright sources is smaller than 0.05 pixels in both detectors, corresponding to ~ 10 mas for the 1999 data and to ~ 9 mas for the 2022 data; summing up these residuals in quadrature we obtain a positional dispersion of ~ 14 mas, to be diluted over a time-baseline of ~ 23 years, i.e. about 0.6 mas yr^{-1}. Given the absolute proper motion of M37, which is about 6 mas yr^{-1} (Griggio and Bedin, 2022), this will allow for a proper-motion-based separation between field objects and cluster members (see Sec. 4.2.4).

4.2.3 Master frame and zero-points calibration

To measure the faintest sources in the field of view, we needed to perform deep photometry as in Griggio et al. (2022a) (which we name 'second-pass photometry', see Sec. 4.2.4). This requires to define a common reference system for all the exposures, to which we then refer the positions in both epochs, that we call 'master frame'. The master frame was defined by the positions of the *Gaia* DR3 catalogue, projected onto the plane tangent to the central point of image `506225p` for CFH12K data, and `2785599p` for MegaPrime data. The *Gaia* positions were again transformed to the epoch of each observation. We used the catalogues of each image to derive the six-parameter transformations to bring the positions measured in the detector reference frame of each exposure onto the corresponding master frame.

The MegaPrime exposures were also dithered enough to allow us measuring the CCDs' relative photometric zero points, which we found to be of the order of 0.01 mag. Our derived BV photometry for the CFH12K dataset, however, was not usable, in part because we could not access the calibration files, and in part because of the non-ideal dither pattern, which did not allow us to register the CCD zero points to a common photometric reference system. Therefore, the 1999 CFH12K images were used only to derive positions in this first epoch, which were in turn employed to derive the proper motions necessary to decontaminate cluster

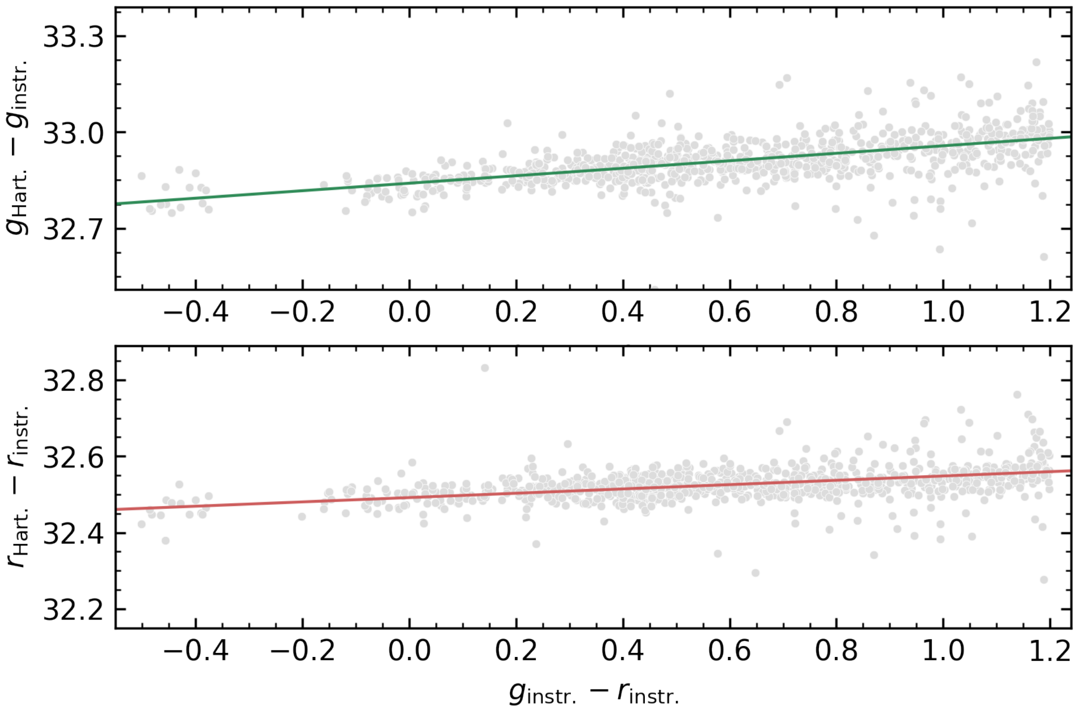

Figure 4.2: Calibration of the *CFHT gr* filters: the coloured lines denote the linear fit to the data. We display the difference in the g and r filters between Hartman et al. (2008) and our instrumental magnitudes, as a function of the instrumental $(g - r)$.

stars from field objects.

4.2.4 Photometry and astrometry

To extract the positions and fluxes for all the sources in the field of view we used the code `KS2`, an evolution of the code developed by Anderson et al. (2008b) for the Hubble Space Telescope data, which was adapted to deal with the *CFHT* data.

The program goes through several iterations, finding and measuring progressively fainter stars, using all the images simultaneously to find the sources, thus increasing the signal-to-noise ratio. This allows to find even the faintest sources that are lost in the noise in single exposure. The software uses a list of bright stars (derived from the preliminary photometry) to construct weighted masks, that help to avoid PSF-related artefacts. The flux is measured performing a PSF fitting of the inner 5×5 pixels of the source, with the appropriate local PSF, and averaged between all the images, with a local sky computed from the surrounding pixels.

Measured stars are subtracted from the image before proceeding with the next iteration. The program outputs also some quality flags (see, e.g., Bedin et al., 2009), that we used to discard sources with galaxy-like shape and diffraction spikes.

The gr instrumental magnitudes have been then calibrated using the deep photometric catalogue by Hartman et al. (2008) by means of a relation in the form $m_{\mathrm{cal}} = m_{\mathrm{instr}} + a(g_{\mathrm{instr}} - r_{\mathrm{instr}}) + b$, with the parameters a and b determined from a linear fit, as shown in Fig. 4.2. The calibrated CMD of all the sources in the field of view is shown in Fig. 4.3.

We extracted the photometry from the Asiago data as described in Sec. 3.1 of Griggio et al. (2022a). We did not perform the second-pass photometry as we needed only the bright sources. We employed the same procedure outlined for the MegaPrime data to calibrate the Asiago photometry.

The flux and position of the sources in the 1999 exposures were extracted with the software `KS2`. However, due to the issues described in the previous section, we did not carry out the photometric calibration.

Proper motions were calculated using the displacements dx and dy between the two epochs, divided by the time baseline of $\sim$23 years, and are shown in Fig. 4.4 (where we used the cluster's mean proper motion as the origin); the displacements were measured by transforming the positions of the stars in the first epoch into the reference system of the second epoch with a six-parameter transformation, and cross-identifying the common sources.

The bottom panel of Fig. 4.4 shows the member selection; we plotted the distance dr from the origin as function of the g magnitude, and we drew by hand the red line following the distribution of cluster stars, with a sharp cut where cluster and field cannot be well separated by eye. In addition, we estimated the field median dx and dy and its intrinsic dispersion $\sigma_{x,y}$ as 1.5 times the 68.27$^{\mathrm{th}}$ percentile of the distribution of dx and dy around their median, and excluded the sources with proper motion inside a circle centred on the field motion with radius given by the sum in quadrature of $\sigma_{x,y}$ (dashed black circle in Fig. 4.4). For sources that are present in the catalogue by Griggio et al. (2022a), we adopted their `member` flag, that, for sources at brighter magnitudes, is more reliable that the selection based on our measured proper motions as it is based on the *Gaia* astrometry.

This selection leads to Fig. 4.5, where we show in light grey all the sources with proper motions (which are less than those in Fig. 4.3, as the 2022 data are deeper and cover a larger area than the 1999 ones) and in blue the selected cluster members. We plotted the *CFHT* photometry up to $g = 12.5$, and the Schmidt data for $g < 12.5$ to complete the TO and red clump regions which are saturated in the *CFHT* short exposures.

Our derived proper motions represent an extension of the *Gaia* astrometry

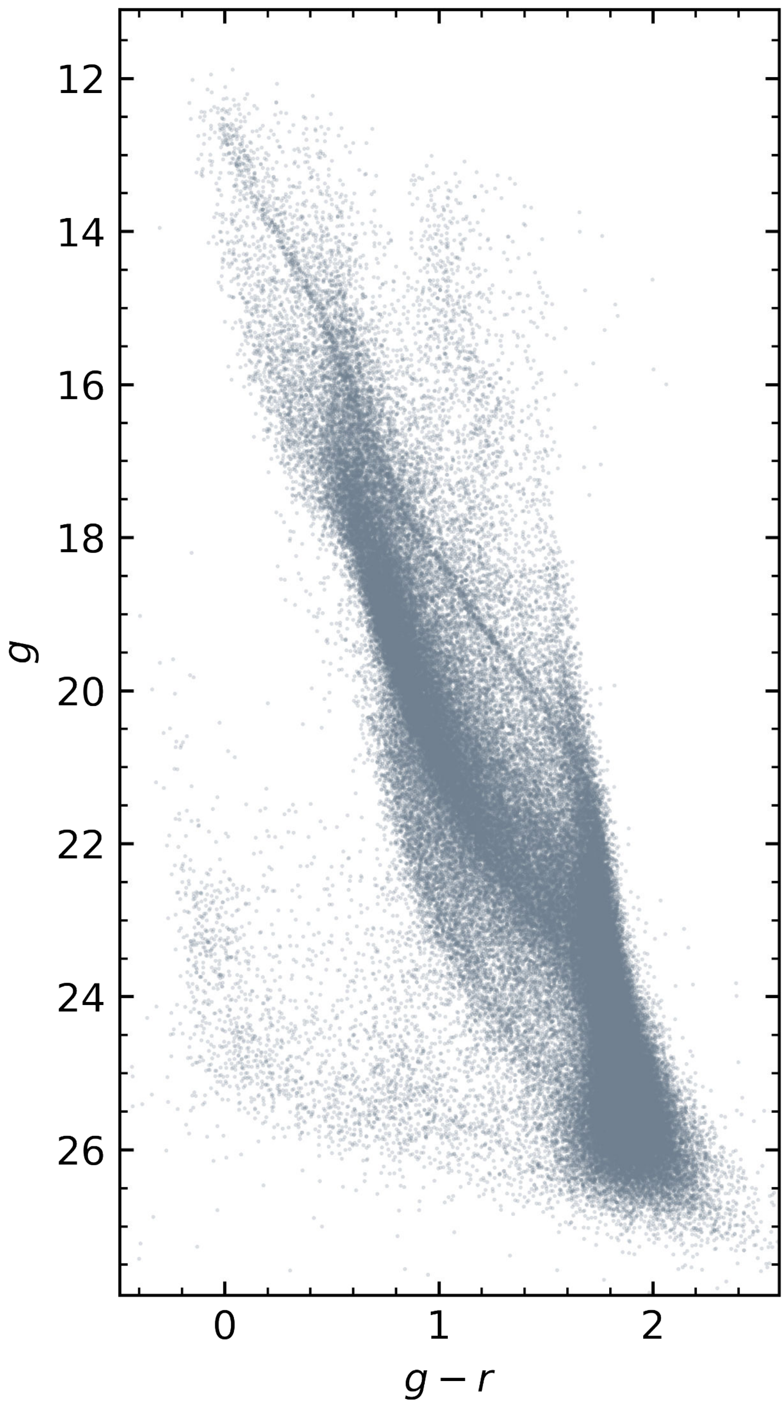

Figure 4.3: CMD of all the sources that passed the quality cuts in the gr filters ($\sim 120\,000$).

down to $g \sim 26$, and the deepest astro-photometric catalogue of M37 available until now. Unfortunately, given the large errors on the positions of faint sources in the first epoch, we cannot discriminate very well between members and field stars for $g \gtrapprox 22.5$. Nonetheless, we proved the capability of ground-based wide-field imagers in providing useful astrometry even in the *Gaia* era.

Finally, we confirm WD1, WD2 and WD3 of Griggio et al. (2022a) as member candidates according to their proper motions obtained in this work, while WD5 proper motions are not compatible with those of the cluster. The other WDs, namely WD4, WD6 and WD7, fall outside the field of view, and we could not measure their motion.

4.2.5 Artificial stars test

To assess the completeness of our data set, we performed the artificial star (AS) test with the `KS2` program (see, e.g., Bedin et al., 2009). Briefly, we injected in the images 100 000 synthetic stars (one at a time, in order to not create false over-crowding), generated with random positions and random g magnitudes, both sampled from a uniform distribution, with r magnitudes such that they lie on the WD CS fiducial drawn by hand on the CMD (Fig. 4.6, left panel). The software then operates blindly, finding and measuring all the sources in the images. We then compared the list of measured stars with the AS input list. We considered an AS as recovered if its measured position is within 1 pixel in x and y from the injected position and its magnitude within 0.1 from the injected magnitudes in both filters.

In the right panel of Fig. 4.6 we show the CMD of the recovered stars, that guided the choice of the region we adopted to derive the WD differential luminosity function (LF). We divided into 0.5 g-magnitude bins the recovered ASs, and for each bin we computed the median colour and the $\sigma = 68.27^{\text{th}}$ percentile of the colour residuals around the median. The orange error bars in the right panel of Fig. 4.6 represents the 3σ interval, and the blue and red curves connecting the edges of the error bars define the region that we will use for our analysis.

The AS test let us infer the completeness of our data set, defined as the ratio between the number of recovered stars and the number of injected stars, which varies across the magnitude range covered by our observations. We computed this ratio for each 0.25 g-magnitude interval, and interpolated the values with a spline. The derived completeness curves are plotted in Fig. 4.7: the two horizontal lines mark the 80% and 50% completeness levels. Notice that the completeness drops below 50% at about $g \sim 24$, and reaches zero at $g \sim 26$.

The completeness has been computed both for the 'cluster' region and 'field'

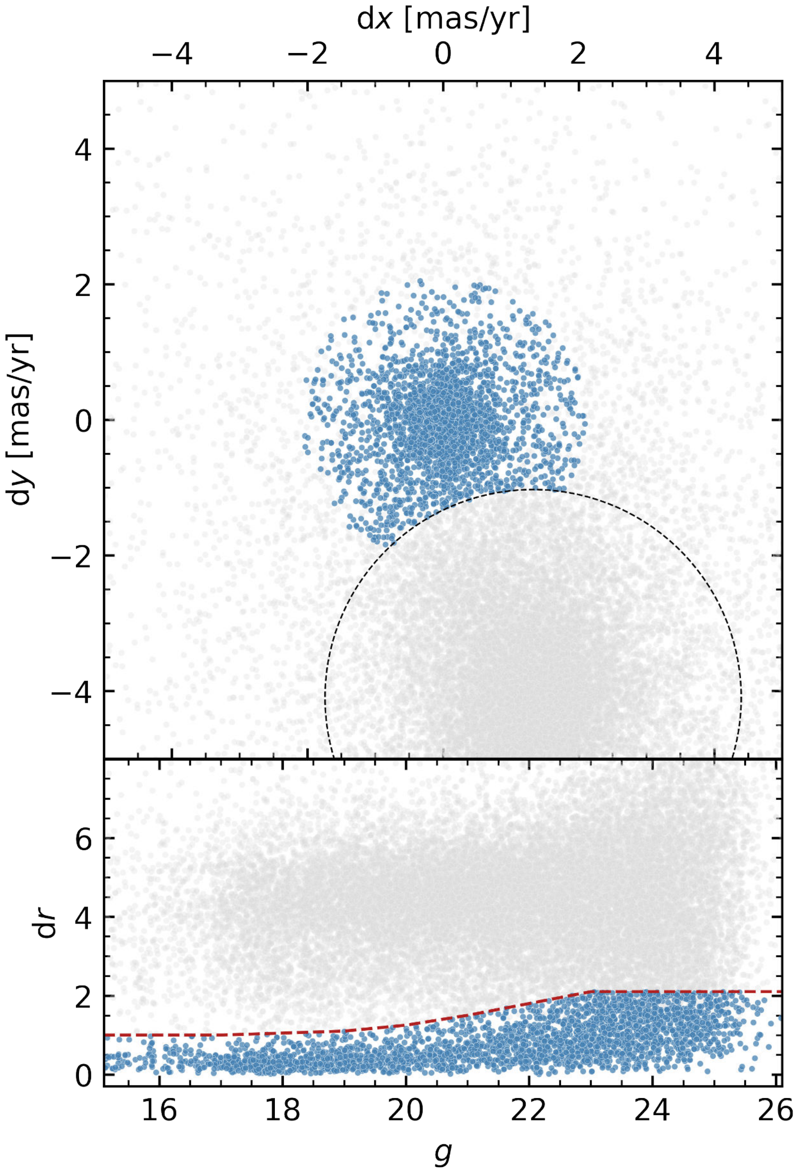

Figure 4.4: *Top panel*: proper motions for all the sources (grey), with selected members highlighted in blue. The dashed black circle is the cut described in the text. The origin is set to the cluster's mean proper motion. *Bottom panel*: dr vs g for all the sources (grey) and cluster members (blue).

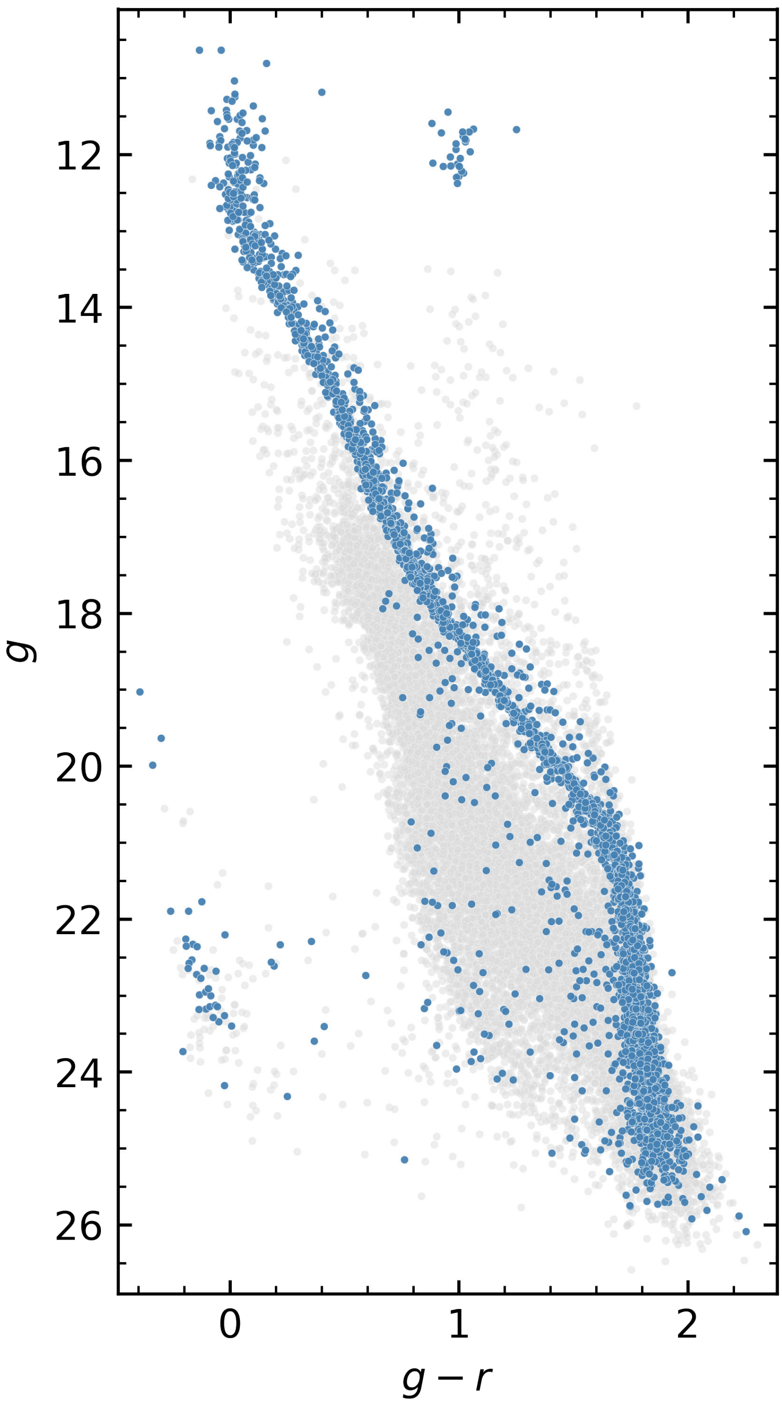

Figure 4.5: CMD for all the sources with proper motions (light grey, $\sim 24\,000$) and for those selected as cluster members (blue, $\sim 3\,200$).

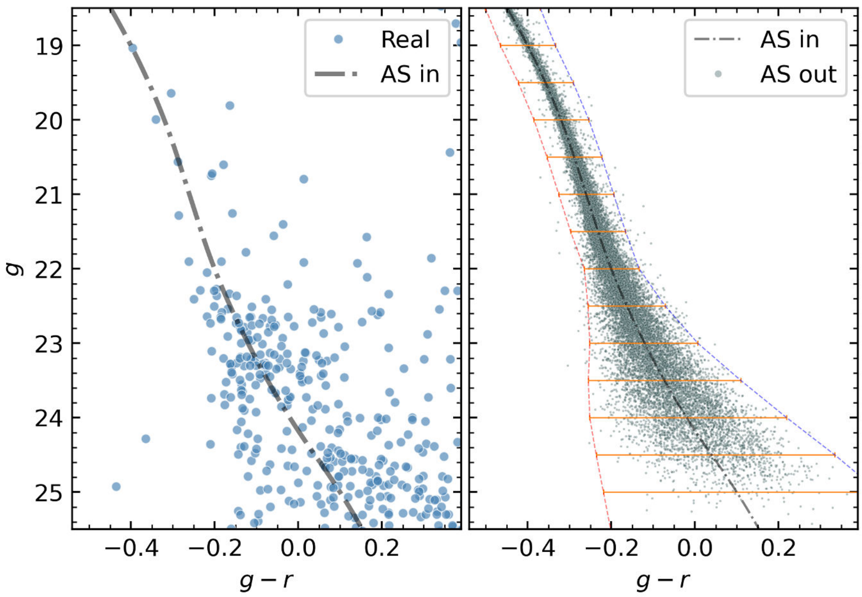

Figure 4.6: Artificial stars test. *Left panel*: blue points denote the observed white dwarfs, the dark grey line represents the fiducial along which we generated the artificial stars. *Right panel*: recovered artificial stars. The orange error bars are calculated as three times the 68.27$^{\mathrm{th}}$ percentile of the colour residuals around the median, in each 0.5 magnitude bin. The dashed lines connecting the edges of the error bars define the region in which we will count the white dwarfs.

regions, shown in Fig. 4.8 in blue and red respectively. The two regions have roughly the same area of about 0.2 deg^2, and will be employed in Sec. 4.3 in the study of the WD CS.

4.2.6 Astro-photometric catalogue

Together with this work we publicly release an astro-photometric catalogue of the sources that we measured in the *CFHT* field of view. Proper motions are available only for sources in the common region of the 1999 data, which is about one-third of the new dataset (as shown in Fig. 4.8).

The catalogue contains x and y positions on the master frame in MegaPrime pixels, with 187 mas px^{-1}, the gr photometry and proper motions along the x and y axes in mas yr^{-1}. In addition, the `quality` flag denotes sources that passed our quality cuts, and the `member` flag those who are selected as member candidates in this work (blue points in Fig. 4.4).

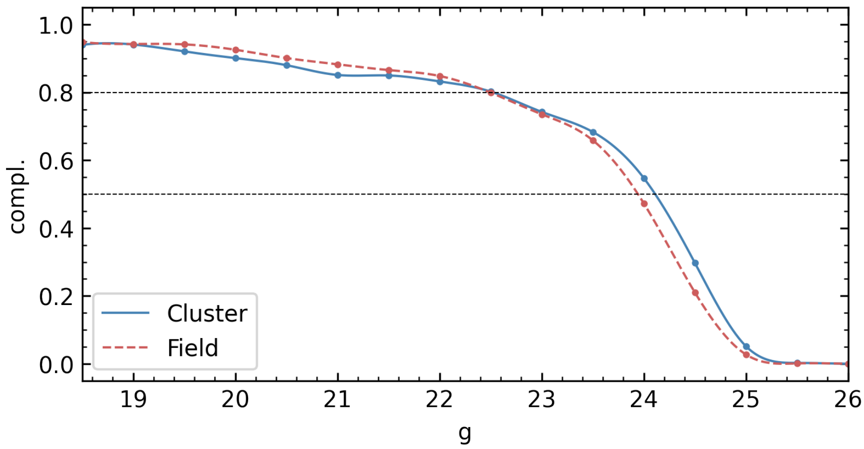

Figure 4.7: Completeness of our data in the 'cluster' and 'field' regions. See text and Fig. 4.8.

4.3 The white dwarf cooling sequence

The 1999 dataset allowed us to measure proper motions for sources well beyond the *Gaia* magnitude limit, down to $g \sim 26$; however, given the large errors, we could not discriminate well between cluster and field stars at magnitudes fainter than $g \sim 22.5$ (see Fig. 4.4, bottom panel). Most faint sources that have a clear point-like shape in the 2022 data are heavily affected by the noise in the 1999 data, making their position (and consequently, their proper motion) measurements very uncertain. For this reason, we did not employ proper motions to remove field objects in the derivation of the LF; we have instead performed a statistical decontamination (cfr. Bedin et al., 2023) using the regions defined in Fig. 4.8 to obtain the WD LF that we will compare to theoretical predictions in the next section.

Fig. 4.9 shows the CMD of the WD CS, for both the 'cluster' and 'field' regions defined in Fig. 4.8. The red and blue lines in these CMDs are those defined by the AS test (Fig. 4.6) and mark the boundaries of the region within which we count WD candidates. The final LF is given by the difference between the completeness-corrected 'cluster' and 'field' LFs, and is shown in sea-green in the right panel of Fig. 4.9 (and reported in Table 4.2), with error bars corresponding to Poisson errors. The dashed dark-grey line represents the LF of WD member candidates selected by proper motions: we note that the two LFs have similar features, and in particular they terminate at the same magnitude $g \sim 23.5$, where the completeness level is still greater than 50% (cfr. Fig. 4.7). This cut-off of the LF is well-defined and can be used as an age indicator for the cluster; for an increasing age of the

Table 4.2: Our derived, completeness-corrected, WD differential LF. Negative values have been set to zero.

g	N	σ_{N}
19.00	1.1	1.0
19.28	0.0	0.0
19.56	1.1	1.0
19.84	0.0	0.0
20.12	1.1	1.1
20.40	0.0	0.0
20.68	0.0	0.2
20.96	0.0	0.0
21.24	0.0	0.0
21.52	0.0	0.0
21.80	1.2	1.1
22.08	0.0	0.0
22.36	4.9	2.2
22.64	15.2	3.9
22.92	7.9	2.8
23.20	24.8	5.0
23.48	15.7	4.0
23.76	0.0	0.0
24.04	0.3	0.5
24.32	0.0	0.0
24.60	0.0	0.0
24.88	0.0	0.0

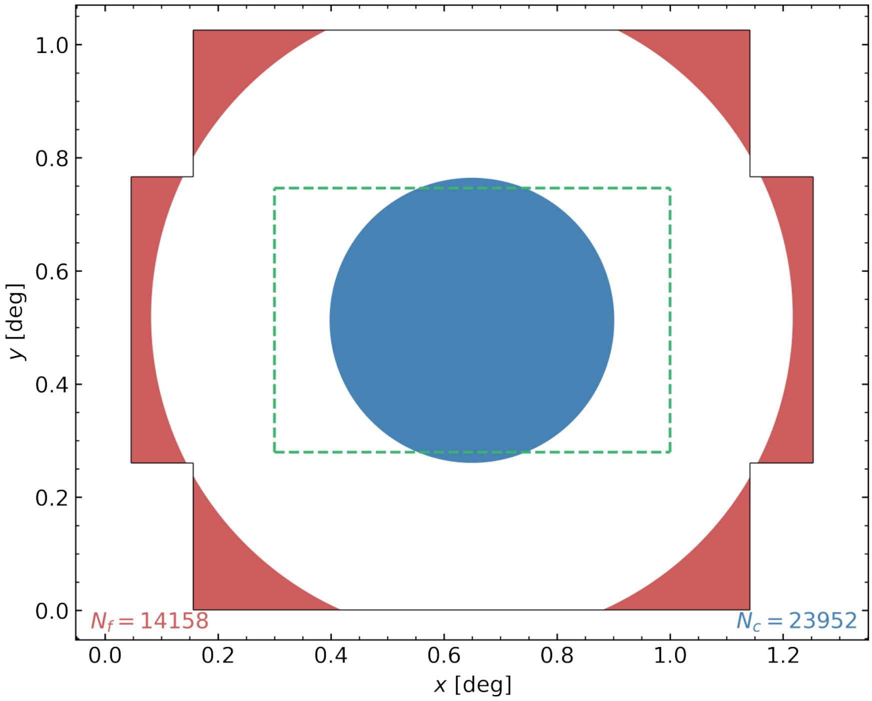

Figure 4.8: Total field of view of the MegaPrime data. The black lines delimit the observed region. The blue filled area is the "cluster" region, while the red filled area is the "field" region. The two regions have the same area of ~ 70 Mpx. The number of stars in each region is annotated in the lower corners. The green dashed line shows the area covered in 1999 by the CFH12K detector.

cluster's population, the oldest (earlier forming) WDs have more time to cool down, thus shifting the LF cut-off towards fainter magnitudes.

4.4 Comparison with theory

In this section we discuss the comparison of the WD LF of Table 4.2 with theoretical WD models, that enabled us to derive important constraints on the origin of the extended TO observed in the cluster CMD. Due to the issue highlighted below, we have only compared the LF in the g band with theory, and not the CS in the CMD.

As already mentioned, we found in Griggio et al. (2022b) that the stellar population hosted by this cluster displays either a range of metallicity Δ[Fe/H]~ 0.15 and a range of differential reddening $\Delta E(B-V) = 0.06$ ([Fe/H] spread scen-

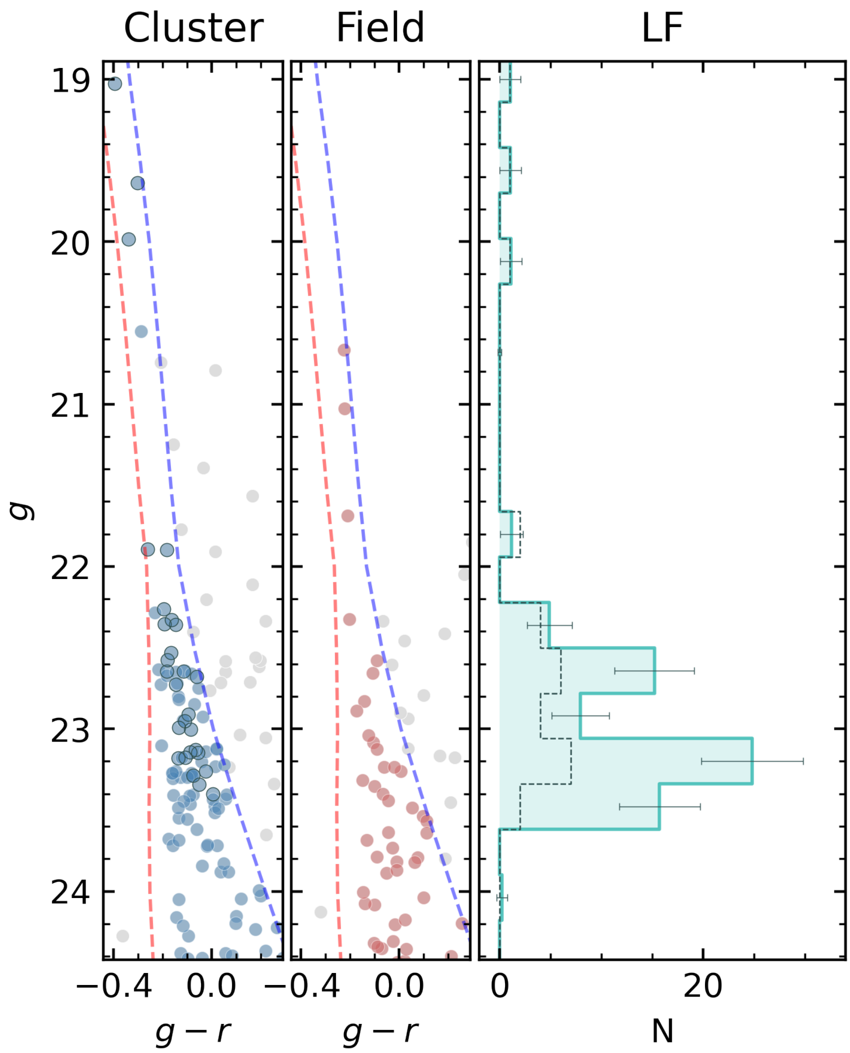

Figure 4.9: CMD of the WD CS in the 'cluster' (*left panel*) and 'field' (*middle panel*) regions. Blue points with solid black edge in the left panel denote the sources that are member candidates according to their proper motions. The red and blue dashed lines are those defined by the AS test (see Fig. 4.6). The *right panel* shows the completeness-corrected LF after field decontamination (sea green). The dark-grey dashed line represents the LF of the proper motion selected WD members. See text for details.

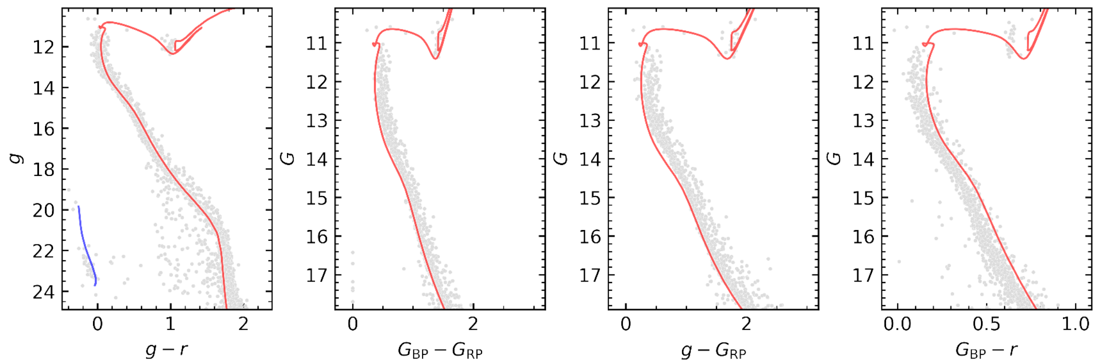

Figure 4.10: CMDs of M37 stars in several magnitude and colour combinations. Theoretical isochrones (including the WD sequence in the left panel) are compared to the observations using $E(B-V) = 0.28$, and a distance $d = 1450\,\mathrm{pc}$ (see text for details). The extinction law is taken from Zhang and Yuan (2023), for the *Sloan* filters and from the *Gaia* website (`https://www.cosmos.esa.int/web/gaia/edr3-extinction-law`) for *Gaia* magnitudes.

ario), or a spread of helium abundance $\Delta Y \sim 0.06$ and a range $\Delta E(B-V) = 0.03$ (helium spread scenario). For the distance – 1450 pc, consistent with the range 1500 ± 100 pc determined by Griggio and Bedin (2022) from *Gaia* EDR3 parallaxes – and reference [Fe/H] = 0.06 – consistent with the existing few high-resolution spectroscopic measurements (Pancino et al., 2010) – used in Griggio et al. (2022b) analysis, in the [Fe/H] spread scenario the reference $E(B-V)$ ranges from 0.28 mag to 0.34 mag and the metallicity ranges from [Fe/H] = 0.06 to [Fe/H] = 0.21. The lowest metallicity isochrone (from the BaSTI-IAC database, Hidalgo et al., 2018) matches the blue envelope of the unevolved MS in the *Gaia* CMD (G magnitudes between ~ 15 and ~ 17) for the lowest value of the reddening, $E(B-V) = 0.28$ (see, e.g., Figs. 1 and 9 in Griggio et al., 2022b). In the Y spread scenario, we found Y ranging from $Y = 0.269$ – the standard value of Y at [Fe/H] = 0.06 in the BaSTI-IAC isochrones – to $Y = 0.369$, for $E(B-V)$ between 0.33 mag and 0.36 mag. In this case, the blue envelope of the unevolved MS in the *Gaia* CMD is matched by the most helium-rich $Y = 0.369$ (hence bluer) isochrones, and $E(B-V) = 0.33$.

The leftmost panel of Fig. 4.10 shows that, in the [Fe/H] spread scenario, when we match a 400 Myr (the exact age is irrelevant to this discussion) [Fe/H] = 0.06 BaSTI-IAC isochrone (from the same sets adopted in Griggio et al., 2022b) to the MS in the *Sloan* g-$(g-r)$ CMD using $E(B-V) = 0.28$ and the extinction ratios by Zhang and Yuan (2023), the models are redder than the blue edge of the unevolved MS in a wide magnitude range. This includes the interval between $g \sim 16$ and ~ 19, which approximately corresponds to the G magnitude range of the *Gaia* CMD where the isochrones match the blue edge of the MS (Griggio et al., 2022b), as shown is the second panel from the left of the same figure.

We also show a 400 Myr WD BaSTI-IAC isochrone calculated from hydrogen-envelope (DA) carbon-oxygen (CO) core WD cooling tracks (computed with the Cassisi et al., 2007, electron conduction opacities) with [Fe/H] = 0.06 progenitors by Salaris et al. (2022), the initial-final-mass relation (IFMR) by Cummings et al. (2018) and progenitor lifetimes from Hidalgo et al. (2018), compared to the observed CS for the same choice of distance and reddening. The WD isochrone also appears redder than the observations.

To investigate the cause(s) of this inconsistency with the fit to the MS in the *Gaia* CMD, the third and fourth panel from the left in Fig. 4.10 display CMDs with the *Gaia* G magnitude on the vertical axis, and colours calculated using one *Gaia* and one *Sloan* magnitude. The same isochrone of the left panel is compared to the data in these two CMDs. We can see that the models in the $G - (g - G_{\mathrm{RP}})$ CMD match the blue edge of the MS, whilst the isochrones are redder than the observed MS in the $G - (G_{\mathrm{BP}} - r)$ CMD. This suggests that the inconsistency between the fits in the two photometric systems arises from a mismatch between the theoretical and observed r magnitudes[2]. For this reason, in our study of the WD cooling sequence, we will consider only the g magnitudes.

To compare the WD g-band LF with models we computed grids of CO-core DA WD isochrones with the same inputs as the one in Fig. 4.10 (from progenitors with [Fe/H] = 0.06), for ages between 150 and 450 Myr at steps of 25 Myr, and calculated synthetic LFs using Monte-Carlo techniques. As shown in Fig. 4.10, at these ages the WD isochrones are sequences of continuously increasing magnitude in the g band, and the WD mass evolving at a given brightness increases monotonously with increasing g. Due to the younger ages, the ranges of progenitor and WD masses along the isochrones are narrower than in the case of globular clusters. At 150 Myr the brightest part of the isochrones is populated by $\sim 0.95\,M_{\odot}$ WDs with progenitor masses equal to $\sim 4.6\,M_{\odot}$, whilst at 450 Myr the WDs have a mass equal to $\sim 0.75\,M_{\odot}$ with progenitors of $\sim 2.9\,M_{\odot}$. The bottom end of the isochrones is populated by $1.1\,M_{\odot}$ WDs with $\sim 6.4\,M_{\odot}$ progenitors.

For each isochrone, we have produced a sample of g magnitudes of synthetic WDs (20 000 for each age, to minimise statistical fluctuations of their magnitude distribution), by drawing randomly progenitor masses according to a Salpeter

[2] This mismatch exists also in comparison with Hartman et al. (2008) photometry, which has been used to calibrate our magnitudes, as shown in Fig. 4.2.

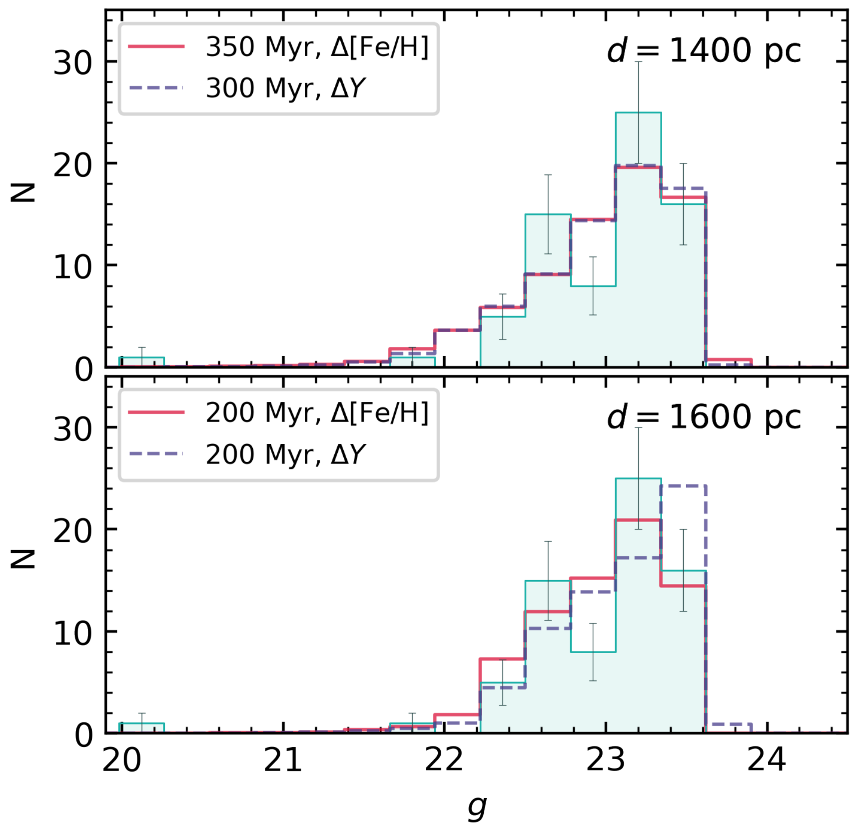

Figure 4.11: Completeness-corrected differential WD LF of the WDs in M37 (sea green) compared to theoretical LFs calculated for the labelled ages and chemical compositions (see text for details). The errors in the number counts of the observed LF are also displayed.

mass function (power law with exponent $x = -2.3$) and interpolating along the isochrone to determine the g magnitude of their WD progeny. We then corrected the magnitude for the assumed cluster distance and applied a random extinction (using the extinction-law by Zhang and Yuan, 2023) from values of $E(B-V)$ drawn with a uniform probability within the range appropriate to the explored scenario ([Fe/H] or Y spread). Each synthetic g was then perturbed by a random Gaussian photometric error with σ estimated from the observations (see Sec. 4.2.5).

For each of these samples (corresponding to a given WD isochrone age) we finally calculated the differential LF with the same binning of the observed one, and rescaled the total number of objects in the LF to the observed (completeness corrected) one, before comparing it with the observations.

Table 4.3: Maximum ages compatible with the WD LF cut-off magnitude, for the two distances and scenarios discussed in the text.

d (pc)	age (Myr)	scenario
1400	350	Δ[Fe/H]
1400	300	ΔY
1600	200	Δ[Fe/H]
1600	200	ΔY

These sets of synthetic samples of WDs and the corresponding LFs have been computed for both the [Fe/H] spread and Y spread scenarios, considering two distances d equal to 1400 and 1600 pc, respectively the lower and upper limits of the distance determination from *Gaia* parallaxes by Griggio and Bedin (2022). For the assumed reference metallicity [Fe/H] = 0.06 the minimum $E(B-V)$ values (determined as described above) for $d = 1400$ pc are 0.26 mag for the Δ[Fe/H] scenario, and 0.31 mag for the ΔY scenario. At $d = 1600$ pc the minimum reddenings are $E(B-V) = 0.31$ for the Δ[Fe/H] scenario, and 0.36 mag for the ΔY scenario. It is important to mention that for the Δ[Fe/H] scenario we have calculated the WD isochrone for just one value of [Fe/H] ([Fe/H] = 0.06). This is because we have found that changing [Fe/H] of the progenitors by ± 0.20 dex produces isochrones virtually indistinguishable at these ages. The same is true also for the ΔY scenario, with isochrones calculated considering just the minimum value of Y.

We have determined the oldest cluster age compatible with the observed WD cooling sequence, by finding the theoretical LFs that match the magnitude of the cut-off of the WD LF. Fig. 4.11 shows the oldest ages compatible with the observed LF – between 200 and 350 Myr, summarised in Table 4.3 – for the two distances and the two scenarios discussed here. The derived ages are typically older (by 100-150 Myr) for shorter distances, as expected, and at a fixed distance they are very similar in both scenarios. At these ages, all WDs along the cluster CS have not yet started crystallization in their CO cores. It is important to stress that, in case the extended TO of this cluster is due to an age range, the WD LF tells us that the maximum age of the cluster stars cannot be older than the values given above, otherwise we should find WDs fainter than the observed LF cut-off.

We have then repeated the same procedure by employing isochrones derived from WD cooling models (again from Salaris et al., 2022) calculated using the alternative Blouin et al. (2020) electron conduction opacities, and found results consistent with what we have previously obtained from calculations with the Cassisi et al. (2007) opacities. As an example, Fig. 4.12 shows how the 350 Myr theoretical

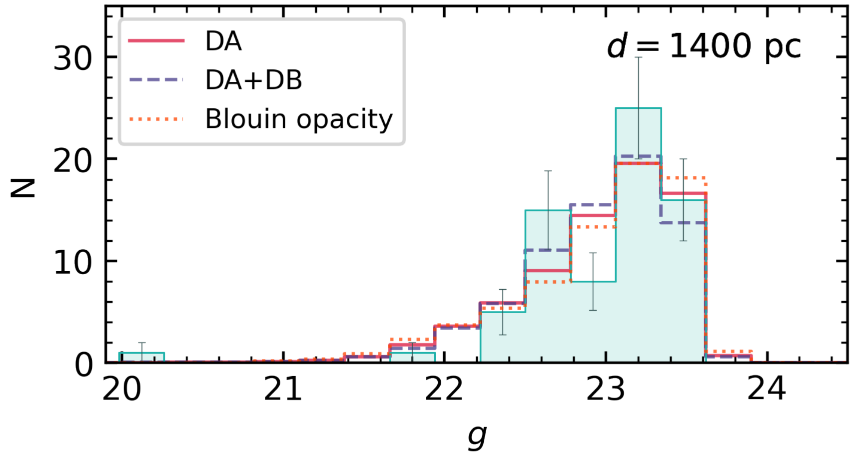

Figure 4.12: As the upper panel of Fig. 4.11. The theoretical LFs are for an age of 350 Myr and correspond to the reference DA calculations of Fig. 4.11, a population of 20% DB (helium envelope) and 80% DA WDs, and a DA population from models calculated using Blouin et al. (2020) electron conduction opacities, respectively (see text for details).

LF in the Δ[Fe/H] scenario calculated using Blouin et al. (2020) opacities and a distance of 1400 pc has the same cut-off magnitude as our reference calculations.

We have also explored the possibility that the cluster hosts not just DA WDs, but also a 20% fraction of WDs with He-dominated atmospheres (this fraction is typical of the Galactic disc field WD population, see, e.g., Koester and Kepler, 2015). In this case, for each age, we have computed isochrones and synthetic samples of g magnitudes from the helium-envelope WD models by Salaris et al. (2022), and merged them with the corresponding DA samples in a proportion 20/80, before calculating the corresponding LF. The results about the WD-based cluster ages are again unchanged (see Fig. 4.12 for an example), because in this luminosity regime H- and He-envelope WD models cool down at very similar rates.

Finally, we have explored the role played by the adopted IFMR. For all isochrones employed in our analysis we have adopted the semiempirical Cummings et al. (2018) IFMR, more specifically the one determined using the Bressan et al. (2012) stellar evolution models (see Cummings et al., 2018, for details) for the determination of the progenitor's lifetimes, because they are very close to the evolutionary lifetimes of Hidalgo et al. (2018) progenitors' models used for the calculation of the WD isochrones. As a test, we have calculated some DA WD isochrones and LFs (in the g band) in the age range between 200 and 350 Myr for [Fe/H] = 0.06, employing the Cummings et al. (2018) IFMR calculated using MIST (Choi et al., 2016) non-rotating stellar models for the progenitor lifetimes. The effect of this alternative IFMR on the magnitude of the LF cut-off at fixed age is only on the order of 0.01 mag, with a negligible impact on the results of our analysis. We have repeated this same test using the independent IFMR determined by El-Badry et al. (2018), and found again a negligible impact on the magnitude of the theoretical LF cut-off.

4.4.1 Constraints on the origin of the extended TO

The impact of these results on the interpretation of the cluster extended TO is shown by Fig. 4.13, which is analogous to Fig. 9 in Griggio et al. (2022b). For each scenario and the same two distances of the WD analysis, we show here the cluster *Gaia* CMD (from Griggio et al., 2022b) together with pairs of isochrones for the combinations of [Fe/H] (or Y) and reddenings that match the blue and red limits of the single-star sequence in the magnitude range studied by Griggio et al. (2022b), and ages equal to the corresponding maximum ages determined from the WD LF. According to the WD-based ages, no single star along the upper MS and TO can be redder than the metal richer isochrone in the Δ[Fe/H] scenario, or redder than the helium poorer one in the ΔY scenario. This is clearly contradicted by the observed CMD, which displays large fractions (if not the whole cluster population) of objects redder than the reddest isochrone around the TO region. This leads to the conclusion that even considering the metallicity or the helium spread derived from the unevolved MS, the ages determined from the WD LF exclude the presence of an age spread as the reason for the observed extended TO.

4.4.2 The role played by oxygen-neon core WDs

In our analysis, we have considered the CS sequence to be populated by CO-core WDs, which are by far the most common type of WDs. However, according to stellar model calculations, stellar progenitors in a fairly narrow mass range between very approximately 6.5-7 and 9-10 $M_{\odot}$, are expected to produce WDs with an oxygen-neon core and masses between ~ 1.1 and $\sim 1.3\,M_{\odot}$, originated from the electron degenerate cores formed at the end of core carbon burning (see, e.g., Doherty et al., 2017; Poelarends et al., 2008; Siess, 2006, and references therein). Predictions, both empirical and theoretical, for the IFMR of these WDs is very uncertain; however, it is still possible to make an informed assessment of their impact on the WD ages determined in our analysis.

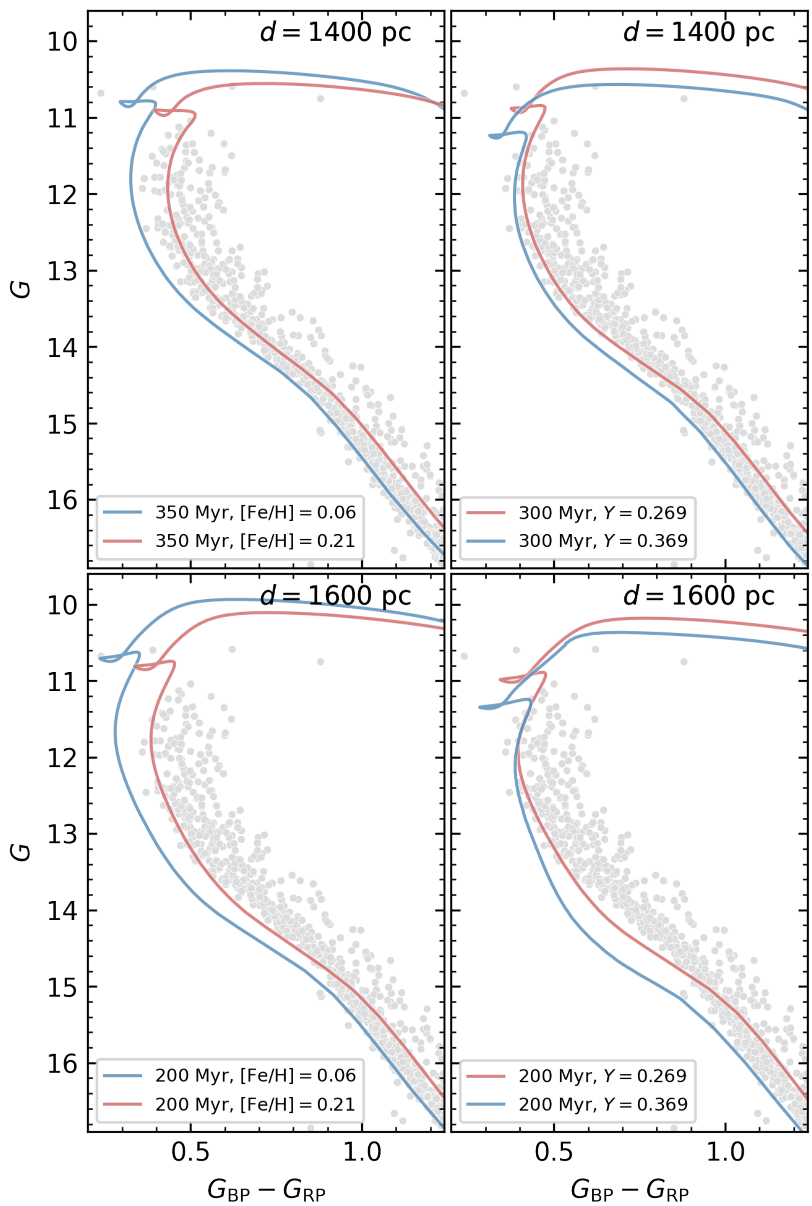

Figure 4.13: Cluster's *Gaia* CMD compared to isochrones with the labelled parameters (see text for details).

To this purpose, we have considered the ONe-core hydrogen-envelope WD models by Camisassa et al. (2019) and the CO-core DA models from the same group (Camisassa et al., 2017) – both from progenitors with roughly solar metallicity – for a strictly differential analysis using models calculated with the same code and physics inputs. We have considered the $1.1\,M_\odot$ CO-core cooling model – corresponding to the mass of the more massive model used in our WD isochrones –, and the $1.2\,M_\odot$ and $1.3\,M_\odot$ ONe-core models, and calculated WD isochrones and luminosity functions in both Δ[Fe/H] and ΔY scenarios for ages between 200 and 400 Myr, using progenitors lifetimes from Hidalgo et al. (2018) and the IFMR by Cummings et al. (2018) for WD masses up to $1.1\,M_\odot$, as in our calculations. For the initial masses of the two ONe WD models we have made various assumptions, with values between 7 and 9-9.5 $M_\odot$, and obtained always the same results in terms of the LF cut-off magnitudes.

We found that the ONe-core WDs are located at fainter magnitudes with respect to the $1.1\,M_\odot$ CO-core objects, because of their slightly faster cooling in the relevant luminosity range; the difference (for the $1.3\,M_\odot$ models) in the g band LF cut-off is on the order of 0.2-0.3 mag. This implies that including massive ONe-core WDs in the calculation of the isochrones would in principle reduce the age necessary to match the observed cut-off by ~ 100 Myr, thus exacerbating the inconsistency between WD ages and the ages required to explain the extended TO in terms of an age spread.

4.5 Conclusions

We have presented a new *Sloan* photometry of the OC M37, from the very low-mass star regime to the main sequence TO and red clump, including the WD cooling sequence down to its termination. We make publicly available these catalogue (positions, photometry, proper motions and flags) and the atlases, as on-line supplementary material of this article. We have focused our analysis on the WD CS, and determined a new, improved WD LF that we have exploited to set constraints on the origin of the cluster extended TO.

We have found that, irrespective of whether the chemical abundance spread revealed by Griggio et al. (2022b) photometric analysis is due to variations of [Fe/H] or Y, for the distance range determined using *Gaia* EDR3 parallaxes the ages determined from the WD LF are incompatible with the ages required to match the observed extended TO region. The maximum age allowed by the analysis of the WD LF is much too young compared to the age required to match the redder and fainter TO region. This is especially true for the Y-spread scenario, and also for the [Fe/H]-spread scenario when considering the upper limit of the parallax-based distance.

Our results indirectly support the notion that stellar rotation is needed to explain the origin of the cluster extended TO, like the case of the OC NGC 2818, Bastian et al. (2018), where spectroscopic observations have confirmed the presence of a range of rotation rates among TO stars, with redder TO objects being faster rotators. A comprehensive analysis of the MS extended TO and WD cooling sequence of M37 using models including the effect of rotation[3] is now needed, together with spectroscopic measurements of the rotation velocities of TO stars, and also spectroscopic metallicities, to determine whether the abundance spread revealed by the photometric analysis of Griggio et al. (2022b) is due to a metal abundance or a helium spread.

[3] Cordoni et al. (2018) have presented a first preliminary comparison of the cluster extended TO with models including rotation.

5. Signature of a chemical spread in the open cluster M37[1]

Recent *Gaia* photometry of the open cluster M37 have disclosed the existence of an extended main sequence turn off –like in Magellanic clusters younger than about 2 Gyr– and a main sequence that is broadened in colour beyond what is expected from the photometric errors, at magnitudes well below the region of the extended turn off, where neither age differences nor rotation rates (the candidates to explain the extended turn off phenomenon) are expected to play a role. Moreover, not even the contribution of unresolved binaries can fully explain the observed broadening. In this chapter we investigate the reasons behind this broadening by making use of synthetic stellar populations and differential colour-colour diagrams using a combination of *Gaia* and *Sloan* filters. From our analysis we have conclude that the observed colour spread in the *Gaia* colour-magnitude diagram can be reproduced by a combination of either a metallicity spread Δ[Fe/H] ~ 0.15 plus a differential reddening across the face of the cluster spanning a total range $\Delta E(B-V) \sim 0.06$, or a spread of the initial helium mass fraction $\Delta Y \sim 0.10$ plus a smaller range of reddening $\Delta E(B-V) \sim 0.03$. High-resolution differential abundance determinations of a sizeable sample of cluster stars are necessary to confirm or exclude the presence of a metal abundance spread. Our results raise the possibility that also individual open clusters, like globular clusters and massive star clusters, host stars born with different initial chemical compositions.

5.1 Introduction

The study of star clusters has been and still is one of the main sources of information about stars and galaxies. Photometric as well as spectroscopic observations allow us to determine a cluster's kinematics, its distance, age, chemical composition, dynamical status and the detailed colour and magnitude distribution of its

[1]The content of this chapter has been published in Griggio et al. (2022b).

stars, all pieces of information that set strong constraints on astrophysical models of galaxy and stellar evolution.

In these studies a first crucial step is the determination of the membership probability of the observed stars, to disentangle actual cluster members from neighbouring field stars not bound to the cluster. Recently, Griggio and Bedin (2022) developed a new formalism to compute the astrometric membership probabilities for sources in star clusters, and applied their technique to the Galactic open cluster NGC 2099 (M37) using *Gaia* Early Data Release 3 (EDR3) data.

This cluster has an age of about 500 Gyr, a metallicity around Solar, and has been the subject over the years of several investigations regarding its distance, age and dynamical status (e.g. Joshi and Tyagi, 2016; Mermilliod et al., 1996; Nilakshi and Sagar, 2002), searches for variable (e.g., Kang et al., 2007; Kiss et al., 2001) and peculiar stars (Paunzen et al., 2003), studies of rotation and photometric activity of its low-mass stellar population (e.g. Chang et al., 2015; Messina et al., 2008), investigations of its white dwarf initial-final mass relation (e.g. Cummings et al., 2015, 2016; Kalirai et al., 2005), and its white dwarf cooling sequence Kalirai et al. (2001b). More recently Cordoni et al. (2018) employed photometry and proper motions from *Gaia* Data Release 2 to reveal the presence of an extended main sequence (MS) turn off (TO) in the colour-magnitude diagram (CMD) of M37 (and a few other Galactic open clusters), qualitatively similar to what found in Magellanic Cloud clusters younger than about 2 Gyr.

In this paper we have exploited the accurate *Gaia* EDR3 CMD provided by Griggio and Bedin (2022) which shows a MS broadened not only around the TO (as found by Cordoni et al., 2018), but also in the lower mass regime (i.e. when $G \gtrsim 15$). We will show that this broadening of the lower MS is not due just to photometric errors, and also that differential reddening plays only a minor role. A moderate spread of metallicity or helium appear to be the main culprit, adding an unexpected new twist to our evolving views about star clusters and their formation. To state it more clearly, this work will not deal with the MSTO phenomenon, but will focus on the part of the MS which is not affected to both rotation and age effects.

The paper is organised as follows. In Section 5.2 we present the *Gaia* photometry; the auxiliary *Sloan* photometry which we used to study the lower MS broadening is briefly described in Section 5.3. This is followed by Section 5.4 which presents our detailed analysis of the broadening of the lower MS. A section with a summary and conclusions brings the paper to a close.

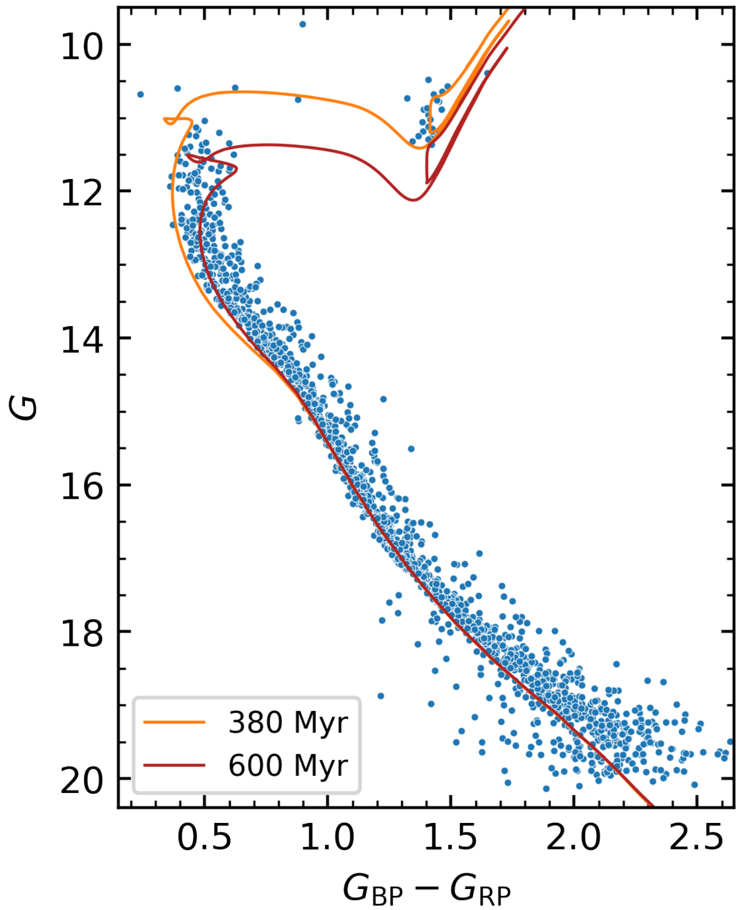

Figure 5.1: *Gaia* EDR3 CMD of M37 with superimposed two non-rotating BaSTI-IAC isochrones with [Fe/H] = 0.06 and the two labelled ages, bracketing the extended TO region (see text for details).

5.2 The *Gaia* colour-magnitude diagram

Figure 5.1 displays the CMD of M37 from *Gaia* EDR3, as obtained by Griggio and Bedin (2022). The diagram clearly exhibits an extended TO region, a red clump of core He-burning stars (around $G \sim 11$ and ($G_{\mathrm{BP}} - G_{\mathrm{RP}} \sim 1.4$), and a MS with a parallel sequence of unresolved binaries with mass ratio greater than $\sim$ 0.6-0.7.

By employing a cluster distance equal to 1.5 ± 0.1 kpc (determined from *Gaia* EDR3 parallaxes by Griggio and Bedin, 2022), we qualitatively checked the general consistency of theoretical isochrones with the cluster CMD. More specifically, we adopted as reference the non-rotating Solar-scaled BaSTI-IAC isochrones (Hidalgo et al., 2018) that include convective core overshooting.

Figure 5.1 displays two [Fe/H] = 0.06 (corresponding to an initial metallicity $Z = 0.0172$ and helium mass fraction $Y = 0.269$) isochrones with ages equal to 380 and 600 Myr respectively, matched to the blue edge[2] of the observed unevolved MS between $G \sim 15$ and $G \sim 17.5$ for a distance equal to 1450 pc. We took into account the extinction by employing the extinction law for the *Gaia* filters given by the *Gaia* collaboration[3] and derived a reddening $E(B-V) = 0.28$. The two ages employed in this comparison approximately bracket the brighter and lower limit of the cluster's extended TO region.

The reddening is consistent with the broad range of values found in the literature ($E(B-V)$ between ~ 0.23 and ~ 0.35, see, e.g., Hartman et al., 2008; Joshi and Tyagi, 2016; Piatti et al., 1995), and the metallicity chosen for the isochrones is also consistent with the values of [Fe/H] measured with high- and low-resolution spectroscopy (see, e.g. Marshall et al., 2005; Netopil et al., 2016; Pancino et al., 2010), typically in the range between about Solar and $\sim +0.10$ dex.

In this comparison we employed non-rotating isochrones, and the extended TO region is bracketed by assuming a total age spread of about 220 Myr (see also Cordoni et al., 2018). Another possibility (likely the one to be preferred, see e.g. Bastian et al., 2018; Cordoni et al., 2018) is that the extended TO is caused by the presence of stars with approximately the same age but with a range of initial rotation rates.

Irrespective of the reasons for the appearance of the extended TO, the cluster MS with G larger than $\sim$ 15-15.5 is predicted to be insensitive to either an age spread (stars in this magnitude range are still essentially on their zero age MS location at these ages) and a spread of initial rotation rates. This is because, at the cluster's metallicity, stars in this magnitude range have masses below $\sim$ 1.25-1.2 $M_{\odot}$, with convective envelopes thick enough for magnetic braking to efficiently spin them down enough and suppress the effects of rotation (on the hydrostatic equilibrium and chemical mixing) that cause the MS broadening (see, e.g, Georgy et al., 2019; Gossage et al., 2019). We could also test empirically that rotation does not play a role in the colour spread of the lower MS, by cross-correlating the measurements of rotational periods of M37 MS stars by Chang et al. (2015) with our *Gaia* photometry. We ended up with a sample of more than 150 member stars with G between 15.5 and 17 and periods centred around $\sim$ 6 days, that do not show any correlation with the $G_{\rm BP} - G_{\rm RP}$ colour at a given G magnitude.

We have therefore studied the thickness of the MS for G magnitudes larger

[2]The blue edge of the observed CMD is determined as described in Sect. 5.4. It will be clearer in Sect. 5.4 why we match the blue edge of the unevolved MS in this qualitative comparison.

[3]https://www.cosmos.esa.int/web/gaia/edr3-extinction-law

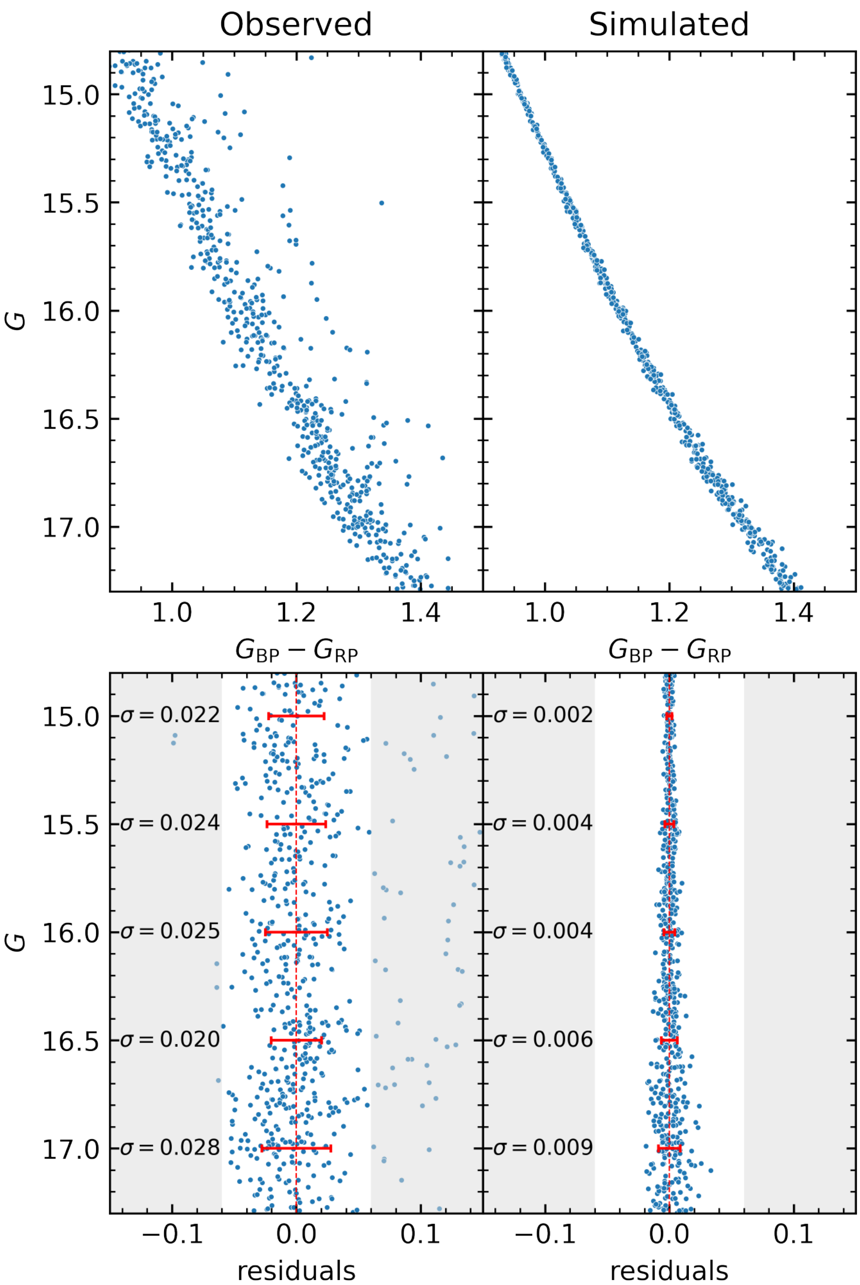

Figure 5.2: *Top panels:* Observed (left) and synthetic (right) CMDs of the cluster lower MS. *Bottom panels:* Colour residuals around the lower MS fiducial lines of the observed (left) and synthetic (right) CMDs, as a function of the G magnitude. The white area encloses the stars employed in the calculation of the 1σ values of the dispersion of the colour residuals reported in the two panels (see text for details).

than 15.5, to avoid the impact of the extended TO phenomenon. As faint limit we considered $G = 17$ (corresponding to a stellar mass $\sim 0.95\,M_{\odot}$), because at larger magnitudes the membership probability is more uncertain (see Griggio and Bedin, 2022), leading to a contamination of the CMD by non-member stars.

In the standard assumption that open clusters host single-metallicity populations, the observed colour width of the MS in the selected magnitude range is expected to be set by the photometric error, the presence of unresolved binaries with a range of values of the mass ratio q, and a possible differential reddening across the face of the cluster. To verify this expectation, we have produced a synthetic CMD of the MS in this G-magnitude range (we will use the term lower-MS from now on, to denote this specific magnitude range along the cluster MS) for the case of single stars all with the same initial metallicity, as described below.

We have defined an observed fiducial line by partitioning the CMD into 0.5 mag wide G-magnitude bins, and interpolated with a quadratic spline the median points of the magnitude and colour number distributions within each bin. We have then uniformly distributed synthetic stars along the fiducial, by adding photometric errors randomly sampled from a Gaussian distribution with zero mean and a standard deviation equal to the median error at the corresponding G-magnitude (individual errors are taken from the *Gaia* EDR3 photometry). The top panels of Fig. 5.2 show the observed cluster CMD (left) and the synthetic CMD described above (right) for the relevant MS region, while the bottom panels display the colour residuals around the fiducial line as a function of G. We also report the values of the dispersion of the colours around the fiducial values at different magnitudes in both CMDs, calculated as the 68.27^{th}-percentile of the distribution of the residuals around zero.

In the calculation of the dispersion of the residuals for the observations we have neglected objects whose place in the CMD is compatible with the position of unresolved binaries with mass ratio $q > 0.6$ (as determined using our isochrones). Even after excluding these objects, the lower panels of Fig. 5.2 show clearly that the synthetic stars are much more narrowly distributed around the fiducial line, when compared to the observations.

Within the standard assumptions described before, the broader colour range spanned by the observed CMD at a given value of G might be ascribed to the presence of unresolved binaries with q lower than 0.6, plus possibly the effect of differential reddening. To understand whether this is the case, we took advantage of an auxiliary photometry in the *Sloan ugi* filters, described in the following section, that we combined with the *Gaia* data as discussed in the Sect. 5.4.

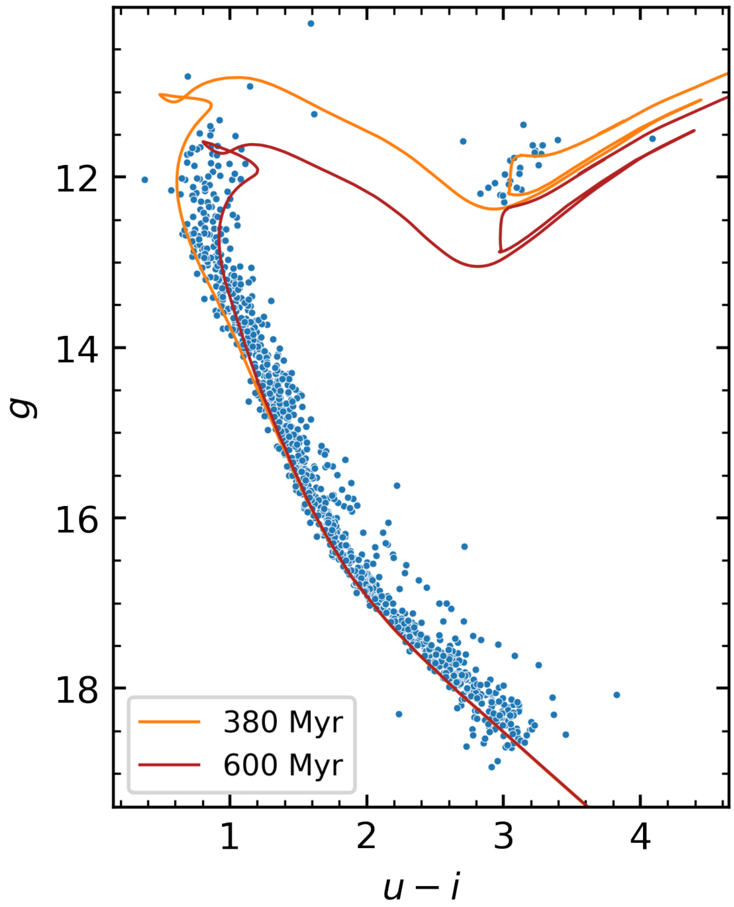

Figure 5.3: As Fig. 5.1 but in the g-$(u-i)$ CMD.

5.3 The *Sloan* colour-magnitude diagram

Our adopted *Sloan* photometry is taken from the catalogue presented and described in Griggio et al. (2022a). Briefly, the data has been collected with the Schmidt 67/92 cm telescope in Asiago (Italy), and the photometry extracted with a version of the `KS2` software by Anderson et al. (2008b) suitably modified to deal with the Schmidt data and wide field mosaics. We selected only the sources with the quality flag `pho_sel` equal to one, to reject sources with poor photometry.

Figure 5.3 shows the g-$(u-i)$ CMD for cluster's members identified with *Gaia*, together with the same isochrones of Fig. 5.1, which are compared to the observations by employing the same distance and $E(B-V)$ values of the match to the *Gaia* CMD.

The effect of interstellar extinction on the magnitudes of the theoretical isochrones has been included using the extinction ratios A_λ/A_V from the NASA/IPAC infrared science archive[4] for the filters u, g and i[5]. Notice that the comparison of the observed CMD with the isochrones is completely consistent with the results for the corresponding CMD in the *Gaia* filters.

5.4 The broadening of the lower MS

To investigate in detail the broadening of the lower MS in the range $15.5 \leq G \leq 17$ (we have a total of 387 stars in this magnitude range) we combined the photometry in the *Gaia* filters with the corresponding u and i magnitudes to build a differential colour-colour diagram, as follows.

As a first step we have defined a MS blue fiducial line in both the G-($G_{\rm BP}-G_{\rm RP}$) and G-($u-i$) diagrams, by partitioning the data into G-magnitude bins 0.2 mag wide. For each bin we have first performed a 3σ-clipping around the median values of the magnitudes and colours, and then we have calculated a representative colour corresponding to the $10^{\rm th}$-percentile of the colour distribution, and the mean G-magnitude. We have finally interpolated with a linear spline among these pairs of colours and magnitudes determined for each bin, to calculate the blue fiducial line for each diagram.

For each observed star we have then computed, in the G-($G_{\rm BP}-G_{\rm RP}$) and G-($u-i$) diagrams, the difference between its colour and the corresponding value of the blue fiducial at the star G magnitude. We notice here that the error on the G magnitudes of the individual stars is on the order of 0.001 mag. We denote these quantities as Δ_{GBR} and Δ_{Gui} respectively (see Figure 5.4).

We finally plotted these colour differences in a Δ_{GBR}-Δ_{Gui} diagram shown in Fig. 5.5, after excluding the relatively small number of sources whose colours are consistent with unresolved binaries with $q \gtrsim 0.6$, which are clearly separated from the bulk of the MS in the *Gaia* CMD. The lower MS stars are distributed along a clearly defined sequence with origin around the coordinates (0,0) –that correspond to stars lying on the blue fiducials– and extended towards increasingly positive values (corresponding to stars progressively redder than the fiducials) with Δ_{Gui} increasing faster than Δ_{GBR}. If the colour spreads are due to random photometric errors only, stars would be distributed without a correlation between Δ_{Gui} and Δ_{GBR}, as we have verified by calculating a synthetic sample of cluster stars including only the photometric errors, as described in more detail below.

[4] https://irsa.ipac.caltech.edu/applications/DUST/

[5] These ratios are $A_u/A_V = 4.239$, $A_g/A_V = 3.303$, and $A_i/A_V = 1.698$

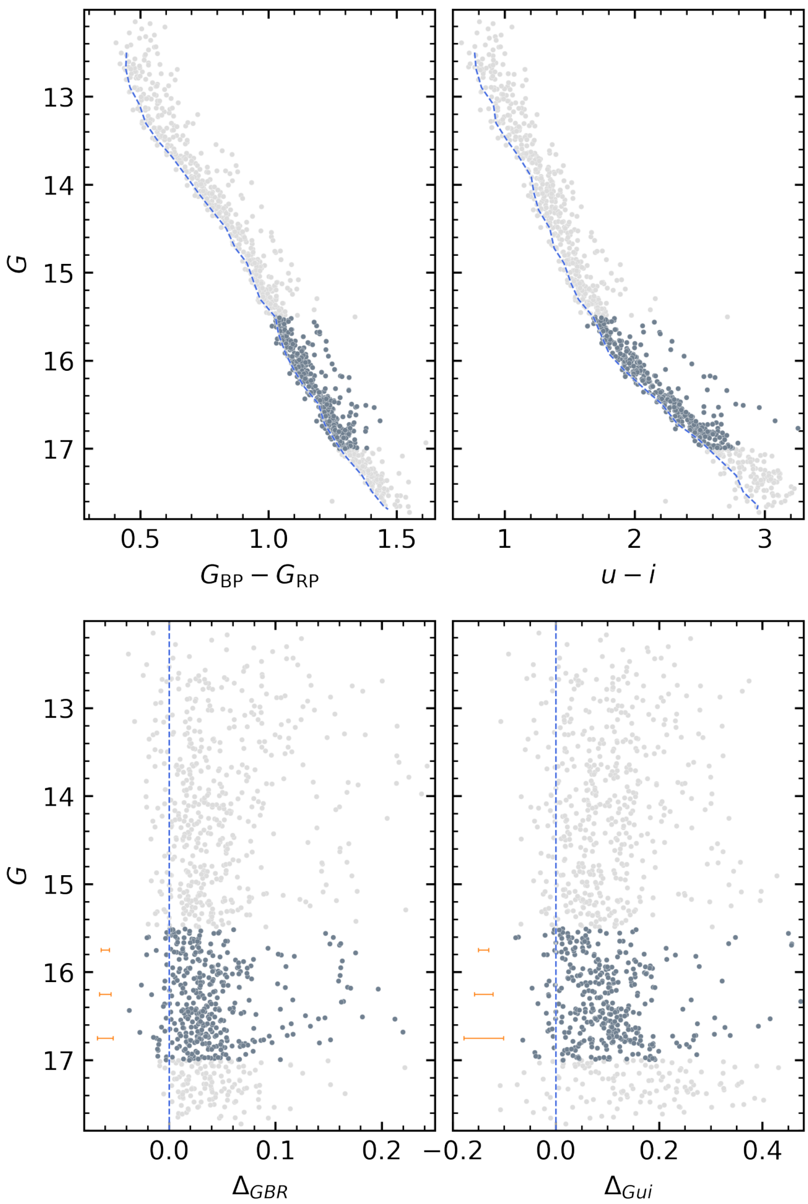

Figure 5.4: *Top panels:* The cluster G-$(G_{\rm BP} - G_{\rm RP})$ and G-$(u - i)$ diagrams. The MS blue fiducials are displayed as dashed lines. Stars in the G magnitude range of interest are displayed in a darker grey shade. *Bottom panels:* The G-Δ_{GBR} and G-Δ_{Gui} diagrams (see text for details). On the left of each panel we display the median $\pm 1\sigma$ colour error at three representative G magnitudes.

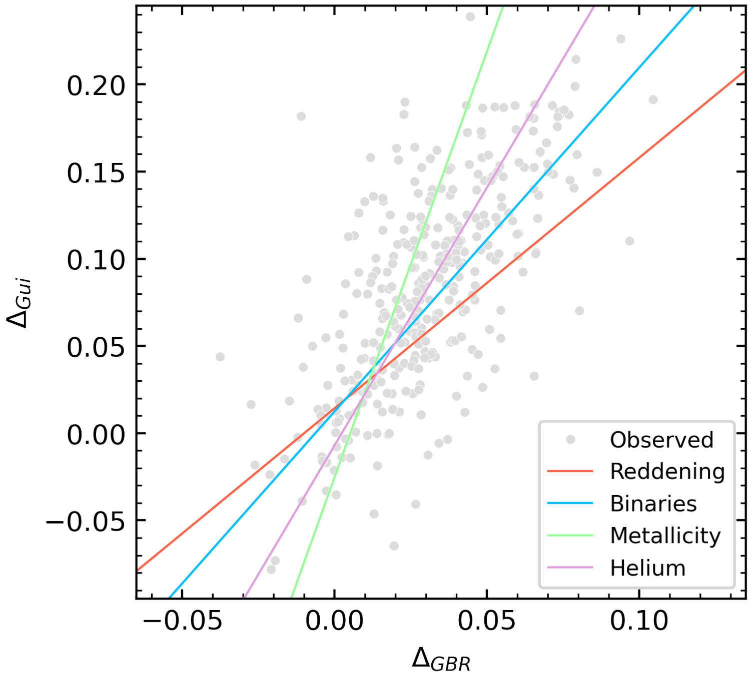

Figure 5.5: Δ_{GBR}-Δ_{Gui} diagram for the lower MS stars, after excluding sources whose colours are consistent with unresolved binaries with mass ratio $q \gtrsim 0.6$. The four straight lines display the the direction along which stars would move due to the effects of differential reddening, unresolved binaries with $q \lesssim 0.6$, spread of initial metallicity, and spread of initial helium abundance (see text for details).

This diagram allows us to exclude that differential reddening is the main reason for the broadening of the cluster lower MS. Figure 5.5 shows together with the data also the direction of the reddening vector, and we can see that differential reddening would move stars at a different angle (shallower) compared to the observed trend. We have also tried the alternative A_λ/A_V extinction ratios for the u and i filters presented in Yuan et al. (2013) and Tian et al. (2014), but the slope of the reddening vector in this diagram hardly changes.

To study in more detail the origin of the distribution of points in this Δ_{GBR}-Δ_{Gui} diagram, we have used the theoretical isochrones of Figs. 5.1 and 5.3 to calculate synthetic samples of lower MS stars as follows. We have considered 600 Myr, [Fe/H] = 0.06 isochrones (the choice of age is irrelevant in this magnitude range) as a reference, and drawn randomly 50000 values of the stellar mass in the range covering the MS, according to a power law mass function with exponent equal to -2.3[6]. By interpolating along the isochrones we determined the *Gaia* and *Sloan* magnitudes of these synthetic objects. We have then considered the contribution of unresolved binaries with $q < 0.6$ by extracting randomly (with a uniform probability distribution) for each synthetic star the value of the mass ratio q to the secondary, to calculate the mass of the unresolved companion. The magnitudes of the companion in the *Gaia* and *Sloan* u and i filters are then derived as described before, and the fluxes of the two components added to determine the total magnitudes of the corresponding unresolved system. To these magnitudes we added the distance modulus and extinction derived from the fit in Fig. 5.1 and applied random Gaussian photometric errors by considering the median 1σ errors of the observations at the G magnitude of the synthetic star.

We determined the Δ_{GBR}-Δ_{Gui} diagram of this sample of unresolved binary stars with low q values in the lower MS magnitude range defined before (which, as we have mentioned in the previous section, corresponds to a mass range of about $0.3\,M_{\odot}$, and contains about 5500 objects in our simulation) by following the same procedure as for the cluster data (after applying distance modulus and reddening determined in the previous section), and fitted with a straight line reported in Fig. 5.5 the direction along which the synthetic stars move in this diagram due to the presence of unresolved companions. Also in this case, the slope is shallower than observed.

Given the inability of unresolved binaries and differential reddening to explain the trend displayed by the lower MS cluster stars in the Δ_{GBR}-Δ_{Gui} diagram, we investigated also the effect of varying the initial chemical composition, namely the metallicity (parametrised in terms of [Fe/H]) and initial helium mass fraction Y.

The synthetic samples have been calculated as described before, but this time we assign to each mass a random value of [Fe/H] or Y according to a uniform probability distribution with a range Δ[Fe/H] = 0.15 (increasing from [Fe/H] = 0.06) or $\Delta Y = 0.10$ (increasing from $Y = 0.269$, the value of the BaSTI-IAC isochrones for [Fe/H] = 0.06, whose corresponding value of the metal mass fraction is kept constant in these simulations with varying Y) in case of variations of helium[7]. An isochrone with the chosen chemical composition was first determined by interpolating quadratically among 600 Myr BaSTI-IAC isochrones of different [Fe/H] (and Y[8]), then the magnitudes (with added photometric errors) were determined

[6] This choice of the mass function provides a good match to the distribution of stars as a function of the G magnitude in the magnitude range of interest.

[7] In this analysis we consider Y increasing above the reference $Y = 0.269$. The reason is that a decrease of just $\Delta Y = 0.02$ would lead to the cosmological helium abundance, which seems unrealistic for a roughly Solar metallicity cluster.

[8] To this purpose we have calculated additional isochrones with varying Y, metallicity $Z =$

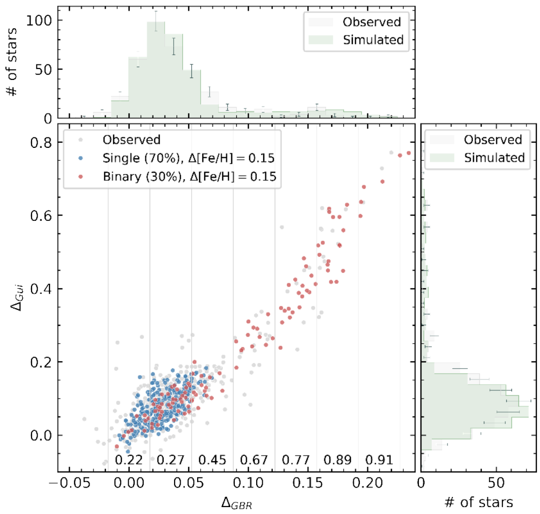

(a)

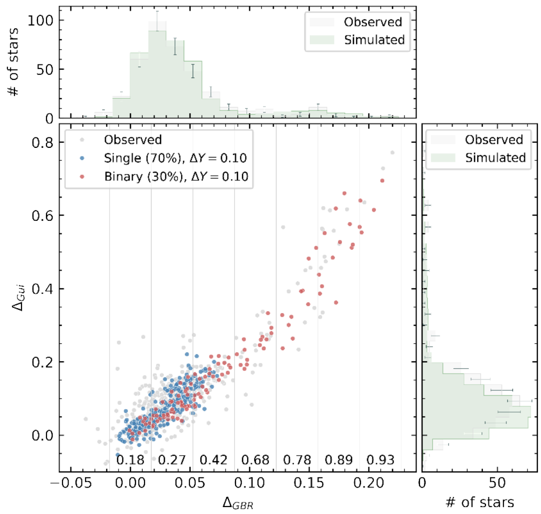

(b)

Figure 5.6: Δ_{GBR}-Δ_{Gui} diagrams for the synthetic populations including binaries plus a metallicity spread Δ[Fe/H] $= 0.15$ (left) and a helium abundance spread $\Delta Y = 0.10$ (right). The simulation in the left panel includes a reddening spread $\Delta E(B-V) = 0.06$, while in the right panel we added a total amount amount of differential reddening $\Delta E(B-V) = 0.03$. The values reported above the x-axis are the mean values of q of the simulated binary stars falling in the regions delimited by the vertical thin lines. Observations are displayed as light grey filled circles. Synthetic single and unresolved binary stars are shown with different colours, to highlight their separate contributions to the diagram. On the right and at the top of each plot we show the histograms of the observed (with Poisson error bars on the star counts) and simulated number counts along the two axes (see text for more details).

as described before.

The direction of the synthetic sequences with [Fe/H] or Y spreads are also reported in Fig. 5.5. It is evident from the figure that the effect of a metallicity spread is predicted to move the stars along a steeper sequence compared to the observations (increasing [Fe/H] moves the objects towards larger values of both Δ_{GBR} and Δ_{Gui}), whilst a spread of Y moves the stars along almost the same direction of the observations (in this case objects with the highest Y would display the lower values of Δ_{GBR} and Δ_{Gui} because an increase of Y moves the MS towards the blue in both the *Gaia* and *Sloan* CMDs).

The conclusion we can draw from the results in Fig. 5.5 is that the observed MS broadening can be explained potentially in two different ways. The first possibility is a spread of metallicity among the cluster's stars, coupled with the presence of unresolved binaries (we know from the CMD that there are unresolved binaries with $q > 0.6$, hence there will be likely objects also with smaller q) and a range of $E(B-V)$ values –meaning differential reddening. These latter two effects tend to compensate for the too steep trend compared to the data predicted by just a metallicity spread.

The second possibility is a spread in Y, together with unresolved binaries and possibly a small amount of differential reddening, smaller than the case of a metallicity spread, otherwise the predicted trend in this diagram would become too shallow.

To set constraints on the size of the metallicity and helium spreads, and the amount of differential reddening for these two scenarios, we have performed additional simulations as those just described, by varying Δ[Fe/H], ΔY and $\Delta E(B-V)$, to reproduce the observed distribution of points in the Δ_{GBR}-Δ_{Gui} diagram. In all these simulations we assumed a binary fraction equal to 0.30, consistent with the value determined by Cordoni et al. (2018) considering the fraction of unresolved binaries with $q > 0.7$ determined from the CMD, and a flat probability distribution of the values of the mass ratios[9].

Given that we do not know the real probability distribution of the values of

0.0172 and Solar scaled metal distribution, using the same code and physics inputs of the BaSTI-IAC models

[9]We also considered the case of a power law distribution of q (probability distribution proportional to $q^{-0.6}$) as found by Malofeeva et al. (2022) for the Pleiades. In this case, the fraction of unresolved binaries with $q > 0.7$ determined by Cordoni et al. (2018) provides a total binary fraction equal to ~ 0.7. The constraints on the values of Δ[Fe/H], ΔY and $\Delta E(B-V)$ however do not change compared to our reference simulations. The reason is that most of this increase of the number of binaries happens for low values of q, and in this situation the magnitudes and colours of the binaries are almost coincident with those of the primary component, hence of single stars.

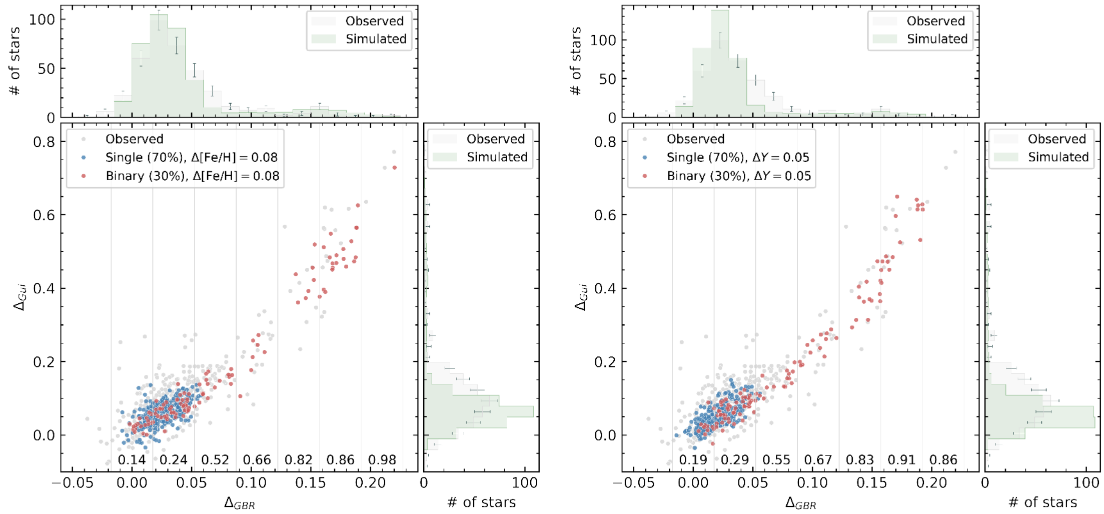

(a) (b)

Figure 5.7: As Fig. 5.6, but with Δ[Fe/H] = 0.08 (left) and $\Delta Y = 0.05$ (right).

reddening and [Fe/H] or Y in the observed sample of stars, we stick to a uniform distribution. This means that in principle we cannot expect to find a perfect match to the observations in the Δ_{GBR}-Δ_{Gui} diagram. However, we can still set important constraints on the size of these spreads by trying to simultaneously reproduce as best as possible the number distributions along the two axes of this diagram.

Figure 5.6 shows two simulations compared to observations in the Δ_{GBR}-Δ_{Gui} diagram, including also objects compatible with being binaries with high values of q. The synthetic samples contain about 5500 objects and include observational errors, unresolved binaries, differential reddening –a spread of $E(B-V)$– and either a spread of [Fe/H] or a spread of the initial helium mass fraction. In the figure we show only one random subset of the full sample, which contains the same number of objects as the observations. The histograms along the horizontal and vertical axis compare the number distributions of the synthetic and real stars as a function of Δ_{GBR} and Δ_{Gui}, respectively. In this case, we have considered the full sample of synthetic stars, and rescaled the histograms to have the same total number of objects as observed. This way we minimize the Poisson error on the number counts for the synthetic sample. The bin size of the histograms is about two times the average 1σ error bars on Δ_{GBR} and Δ_{Gui} over the G magnitude range of the observed sample.

These simulations have been performed considering Δ[Fe/H] = 0.15, ΔY = 0.10, and $\Delta E(B-V) = 0.06$ and 0.03 for the case of metallicity and helium spread, respectively, and provide a general satisfactory agreement with the distribution of the observed stars in this diagram. The synthetic samples cover nicely the region of the diagram populated by the cluster stars, even when considering the binaries with high q values. Also the number distributions along the two axes are reasonably consistent with the data, within the error bars on the star counts.

Of course, combinations like Δ[Fe/H] $= 0.16$ together with $\Delta E(B-V) = 0.07$, or $\Delta Y = 0.10$ with $\Delta E(B-V) = 0.01$, cannot be excluded from this kind of comparisons, but values of Δ[Fe/H], ΔY, and $\Delta E(B-V)$ very different from those chosen for the simulations in Fig. 5.6 can indeed be discarded, as shown below.

Figure 5.7 compares the data with two simulations like those in Fig. 5.6, keeping the $\Delta E(B-V)$ values unchanged, but reducing the spread Δ[Fe/H] to 0.08 dex and ΔY to 0.05. The agreement with the observations is in this case much worse. In both cases the synthetic samples are clearly short of stars in the region with Δ_{GBR} between ~ 0.06 and ~ 0.08 mag, and Δ_{Gui} between ~ 0.10 and ~ 0.2 mag. The synthetic single stars do not reach that area and changing the probability distribution of q to a power law (Malofeeva et al., 2022, with the consequent increase of the overall binary fraction) simply replaces many of the current single stars with unresolved binaries, but it does not help populating that region of the diagram. The opposite would happen if we increase Δ[Fe/H] and ΔY well above the values in Fig. 5.6, with the bulk of the synthetic sequences (essentially the single star sequence) too extended towards higher values of Δ_{GBR} and Δ_{Gui} compared to the observations.

Figure 5.8 displays the effect of varying $\Delta E(B-V)$ in the simulations, by keeping fixed Δ[Fe/H] and ΔY to the values of the simulations in Fig. 5.6 (Δ[Fe/H] $=$ 0.15, $\Delta Y = 0.10$). We can see here that a smaller amount of differential reddening for the case with metallicity spread makes the single star sequence too steep compared to the observations, consistently with the results in Fig. 5.5, whilst a larger $\Delta E(B-V)$ makes the overall slope of the synthetic sequence shallower than the observations. This can be clearly appreciated in the figure when looking at the region populated by binaries with high q. In case of the helium abundance spread, increasing $\Delta E(B-V)$ makes again the whole sequence shallower, again consistent with the results of Fig. 5.5.

Finally, we have repeated this whole analysis by considering for each star the two completely independent CMDs G-($G_{\rm BP} - G_{\rm RP}$) and g-($u - i$). From these CMDs we have calculated Δ_{GBR} as described before, and Δ_{gui}, and compared data with simulations in Δ_{GBR}-Δ_{gui} diagrams. The quantity Δ_{gui} is analogous to Δ_{Gui}, but this time the difference in $(u - i)$ colour is taken with respect to the corresponding value of the blue fiducial in the g-($u - i$) CMDs at the star

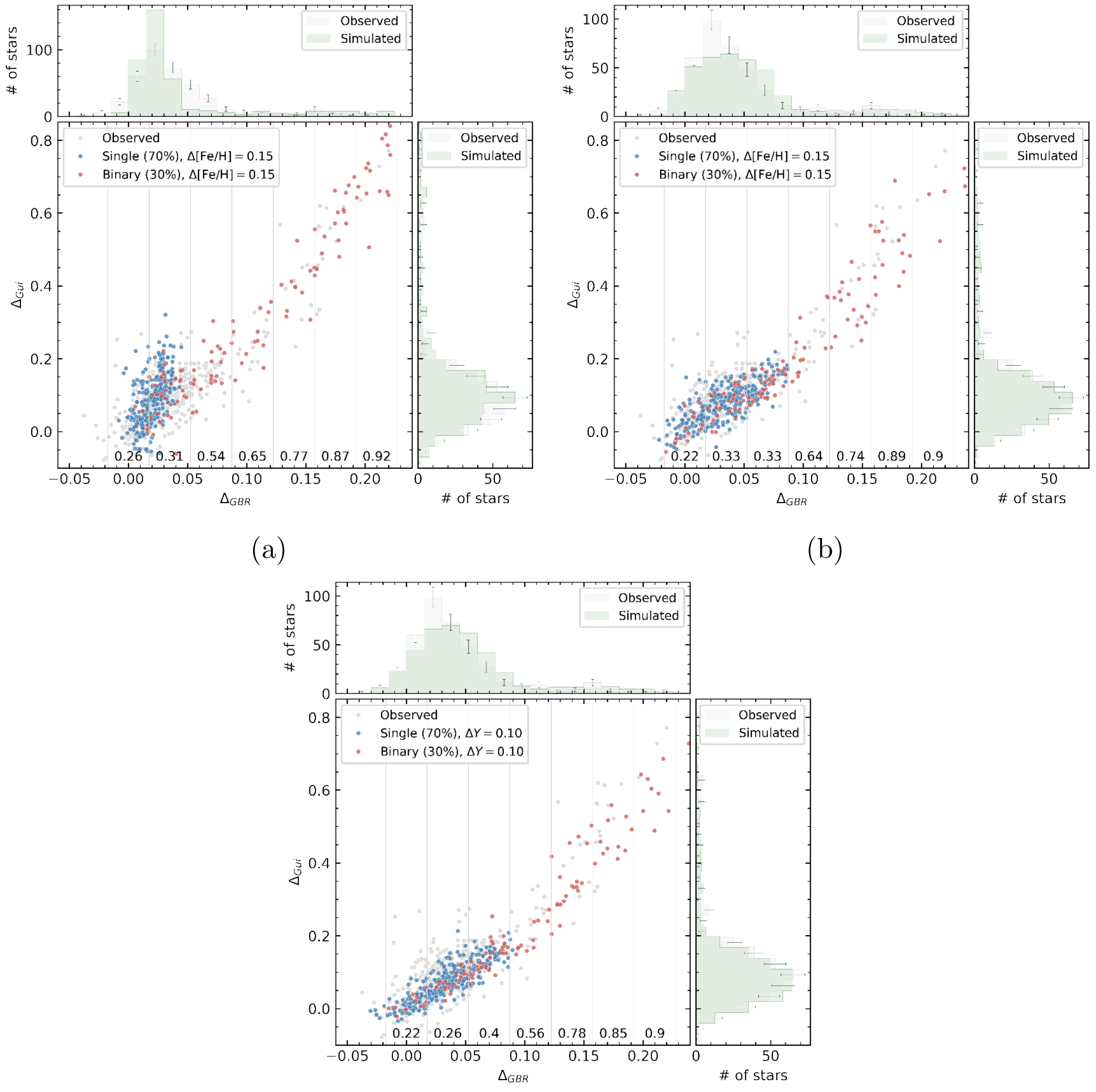

(a) (b)

(c)

Figure 5.8: As Fig. 5.6, but with Δ[Fe/H] $= 0.15$ and $\Delta E(B-V) = 0$ (a), Δ[Fe/H] $= 0.15$ and $\Delta E(B-V) = 0.10$ (b), $\Delta Y = 0.10$ and $\Delta E(B-V) = 0.08$ (c).

g magnitude. The conclusions are exactly the same as when using Δ_{GBR}-Δ_{Gui} diagrams, as shown by the figures included in the Appendix 5.6.

5.5 Discussion and conclusions

The very accurate *Gaia* EDR3 photometry for the members of M37 presented by Griggio and Bedin (2022) shows a MS broadened in colour beyond what expected from photometric errors only, well below the region of the extended TO, where neither age differences nor rotation are expected to play a role. Even when we neglected redder objects compatible with being unresolved binaries with mass ratios above $q \sim 0.6$-0.7, the cluster MS is still broader than expected from the small photometric errors.

To investigate the causes of this broadening we made use of an auxiliary photometry in the *Sloan* system, and built a differential colour-colour diagram of the lower MS, using a combination of *Gaia* and *Sloan* filters. By employing synthetic stellar populations to reproduce the observed trend of the cluster stars in this diagram, we have concluded that the observed colour spread in the *Gaia* CMD can be reproduced by a combination of either a metallicity spread Δ[Fe/H] ~ 0.15 plus a differential reddening across the face of the cluster spanning a total range $\Delta E(B-V) \sim 0.06$, or an initial helium abundance spread $\Delta Y \sim 0.10$ plus a smaller range of reddening $\Delta E(B-V) \sim 0.03$.

Figure 5.9 shows the impact of these two scenarios on the TO region of the cluster's population. We display in the two panels a 380 Myr isochrone with either different combinations of metallicity and reddening (left panel) or different combinations of Y and reddening, keeping the metallicity fixed (right panel). In the reasonable assumption that there is no correlation between reddening and chemical composition, the combinations we display match the blue and red limits of the single star sequence in the G magnitude range we have studied. Notice that in case of a helium abundance spread the smallest value of $E(B-V)$ is higher than that for the case of a metallicity spread. The reason is that an increase of the helium abundance shifts the MS to the blue, hence in this scenario a match of the blue edge of the observed CMD with the bluest stellar component (the population with the highest helium and lowest reddening) requires a value of $E(B-V)$ larger than that determined from the fit in Fig. 5.1, and used in the left panel for the case of a metallicity spread.

The metallicity (and reddening) spread has a major impact around the TO, with single age non rotating isochrones able to cover in this case a large portion of the extended TO of the cluster CMD. The impact at the TO is much less

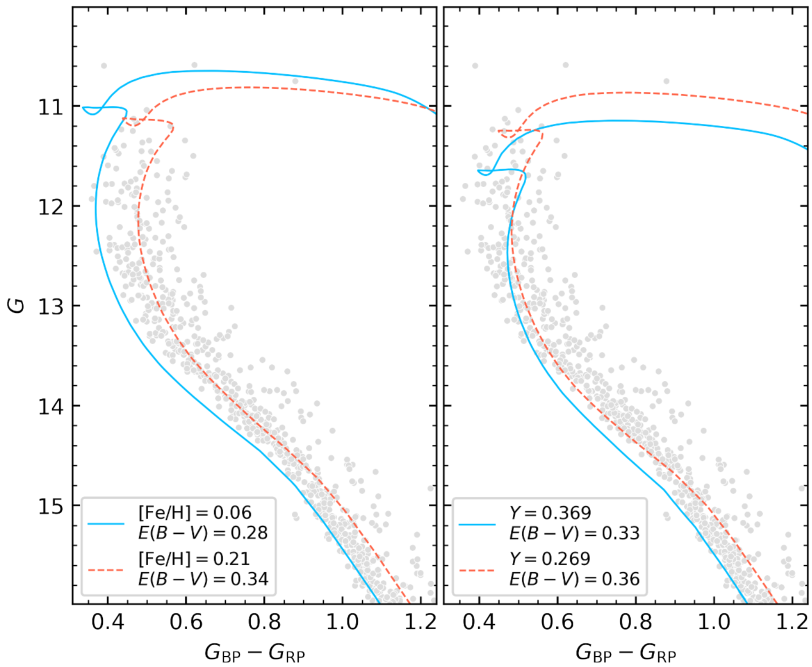

Figure 5.9: Effect of the metallicity plus reddening spread (left) and Y plus reddening spreads (right) scenarios on the TO region of the cluster *Gaia* CMD. We show 380 Myr isochrones with the combinations of [Fe/H], Y and $E(B-V)$ displayed in the two panels (see text for details).

pronounced for the case of a helium (and reddening) spread.

Another consequence of these abundance spreads is that we need to be very cautious when applying differential reddening corrections to the cluster CMD. In fact, none of the CMDs displayed in our study has been corrected for this effect.

Nowadays it is a standard procedure to correct for differential reddening the CMDs of star clusters (e.g., Bellini et al., 2017; Milone et al., 2012; Sarajedini et al., 2007); the basic physical principles underlining the method are summarised in the following.

First, stars along a portion of the cluster MS are selected as 'reference stars', and a reference fiducial line for these stars is calculated, by determining a median colour at varying magnitude. The magnitude range of this reference sequence of stars is chosen such that the direction of the reddening vector can be more easily discriminated from the effect of photometric errors. To a generic target star in any evolutionary phase at a given spatial position within the cluster is then assigned a number of neighbouring (spatially) reference stars, and the median distance along the reddening vector between the position of these neighbouring reference stars and the reference fiducial line is calculated (this distance can be then transformed into a value of $\Delta E(B-V)$). The position in the CMD of the target star is then shifted along the reddening vector by the value of this median distance and the procedure is repeated for all cluster stars, including the individual reference objects.

An underlying assumption of this method is that the cluster stars are a homogeneous stellar population, but it could still work in case of chemical inhomogeneities, provided that two conditions are satisfied. The first one is that the chemical properties of the stellar population are not spatially dependent (the size and probability distribution of the abundance spreads are not dependent on the location within the cluster). The second one is that for any object there is a sufficiently large number of neighbouring reference stars, such that they properly sample the full range of chemical inhomogeneities. This way they would define a sequence in the CMD that is equivalent (in terms of stellar properties) to the fiducial reference line.

If we were to be able to determine with confidence the amount of differential reddening in our CMD, we might possibly discriminate between the metallicity and helium spread scenarios, because they require different values of $\Delta E(B-V)$. Unfortunately, we do not have enough reference stars to do that. The best portion of the MS to use for the reference fiducial line is in the range between $G \sim 15$ and ~ 17, and by following the technique described before, we find that for objects in large portions of the cluster we have only 10 or less neighbouring reference stars (within a circle of radius $\sim 3\,\mathrm{arcmin}$). With this method we get a total range $\Delta E(B-V)$ across the cluster equal to $\sim$ 0.06-0.07 mag supporting the scenario with a metallicity spread, but with such small numbers of local reference stars we cannot be sure they are sufficient to properly sample the distribution of chemical abundances, hence we might have biases in the estimate of the local differential reddening.

To discriminate more reliably between metallicity and helium spread, high-resolution differential abundance determinations of a sizeable sample of cluster stars are then necessary, because they can confirm or exclude the presence of a metal abundance spread. The existing more direct measurements –based very small samples of targets– do not allow to draw solid conclusions. Marshall et al. (2005) published moderate resolution spectroscopy of a sample of eight red clump stars in the cluster, and found that the derived metallicities of the target-cluster stars displayed a scatter of 0.14 dex, about twice what expected from measurement errors. On the other hand, the high-resolution spectroscopy of three red clump stars by Pancino et al. (2010) does not reveal any clear abundance spread.

Irrespective of the uncertainty between metallicity and helium spread, our results raise the possibility that also open clusters –like globular clusters and in general massive star clusters (see, .e.g. Bastian and Lardo, 2018; Gratton et al., 2012; Lardo et al., 2022; Legnardi et al., 2022; Marino et al., 2019; Martocchia et al., 2019, and references therein)– do not host stars all with the same initial chemical composition. So far, there has been some debate about the presence of a metallicity spread in the open cluster Tombaugh 2, with the high-resolution spectroscopy by Frinchaboy et al. (2008) who found the presence of a metallicity spread in the cluster, that was however not confirmed by the subsequent spectroscopic analysis by Villanova et al. (2010). Our work adds a new candidate open cluster hosting chemical abundance spreads.

5.6 Complementary analysis

We show here some results of the same analysis described in Sect. 5.4, but using the Δ_{GBR}-Δ_{gui} diagrams instead of Δ_{GBR}-Δ_{Gui} ones. Figure 5.10a is the equivalent of Figure 5.5, and displays the lower MS stars, after excluding sources whose colours are consistent with unresolved binaries with mass ratio $q \gtrsim 0.6$. The four straight lines display the direction along which stars are displaced due to the effects of differential reddening, unresolved binaries with $q \lesssim 0.6$, spread of initial metal content, and helium abundance, respectively.

Figures 5.10b and 5.10c are the equivalent of Fig. 5.6 and display the lower MS stars including unresolved binaries with high q values, together with synthetic stars calculated including a spread in metallicity Δ[Fe/H] = 0.15 and reddening $\Delta E(B-V) = 0.06$ (b), and a spread of initial helium $\Delta Y = 0.10$ and reddening $\Delta E(B-V) = 0.03$ (c).

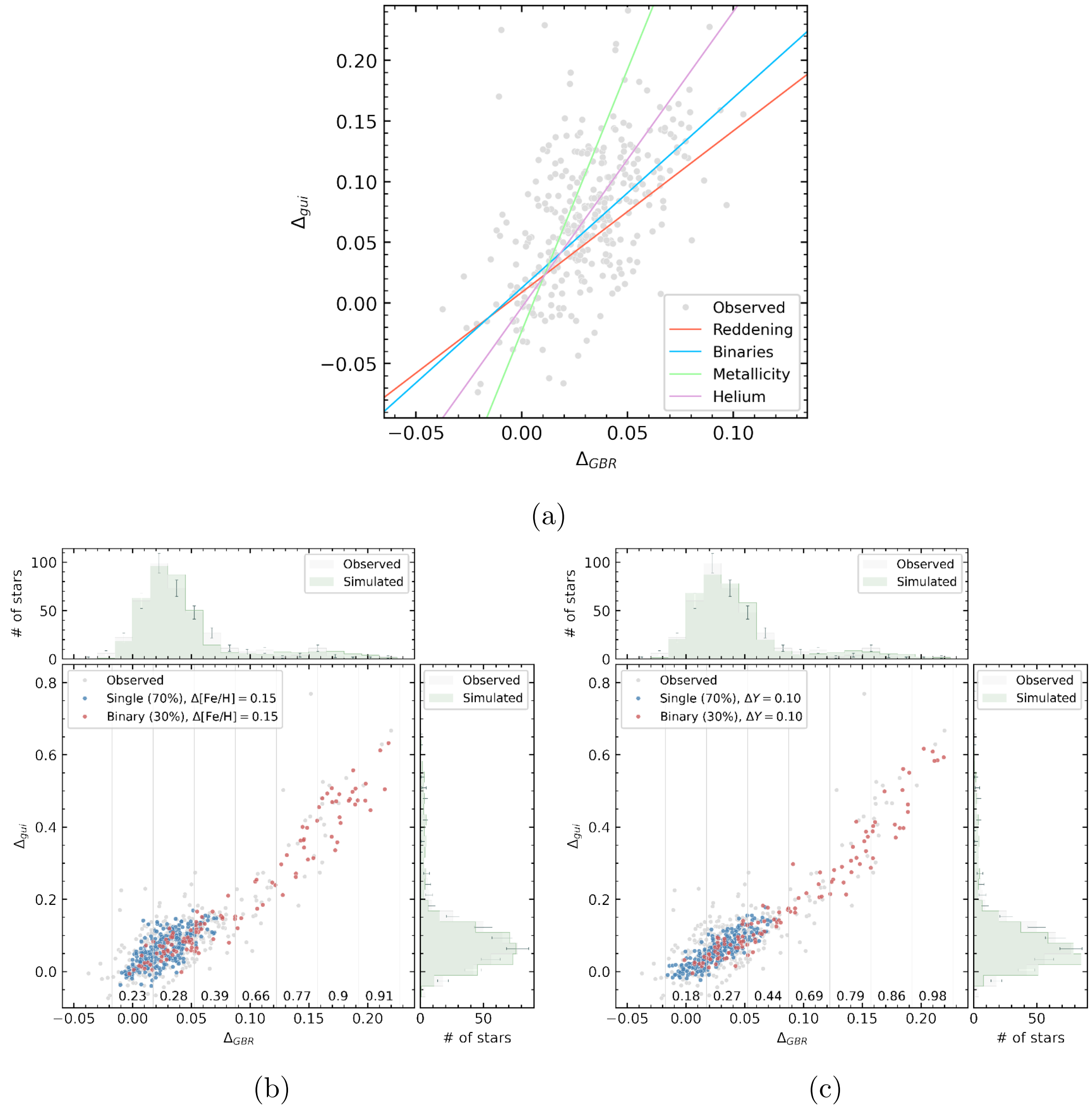

Figure 5.10: Panel (a): As Fig. 5.5 but in the Δ_{GBR}-Δ_{gui} diagram. Panels (b) and (c): As Fig. 5.6 but in the Δ_{GBR}-Δ_{gui} diagram.

6. The broadening of the main sequence in M38[1]

Our recent multi-band photometric study of the colour width of the lower main sequence of the open cluster M37 has revealed the presence of a sizeable initial chemical composition spread in the cluster. If initial chemical composition spreads are common amongst open clusters, this would have major implications for cluster formation models and the foundation of the chemical tagging technique. Here we present a study of the unevolved main sequence of the open cluster M38, employing *Gaia* DR3 photometry and astrometry, together with newly acquired *Sloan* photometry. We have analysed the distribution of the cluster's lower main sequence stars with a differential colour-colour diagram made of combinations of *Gaia* and *Sloan* magnitudes, like in the study of M37. We employed synthetic stellar populations to reproduce the observed trend of M38 stars in this diagram, and found that the observed colour spreads can be explained simply by the combined effect of differential reddening across the face of the cluster and the presence of unresolved binaries. There is no need to include in the synthetic sample a spread of initial chemical composition as instead necessary to explain the main sequence of M37. Further photometric investigations like ours, as well as accurate differential spectroscopic analyses on large samples of open clusters, are necessary to understand whether chemical abundance spreads are common among the open cluster population.

6.1 Introduction

Open clusters have been traditionally considered to host populations of stars born all with the same initial chemical composition in a burst of star formation of negligible duration (simple stellar populations).

The recent discovery of extended turn offs (TOs) in the *Gaia* colour-magnitude

[1]The content of this chapter has been published in Griggio et al. (2023c).

diagrams (CMDs) of a sample of about 15 open clusters with ages in the range $\sim$0.2-1 Gyr and initial metal mass fractions Z between $\sim$0.01 and $\sim$0.03 (Bastian et al., 2018; Cordoni et al., 2018; Marino et al., 2018b) has somehow challenged this paradigm, given that extended TOs can be naturally explained by a range of ages amongst the cluster's stars (e.g. Correnti et al., 2014; Mackey and Broby Nielsen, 2007). Further detailed studies of the extended TO phenomenon, which is seen also in CMDs of Magellanic Clouds' clusters younger than 2 Gyr (see, e.g., Goudfrooij et al., 2017; Mackey et al., 2008; Piatti and Bastian, 2016, and references therein), strongly point to the effect of rotation (e.g. Bastian et al., 2018; Kamann et al., 2018, 2020, 2023) as the main culprit (see also D'Antona et al., 2023). In this case, stellar populations in individual open clusters might still be simple stellar populations, born with uniform age and initial chemical composition.

Very recently, our photometric multi-band study of the main sequence (MS) of the open cluster M37 (Griggio et al., 2022b) has disclosed the presence of a sizeable initial chemical composition spread in the cluster (either a full metallicity range Δ[Fe/H]$\sim$0.15 dex or a helium mass fraction total range $\Delta Y \sim 0.10$). This result is independent of whether rotation or age spread is responsible for its observed extended TO, because it is based on an analysis of the lower MS, populated by stars with convective envelopes that are anyway slow rotators.

This result has important implications for our understanding of open cluster formation (see, e.g. Clarke et al., 2000) and the technique of 'chemical tagging' of Galactic field stars (e.g., Freeman and Bland-Hawthorn, 2002; Hogg et al., 2016), especially if high resolution spectroscopic investigations of M37 will disclose that the chemical spread is due to an inhomogeneous initial metal content. Indeed, the basic idea of chemical tagging is that stars are born in unbound associations or star clusters (like open clusters) that disperse rapidly, and over time they populate very different parts of the Milky Way phase space; stars of common birth origin should however be identifiable through their measured photospheric abundances, in the assumption that their birth cluster has a chemically homogeneous composition. It is therefore important to assess whether initial abundance spreads among the Galactic open clusters are a common phenomenon.

In this paper we have investigated the poorly-studied open cluster M38 that, like M37, displays in the *Gaia* Data Release 3 (DR3, Gaia Collaboration et al., 2023) CMD a MS broader than what is expected from photometric errors only. We have applied the same multi-band technique developed for M37 that combines both *Gaia* and *Sloan* photometry, to assess whether the broadening of the MS can be explained by differential reddening and binaries only, or whether a chemical abundance spread is also required.

The plan of the paper is as follows. Section 6.2 presents our membership

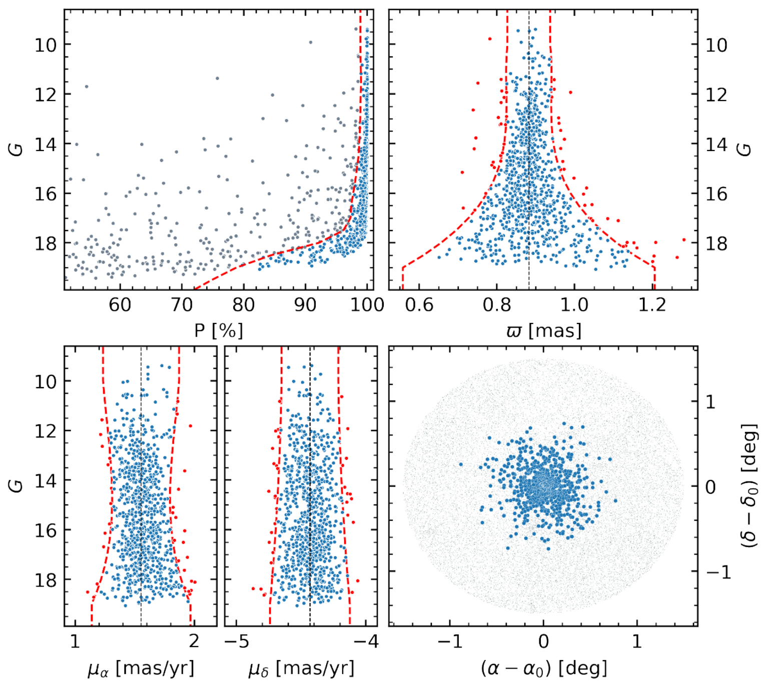

Figure 6.1: Cluster member selection. *Top left panel:* Membership probability for all the sources. In our analysis we reject stars with $P < 50\,\%$. *Top right panel:* G magnitude vs parallax. In this case we reject stars that fall outside the region bounded by the two red lines (red dots). The black dashed line denotes the median parallax. *Bottom left panel:* Proper motions vs G magnitude of all sources that passed the two previous selections. In this case we kept the sources lying between the red dashed lines. *Bottom right panel:* spatial distribution of the sources. The blue dots denote our selected members of M38.

analysis and the resulting *Gaia* DR3 CMD, and is followed by Section 6.3 which describes the complementary *Sloan* photometry used in this work. Section 6.4 describes the theoretical analysis of the MS width and Section 6.5 closes the paper with our conclusions.

6.2 The *Gaia* colour-magnitude diagram

The analysis of the CMD diagram of a star cluster requires a sample of member stars free from field sources contamination. To obtain such a sample we have derived the membership probabilities for all the sources in the *Gaia* DR3 catalogue within a circle with a $\sim$1.5 deg radius, centred on the cluster ($\alpha_0 = 82.167$, $\delta_0 =$

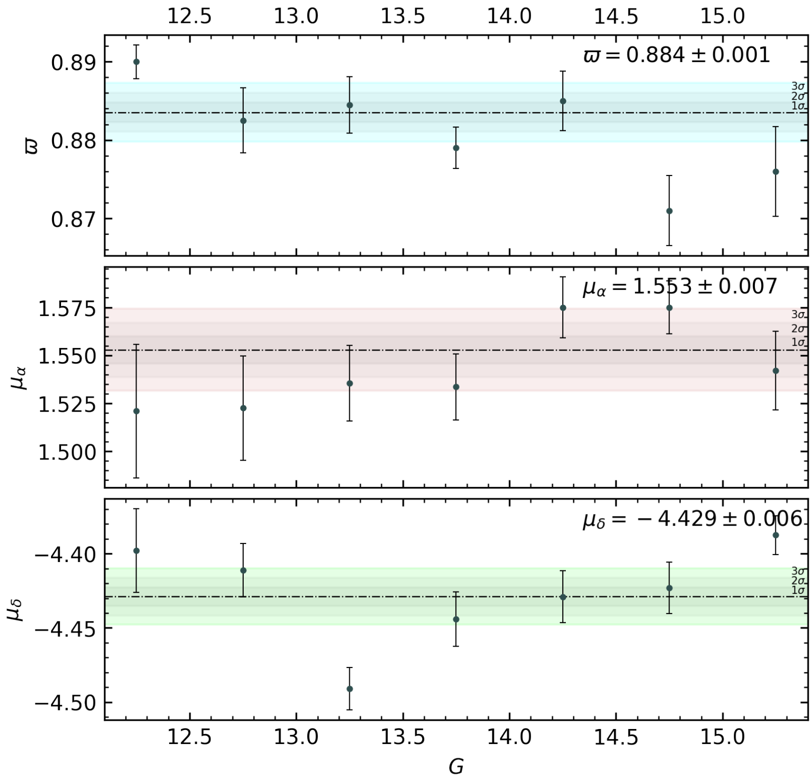

Figure 6.2: Mean values of the parallax and the components of the proper motion in each magnitude bin; the dash-dotted line denotes the overall weighted mean values, also reported at the top right corner of each panel (in mas and mas yr^{-1} respectively.) and in Table 6.1.

35.824, Tarricq et al., 2021).

The membership probabilities were computed following the approach described by Griggio and Bedin (2022), which relies on *Gaia* DR3 astrometry. Cluster members were selected by performing a series of cuts on the astrometric parameters, as displayed in Fig. 6.1. In the top left panel we show the membership probability P: we applied a cut by-eye, following the profile of the bulk of sources with cluster membership at each magnitude (dashed-red curve). This selection becomes less strict at fainter magnitudes, as the measurement errors increase and memberships become less certain. We then applied a cut on the parallax (top right) and proper motions (bottom left) distributions. The red lines were defined by the 68.27$^{\text{th}}$ percentile of the residuals around their median value in each 1-magnitude bin, multiplied by a factor of two (as in Griggio et al., 2022a). The bottom right panel show the spatial distribution of the selected members.

Table 6.1: M38's astrometric parameters estimated in this work.

μ_α [mas yr^{-1}]	μ_δ [mas yr^{-1}]	ϖ [mas]	Distance [pc]
1.553 ± 0.007	-4.429 ± 0.006	0.884 ± 0.001	1130 ± 50

The derived list of probable cluster members allowed us to estimate the cluster astrometric parameters; we followed the same procedure as in Griggio and Bedin (2022), by applying some quality cuts to the *Gaia* data, i.e.:

- `astrometric_excess_noise` < 0.25;

- `phot_bp_rp_excess_factor` < 1.4;

- `phot_proc_mode` $= 0$;

- `astrometric_gof_al` < 4;

- $\sigma_\varpi/\varpi < 0.1$, $\sigma_{\mu_\alpha}/\mu_\alpha < 0.1$ and $\sigma_{\mu_\delta}/\mu_\delta < 0.1$.

With this selected sample of members we have estimated the cluster's mean proper motion and parallax. The mean values in each magnitude interval are shown in Fig. 6.2, with the weighted average reported on the top right corner of each panel. The cluster parameters are also reported in Table 6.1

The average parallax gives a distance d of 1132 ± 2 pc, that, accounting for the parallax zero-point correction by Lindegren et al. (2021a), becomes 1183 ± 2 pc. In the following, we consider this correction to represent a maximum error in the distance, hence $d = 1130 \pm 50$ pc. Our estimate is also in agreement, within the errors, with the distances given by Bailer-Jones et al. (2021) which provide a median value for M38 stars equal to 1186 ± 2 pc.

The CMD of the selected cluster members is shown in Fig. 6.3. The MS is very well-defined and does not exhibit a clear extended TO. However, a detailed analysis of the TO region is hampered by the fact that there are only 40 MS stars with $G > 12$.

The metallicity of this cluster is not well determined, given that spectroscopic analyses of small samples of cluster stars have provided a range of [Fe/H] determinations between ~ -0.07 and ~ -0.38, and $E(B-V)$ estimates range between ~ 0.25 and ~ 0.35 mag (see, e.g., Carrera, R. et al., 2019; Dias et al., 2002; Donor et al., 2020; Frinchaboy et al., 2013; Li et al., 2021; Majaess et al., 2007; Subramaniam and Sagar, 1999; Zhong et al., 2020).

In the same Fig. 6.3 we show for reference a 300 Myr[2] BaSTI-IAC (Hidalgo et al., 2018) solar scaled isochrone with [Fe/H] = 0.06, matched to the blue edge of the lower MS (see below and Sect. 6.4 for the definition of lower MS and its blue edge). We adopted the distance $d = 1130$ pc, and for the assumed metallicity we determined $E(B-V) = 0.26$ from the match to the lower MS colour, which can be considered to be the minimum value of the reddening, given the presence of differential reddening across the face of the cluster, as discussed later in Sect. 6.4. We employed extinction coefficients in the *Gaia* bands obtained from the relations given in the *Gaia* website[3].

We tried also isochrones with lower [Fe/H] more in line with the uncertain spectroscopic estimates ([Fe/H] = −0.08 and −0.20 dex). After adjusting (actually increasing) $E(B-V)$ to match the blue edge of the lower MS, and the isochrone age to approximately reproduce the observed brightness of the TO region, the fit of the upper MS was poorer when considering these subsolar metallicities.

We stress at this stage that –as for the case of M37– the results of the analysis in Sect. 6.4 are insensitive to the exact values of the adopted isochrone metallicity, the cluster distance (within the adopted error bar), and the minimum value of $E(B-V)$, because of the differential nature of the technique applied.

6.2.1 The width of the MS

As discussed for M37 (Griggio et al., 2022b), if open clusters host single-metallicity populations, the observed colour width of the unevolved MS is expected to be set by the photometric error, the presence of unresolved binaries with a range of values of the mass ratio q, and the differential reddening across the face of the cluster, if any. To verify this hypothesis in the case of M38, we have followed the same procedure detailed in Griggio et al. (2022b).

In brief, we first calculated an observed fiducial line of the unevolved MS in the G-magnitude range between 15.2 and 16.6 (denoted as lower-MS from now on). According to the isochrone in Fig. 6.3, in this magnitude range the single star population covers a mass range between ∼0.9 and 1.15 $M_\odot$, approximately the same range as in our analysis of the lower MS of M37 (see Griggio et al., 2022b). We have calculated the fiducial line assuming that the observed MS is populated just by single stars all with the same initial metallicity, as described in Griggio et al. (2022b). Synthetic stars have been then distributed with uniform probability along this fiducial; each synthetic magnitude has been then perturbed

[2] This value is consistent with the age of 302 Myr assigned to this cluster by Tarricq et al. (2021).

[3] https://www.cosmos.esa.int/web/gaia/edr3-extinction-law

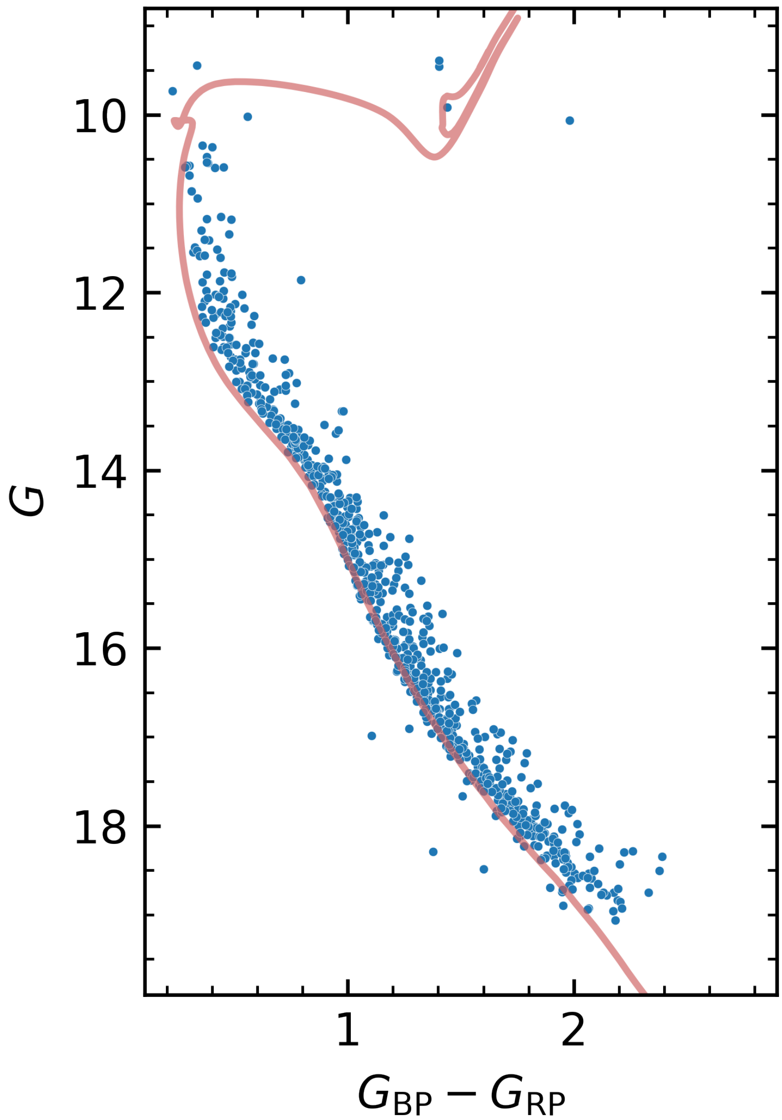

Figure 6.3: *Gaia* CMD for the selected members of M38. The red line is a 300 Myr BaSTI-IAC isochrone, with [Fe/H] = 0.06, shifted by $E(B-V) = 0.26$ and $d = 1130\,\mathrm{pc}$ (see text for details).

Table 6.2: Log of the observations.

Filter	N_{exp}	t_{exp}	Seeing	Airmass
u	57	400 s	2.25 arcsec	1.08
g	57	400 s	2.20 arcsec	1.09
i	57	400 s	2.17 arcsec	1.07

by a photometric error obtained by randomly sampling a Gaussian probability distribution with zero mean and a standard deviation set to the median error at the corresponding G-magnitude, taking advantage of the individual errors from the *Gaia* DR3 catalogue. Figure 6.4 (top panels) compares the observed CMD (left) with the simulated counterpart (right) in the selected magnitude range, and the colour residuals around the fiducial line as a function of G (bottom panels). We also show the values of the colour dispersion around the fiducial values at varying magnitudes in both CMDs. They have been computed as the 68.27^{th}-percentile of the distribution of the residuals around zero.

Notice that we have discarded objects with the position in the CMD consistent with being unresolved binaries with mass ratio $q > 0.7$ (according to the adopted isochrone), when we calculated the dispersion of the residuals from the observations. But even neglecting these objects, it is clear from Fig. 6.4 that the simulated stars display a much narrower distribution around the fiducial line than the observations.

To assess the origin of the colour spread of the observed CMD, we employed an auxiliary photometry in the *Sloan ugi* filters –described in the following section– and applied in Sect. 6.4 the same technique developed in Griggio et al. (2022b).

6.3 *Sloan* observations and data reduction

The data were collected with the Asiago Schmidt telescope between October, 2 and November, 15 2022. We obtained a set of 57 images in the *Sloan*-like filters *ugi*, with an exposure time of 400 s. The images were dithered to mitigate the effect of bad pixels and cosmic rays, and covered a total area of about 1 sq. deg. The observation log is reported in Table 6.2. A three colour stack of the field of view is shown in Fig 6.5, where we used the u filter for the blue colour, g for the green and i for the red colour.

To measure position and flux of the sources in this dataset we followed the same approach as in Griggio et al. (2022a). Briefly, we first derived a grid of 9×9 empirical point-spread functions (PSFs) for each image considering bright,

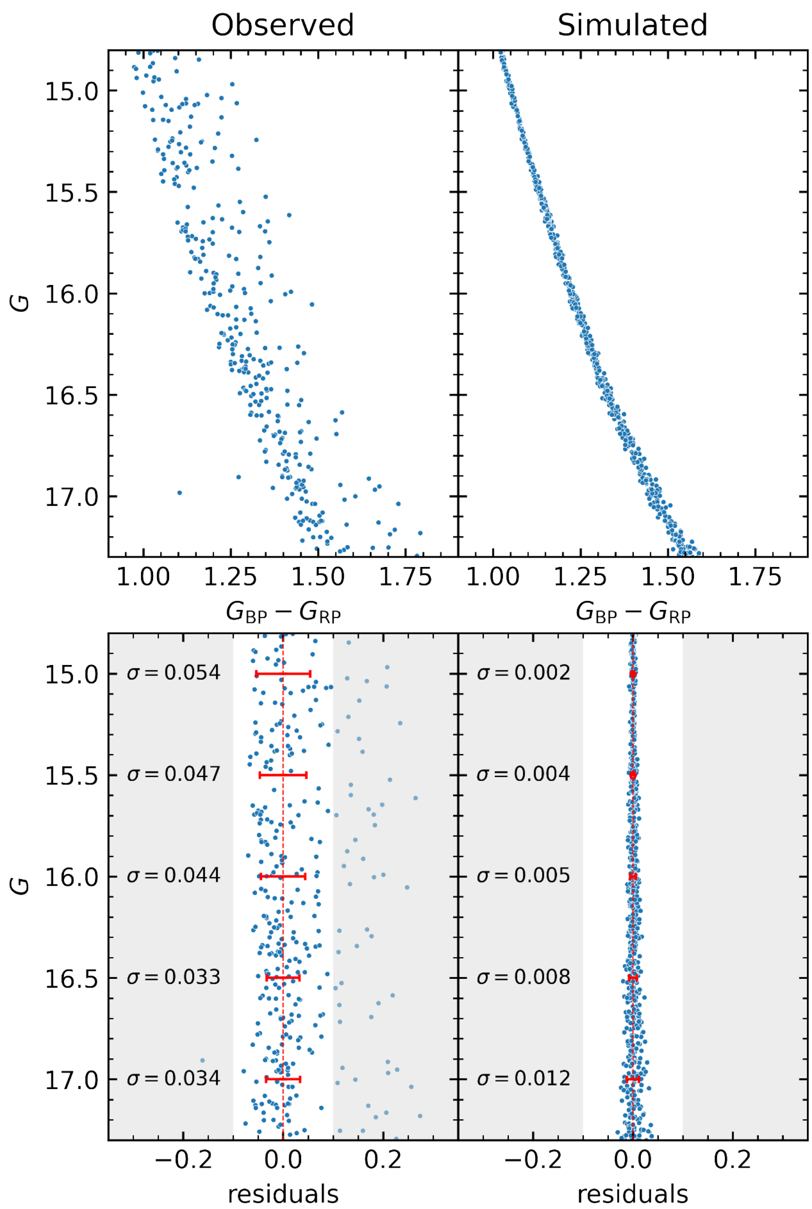

Figure 6.4: *Top panels*: Observed (left) and simulated (right) CMDs of the lower MS of M38. *Bottom panels*: Colour residuals as a function of the G magnitude around the observed (left) and the synthetic (right) CMD fiducials. The area shown in white contains the stars employed to compute the 1σ values of the dispersion of the residuals also shown in the two panels (see text for details).

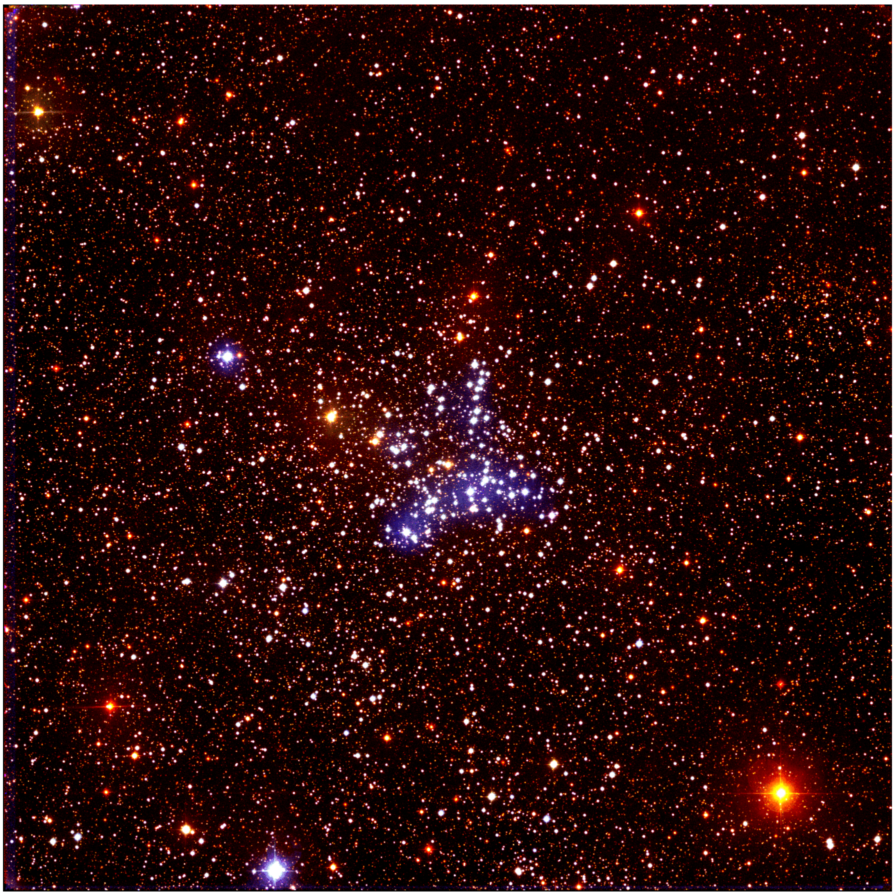

Figure 6.5: Three colour stack of the Asiago Schmidt Telescope data. The field of view is approximately 1×1 sq. deg.

isolated and unsaturated sources, by using the software originally developed by Anderson et al. (2006). The grid is necessary to account for spatial variations of the PSF across the CCD. We then proceeded by measuring the position and flux of individual sources in each image with the appropriate local PSF, obtained by a bilinear interpolation between the four nearest PSFs in the grid, using the software described by Anderson et al. (2006). This routine goes through a series of iterations, finding and measuring progressively fainter sources, until it reaches a specified level about the sky background noise. The software outputs a catalogue with positions and instrumental magnitudes for each image.

We transformed the positions and magnitudes of each catalogue to the reference system defined by the first image in each filter (namely, `SC233176`, `SC233182` and `SC233188`). Finally, we cross identified the sources and produced a catalogue containing the averaged positions and magnitudes for all the stars measured in at least five exposures. These catalogues were matched with the *Gaia* one, to have *Sloan* magnitudes for all the *Gaia* sources detected with the Schmidt telescope.

The instrumental magnitudes have been calibrated as in Griggio et al. (2022a) exploiting the IGAPS catalogue Monguió et al. (2020). We cross identified our sources with those in the IGAPS catalogue, and derived the coefficients of the relation $m_{\rm cal} = m_{\rm instr} + a(g_{\rm instr} - i_{\rm instr}) + b$ with a linear fit.

The CMD of member stars in the *ugi* filters is shown in Fig. 6.6, together with the same isochrone (purple line) of Fig. 6.3, employing the same distance and reddening, and the extinction law from the NASA/IPAC infrared science archive[4] for the *Sloan* filters.

6.4 The broadening of the lower MS

To investigate in detail the origin of the broadening of the lower MS we followed the same technique described in Griggio et al. (2022b). We considered stars in the *Gaia* CMD with G between 15.2 and 16.6 (we have a total of 132 stars in this magnitude range) and combined the photometry in the *Gaia* filters with the corresponding u and i magnitudes to build a differential colour-colour diagram, as summarised below.

We have defined an MS blue fiducial in both the G-$(G_{\rm BP} - G_{\rm RP})$ and G-$(u - i)$ diagrams as described in Griggio et al. (2022b) and for each observed star we have computed, in both G-$(G_{\rm BP} - G_{\rm RP})$ and G-$(u - i)$ diagrams, the difference between its colour and the colour of the corresponding blue fiducial at the star G magnitude. These quantities are denoted as Δ_{GBR} and Δ_{Gui} respectively (see Fig. 6.7).

We then plotted these colour differences in the Δ_{GBR}-Δ_{Gui} diagram shown Fig. 6.8. As for the case of M37, the lower MS stars are distributed along a well-defined sequence which starts around the coordinates (0,0) –corresponding to the stars lying on the blue fiducials– and stretches towards increasingly positive values (denoting stars increasingly redder than the fiducials) with the quantity Δ_{Gui} increasing faster than Δ_{GBR}. These colour spreads cannot arise from (underestimated) random photometric errors only, because in this case they would be distributed without a correlation between Δ_{Gui} and Δ_{GBR}.

In the same figure, together with the data, we show the reddening vector, calculated using the extinction laws for the *Gaia* and *Sloan* filters referenced above. We also plot the vector corresponding to the predicted position of binaries with varying mass ratio q (blue) and the range of colours spanned by isochrones

[4] https://irsa.ipac.caltech.edu/applications/DUST/

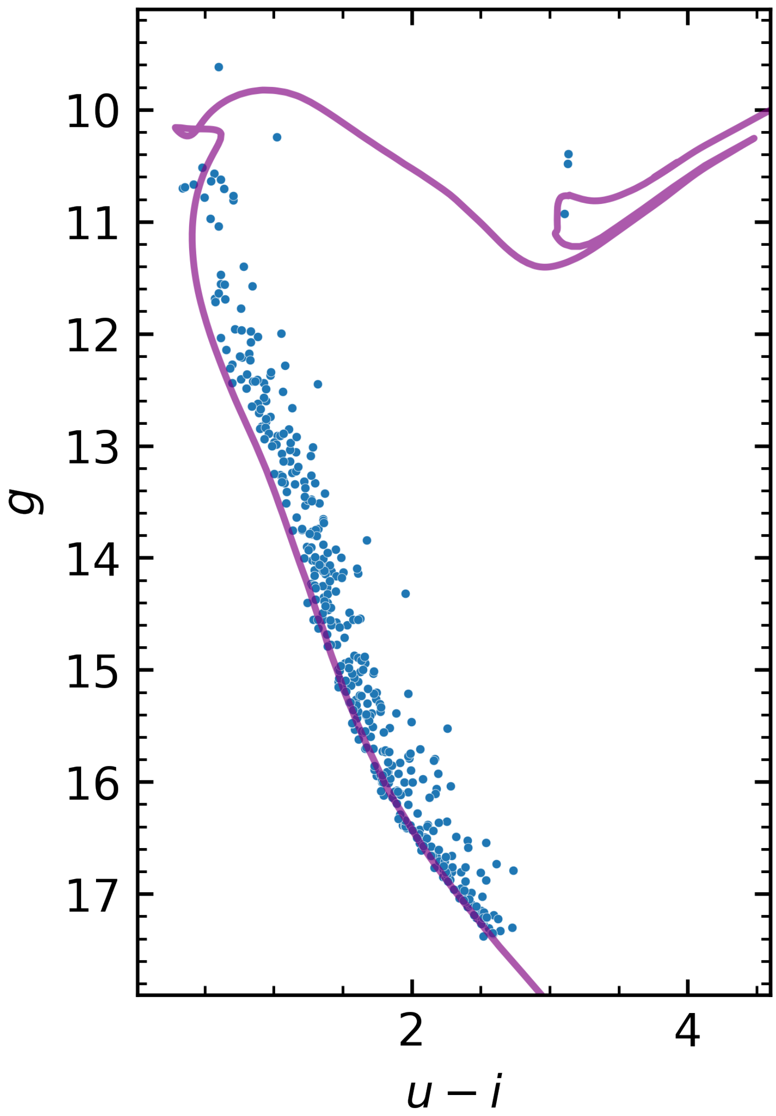

Figure 6.6: CMD in the *Sloan* filters for M38 members. The purple line is the same isochrone of Fig. 6.3 (see text for details).

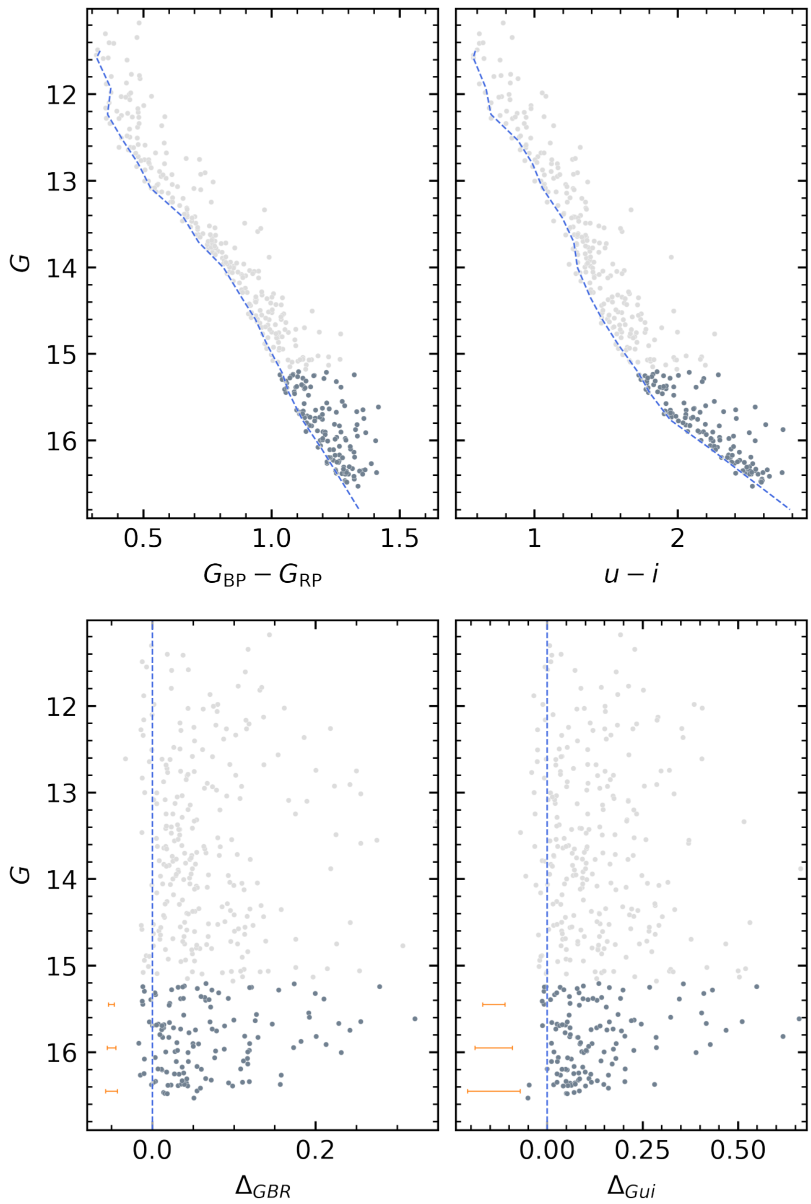

Figure 6.7: *Top panels*: cluster G-($G_{\rm BP} - G_{\rm RP}$) and G-($u - i$) diagrams. The blue dashed line denotes the MS blue edge fiducial. The lower-MS stars considered in our analysis are displayed in dark grey. *Bottom panels*: G-Δ_{GBR} and G-Δ_{Gui} diagrams (see text for details). Along the left side of each panel, we display the median $\pm 1\sigma$ colour error for three representative G magnitudes, as estimated from the individual catalogues.

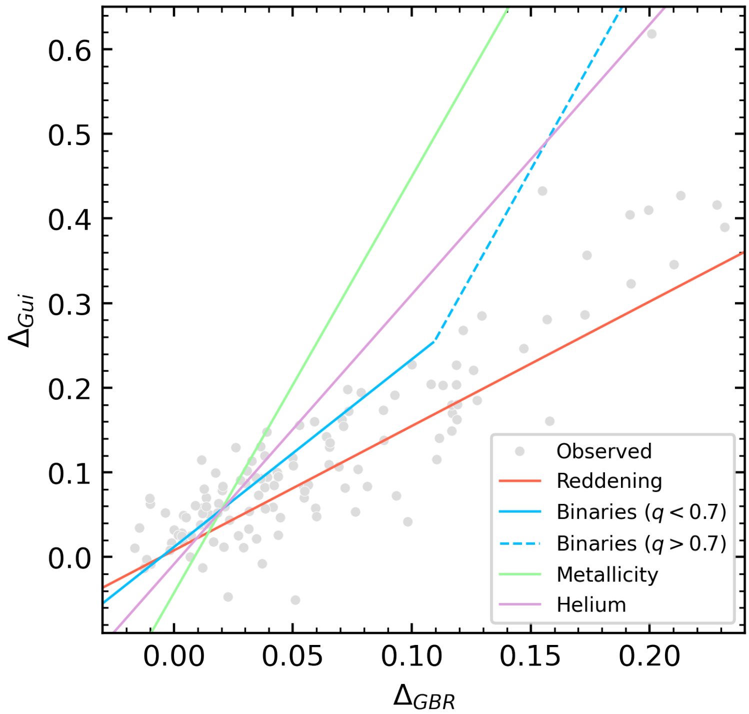

Figure 6.8: Δ_{GBR}-Δ_{Gui} diagram for the lower MS stars. The lines show the directions along which stars would be displaced by differential reddening, unresolved binaries, and initial chemical spread (see text for details).

with increasing [Fe/H] and increasing Y (green and magenta). These vector have been calculated as described by Griggio et al. (2022b) for M37, using as reference the isochrone in Fig. 6.3, and the corresponding values of d and $E(B-V)$ (see Sect. 6.2). In this figure, we display the effect of binaries as a two-slope sequence, because it is a better representation of the trend predicted by synthetic stellar populations, compared to a single slope as shown in Griggio et al. (2022b).

The figure shows that, in the case of M38, the distribution of the stars' colours in this diagram follows a trend consistent with a combination of differential reddening across the face of the cluster and the presence of unresolved binaries with varying q. There is no need to invoke the presence of a range of [Fe/H] or Y among the clusters' stars. This is at odds with the case of M37, where binaries and differential reddening produced too shallow slopes in this diagram, compared to the observations (see the Appendix for a comparison of the CMDs and Δ_{GBR}-Δ_{Gui} diagrams of M37 and M38).

Figure 6.9 shows a synthetic sample of stars –computed as in Griggio et al.

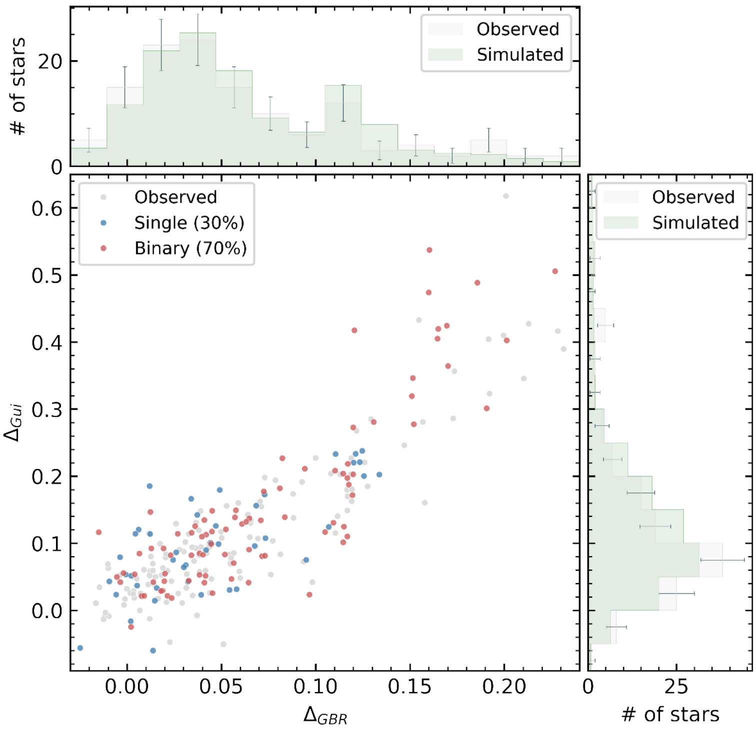

Figure 6.9: Comparison of the distribution of the synthetic population (including binaries and a spread of $E(B-V)$ to account for differential reddening – see text for details) and the observed cluster stars (grey filled circles) in the Δ_{GBR}-Δ_{Gui} diagram. Synthetic single and unresolved binary stars are shown in blue and red respectively. Histograms of the observed (with Poisson error bars) and simulated number counts along the two axes are also shown (see text for details).

(2022b), using isochrone, distance, and reference reddening previously discussed– compared to observations in the Δ_{GBR}-Δ_{Gui} diagram. The purpose of this comparison is just to see how binaries and differential reddening only can account qualitatively for the observed distribution of lower-MS stars in this diagram.

The full synthetic sample of 50 000 objects includes observational errors in both the *Gaia* and *Sloan* magnitudes, and contains a 70 % fraction of unresolved binaries with mass-ratios q distributed as $f(q) \propto q^{-0.6}$ following Malofeeva et al. (2022). It is worth pointing out that in the case of assuming a flat probability distribution for q, the same results described below are obtained with a 10-15 % binary fraction.

We display here one random subset of the full sample, containing the same number of objects as the observations. The figure also shows along the horizontal and vertical axis a comparison of the number distributions of synthetic and observed stars as a function of the two quantities Δ_{GBR} and Δ_{Gui}, respectively. When calculating these histograms we have considered the full sample of synthetic stars and rescaled the derived histograms to have the same total number of objects as observed.

The contribution of differential reddening has been accounted for by using a double Gaussian distribution; only in this way, we are able to reproduce the clump of stars clearly visible in the Δ_{GBR} histogram at $\Delta_{GBR} \sim 0.12$. The parameters of the distributions have been adjusted to roughly reproduce the observed trends of the number distributions in both Δ_{GBR} and Δ_{Gui}, because we could not determine a reliable differential reddening map for M38 using the technique described by, e.g., Milone et al. (2012), given the relatively low number of objects. The first Gaussian accounts for a random sample of $\sim 80\,\%$ of the synthetic stars (both single and binary objects) and is centred on $E(B-V) = E(B-V)_{\mathrm{ref}} + 0.04$, with $\sigma = 0.033\,\mathrm{mag}$, where $E(B-V)_{\mathrm{ref}} = 0.26$. The second Gaussian distribution is centred on $E(B-V) = E(B-V)_{\mathrm{ref}} + 0.15$, with $\sigma = 0.01\,\mathrm{mag}$, and accounts for the remaining objects in the synthetic sample.

It is remarkable how this synthetic sample, which includes just unresolved binaries and the effect of differential reddening, follows nicely the observed trend in this diagram. Also, the observed number distribution across the diagram can be followed quite well by using two simple Gaussian $E(B-V)$ distributions and the power-law q distribution determined by Malofeeva et al. (2022). This shows that there is no need to invoke a chemical abundance spread to explain the width of the lower MS in this cluster.

We have then repeated the analysis previously described considering this time stars in the brighter G magnitude range between 12.5 and 14, corresponding to single star masses between ~ 1.5 and $\sim 2.2\,M_{\odot}$. Using the same binary fraction, q and $E(B-V)$ distributions of the previous comparison, we have found the same agreement of the number distributions of synthetic and observed stars across the Δ_{GBR}-Δ_{Gui} diagram as in Fig. 6.9.

The same comparison could not be performed for objects in the TO region of the CMD, because of the small sample of cluster stars in this magnitude range (see Sect. 6.2).

6.5 Summary and conclusions

We have employed the accurate *Gaia* DR3 photometry and astrometry of the poorly studied open cluster M38 to select *bona fide* members and determine the cluster distance and mean proper motion. The *Gaia* CMD does not show an obvious extended TO despite the cluster being $\sim$300 Myr old, but the number of stars in the TO region is too small to investigate quantitatively this matter. The unevolved MS is broader than expected from photometric errors only and to determine the origin of this broadening we have applied the same technique developed to study the open cluster M37 (Griggio et al., 2022b), making use of auxiliary photometry in the *Sloan* system to build a differential colour-colour diagram of the lower MS from combinations of *Gaia* and *Sloan* magnitudes.

We employed synthetic stellar populations to reproduce the observed trend of M38 stars in this diagram, and found that the observed MS colour spread can be explained simply by the combined effect of differential reddening and unresolved binaries. There is no need to include a spread of initial chemical composition (either metals or helium) as instead necessary to explain the same differential colour-colour diagram for the lower MS of M37.

Despite having similar total masses (estimated total masses on the order of 1 000-1 500 $M_\odot$, mutually consistent within the associated errors, see Piskunov, A. E. et al., 2008) and metallicities different on average by no more than at most a factor 2-3, the open clusters M38 and M37 seem to host stellar populations with a clear difference: single vs multiple chemical compositions. The origin of this difference is unknown and we do not know as well whether the chemical abundance spread found photometrically in M37 is a feature common to many more open clusters, and if there is any connection with the extended TO phenomenon.

Further photometric investigations like ours, as well as accurate differential spectroscopic analyses on a large sample of open clusters are necessary to shed light on this phenomenon, and its implications for cluster formation and the use of open clusters and chemical tagging to study the formation and evolution of the Galactic disk.

6.6 Comparison of M37 and M38 diagrams

We present here a comparison of the *Gaia* CMD and the Δ_{GBR}-Δ_{Gui} diagrams of M37 and M38. The top panels of Fig. 6.10 show the CMDs of our M37 (left) and M38 (right) *bona-fide* members, highlighting in a darker shade of grey the sources employed in the analysis of the width of the MS. The bottom panels display the Δ_{GBR}-Δ_{Gui} diagrams of both cluster's lower MS. The points are clearly distributed along different slopes in the two diagrams; in particular, we also notice the behaviour of high-q binaries ($\Delta_{GBR} \gtrsim 0.1$) in the case of M37, that are distributed along a steeper line, while M38 stars in the same region follow a shallower direction.

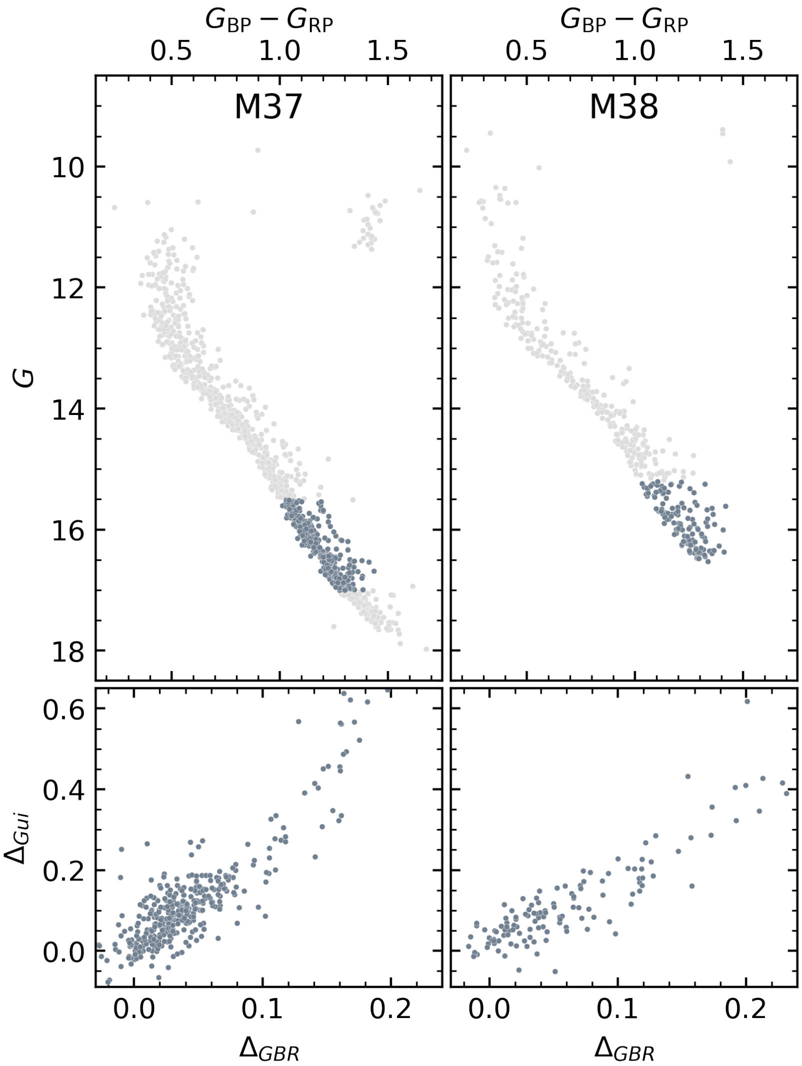

Figure 6.10: Comparison of M37 and M38 CMDs and Δ_{GBR}-Δ_{Gui} diagrams.

7. Photometry and astrometry with *JWST* – NIRCam distortion correction[1]

In preparation to make the most of our own planned *James Webb Space Telescope* investigations, we take advantage of publicly available calibration and early-science observations to independently derive and test a geometric-distortion solution for NIRCam detectors. Our solution is able to correct the distortion to better than $\sim$0.2 mas. Current data indicate that the solution is stable and constant over the investigated filters, temporal coverage, and even over the available filter combinations. We successfully tested our geometric-distortion solution in three cases: (i) field-object decontamination of M 92 field; (ii) estimate of internal proper motions of M 92; and (iii) measurement of the internal proper motions of the Large Magellanic Cloud system. To our knowledge, the here-derived geometric-distortion solution for NIRCam is the best available and we publicly release it, as many other investigations could potentially benefit from it. Along with our geometric-distortion solution, we also release a `Python` tool to convert the raw-pixels coordinates of each detector into distortion-free positions, and also to put all the ten detectors of NIRCam into a common reference system.

7.1 Introduction, Observations, Data-Reduction

The characterisation of the geometric distortion (GD) of an imager is of paramount importance to assess its use for high-precision astrometry. This is particularly important in the case of cameras of an out-of-atmosphere, brand-new instrument, such as the *James Webb Space Telescope (JWST)*, arguably the world-wide most-important astronomical facility.

In this work, we made use of part of *JWST* public data collected with the

[1]The content of this chapter has been published in Griggio et al. (2023a).

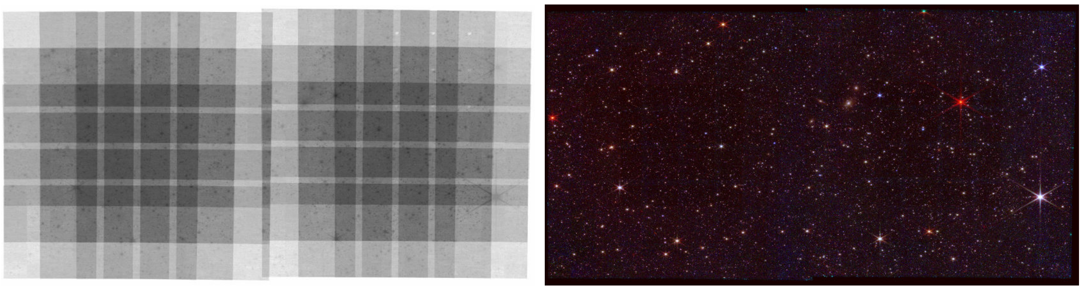

Figure 7.1: *(Left:)* depth-of-coverage of the 9 pointings for each considered filter in the SW channel. The studied region in the LMC cover about $6' \times 3'$, and shows large overlaps between the SW's detectors. *(Right:)* a three-colour view of the region, where F090W, F150W and F444W were used for blue, green and red colour, respectively.

Figure 7.2: To give an idea of the richness of isolated well-measurable sources in the field we show a zoom-in of a portion of $\sim 150'' \times 44''$, around the brightest and reddest source (*Gaia* DR3 `4657988450340570624`, `2MASS 05212923-6927554`, `WISE J052129.23-692755.4`) visible in right panel of Figure 7.1(a red super-giant belonging to LMC classified as an extreme AGB star by Boyer et al. (2011)) .

Near Infrared Camera[2] (NIRCam) under the Cycle 1 Calibration Program 1476 (PI: M. Boyer) to derive its GD correction. While standard pipeline products for GD corrections of *JWST*'s cameras are expected to be released in the future by other teams, we provide with this work the first, independent, documented and publicly available GD correction that allows an accuracy of ~ 0.2 mas on the stellar positions.

This paper is part of a series to build-up our capabilities to obtain *state-of-the-art* imaging astrometry and photometry with *JWST*. This is a necessary task for us to properly prepare and maximise the scientific returns of our planned (March 2023) proprietary *JWST* observations (GO-1979, PI: Bedin).

[2] `https://jwst-docs.stsci.edu/jwst-near-infrared-camera`

Table 7.1: Log of the observations employed in this work.

Filter	Pupil	t_{exp} [s]	Readout pattern	N_{exp}
F090W	CLEAR	21.474	`RAPID`	9
F150W	CLEAR	21.474	`RAPID`	9
F150W2	CLEAR	21.474	`RAPID`	9
F150W2	F162M	85.894	`BRIGHT2`	9
F150W2	F164N	118.104	`BRIGHT1`	18
F277W	CLEAR	21.474	`RAPID`	9
F444W	CLEAR	21.474	`RAPID`	9
F444W	F405N	118.104	`BRIGHT1`	9
F444W	F466N	257.682	`SHALLOW4`	9
F444W	F470N	257.682	`SHALLOW4`	9

In our first paper Nardiello et al. (2022) (hereafter Paper I), we describe the procedure to derive high-accuracy point-spread functions (PSFs) for NIRCam in some filters, an essential step to derive high-precision photometry, especially in crowded environments. We made those PSFs publicly available[3]. In this second paper, we also release to the public our GD correction of NIRCam.

Calibration Program 1476 will derive the GD for both channels of NIRCam by observing with *JWST* the Large Magellanic Cloud (LMC) calibration field observed multiple times with the *Hubble Space Telescope (HST)*. This field is centred at $\alpha = 80^{\circ}\!.49030$, $\delta = -69^{\circ}\!.49816$, and is described in the *JWST* technical report Anderson et al. (2021).

However, in the present work we will not make use of this *HST* astrometric catalogue to derive our GD correction of NIRCam. Instead, we will make use just of the new *JWST* observations to self-calibrate (i.e. to calibrate without exploiting observations of standard astrometric fields), leveraging the existing *Gaia* Data Release 3 (DR3) (Gaia Collaboration et al., 2023) to constrain the linear terms of our GD solution. In this sense, our work is an independent analysis and solution of the NIRCam GD, to be compared in the future with those that will be released by the instrument team.

We employed the set of images collected with the Short Wavelength (SW) channel in F090W, F150W, and F150W2 filters, and with the Long Wavelength (LW) channel in F277W and F444W. We also, test the derived geometric distortion solution in the available filter combos: F150W2+F162N, F150W2+F164N, F444W+F405N, F444W+F466N and F444W+F470N.

[3] `https://web.oapd.inaf.it/bedin/files/PAPERs_eMATERIALs/JWST/Paper_01/`

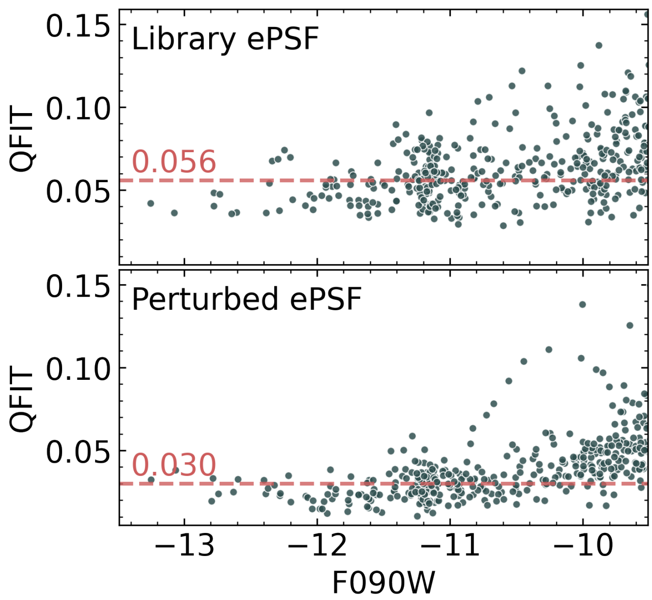

Figure 7.3: The quality-of-fit (`QFIT`) distribution before (top panel) and after (bottom panel) the ePSF perturbation. The median `QFIT` value decreases from 0.056 to 0.030, with an improvement of ∼50 % in the PSF fitting. The figure refers to an image in F090W filter, namely `jw01476001003_02101_00001`, module B, detector 2.

For each filter, *JWST* observed the field with 9 different pointings in such a way a given star is placed in 9 different positions of a detector (Fig. 7.1). Each pointing is an exposure obtained with a single integration. In Table 7.1 we report all the observations used in this work.

We extracted catalogues of positions and fluxes for point sources from the NIRCam calibrated images[4] (`_cal`) by adopting the procedure described in PaperI. Briefly, for each image, we used a list of bright, isolated, unsaturated stars to perturb the 5×5 library effective PSFs (ePSFs) obtained in PaperI, in such a way as to take into account the time variations of the *JWST* ePSFs. Briefly, the software we adopted measured the flux and the positions of the stars by fitting the library ePSFs, subtracted the models of these stars from the image, and calculated the average of the normalized residuals that are finally added to the library ePSFs. The routine carried out 11 rounds if iterations, and at each iteration the residuals are used to adjust the last obtained PSFs. Figure 7.2 shows a zoom-in of the studied region at a meaningful scale to display individual sources; it is representative of

[4] `https://jwst-pipeline.readthedocs.io/`

the entire field, which is rather homogeneous and rich in bright sources, relatively isolated, and well-measurable.

In Fig. 7.3 we show why it is important to perturb the library ePSF. In the top panel, the quality-of-fit parameter (`QFIT`) obtained employing the library ePSFs (from PaperI) is shown as a function of the instrumental magnitudes ($m_{\rm instr} = -2.5 \log \Sigma(\text{counts})_{\text{used pixels}}$). The parameter `QFIT` essentially quantifies the difference between the adopted ePSF model and the observed stars on the images. In the bottom panel, the same PSF diagnostic is shown when the perturbed ePSFs are used. In this case, the `QFIT` parameter significantly decreases, getting closer to zero, so the PSF better resembles the real stars. This translates into improved astrometry, photometry, and source separations.

We adopted the software `img2xym` developed by J. Anderson (Anderson et al. (2006)), and adapted to the NIRCam images, to extract positions and fluxes of the stars by fitting the perturbed ePSFs; we searched for sources with a total flux ≥ 50 counts and whose peaks are isolated at least 5 pixel from the closest brighter pixel. The software identifies the peaks that satisfy these criteria among the image, and for each of them, it fits the local ePSF obtained by the bi-linear interpolation of the 4 closest perturbed ePSF of the grid. Through a chi-square minimisation, it measures the position and flux of each source. We refer the reader to PaperI for a more detailed description of the data reduction.

7.2 Geometric distortion correction

Our derivation of the GD correction for NIRCam followed the empirical approach and procedure successfully applied to derive the GD correction of many other cameras at the focus of space- and ground-based telescopes (Anderson et al., 2006; Anderson and King, 2003; Bellini et al., 2011; Bellini and Bedin, 2009; Kerber et al., 2019; Libralato et al., 2014, 2015).

Our GD solution is derived independently for each of the ten 2048×2048 pixels NIRCam detectors (8 for SW, and 2 LW), and it is made up of three parts. First, a backbone third-order polynomial (Section 7.2.1) derived through a self-calibration procedure; second, a first-order polynomial derived by exploiting the *Gaia* DR3 reference system, to fix the linear terms of the GD (Section 7.2.2), and third, a fine-scale table that accounts for spatial high-frequency systematic residuals that the polynomial correction can not absorb (Section 7.2.3). More details on self-calibration of the GD can be found in the work by Anderson and King (2003), of which we will give a brief description in next sub-section.

The procedure that we will describe in the next sections have been applied in-

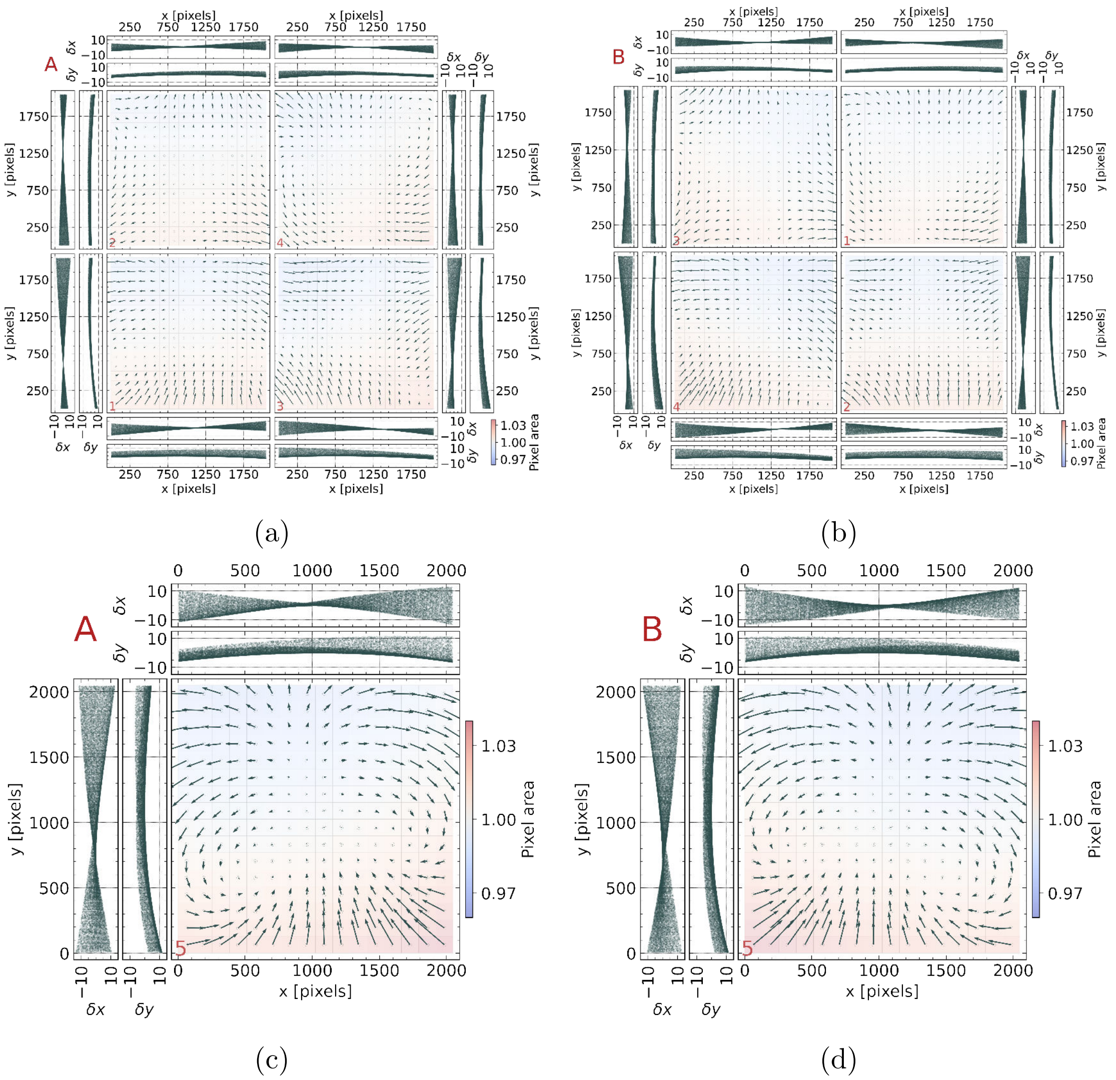

Figure 7.4: Geometric distortion map of NIRCam short (top) and long (bottom) wavelength channel for both module A (left) and module B (right); detector number is shown in red on the bottom left corner of each vector plot. The size of the residual vectors is magnified by a factor 20. For each detector we also show the single residual trends along x and y axes. Units are in raw NIRCam pixels. The colour map represents the pixels' area variation across the detectors (see text).

dependently to each detector of both modules (A and B). The final distortion map is shown in Figure 7.4. The colour map represents the pixels' area variation across the detectors due to the GD, which is relevant to show for those investigations dealing with surface brightness. Each 128×128 pixels region in the vector plots of Figure 7.4 is coloured according to the ratio between the GD corrected area and the raw area. We computed the GD corrected area using the corrected positions of the corners of each region, thus the value represents the mean area variation of the pixels in that region.

7.2.1 Polynomial correction

The polynomial GD solution is represented by a third-order polynomial; we checked that higher-orders (fifth and seventh) do not provide better results. We chose the pixel $(x_0, y_0) = (1024, 1024)$ in each detector as a reference position and solved for the distortion with respect to it, using the normalised coordinates $(\tilde{x}, \tilde{y}) = \left(\frac{x-x_0}{x_0}, \frac{y-y_0}{y_0}\right)$ (cfr. Anderson and King, 2003; Bellini et al., 2011).

To derive the polynomial coefficients we performed a series of iterations in which we alternate two main tasks: building the master frame, which will be the temporary reference system closer to the distortion-free solution than the previous iteration, and calculating the residuals between the positions of the sources as measured on the master frame and those measured in the raw catalogues. These residuals are then used to derive the polynomial coefficients. The polynomial correction is performed as follows:

- We selected the sources in each catalogue with instrumental magnitude in the range $-12.5 < m_{\mathrm{instr}} < -8$ and with `QFIT` lower than 0.1, to avoid artefacts, saturated and poorly measured stars which would affect the distortion solution.

- We conformally transformed the positions of each star in each catalogue into the reference system of the central dither, and we built a master frame by averaging the positions and fluxes of the sources that are measured in at least three exposures.

- At this point, we computed the conformal transformations (T) between stars in each catalogue and the master frame.

- The inverse transformation (T^{-1}) is then used to compute the positions of the master frame's stars in the raw-coordinate system of each image, that are then cross-identified with the closest source after applying the inverse GD correction derived in the previous iteration (which, of course, at the first iteration is equal to the identity). Each such cross-identification generates a pair of positional residuals $\delta x = x_{\rm raw} - X^{T^{-1} \circ GD^{-1}}$ and $\delta y = y_{\rm raw} - Y^{T^{-1} \circ GD^{-1}}$, where $(x_{\rm raw}, y_{\rm raw})$ and (X, Y) are the coordinates in the raw catalogues and the master frame reference systems respectively.

– We performed a least-square fit of the residuals to obtain the coefficients for the two third-order polynomials that are added to those derived at the previous iteration. To ensure convergence, the 75 percent of the correction is then applied to all stars' positions.

The procedure is iterated over up to 45 iterations, until convergence is reached, starting from the corrected catalogues, each time refining the master frame and the polynomial coefficients. At the end of the procedure, we had a set of coefficients for each filter. The polynomials derived independently for each filter turned out to be in agreement within the uncertainties, therefore we computed a weighted mean (using the inverse of the errors on the coefficients as weights) to get a single final polynomial for each individual detector. While the polynomials for filter combinations were marginally in agreement with those obtained for single filters, they were not used to compute the average polynomials.

7.2.2 GD linear terms

So far, the first epoch of calibration program 1476 has observations collected at one single orientation of the telescope. This makes it not possible to solve for the linear terms of the GD (Anderson and King, 2003). For this reason, we will make leverage of the existing astrometric flat field provided by *Gaia* DR3 to perform this task.

While common sources are very few, faint and poorly measured, we need only 3 stars, in principle, to fix these linear terms, as the most general linear transformation has only 6 parameters (therefore the 2D positions of three stars would be sufficient).

Nevertheless, in each detector, there are always at least 350 stars in common between *Gaia* and NIRCam observations of program 1476 for the SW channel, and at least 1200 for LW channel, more than enough for our purposes.

We then proceeded in the same way as described in the previous section, but this time using *Gaia* (projected onto the tangent plane of each exposure) as a master frame, starting with the catalogues corrected with the third-order polynomial, and using all the filters together. We needed 10 iterations to reach convergence.

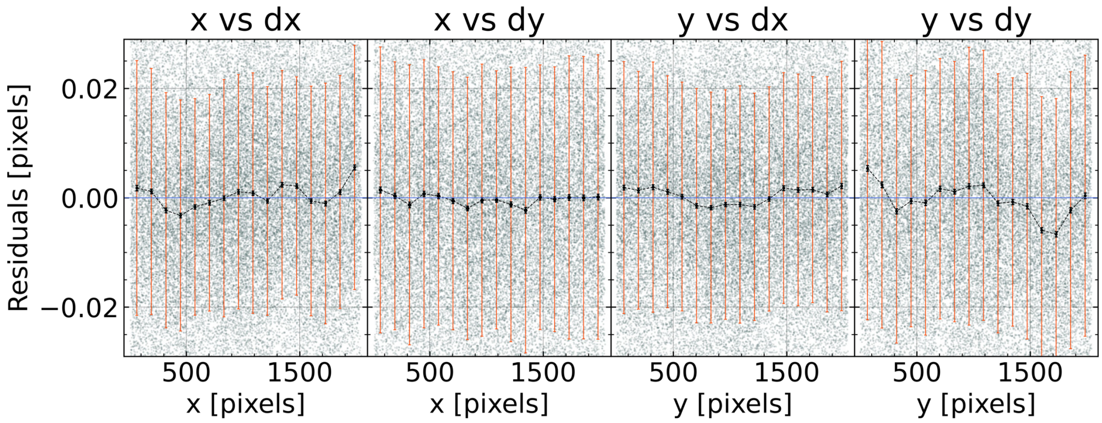

Figure 7.5: Positional residuals given by the inter-comparison between all the dithered exposures (for detector A1) in F150W and F150W2 filters after the two polynomial have been applied. The black dots represent the mean residual in each slice of 128 pixels. The red error bars are calculated as $\sigma = 68.27^{\text{th}}$ percentile of the residual distribution (after a 3σ-clipping), and the black error bars are $\sigma/\sqrt{n-1}$, with n the number of points used to compute the mean.

The residuals between the inter-comparison between all the dithered exposures for detector A1 are shown in Figure 7.5: we notice the presence of small spatial residuals, that we wanted to remove. We corrected these systematics with a lookup table as described in the next section.

7.2.3 Fine-structure table of residuals

The systematic residuals observed in Fig. 7.5 could not be removed with the polynomial corrections. Additional iterations did not provide any improvements. For this reason, we decided to proceed with a fine-structure table of residuals.

We followed two different procedures for the SW channel and the LW channel; for the SW channel we employed again a self-calibration procedure. We started from the catalogues corrected with the two polynomials and followed the first four steps of the bullet list in Section 7.2.1. We then divided the residuals into a lookup table of 16×16 cells in x and y. To each cell, we assigned a residual in x and y using the 3σ-clipped mean of the residuals in that cell. The positions of the stars are then corrected with the residual calculated with a bilinear interpolation of the four most adjacent cells (cfr. Libralato et al., 2014). This procedure is iterated over 10 times to converge. The systematic residuals were successfully corrected; after the correction, the inter-comparison of corrected frames is consistent to the

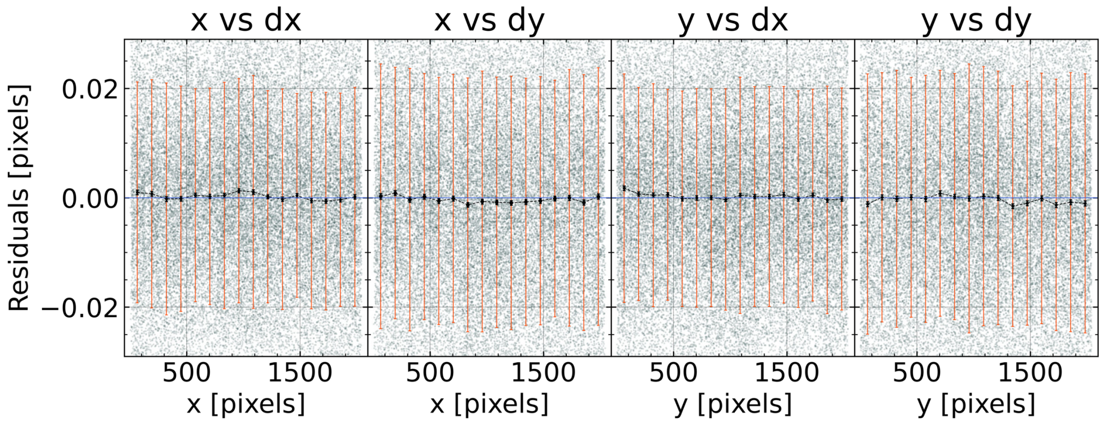

Figure 7.6: As Fig. 7.5 but after applying also the fine-scale table correction. These black dots are our internal errors, which are always smaller than 20 μas, and are the formal uncertainty of our GD correction; whereas the larger error bars (in red) show the positional random error for the individual "typical" source.

sub-mas level (Figure 7.6, assuming a pixel scale of 31.23 mas, see Section 7.2.6).

We applied the same self-calibration procedure to the LW channel, unsuccessfully. After 10 iterations, the residuals between the inter-comparison of dithered exposures did not show any clear trend. However, the comparison of these positions with the *Gaia* catalogue showed a global trend in the residual distribution: we suspect that the data are insufficient for a self-calibration of the GD for the LW channel. Indeed, the dither pattern (which is the same for both channels) offers larger inter-comparison overlaps for SW than for LW.

Therefore, we exploited our just corrected SW catalogues to build a distortion-free master frame, on which we can calibrate also the LW channel. We proceeded with the same steps that we followed to derive the SW channel lookup table, but this time as a master frame we employed the one built employing the SW corrected catalogues. Adopting this procedure, also in this case, 10 iterations were sufficient to reach convergence.

This is the final step that concludes the derivation of our GD correction for the NIRCam detectors. In Sect. 7.5 we will give details about the `Python` routine, which we release as electronic material part of this publication, that will enable readers to transform the raw pixel coordinate of each of the 10 individual detectors of NIRCam into a distortion-free frame.

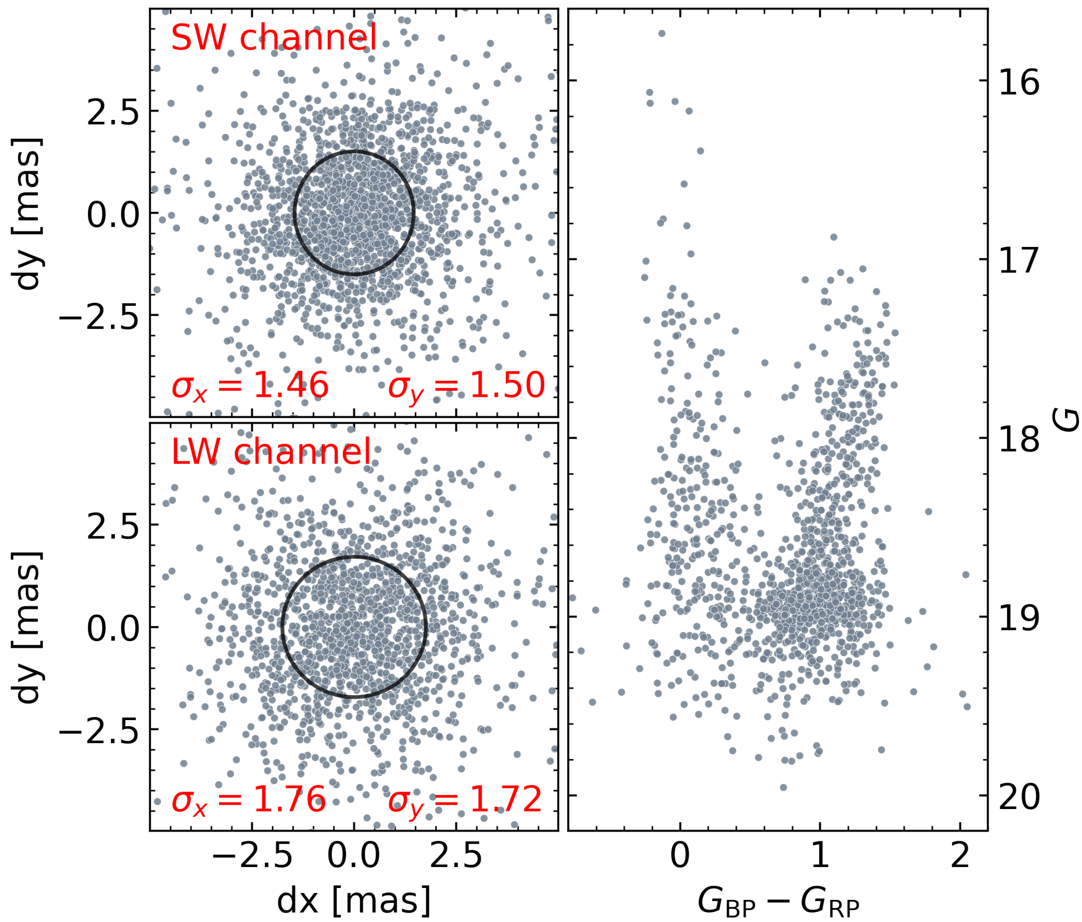

Figure 7.7: *Left*: positional residuals between the positions measured by us and those given by *Gaia* DR3 catalogue, for the SW channel (top) and the LW channel (bottom). *Right*: colour-magnitude diagram in the *Gaia* filters for the common sources.

7.2.4 *Gaia* validation

Although our formal (internally estimated) errors provide uncertainties smaller than 20 μas, these very likely are underestimates of the true errors. However, it is not easy to compare these corrected positions with other catalogues able to reach similar accuracy for such faint stars. The only available is *Gaia* DR3 which, however, we used to fix the linear terms. Therefore, while we will not be able to independently test the linear terms of our solution, we will nonetheless still be able to test the accuracy of the non-linear terms of our GD correction.

Unfortunately, common sources are faint for *Gaia* and we end up being limited by the errors in the *Gaia* catalogue in both positions and motions. *Gaia* DR3 gives positions at the epoch 2016.0, while the new *JWST* observations are collected at epoch ∼2022.53. Given the internal proper-motion dispersion for LMC stars in this field (which also has a distribution far from being Gaussian) of about 40 km s^{-1} (Anderson et al. (2021), and assuming a distance of 50 kpc, in 6.53 years (2022.53-2016.0), we expect a dispersion of 1.1 mas.

We cross-identified the sources in our SW and LW catalogue of a single image (namely `jw01476001003_02101_00001` in F090W and `jw01476001001_02101_00001` in F277W) with the *Gaia* DR3 catalogue, projected onto the tangent plane of each detector (as in Sec. 7.2.2), and derived the transformations to bring the positions of our catalogues into the tangent plane coordinate system. The residuals between the transformed positions and *Gaia* are shown in Fig. 7.7 (left panels), where the dispersions are labelled within each panel as σ and expressed in mas, for both coordinates. The right panel shows the CMD in Gaia bands for sources in common with *JWST*. We have tried to extrapolate *Gaia* positions to epoch 2022.53 by employing the tabulated *Gaia* proper motions, however, this had the effect to significantly enlarging the residual dispersion, making these extrapolations useless. This is mainly due to both the large errors (0.1-0.5 mas/yr) on proper motions for faint sources ($G > 17$) in the *Gaia* catalogue, that produce sizeable effects in six years, and the lack of proper motion measurements for very faint stars ($G > 20$).

The average observed dispersion for the two coordinates in the SW channel is 1.48 mas; 1.74 mas for LW channel. To infer from this the errors of our GD correction, one should subtract in quadrature the other contributions that participate to enlarge the dispersion, such as the LMC's internal motions (∼1.1 mas), the errors in the *Gaia* catalogue (∼0.25, mas Gaia Collaboration et al., 2021), and the positioning errors for the bulk of these stars in the *JWST* images (0.7 mas, i.e., the red error bars in Fig. 7.6). Summing in quadrature these contributions for the bulk of the stars we obtain ∼1.3 mas. Subtracting in quadrature this value from the observed dispersion for SW, we obtain a residual of ∼0.6 mas, which here we entirely ascribe to the residual in our GD correction. Doing the same for the LW we obtain again $\sim$0.6 mas.

This is a rough estimate for the minimum limit in the accuracy of our GD correction and is mainly affected by the strongly non-Gaussian internal proper-motion distributions for LMC stars (see Fig. 15 of Anderson et al. (2021), and Sect. 7.4.3 of this work). Indeed, in next the sections, we will put significantly smaller upper limits to this estimated accuracy for the here-presented GD correction.

7.2.5 Internal errors

Figures 7.5 and 7.6 give positional residuals for the bulk of the measured sources in the field (red error bars), here instead, we want to show these quantities as a function of the instrumental magnitude for the individual sources. This is possible by inter-comparing the positions and magnitudes measured employing the same filter (9 dithered images), which provide an estimate of the expected r.m.s. of the quantities, as measured in a single image, for individual sources. In Fig. 7.8, we show for the case of detector A1 in F090W these trends, with median values of 0.013 pixels (i.e., 0.4 mas) for the 1-D positioning, and 16 milli-mag in the photometry for well-measured sources, i.e. those with $-13.5 < m < -10$ and `QFIT`< 0.2. Similar results are obtained for the other detectors/filters. In the following applications and considerations, it is important to distinguish the difference between these random errors for individual sources and the systematic errors of geometric distortion residuals.

7.2.6 Putting detector-based positions into a common reference system

In this section we derive the transformations to bring the positions measured by each detector of a given image into a common reference system (which arbitrarily we chose to be that of A1). We remark that for investigations requiring the most possible accurate differential astrometry, it is always optimal to compare position measurements as locally as possible, provided that there are enough reference sources within the field. However, some projects might have limited reference objects, and would require an understanding of the distortion across the entire NIRCam field of view. To derive these transformations we exploited the *Gaia* catalogue. We considered each of the nine dithers separately, and we treated every filter independently. We proceeded as follows:

– first, we downloaded a portion of the *Gaia* DR3 catalogue large enough to

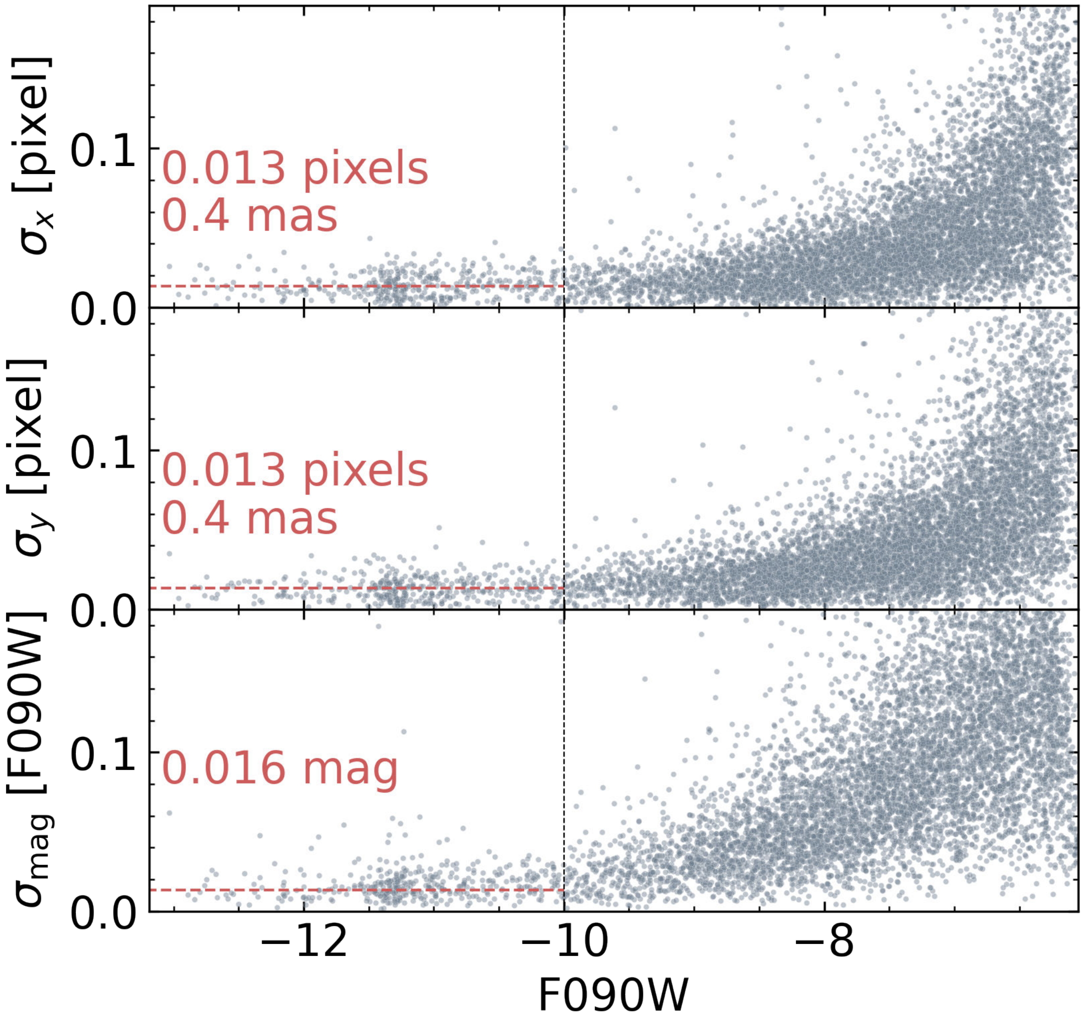

Figure 7.8: Positional residuals in x and y (top and middle) and magnitude residuals (bottom) from the inter-comparison of dithered images in F090W after the GD correction have been applied. Red lines indicate the median value of the residuals for well-measured sources ($-13.5 < m < -10$, `QFIT`< 0.2).

cover both modules A and B of the considered exposure;

– we projected it onto the plane tangent to the centre of the two modules;

– we transformed *Gaia* positions into the reference system of A1;

– finally, we used the *Gaia* positions on A1 to derive the six parameters transformations to bring all the other detectors on the reference system of A1.

At the end of this procedure, for each filter, we have nine transformations for each detector (one for each of the nine dithers). We checked the consistency between the coefficients derived from each dither, and given the general agreement among them, we computed the final transformation averaging all the nine estimates. Furthermore, as the coefficients were compatible even in different filters, we also averaged the coefficients obtained in the three filters for the SW-channel, and averaged those in the two filters for the LW channel, resulting in six parameters for the transformation of each detector into a common reference system, independently of the adopted filter.

In Sect. 7.5, we describe the `Python` software, which we release with this publication, that enables users to put all the 10 individual detectors of NIRCam into a common distortion-free meta-chip frame.

7.2.7 The absolute scale

The transformation between A1 and *Gaia* let us infer the pixel scale of our GD-corrected pixel reference system. For each of the filters, we observe the nine dithers to agree within few 10^{-5}, with a pixel scale of about 31.23 mas/px (see Table 7.2).

In the case of *HST* the telescope was orbiting at 7 km s^{-1} around the Earth, a speed that causes scale variation due to velocity aberration of about 7/300 000 parts, i.e., *also* of few 10^{-5}, and every 2 hours (Cox and Gilliland, 2003); therefore variations of the same order of what we observe here for *JWST*. However, unlike *HST*, *JWST* it is not orbiting at 7 km/s around the Earth. Nevertheless, *JWST* (as well as *HST*) is still orbiting the Sun with a velocity slightly less than 30 km s^{-1}, i.e., causing scale variations due to velocity aberration of about 30/300 000, or 1 part in 10 000, a very sizeable effect, although with a much slower ∼6 months time-frame. These effects (of 1 part in 10 000) needs to be properly accounted for in all applications which blindly rely on the absolute scale of the telescope (assuming *JWST* will prove to have a scale stable down to this level). For this purpose, the calibration pipeline includes in the header of each image the expected velocity aberration scale factor (`VA_SCALE`) calculated on the base of the expected absolute

Table 7.2: Mean pixel scale (S) and `VA_SCALE`.

Filter	S[mas/px]	σ_S[mas/px]	`VA_SCALE` $- 1$
F090W	31.23227	0.00005	3.65488×10^{-6}
F150W	31.23115	0.00006	3.64514×10^{-6}
F150W2	31.23086	0.00008	3.64028×10^{-6}

velocity of the Observatory. We note that the values of the `VA_SCALE` reported in the header of each image of the here-employed 1476 data-set, remains well below the few 10^{-5} scatter observed. In the lack of other observations, we assumed this to be the limit of the plate-scale stability for *JWST*.

We are deriving our absolute scales comparing directly to the absolute astrometric reference frame of *Gaia* DR3, therefore, to retrieve the true scale of our GD solution we should first divide for the `VA_SCALE` factor. The results obtained for the average of the scale of detector A1 compared to *Gaia* DR3, for all images collected in filters F090W, F150W, and F150W2, are shown in Table 7.2. The values for each filter are the averaged values obtained from the nine dithers. Note that the scale for filter F090W is significantly different (at $\sim 14\,\sigma$) from the one for the two filters F150W and F150W2, which are instead marginally consistent ($\sim 2.8\,\sigma$) among them.

Finally, we note that this is the scale to apply to our –here-derived– GD solution, that is normalised to a specific chip location. Other GD solutions might refer to different pixels, and therefore might have slightly different scales.

7.3 Colour-magnitude diagrams

The dither pattern of the observations provides large overlaps, which in turn, allows us to compare the photometry obtained from the different detectors of a module to register the zero points of the detectors into a common photometric reference system. In the case of the SW channel, we chose as reference system the first image obtained with detectors A1 and B1, and, for each filter and module, we transformed the positions and magnitudes of the stars measured in all the images into the reference system defined by this first image. We do this for each module, separately. We averaged the transformed positions and magnitudes of each detector, to obtain a more robust catalogue of stars measured in at least three images and we iterated refining the transformations by using as reference system the new catalogue containing the mean positions and magnitudes. We report in Table 7.3 the photometric zero-points of each detector within each module of

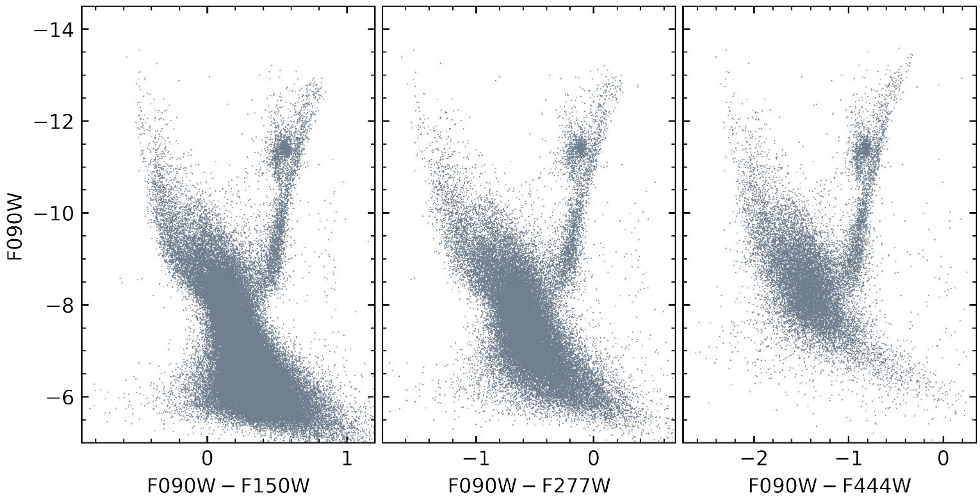

Figure 7.9: The F090W versus F090W−X CMDs, with X = F150W, F277W, F444W, of the stars in the LMC, obtained with the data used in this work.

the SW channel compared to detectors A1 and B1 (which by definition have null shifts).

Even if the overlap between modules A and B is small, we also were able to measure the zero points δmag=mag[A]-mag[B] between the catalogues obtained with the different modules in one filter (it means the zero-point between A1 and B1 in the case of SW channel, and A and B in the case of LW channel). We found δF090W $= -0.31 \pm 0.06$, δF150W $= -0.20 \pm 0.07$, δF277W $= +0.03 \pm 0.11$, and δF444W $= -0.06 \pm 0.07$.

For each filter, we carried out selections by using quality parameters like the photometric RMS and the quality-of-fit, as done in PaperI. Figure 7.9 shows the F090W versus F090W−X instrumental CMDs of the stars in the LMCs observed by NIRCam in the F090W, F150W, F277W, and F444W filters and that passed the quality selections. The deepest CMD is the F090W−F150W one, which reaches two magnitudes below the MS turn-off with a SN$\sim$5; the same signal is reached by the F444W filter two magnitudes brighter, making this filter the shallowest among those used in this work to follow the MS stars of the LMC.

7.4 Demonstrative applications

In this section, we demonstrate that applying our just-derived GD correction to positions of sources, and comparing these positions with those measured in an

Table 7.3: Relative photometric zero-points for SW and LW channels.

	SW Channel	
Detector	**F090W**	**F150W**
A1	$+0.00 \pm 0.00$	$+0.00 \pm 0.00$
A2	$+0.06 \pm 0.03$	$+0.02 \pm 0.02$
A3	$+0.06 \pm 0.02$	$+0.06 \pm 0.02$
A4	$+0.00 \pm 0.02$	-0.04 ± 0.02
B1	$+0.00 \pm 0.00$	$+0.00 \pm 0.00$
B2	-0.02 ± 0.02	-0.01 ± 0.02
B3	-0.09 ± 0.02	-0.06 ± 0.02
B4	-0.17 ± 0.02	-0.18 ± 0.01
δ(A1B1)	-0.31 ± 0.06	-0.20 ± 0.07
	LW Channel	
Detector	**F277W**	**F444W**
δ(AB)	$+0.03 \pm 0.11$	-0.06 ± 0.07

earlier archival *HST* data set, we are able to detect stellar motions at sub-mas level precision.

To this aim, we considered three applications, sorted by increasing difficulty: *(1)* the cluster-field separation in the case of the globular cluster M92; *(2)* the estimate of the internal motion of the same cluster; and finally *(3)* the clear detection of the internal motions in the LMC system, a stellar system at ∼50 kpc.

7.4.1 Field-object decontamination in M92

To compute the displacements of the stars in a field centred in M92, we adopted as the first epoch the *HST* observations collected under programme GO-10775 (PI: Sarajedini, Sarajedini et al. (2007), epoch 2006.27), and as a second epoch the *JWST* data from the ERS-1334 (PI: Weisz, epoch 2022.47). For the first epoch, we used the catalogue obtained by Nardiello et al. (2018b), while for the second epoch we used the catalogues obtained in PaperI, corrected by using the GD solution of this work. We matched the *HST* F814W catalogue with the *JWST* F090W and F150W catalogues by using 6-parameter global transformations. Sources that moved the least, and by far the large majority, are M92 member stars, therefore the zero of the motion coincides with the mean motion of the cluster. Top panel of Figure 7.10 shows the resulting vector-point diagram (VPD) of the displacements of the stars in $\delta t = 16.2$ yrs. We arbitrarily defined as field stars all the sources

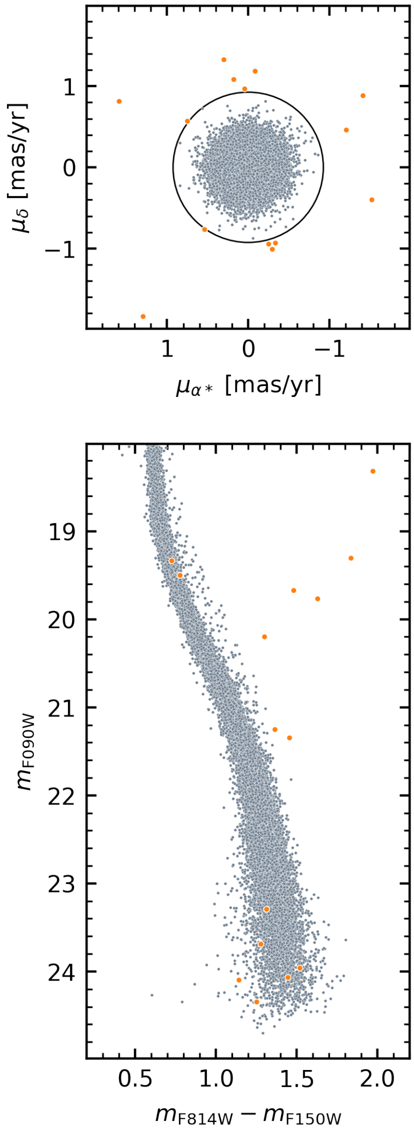

Figure 7.10: *Top*: vector-point-diagram of proper motions for sources in the common field between images collected with *HST* under program GO-10775, and the available images from *JWST* program ERS-1334. A black circle defines our arbitrary criterion to separate members (grey) and field objects (orange). *Bottom*: CMD in filters F814W−F150W vs. F090W; colour code is the same as top panel.

with a proper motion larger than $\sim 0.9\,\mathrm{mas/yr}$ (red points), which is about $3.5\,\sigma$ of the internal distribution (see next sect.). The bottom panel shows, for the same sources in the VPD, the $m_{\rm F090W}$ versus $m_{\rm F814W} - m_{F150W}$ CMD, employing the same symbols and colour codes.

Unfortunately, M92 is not an ideal target for a striking demonstration of the cluster-members field-objects decontamination, mainly because of the extremely sparse density of Galactic and extra-galactic sources in the direction of M92, where we count about 15 sources.

7.4.2 M92 internal dispersion

The globular cluster M92 (NGC 6341) is a relatively massive system ($3.5\times10^5\,\mathrm{M}_\odot$) located at a distance of $\sim$8.5 kpc and with a half-mass of 4.5 pc, i.e., $110''$ (Vasiliev and Baumgardt, 2021, hereafter VB21). In the radial range explored by the combined *HST*-*JWST* epochs, i.e., 20-100 arcsec from the centre of the cluster, according to the literature, we expect internal-velocity dispersion between 8 and $5.5\,\mathrm{km\,s^{-1}}$ (i.e., between 0.20 and $0.12\,\mathrm{mas\,yr^{-1}}$, VB21).

In this section, we further test our GD correction estimating the internal-proper motion dispersion for M92, and in the process we will also obtain a check on the precision of NIRCam astrometry.

We consider positions (X, Y) measured within *JWST* at epoch 2022.47, in the two filters F090W and F150W, separately. With those positions, we computed the displacements of sources in F090W and F150W, with respect to those measured within *HST* at epoch 2006.27, for each filter separately. We selected best-measured sources in all data sets, in the brightest 2 magnitudes just below the saturation and with photometric diagnostics `QFIT` and r.m.s. selected as described in Fig 5 of PaperI. We plot the two displacements in top panels of Fig. 7.11. The first epoch is identical for the two computed displacements, and the second epoch is essentially *also* the same. Indeed, F150W images were collected only a few minutes after F090W images, which does not change much the time baseline of $\sim$16.2 years. The two displacements correlate with the identity (red line, not a fit) in both coordinates (X on the left, Y on the right). Assuming Gaussian distributions for both the dispersion along the red line ($\sigma_\parallel$), and perpendicularly to it ($\sigma_\perp$), we can derive crude estimates for both dispersion in the M92's internal motions ($\sigma_{\rm intr}$) and for the errors ($\sigma_{\rm err}$). Bottom panels in Fig. 7.11 show the histograms for displacements along the parallel (in orange) and perpendicular (in blue) to the identity line.

Any error in the *HST* 2006 epoch has the effect to move a source only along the red line. So, the cross dispersion, i.e., perpendicular to the red line, reflects the

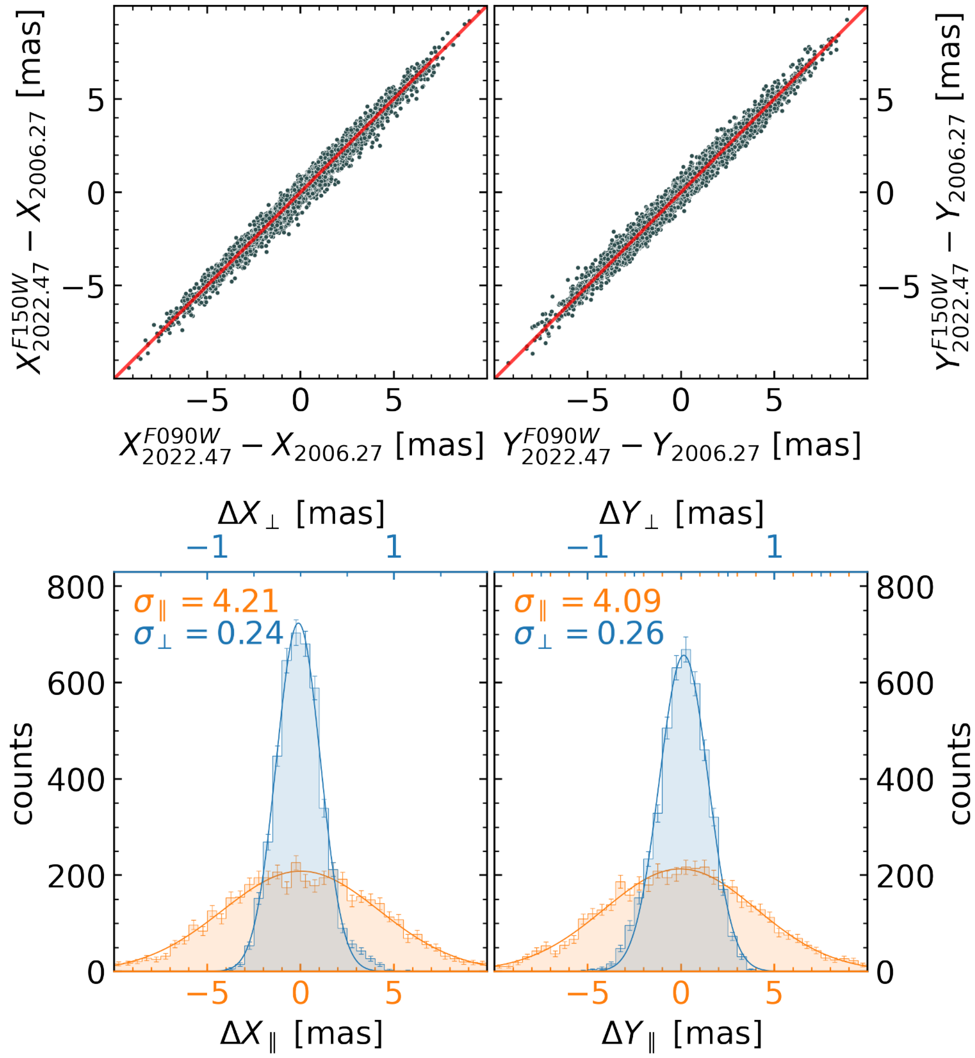

Figure 7.11: *(Top:)* Correlation between positional displacements obtained using an *HST* epoch collected in 2006.27 with filter ACS/WFC/F814W, and two different *JWST* data sets, in filters NIRCam/SW/F090W and F150W, both collected in 2022.47. The identity is indicated by the red line. X-coordinate on the *(left)*, and Y on the *(right)*. *(Bottom:)* Histogram of the displacement distributions along and perpendicular to the identity line. Note the different scale for the two quantities, given in the opposite axes (see text).

errors only in the two *JWST* epochs. Assuming the same dispersion for the two filters, $\sigma_{\rm JWST}$, we can write $\sigma_{\rm JWST} = \sigma_{\perp}/\sqrt{2}$. Taking the average in X and Y we obtain $\sigma_{\perp} = 0.25$ mas, and therefore $\sigma_{\rm JWST} = 0.18$ mas for the single *JWST* epoch (note, dispersion of displacements not of proper motions). This is essentially, just another way to put an upper limit to the errors in on our GD correction, although, internal to the method.

As four single *JWST* images participate in the precision of the single filter, we can multiply by a factor $\sqrt{(4-1)}$ to get the precision for the typical star in the individual image, about 0.3 mas, or ∼0.01 pixel; consistent with positioning precision for the best measured sources, which means that the errors in our GD corrections should be negligible with respect to it.

Now, we try to infer an estimate of the intrinsic proper-motion dispersion of M92 stars in the region covered by the two epochs. Similarly to what was done for the errors, we can assume that $\sigma_{\rm obs} = \sigma_{\parallel}/\sqrt{2}$. Again, taking the average of X and Y we obtain a $\sigma_{\parallel} = 4.15$ mas, and therefore $\sigma_{\rm obs} = 2.93$ mas. To know the intrinsic displacement dispersion we need to subtract in quadrature the errors. To the errors this time participate one *JWST* and one *HST* epoch. So, we sum in quadrature the errors just derived above $\sigma_{\rm JWST} = 0.18$ mas, and assume *HST* errors from the literature. For best stars we expect 0.32 mas (from Bellini et al., 2011), but as four *HST* images from 2006 participate to determine the positions, we take $\sigma_{\rm HST} = 0.32\,{\rm mas}/\sqrt{(4-1)} = 0.18$ mas. This makes the total errors, sum in quadrature of $\sigma_{\rm JWST}$ and $\sigma_{\rm HST}$, amount to $\sigma_{\rm err} = 0.25$ mas; negligible when compared to $\sigma_{\rm obs}$ (as obvious from a glance to Fig. 7.11). Nevertheless, the intrinsic dispersion of the observed displacement is $\sigma_{\rm intr} = \sqrt{\sigma^2_{\rm obs} - \sigma^2_{\rm err}} = 2.92$ mas.

Finally, taking into account the time base-line of 16.2 yr, we derive an estimate for the internal proper motion of M92 stars of 0.18 mas yr^{-1}; consistent with the value found by VB21 in the core (0.2 mas yr^{-1} in the centre, and 0.1 mas yr^{-1} at 100 arcsec). Indeed, our star sample is biased toward the centre, due to the spatial distribution of sources in a globular cluster.

The result is even more remarkable, taking into account that in the process of deriving displacement, we use a global transformation to transform from *HST* into *JWST* master frames, letting us completely at the mercy of residual in the geometric distortion of both *JWST* and *ACS* (which are sizable in this particular data set, cfr. Sect. 4.3 of Anderson et al. (2021), but thankfully diluted in a 16.2 yr time baseline). This means that by using a local transformations approach (as described in, e.g. Anderson et al., 2006; Bedin et al., 2003; Bellini et al., 2018) residual errors of various origins, could be suppressed. For these reasons, the results presented in this section are even more impressive.

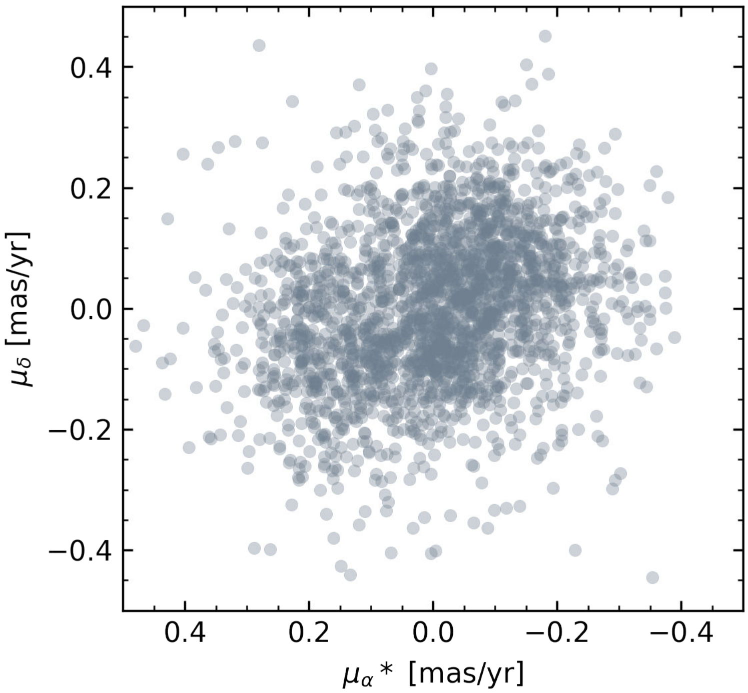

Figure 7.12: Displacements positions for sources in the LMC field as measured in archival *HST* images in year 2006.39, and the corresponding positions as measured in *JWST* in filter F090W at epoch 2022.53.

7.4.3 LMC internal dispersion

To detect the internal proper motion dispersion of LMC stars, we adopted as a first epoch the *HST* data collected during the calibration program CAL/OTA-10753 (PI: Diaz-Miller). The data set consists of 5×19 s$+2 \times 32$ s$+25 \times 343$ s$+10 \times 423$ s ACS/WFC images in F606W filter and observations were carried out between 25 April and 9 July 2006 (mean epoch $t \sim 2006.39$). A catalogue of sources was extracted for each image by using the software `hst1pass` (Anderson, 2022). These catalogues were matched with *Gaia* DR3 catalogue of the same region by using 6-parameter global transformations to orient and transform all the positions of the stars in the same reference system; the transformed positions were then (3σ-clipped) averaged to obtain a catalogue of stars with positions referred to the epoch 2006.39. We performed the same transformations with the *JWST* GD corrected catalogues in F090W; the final product consists of a catalogue with positions corresponding to the epoch 2022.53. We matched the *HST* ACS/WFC/F606W catalogue from 2006.39 with the F090W catalogue obtained with *JWST* in 2022.53, by using 6-parameter global (i.e., not local) transformations.

The displacements, converted in proper motions assuming a time baseline of δt = 16.14 yr, are shown in Fig. 7.12. Beside the flip of the μ_α^* axis, and the zero of the motions referred to LMC stars rest frame, the VPD distribution we obtained employing *JWST* is completely consistent with the one characterised in great detail by Anderson et al. (2021), for the same region of the LMC. The VPD has the same strongly non-Gaussian distribution in both α and δ, with three-lobed shape, clearly recognisable also in our Fig. 7.12. This further, demonstrate that our NIRCam GD correction enables us to obtain high-precision results comparable to what obtainable with *HST*.

As a final note, a more solid estimate of the internal velocity dispersion within LMC would be obtained by performing a local transformation approach (as for example in Bedin et al., 2014).

7.5 Conclusion

In this work, we have exploited *JWST* observations of a field in the LMC and *Gaia* DR3 to calibrate the geometric distortion of the ten NIRCam detectors. We exploited the calibrated positions coupling them with archival *HST* observations to measure the proper motions of sources within a field in the core of the Galactic globular cluster M92. Our measurements were able to clearly disentangle field objects from cluster members, and even to measure their internal kinematic. We also were able to measure the internal dispersion of stars within one extra-galactic system, the LMC. In all cases, our results are in agreement with the literature and in line with state-of-the-art astrometry.

Indeed, it is worth mentioning that the here-presented GD correction was successfully employed in the recent work by Nardiello et al. (2023a): where it allowed for the first detection of brown dwarf candidates in a GC, as result of careful image registration, and accurate proper-motion memberships derived by the coupling with existing *HST* archival material collected ∼12 years earlier.

Finally, we publicly release two `Python` tools to apply our geometric distortion correction to the raw coordinates of NIRCam detectors, and to put all the detector-based positions into a common, distortion-free, global reference system. The routine `raw2cor.py` takes as input a list of raw coordinates, the module (A or B) and the detector (1-5), and applies the third-degree polynomial, the linear terms, and the fine-scale table, giving as output the corrected coordinates. The routine `xy2meta.py` requires the same input as `raw2cor.py`, but in addition to the GD corrections it also applies the transformations to bring all the coordinates into a common reference system, which are given as output. These routines are released as electronic material with this paper and are also downloadable from the following url: https://oapd.inaf.it/bedin/files/PAPERs_eMATERIALs/JWST/Paper_02/Python.

8. *JWST* unveils the brown dwarf sequence of 47 Tucanæ[1]

In this chapter we apply our techniques to derive high-precision photometry and astrometry to compromised (publicly-available) images collected with *JWST* of the Galactic globular cluster NGC 104 (47 Tucanæ). In spite of the degradation and limited data, we were able to recover photometry and astrometry for the coolest stellar objects ever observed within a globular cluster, possibly unveiling the brightest part of the brown dwarf (BD) sequence. This is supported by: *(i)* proper motion membership, derived by the comparison with positions obtained from *Hubble Space Telescope* archival early epochs; *(ii)* the predicted location of the BD sequence; and *(iii)* the mass function for low-mass stars derived from models. Future *JWST* observations will provide the necessary deep and precise proper motions to confirm the nature of the here-identified BD candidates belonging to this globular cluster.

8.1 Introduction

Globular clusters (GCs) have always been fundamental benchmarks to test models of stellar evolution, as they are formed by stars spanning a wide range of masses and with roughly the same age, chemical composition and distance. GCs are among the oldest known objects of the Milky Way and possibly in the Universe, and their properties can be determined using stellar colour-magnitude diagrams (CMDs).

The *Hubble Space Telescope* (*HST*) has made significant contributions to our understanding of these systems, both in the Galactic (e.g., Bedin et al. (2004) and Piotto et al. (2007)) and extra-galactic context (Nardiello et al. (2019)). With its superior resolution and infrared (IR) sensitivity we can expect that the *James Webb Space Telescope* (*JWST*) will also greatly enhance the study of GCs. Argu-

[1] The content of this chapter has been published in Nardiello et al. (2023a).

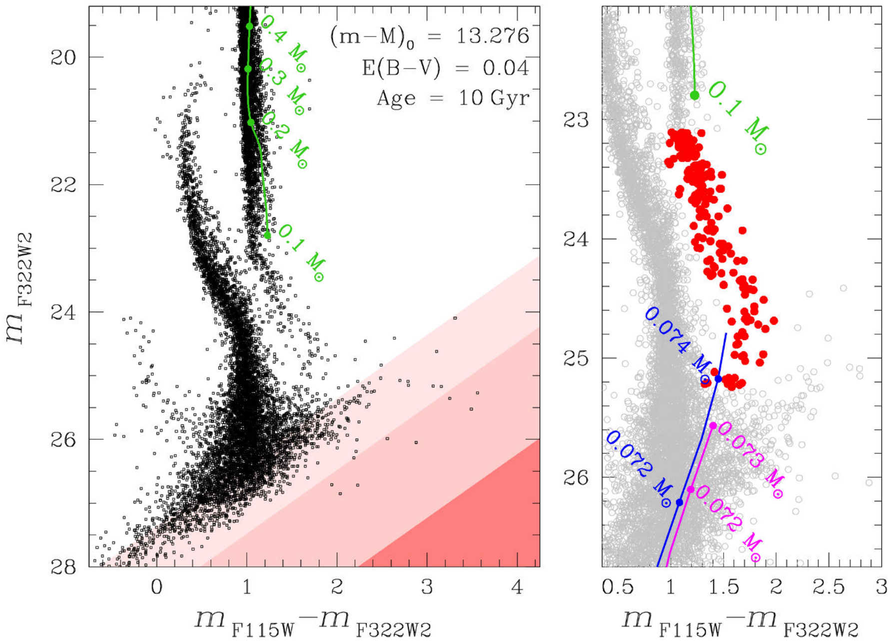

Figure 8.1: Left panel: $m_{\rm F322W2}$ versus $m_{\rm F115W} - m_{\rm F322W2}$ CMD for all the well measured stars in the *JWST* field. Green line represents the 10 Gyr `BaSTI-IAC` isochrone. Shaded regions are our detection limits in both the filters: dark red corresponds to the background noise (1σ) converted in magnitude, middle and light red are the 3σ and 5σ limits, respectively. Right panel is a zoom of the CMD around the region where the high-mass BDs are expected. We highlighted in red objects whose mass should be between 0.07 and 0.1 $M_\odot$. In blue and magenta are reported the solar-metallicity BD 10 Gyr isochrones (ATMO2020 CEQ and NEQ strong models, respectively) from Phillips et al. (2020).

ably, the most probable finding of *JWST* will be the complete characterisation of GCs down to the entire lowest masses along the Main Sequence (MS), and in the so far unexplored regions of brown dwarfs (BDs).

BDs are objects that do not have enough mass to fuse Hydrogen in their cores and instead contract to the size of Jupiter, cooling and dimming over time (Hayashi and Nakano (1963) and Kumar (1963)). While thousands of BDs of Solar metallicity have been identified and studied near the Sun and in nearby young clusters and associations (Best et al. (2021), Kirkpatrick et al. (2019) and Rebolo et al. (1995)), they have not yet been observed in GCs despite dedicated searches (Dieball et al. (2016, 2019)). Identifying BDs in old and metal-poor GCs would greatly improve our knowledge of BDs and GCs. Indeed, the chemical composition of BDs has a major impact on their properties. For example, the mass at the Hydrogen burning limit (HBL) is set by the internal opacity and metallicity: metal-free BDs have higher HBL mass ($0.090\,M_{\odot}$) than BDs of Solar abundance ($0.072\,M_{\odot}$; Saumon et al. (1994)). Cooling is also affected by the chemical composition through opacity. Low temperatures allow for the formation of complex molecules in BDs' atmospheres, which in turn, affect significantly their spectra (Birky et al. (2020)). As BDs cool down (i.e., age), they increasingly separate in luminosity from stars. In the case of the extreme ages of GCs (>10 Gyrs), a significant *gap* in luminosity is expected, the width of which depends on the interior equation of state and low-temperature fusion processes. Studies of GCs with the *HST* have identified the beginning of this gap, but the most massive BDs (the brightest) at the bottom of the gap have not been detected yet. It is expected that the capabilities of *JWST* will reach these BDs in GCs, allowing for an independent measurement of the age of GC populations through the HBL gap (Caiazzo et al. (2017, 2019)).

Concerning the multiple population phenomenon observed within GCs (Bastian et al. (2019), Nardiello et al. (2015, 2018a) and Piotto et al. (2015)), particularly in the most massive and dynamically less evolved ones (Bedin et al. (2004), Piotto et al. (2007) and Siegel et al. (2007)), BDs can provide important information. Indeed, BDs are highly sensitive to variations in composition and can serve as amplifiers of these differences, which can help to fine-tune models of the atmospheres of ultra-cool stars and sub-stellar objects of different masses, ages, and chemical properties. This can help relate the properties of observed stellar populations at higher masses, in order to better understand the observed differences in chemical compositions among multiple generations of stars, which are not yet fully understood (Renzini et al. (2015)).

In this letter, we derived photometry and astrometry for the coolest stellar objects ever observed in a GC, possibly unveiling for the first time the brightest part of the BD sequence in a GC.

8.2 Observations and data reduction

The data employed in this paper are *JWST* public archival material which was compromised by technical problems. The program is GO-2560 (PI: Marino) which focus on characterizing multiple stellar populations in very-low mass M-dwarfs of the relatively close and massive Galactic GC 47 Tucanæ (NGC 104). Visit 13 of GO-2560 suffered of a guide star acquisition failure, that has resulted in imperfect images. These images were judged unsuitable for the main science of that program and requested (and approved) to be repeated in June 2023. The discarded data,

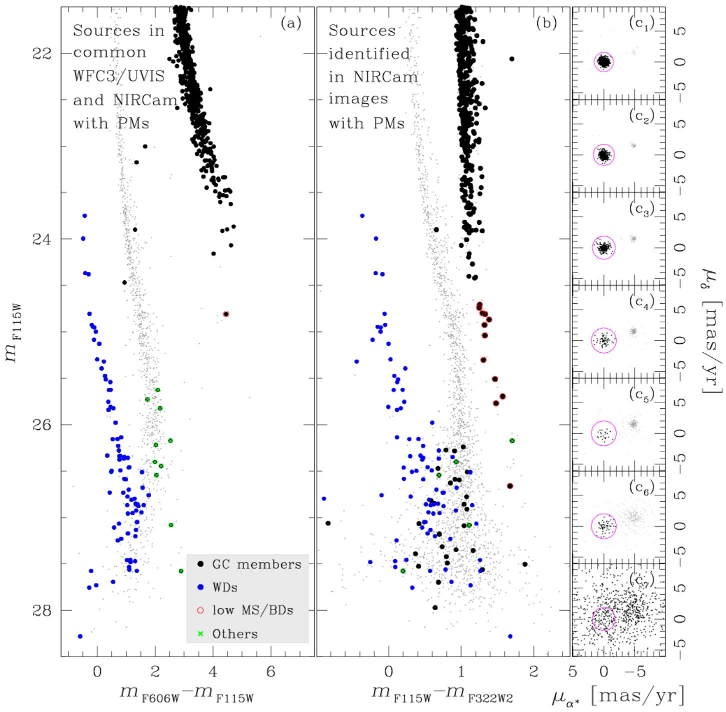

Figure 8.2: Identification of 47 Tuc's members through PMs. Panel (a) shows the $m_{\rm F115W}$ versus $(m_{\rm F606W} - m_{\rm F115W})$ CMD, used to identify likely WDs (in blue) and faint objects visible in the F606W band (green crosses). These selections are used to exclude some candidate low MS/BDs (in red) in the $m_{\rm F115W}$ versus $(m_{\rm F115W} - m_{\rm F322W2})$ CMD of panel (b), that shows all the stars identified in the *JWST* data and for which we measured PMs with F606W, F110W, and F160W images. Panels (c) illustrate the PMs in the magnitude intervals corresponding to the ordinate axis of panels (a) and (b); black stars in the magenta circles are the likely GC members.

according to STScI policies, becomes immediately public.

The data for this article was collected using the Near Infrared Camera (NIRCam) on *JWST* and centred on a region located about 6 arcmin from the 47 Tuc's centre. The observations took place on July 13–14, 2022 and utilised two filters: F115W (short wavelength) and F322W2 (long wavelength); 40 exposures of 1030.7s were taken with each filter, using the `DEEP8` readout mode. The observations were collected with two large dithers to fill gaps between the detectors within a module, but not the gap between the two modules.

In our efforts to extract optimal astrometric and photometric capabilities of *JWST* cameras (Griggio et al. (2023a) and Nardiello et al. (2022)), we searched the archive for dense stellar fields, and quickly realised that these failed images are an optimal benchmark to test our algorithms. Our procedures derive completely empirical effective PSFs (ePSFs) of any shape, and rely on well-characterised geometric distortion for the cameras. In the following, we briefly describe the data reduction. First, taking advantage of the large dithers of the images and of the geometric distortion solution obtained by Griggio et al. (2023a), we extracted a grid of 5×5 library ePSFs both for the F115W and F322W2 filters, following the procedure described by Nardiello et al. (2022). By using the brightest and most isolated stars in each image, we perturbed the ePSFs to take into account their time variations and we used them to obtain positions and fluxes of the sources detected in any given image (we refer to this as *first-pass* photometry). For each filter, we transformed positions and magnitudes in a common reference frame, defined by the Gaia DR3 catalogue (Gaia Collaboration et al. (2021)) and the first image in each filter. We used images, perturbed ePSFs, and transformations to carry out the so-called *second-pass* photometry, by using the `KS2` software, developed by J. Anderson (Anderson et al., 2008b), which was employed and described in several works (e.g., Bellini et al. (2017), Nardiello et al. (2018b) and Scalco et al. (2021)), and here adapted to NIRCam images. This routine, analysing all images simultaneously in a consistent reference frame, allows us to go deeper than the first-pass photometry and to detect extremely faint sources which would be otherwise lost in the noise of individual exposures. We carefully cleaned the final catalogue from the artifacts and bad sources (in part due to the imperfection of the images) by using the quality parameters output of the `KS2` routine (Anderson et al., 2008b). Calibration of the instrumental magnitudes were obtained as in Nardiello et al. (2022).

In this study, we made also use of the partially overlapped *HST* Wide Field Camera 3 (WFC3) optical and IR observations collected during the GO-11677 (PI: Richer, Kalirai et al. (2012)) in F606W, F110W, and F160W. Astro-photometric catalogues were obtained from this data-set following the data reduction procedure described by Nardiello et al. (2018b) and Bedin and Fontanive (2018, 2020).

8.3 Colour-magnitude diagrams & motions

In spite of the degradation suffered by these *JWST* images, our procedures were able to recover exquisite photometry and astrometry, which allowed us to undertake an independent investigation –on a quite different subject– off the nominal main goal of program GO-2560. In this paper we present our study of the BDs of 47 Tuc.

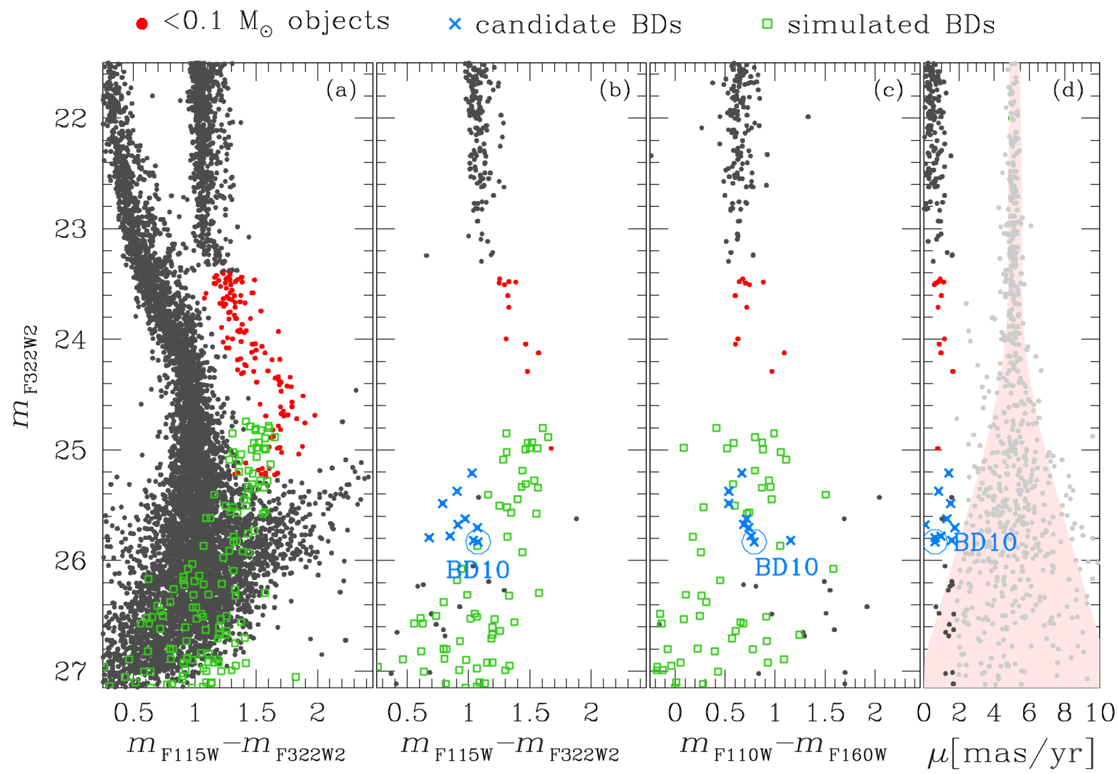

Figure 8.3: Comparison between simulated BDs (green squares) and observed CMDs. In panel (a), all the stars measured in the *JWST* images are plotted in black, while in red are indicated objects consistent with mass $< 0.1\ M_{\odot}$. In next three panels to the left, for clearness purposes, we do not show those WDs clearly identified in Fig. 8.2. Panels (b) and (c) show the $m_{\rm F322W2}$ versus $(m_{\rm F115W} - m_{\rm F322W2})$ and the $m_{\rm F322W2}$ versus $(m_{\rm F110W} - m_{\rm F160W})$ CMDs, respectively, for the stars with proper motions in agreement with the mean cluster's motion. Azure crosses are the candidate BDs we identified in this study. Panel (d) shows the proper motion distribution referred to the mean cluster's motion. The shaded, rose region contains the stars whose proper motion is within 2σ from the mean motion of the SMC's stars. The azure circle is the faintest candidate BD we found, whose multi-filter finding charts is shown in Fig. 8.4.

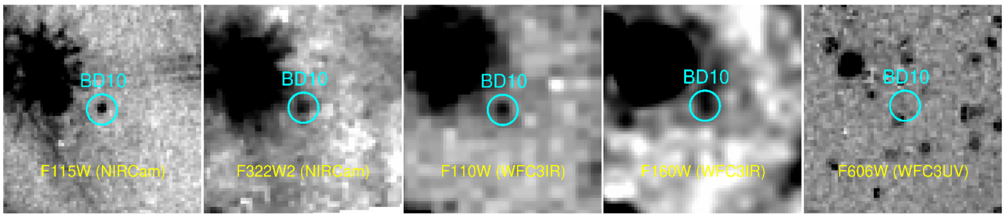

Figure 8.4: Finding charts of the faintest candidate BD found in this paper. The star is visible in all the adopted IR bands, but not in the optical band F606W, as expected for a BD.

In left-panel of Figure 8.1 we show the $m_{\rm F322W2}$ versus $m_{\rm F115W} - m_{\rm F322W2}$ CMD for the all stars in the field, where the cluster's lower MS, the white dwarf (WD) sequence, and the Small Magellanic Cloud (SMC) MS are all well populated and clearly defined. Shaded regions show the 1, 3, 5 σ floor-noise level (computed as described in Bedin et al. (2023)). We overlapped (in green) a `BaSTI-IAC` 10 Gyr isochrone (Hidalgo et al. (2018) and Pietrinferni et al. (2021)) to the MS of 47 Tuc. We used the distance modulus $(m-M)_0 = 13.276$ tabulated by Vasiliev and Baumgardt (2021) and the reddening $E(B-V) \sim 0.04$ as reported by Harris (1996). Beside usual uncertainties of models in reproducing the observed very low-mass MS stars, it is also clear that the lower MS of 47 Tuc (down to $m_{\rm F322W2} \sim 23$) is far from being well represented by a single stellar population (as expected). A more detailed analysis of the multiple population phenomenon in the lower MS of 47 Tuc will be the subject of a future article (Nardiello et al. in prep.). These theoretical models end at the lower limit $M = 0.1 M_\odot$ at magnitude $m_{\rm F322W2} \sim 23$.

In right-panel of Fig. 8.1 we highlighted in red the stars that are likely cluster members and have masses $M < 0.1\ M_\odot$. To interpret the sub-stellar objects we employed the BD tracks by Phillips et al. (2020, ATMO2020) and computed 10 Gyr isochrones for solar-metallicity BDs (being not available to us BDs models at 47 Tuc metallicities). The line in blue shows the isochrone obtained from chemical equilibrium atmosphere (CEQ) models, while the one in magenta shows the one obtained employing atmosphere with non-equilibirum chemistry and 'strong' mixing (NEQ strong). Although these models do not reflect the exact chemistry of the stars in 47 Tuc, it is possible to note that the most massive BDs ($M > 0.07\ M_\odot$) positions on the CMD are consistent with the observed sources highlighted in red.

In order to verify the cluster membership of these low-mass stars (indicated in red in Fig. 8.1), and the membership of even fainter stellar-object (which are completely lost in the MS of the SMC in these CMDs), we reduced deep *HST* observations collected with the WFC3 (see Sect. 8.2). These early epochs, along with the new *JWST* positions, were then employed to compute the relative proper motions (PMs) as in Bedin et al. (2014), by using 47 Tuc's stars as reference system for the motion, and MS stars as reference for the local transformations. The average temporal baseline between the two epochs is $\Delta t = 12.4$ years. The resulting PMs are reported in panels (c) of Fig. 8.2: we selected the likely cluster members by tagging the stars inside the magenta circles as sources with a proper motion in agreement with the cluster motion. Very red, cool objects are not visible in the $m_{\rm F115W}$ versus $(m_{\rm F606W} - m_{\rm F115W})$ CMD, and we used this CMD (panel (a) of Fig. 8.2) to identify, among the likely cluster members, the WDs (in blue) and other faint objects that can not be low MS stars/BDs (in green). In panel (b) we show the stars for which we have proper motions; likely WDs and other objects are marked as in panel (a), while with a red circle we highlighted $< 0.1 M_{\odot}$ stars and candidate BDs.

In the next section we compare the observed CMDs with synthetic CMDs obtained from theoretical models.

8.4 Comparison with theoretical isochrones

To obtain a qualitative estimate of the expected number of BDs at different magnitudes and their approximate location in the CMD, we first derived the mass-function (MF) for the observed MS stars, employing the `BaSTI-IAC` models. The derived masses turned-out to be rather flat in the mass range 0.15-0.35 $\rm M_{\odot}$. We then extrapolated this derived flat MF value down to the BDs mass range (0.015-0.075 $\rm M_{\odot}$), and computed a synthetic CMD (ignoring completeness) by employing the only BD isochrones at our disposal (described in previous section), which however are for Solar metallicity. To generate the synthetic CMD we proceeded as follows: we first generated a random $\log_{10}$(Mass) in the interval [−1.8,−1.12] following a uniform distribution. For each random mass we associated a magnitude in the *JWST* and *HST* filters using the BDs models, linearly interpolating between the two nearest theoretical points. We then added a random noise in magnitude with errors as estimated from the real data.

Synthetic BDs are shown with green symbols (squares) in Fig. 8.3, while the observed sources with black points. Panel (a) shows all the observed stars, while panels (b) and (c) only the sub-sample of the observed stars with an estimate for the PMs, for the CMDs $m_{\rm F322W2}$ versus $m_{\rm F115W} - m_{\rm F322W2}$ (*JWST*-only) and $m_{\rm F322W2}$ versus $m_{\rm F110W} - m_{\rm F160W}$ (*HST*-only), respectively. Finally, panel (d) shows the combined 2-D proper motions as a function of *JWST*'s magnitude $m_{\rm F322W2}$. This panel reveals an almost-perfect separation between field objects (mainly SMC stars) and cluster members down to $m_{\rm F322W2} \simeq 26$, below which the membership become less clear. We have identified (and highlighted with azure crosses) a group of ten sources, which had proper motion consistent with the cluster's mean motion, survived to all the selections and were located in the area of the CMDs where BDs with mass of $\sim 0.072 M_{\odot}$ are expected (synthetic BDs in green). We can also exclude that these objects are foreground BDs, as those would be close-by, with considerably large dispersion and high proper motions.

In summary, in this observational effort, we have employed compromised public images collected with NIRCam at the focus of *JWST*, recovering exquisite photometry and astrometry that enable scientific investigations. We used our reduced data to explore the faintest stellar objects in a field of 47 Tuc, where we isolated a group of 10-objects that we identify as candidate BD members of 47 Tuc. Their membership is supported by the following arguments: *(i)* their PMs are consistent with them being cluster members; *(ii)* their location on CMD is qualitatively consistent with the expected location by approximate models; and finally, *(iii)* the observed number of candidate BDs is consistent with the simulated number obtained extrapolating the MS MF into the BD domain, also considering all the uncertainties (models, MF extrapolated, completeness, etc.).

Only adequate *JWST* follow-up observations will be able to confirm the nature of these BD candidates as true members of 47 Tuc, by means of multi-wavelength deep observations and *JWST*-only derived proper-motion.

9. A near-infrared extension of *Gaia* into the Galactic plane[1]

In this chapter we use near-infrared, ground-based data from the *VISTA Variables in the Via Lactea* (VVV) survey to indirectly extend the astrometry provided by the *Gaia* catalog to objects in heavily-extincted regions towards the Galactic bulge and plane that are beyond *Gaia*'s reach. We make use of the state-of-the-art techniques developed for high-precision astrometry and photometry with the *Hubble Space Telescope* to process the VVV data. We employ empirical, spatially-variable, effective point-spread functions and local transformations to mitigate the effects of systematic errors, like residual geometric distortion and image motion, and to improve measurements in crowded fields and for faint stars. We also anchor our astrometry to the absolute reference frame of the *Gaia* Data Release 3. We measure between 20 and 60 times more sources than *Gaia* in the region surrounding the Galactic center. Our astrometry provides an extension of *Gaia* into the Galactic center. We publicly release the astro-photometric catalogs of the two VVV fields considered in this work, which contain a total of ~ 3.5 million sources.

9.1 Introduction

The *Gaia* mission (Gaia Collaboration et al., 2016b) has revitalized many scientific research fields by providing the community with exquisite astrometry and photometry for more than a billion sources. All-sky coverage and astrometric accuracy and precision also make the *Gaia* catalogs among the best resources for technical projects like catalog/image registration to the International Celestial Reference System. The *Gaia* mission in fact provides an absolute astrometric reference frame on the sky, which can be used to derive geometric-distortion corrections for many cameras, as shown by, e.g., Griggio et al. (2022a).

[1]The content of this chapter has been submitted for publication to Astronomy and Astrophysics.

However, *Gaia* suffers from a few shortcomings, one of which being highly incomplete even for bright sources in high-density fields, such as in the proximity of globular clusters or the Galactic bulge (Fabricius et al., 2021). In addition, *Gaia* is limited to sources brighter than $G \sim 21$, which makes it essentially blind in dust-enshrouded regions like those towards the Galactic plane. For these reasons, *Gaia* has limited applications for scientific or technical programs requiring high-precision astrometry for reddened Bulge and Disk objects.

The Galactic bulge is the ideal laboratory to study stellar interactions in high-density environments on galactic scales, providing insights into the early history of the Milky Way (e.g., Barbuy et al., 2018; Fragkoudi et al., 2020; Zoccali, 2019), and astrometry represents a valuable tool to investigate the stellar populations in the Bulge. In particular, proper motions allow to separate Bulge and Disk stars and to identify gravitationally-bound systems such as comoving groups, star clusters and stellar streams (e.g., Garro et al., 2022a; Kader et al., 2022). Moreover, the Galactic bulge is where most of the microlensing events have been discovered – given the high density of sources in the Bulge – and precise astrometry plays a fundamental role in the determination of the geometry of the event and of the masses of the involved bodies (Mróz et al., 2019). Proper motion measurements have also been essential for studies of new and old globular clusters in the Milky Way (Contreras Ramos et al., 2018; Garro et al., 2020, 2022b; Minniti et al., 2017, 2021b), and the accurate measurement of proper motions is key to identify old globular clusters in the vicinity of the Galactic center and to measure their orbital properties (Minniti et al., 2021a, 2023).

The *VISTA Variables in the Via Lactea* (VVV, Minniti et al., 2010) is a near-infrared survey of the Galactic bulge and most of the Disk obtained with the wide-field camera mounted at the Visible and Infrared Survey Telescope for Astronomy (VISTA, located at the Paranal Observatory in Chile). The VVV survey covers ~ 528 sq. deg of some of the most complex regions of the Milky Way in terms of high extinction and crowding. Its extension, VVVx (Minniti, 2018), re-observed the same regions covered by its predecessor, and observed for the first time new areas that were not included in the original VVV plan. The combination of VVV and VVVx data provides an incredible dataset covering about 1700 sq. deg observed between 20 and 300 times, with a temporal baseline of up to 10 years.

The VVV survey is carried out with the near-infrared, wide-field imager VIRCAM (VIsta InfraRed CAMera). VIRCAM is an array of 16 Raytheon VIRGO Mercury Cadmium Telluride 2048×2048-pixels detectors, arranged in a 4×4 grid. The gap between the VIRCAM detectors are 42.5% and 90% of the detector's size along the x and y directions, respectively. This layout allows VIRCAM to cover a

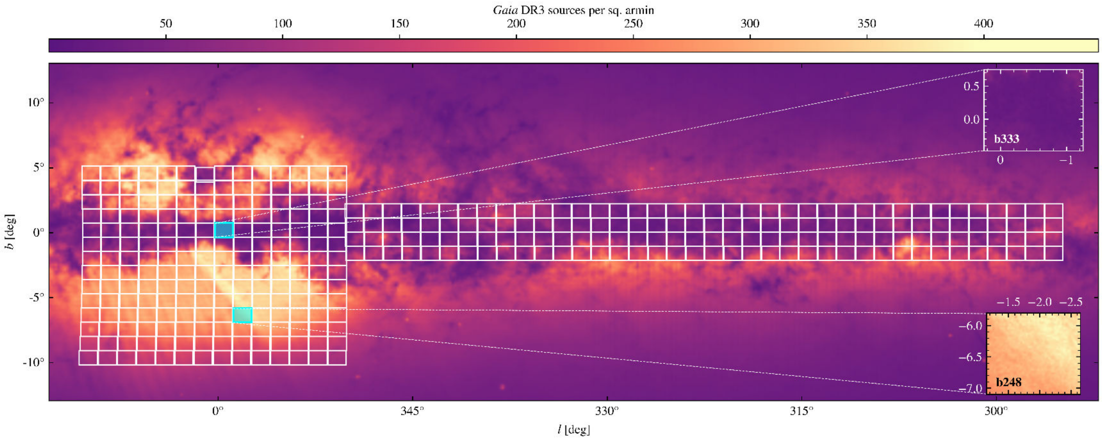

Figure 9.1: *Gaia* DR3 source density around the region covered by the VVV survey. White boxes represent VVV tiles. We highlighted in light blue the two tiles considered in this work, namely `b333` in the Galactic center, and `b248` on the southern Bulge. Density map data taken from the *Gaia* archive.

field of view of 0.6 deg^2 in a single pointing (a "pawprint", following the official nomenclature). The VVV survey observed a given patch of sky (a "tile") with a 3×2 mosaic, covering about 1.4×1.1 deg^2 without gaps. The Cambridge Astronomical Survey Unit (CASU) is responsible for the data reduction, catalog generation, and calibration of both photometry and astrometry (Irwin et al., 2004; Lewis et al., 2010). The survey lasted five years, from 2010 to 2015, and observed the Disk and Bulge between 50 and 80 times in the K_S filter. Additionally, two epochs in Z, Y, J and H filters were acquired at the beginning and at the end of the survey. The VVV and VVVx surveys were mainly designed for photometric variability studies, but their multi-epoch strategy also enables astrometric analyses, as demonstrated by, e.g., Libralato et al. (2015) and Smith et al. (2018).

Libralato et al. (2015, hereafter Paper I) presented a new pipeline to process the VIRCAM data. They used a calibration field centered on the globular cluster NGC 5139 to derive a new geometric distortion (GD) solution for the VIRCAM detector, which enables high-precision astrometry with the VVV data. They reprocessed the data of the VVV tile containing the globular cluster NGC 6656 and derived proper motions with a precision of $\sim$1.4 mas yr^{-1}, using 45 epochs over a time baseline of 4 years.

Smith et al. (2018) presented an astrometric catalog (*VIRAC*) of proper motions and parallaxes for the entire VVV area based on the CASU pipeline data; this catalog contains 312 million sources with proper motions and 6935 sources with parallaxes, and currently represents the largest astrometric catalog derived from VVV. Their proper motions achieve a precision of better than 1 mas yr^{-1} for bright sources, and few mas yr^{-1} at $K_S = 16$. However, their astrometry is not absolute, as they didn't have at the time the *Gaia* all-sky reference frame to anchor their positions. Moreover, uncertainties on the the relative to absolute proper motion calibration limits the accuracy of investigations on large Galactic scales.

In this paper, we use the VVV data (not VVVx) to extend the *Gaia* astrometry to reddened sources in the Galactic plane. In Fig. 9.1 we show the coverage of the VVV survey in Galactic coordinates, superimposed to a source-density map of the *Gaia* Data Release 3 (DR3 Gaia Collaboration et al., 2023) catalog. We highlighted in light blue the two tiles considered in this work, namely `b248` (South-East of the Galactic center) and `b333` (which contains the Galactic center). The density map shows that the number of sources accessible to *Gaia* in the Galactic plane is limited by dust and crowding. As anticipated, this limit makes certain investigations unfeasible in this region, and it is the primary motivation behind our work. We chose these two fields to test our methods in two environments with very different densities of *Gaia* sources: the tile `b248` has about 350 *Gaia* sources per sq. arcmin, whereas the tile `b333` has an average of 25 sources per sq. arcmin. As in Paper I, we use spatially variable empirical point-spread functions (ePSFs; see e.g., Anderson et al., 2006) to precisely measure positions and fluxes of all sources in any given VVV image, and adopt local transformations (Anderson et al., 2006) to collate multiple single-image astro-photometric catalogs, to minimize systematic errors such as residual GD and atmospheric effects, and to achieve the best astrometric precision possible. In addition, we significantly improve over previous efforts by: (i) employing a combination of first- and second-pass photometric stages specifically designed to improve measurements in crowded fields and for faint stars, and (ii), linking our astrometry to that of the *Gaia* DR3 catalog, as done in, e.g., Bedin and Fontanive (2018, 2020) and Libralato et al. (2021).

The paper is organized as follows. In Sec. 9.2 we describe the data reduction process, the construction of the master frame by leveraging on the *Gaia* DR3 catalog and the photometric registration. Section 9.3 provides an overview of the proper motions fit procedure. Section 9.4 shows the consistency of our catalog with respect to *Gaia*. In Sec. 9.5, we compare our results with the current public release of the *VIRAC* catalog (version 1) and we show the improvements enabled by our method. In Sec. 9.6, we present an application of our new data reduction by measuring the parallax of a sample of sources, and compare them with those in the *Gaia* catalog. Finally, in Sec. 9.7 we outline our data reduction strategy and conclude the paper in Sec. 9.8 with a summary of our work.

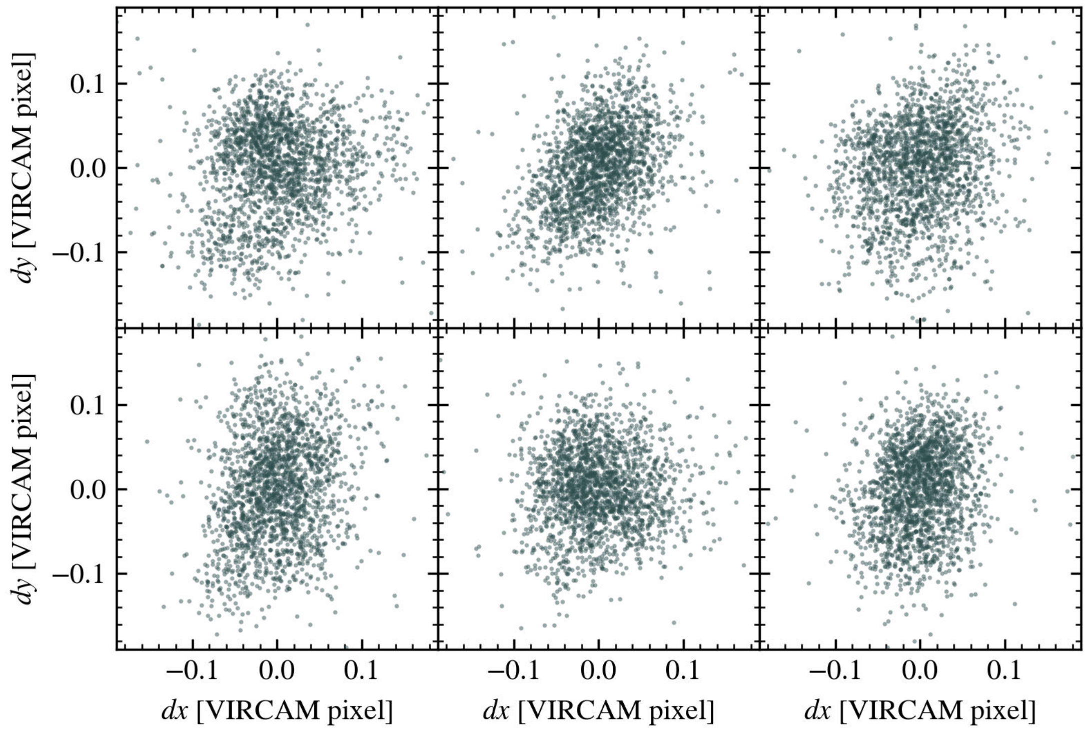

Figure 9.2: Positional residuals obtained by cross-matching the catalogs of a set of consecutive images with *Gaia* after the GD solution derived with the VVV dataset is applied. Notice that the residuals display different trends, preventing precisions of less than ~ 0.1 pixels (~ 35 mas) in a single exposure with this approach.

9.2 Data reduction

In the first stage of the data reduction, i.e. "preliminary photometry", we focus on the bright, unsaturated members. These sources are used to define the master frame by cross-matching their positions with those measured by *Gaia*. Preliminary photometry was obtained as described in Paper I. We started from the pre-reduced images downloaded from the CASU archive and we treated each of the sixteen detectors separately. Our pre-processing routine is responsible for applying a series of cleaning algorithms to flag cosmic rays and mask bad pixels and saturated stars.

For each detector, we derived a 5×5 array of effective point-spread functions (ePSFs) using bright, isolated and unsaturated sources as described by Anderson et al. (2006). We used these ePSF models to measure positions and fluxes of the sources in each image. Our preliminary photometric catalogs contain positions, instrumental magnitudes defined as $-2.5 \cdot \log(\text{flux})$, and a parameter called quality-of-fit (`QFIT`), which represents the goodness of the ePSF-model fit for each star (see, e.g., Anderson et al., 2008a). A `QFIT` values close to 0 represents a good ePSF fit. In our VVV catalogs, bright and isolated sources typically have `QFIT` < 0.15. Bright, unsaturated stars close to saturation (with instrumental magnitudes within ~ -13.5 and ~ -12, depending on the detector) show higher (> 0.2) `QFIT` values. These sources appear to exhibit inaccuracies in their flux measurements also in the *VIRAC* catalog (see Fig. 9.10). What causes these bright stars, which should have a `QFIT` close to 0, to behave differently from the other bright, unsaturated sources is unclear. Nevertheless, we treated them as saturated and excluded the centermost pixels from the ePSF fitting to improve their photometry and astrometry. The threshold used to identify these objects was empirically defined for each detector.

The calibration of the GD cannot be performed via auto-calibration techniques with the VVV data, as the dither pattern is not suited for this purpose (see, e.g., Häberle et al., 2021; Libralato et al., 2014). We attempted to derive the GD solution by exploiting the *Gaia* DR3 catalog, following the procedure described in Griggio et al. (2022a, 2023b). However, given the short exposure time of the VVV images (~ 4 s), we were ultimately limited by the atmospheric image motion. In fact, the minimum exposure time needed to mitigate the impact of large-scale semi-periodic and correlated atmospheric noise, which can adversely affect ground-based astrometry, is approximately 30 seconds, as determined by, e.g., Platais et al. (2006, 2002) or Libralato et al. (2014). To show the effect of image motion, we cross identified the stars in the astro-photometric catalogs of a set of consecutive VVV images and in the Gaia DR3 catalog. Gaia positions were propagated at the epoch of the VVV images by means of the *Gaia* DR3 proper motions and projected on the tangent plane of each VVV exposure. We then used six-parameter linear transformations to transform the GD-corrected positions in each VVV frame on to the *Gaia* reference frame system. Figure 9.2 shows the positional residuals generated by this comparison for a set of consecutive VVV images. Even though these images were taken within less than one minute, the residuals show different trends. Computing the GD solution from these images results into a null mean correction, as the random residuals due to image motion cancel out. For this reason, it is not possible to improve the GD solution derived in Paper I using the VVV data itself. We then corrected the VVV raw positions with the GD solution of Paper I, which we consider more reliable as it was computed from well-exposed images of a calibration field specifically observed to calibrate the GD. We will explain later, in Sec. 9.3, how we mitigated the effect of image motion.

Besides the GD, we also needed to consider projection effects resulting from the large dithers of the images and the wide field of view of VIRCAM (see discussion inPaper I). As a result, images lie in different tangent planes, and we need to account for this as done in, e.g., Griggio et al. (2022a). To do so, after correcting the raw positions with the GD solution, we used the information contained in the `fits` header of each image to project the detector-based coordinates onto equatorial coordinates, as in Bedin and Fontanive (2018), adopting a pixel scale of 0.339 arcsec/px (Paper I). We then projected all positions from all catalogs back into a common plane, using as tangent point the average pointing position of all the images of the same tile. After this procedure, all single-exposure catalogs lie on the same tangent plane.

9.2.1 The master frame

A key step for our goal is the construction of a common reference frame, hereafter "master frame", where we can combine our images. Thanks to the *Gaia* mission, we already have an all-sky, absolute reference frame to which we can anchor our astrometry. We used the *Gaia* DR3 catalog to define the master frame as follows:

- We propagated the *Gaia* positions to the corresponding epoch of each VVV pawprint set using *Gaia* proper motions.
- We projected these adjusted positions onto the same tangent plane adopted for the tile.
- We cross-matched the sources in each single-exposure catalog with those in the *Gaia* DR3 catalog, and derived the coefficients of the six-parameters linear transformations that bring the image-based coordinates onto the *Gaia* absolute reference frame.

9.2.2 Photometric registration

We registered the photometry to the *2MASS* photometric system (Skrutskie et al., 2006) using the *Gaia-2MASS* cross-matched table available in the *Gaia* archive. We selected the best measured sources in both our catalogs and *2MASS*, and use these sources to calculate the photometric zero-points to transform the instrumental magnitudes measured in each single image into the *2MASS* photometric system.

The *2MASS* filter passbands are slightly different from those of the VISTA filters, and a more precise calibration would need to account for several factors, as described in González-Fernández et al. (2018) and Hajdu et al. (2020). However, since in this work we are focused on obtaining high-precision astrometry, we

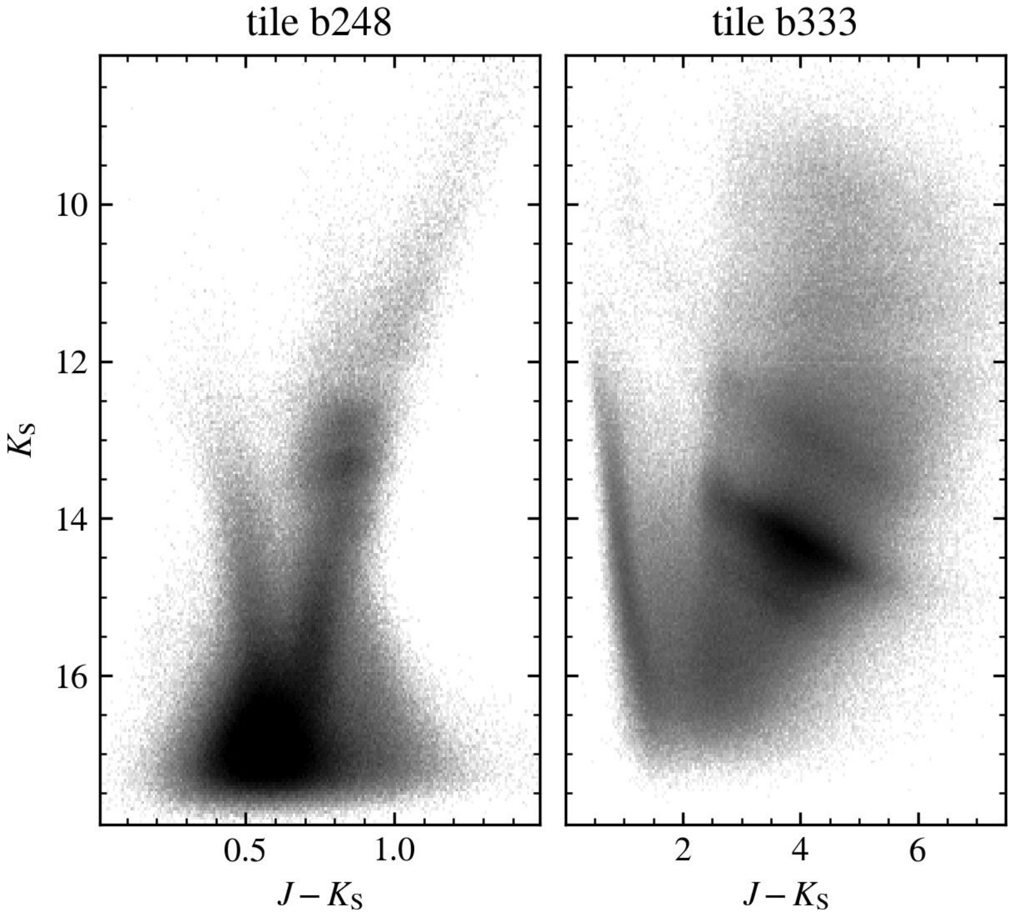

Figure 9.3: Color-magnitude diagrams for tiles `b248` (left) and `b333` (right). See the text for details.

neglected second-order corrections. In fact, the largest term in the photometric-calibration equation between the *2MASS* and VISTA magnitudes is the color term, and it is of the order of few hundredths of magnitudes at most. As such, the correction introduced by this term would be very small. Nonetheless, we plan to perform a more accurate calibration in the next releases, including airmass, extinction and color terms.

9.2.3 Second pass photometry

The "second-pass" photometry has been performed using a version of the software `KS2` (an evolution of the code presented in Anderson et al., 2008b, developed for *HST*), opportunely modified to work with VIRCAM images, and adapted to wide-field imagers by Griggio et al. (2022a, 2023b). The software is designed to obtain deep photometry in crowded fields, by iterating a find-measure-subtract routine, that employs all images simultaneously to improve the finding of faint sources. A description of `KS2` can be found in, e.g., Bellini et al. (2017) and Scalco et al. (2021). Briefly, the flux is measured by fitting the ePSF to the inner 5×5 pixels of the source after subtracting the local sky, using the appropriate ePSF for each image, and then averaged out between all the exposures. Stars measured in the previous iteration are subtracted from the image at each step. The second-pass photometry has been carried out separately for each epoch in the $K_{\rm S}$ filter: we considered as an epoch each set of images taken in the same day. A list of stars (derived from the preliminary photometry) is given as input to the routine, and it is used to construct a weighted mask around bright sources which help to avoid PSF-related artifacts. In addition to the averaged master frame positions, the `KS2` software outputs a file that contains, for each source, the raw position and neighbor-subtracted flux as measured in every single exposure. In addition to positions and fluxes, `KS2` also outputs a few diagnostic parameters (see, e.g., Bedin et al., 2009), that can be used to reject poorly measured sources and detector's artifacts, or to identify galaxies. In addition to the $K_{\rm S}$ exposures, we also performed the second-pass photometry on all the J images of each tile, that we used *only* to build the color-magnitude diagrams. The color-magnitude diagrams of the two tiles analyzed in this work are shown in Fig. 9.3. The non-physical drop in the number of sources around $K_{\rm S} \sim 12$ is due to our quality cut in the `QFIT` parameter: at this magnitude level there is a transition between unsaturated and saturated sources, and it is here where most of the stars showing unexpectedly-high `QFIT` values lie, as discussed in Sect. 9.2. Some of these problematic sources end up being measured as unsaturated as the thresholds that we set to identify these objects are not perfect, resulting in an overall high `QFIT` value.

9.3 Proper motions

Image motion poses a severe limitation to the astrometric precision achievable with VVV data. Indeed, it leads to local systematic position errors whose pattern changes even between subsequent exposures, up to ~ 0.15 pixels (~ 50 mas, see Fig. 9.2). This is far more than the single-measurement astrometric precision enabled by the GD solution, which have been shown to reach ~ 8 mas (Paper I). We employed a local mitigation to the effects of image motion through a so-called "boresight" correction (see, e.g. Anderson and van der Marel, 2010). Our correction leverages on the *Gaia* catalog, as it provides a sufficient number of reference *Gaia* sources even in extincted regions towards the Galactic center. The number

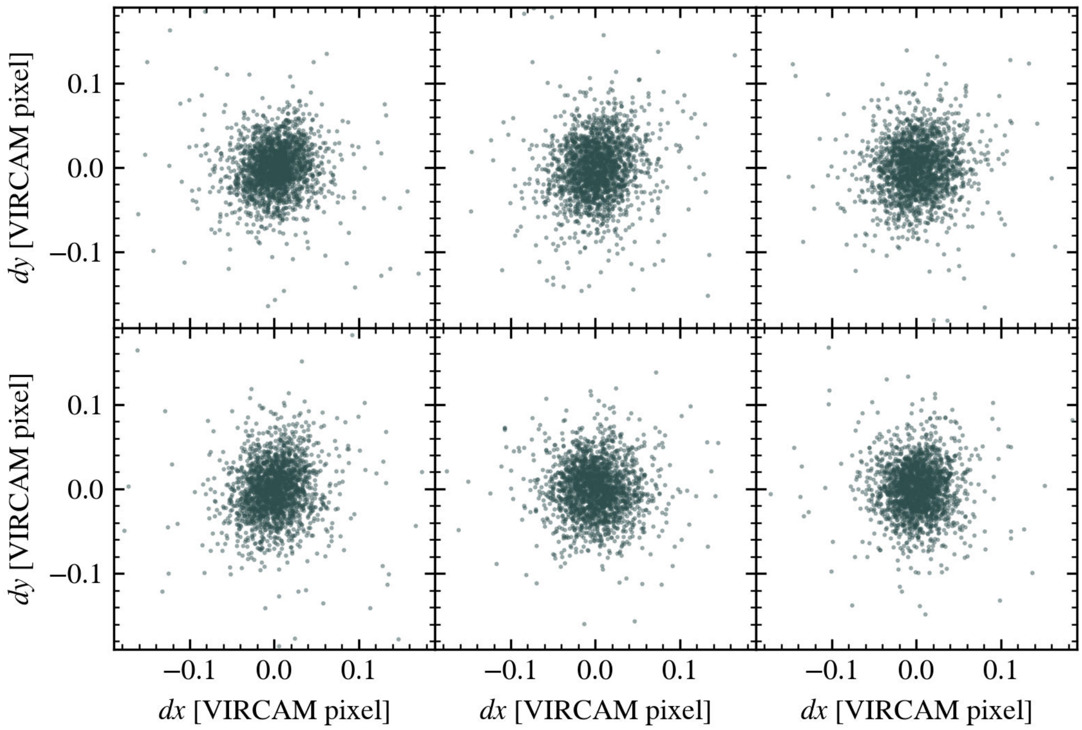

Figure 9.4: Similar to Fig. 9.2, but after the boresight correction is applied. The dispersion of the residuals is about 0.035 pixels (~ 12 mas) along each coordinate.

of neighboring reference sources for the correction is a compromise between the need for high statistics and for the correction to be as local as possible, even in regions where the Gaia source density is low. We achieved this by requiring at least 15 reference sources within a circular region of radius at most 300 pixels (and at least 50 pixels) from the target source,

For each epoch, we calculated the mean position of each source as follows:

- we applied the GD correction to the raw positions of the sources in each image;
- we projected the corrected positions onto the sky, and then we project them back onto the common tangent plane of the tile;
- using well-measured sources in common with *Gaia* (excluding the target), we computed the transformations to bring the positions from the tangent plane to the master frame;

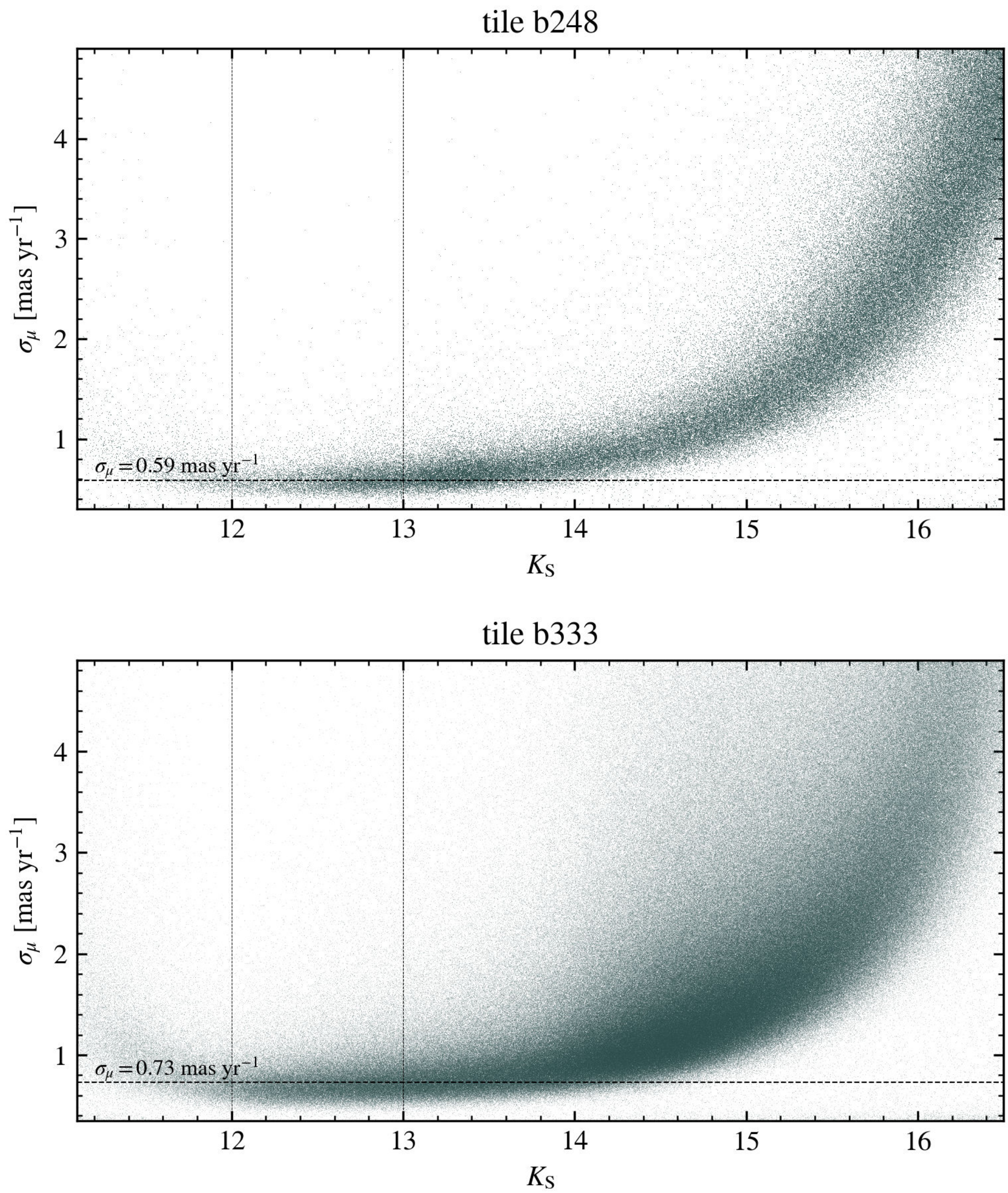

Figure 9.5: Total proper-motion errors for sources in tile `b248` (top) and tile `b333` (bottom) as a function of the K_S magnitude. The horizontal line represents the median error of the sources in the range $12 < K_\mathrm{S} < 13$.

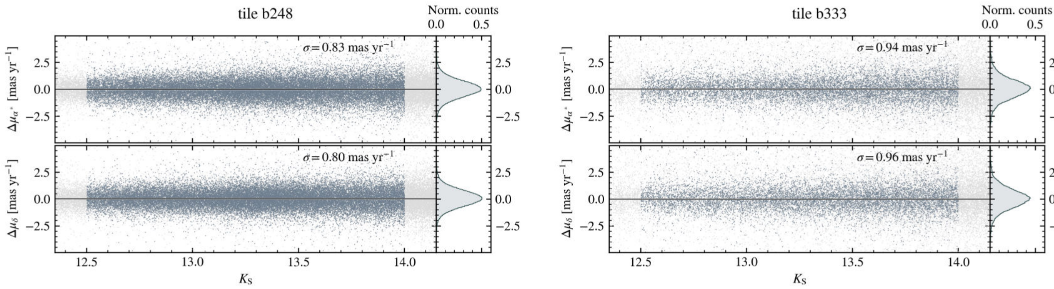

Figure 9.6: Comparison between proper motions computed in this work and *Gaia* proper motions for tile `b248` (left) and tile `b333` (right). The black line is the median offset, calculated using the sources in dark grey.

- for each star, we selected the neighboring sources in common with *Gaia* in each image, and we calculated the residuals between their positions transformed into the master frame and those given by *Gaia* (again, excluding the target star). The mean residual gives the boresight correction for each star of each image.

- We then transformed the positions of the target star as measured in the single images into the master frame, and apply to these values their boresight correction.

- Finally, we calculated the average position, to which we associate the error on the mean as an estimate of the uncertainty.

Figure9.4 is similar to Fig. 9.2, but with the positional residuals computed after the image-motion correction is applied. It is clear that the distribution of the residuals is much tighter than before, with a dispersion of about 12 mas in each coordinate in a single exposure, a value that is compatible with the results obtained in Paper I.

Proper motions were obtained by via a maximum likelihood approach using the affine-invariant Markov Chain Monte Carlo method `emcee` (Foreman-Mackey et al., 2013), to sample the parameter space. This approach allows us to obtain the posterior probability distribution functions for the quantities μ_x, μ_y, x_0, y_0, where μ_x, μ_y are the displacements in the x and y directions, and x_0, y_0 are the positions at the reference epoch t_0, that we set to be $t_0 = 2013.0$. We ran the Markov Chain Monte Carlo with 32 walkers, performing 5000 steps, with 200 burn-in steps, allowing some scaling on the positional errors as an additional free parameter to be fitted. The medians of the probability distribution functions give our final estimate of μ_x, μ_y, x_0, y_0, and the errors on these quantities were computed as the average

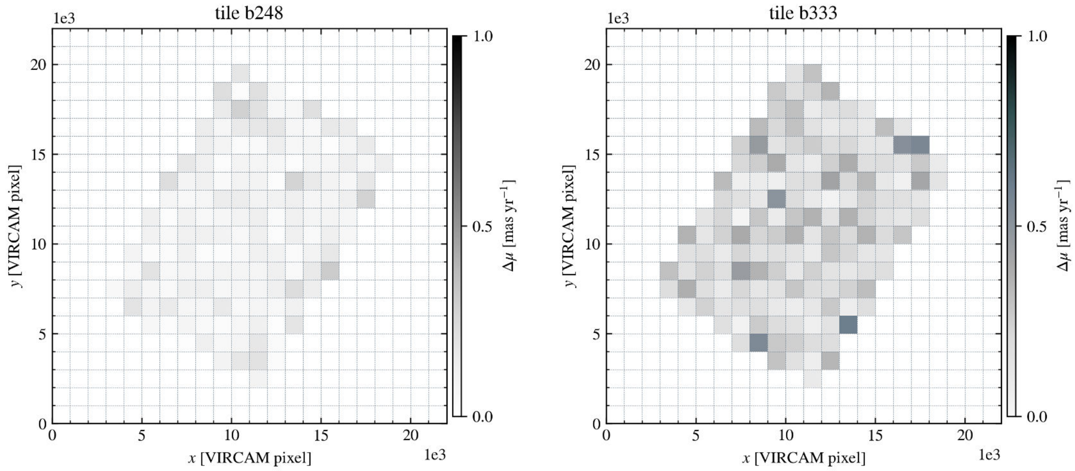

Figure 9.7: Similar to Fig. 9.6, but as a function of position for tile `b248` (left) and tile `b333` (right). Each region is color-coded according to the 3σ-clipped median value of the absolute deviation between *Gaia*'s and our proper motions, according to the color bars on the right of each panel.

between the 16$^{\text{th}}$ and 84$^{\text{th}}$ percentiles of the samples in the marginalized distributions. The displacements in pixel yr^{-1} are converted in $\mu_{\alpha*}, \mu_\delta$ by multiplying by the pixel scale that we adopted (0.339 arcsec pixel^{-1}), as the master frame axes are already oriented as North and East. At odd with the *VIRAC* proper motions, which are relative, our proper motions are naturally defined on an absolute system, since their computation is based on the *Gaia* reference frame.

Figure 9.5 presents the total proper motion ($\mu^2 = \mu_{\alpha*}^2 + \mu_\delta^2$) errors as function of the K_S magnitude, obtained by propagating the errors on the two components. Given the extreme crowding environment of the Galactic center, proper-motion errors of tile `b333` are larger than those of tile `b248`: the median proper-motion error of sources in the range $12 < K_\mathrm{S} < 13$ – i.e. best measured sources – is 0.59 mas yr^{-1} in tile `b248`, compared to 0.73 mas yr^{-1} in tile `b333`. Sources with $K_\mathrm{S} \gtrsim 12$ are close to saturation/non-linearity regime, and thus their proper-motion errors tend to increase.

9.4 An extension of *Gaia* into the Galactic plane

Our astrometry is, by construction, linked to the *Gaia* absolute reference frame. We can see the consistency between *Gaia*'s and our proper motions in Fig. 9.6, where we show the residuals between the two datasets, $\Delta\mu_{\alpha*}, \Delta\mu_\delta$, for tile `b248`

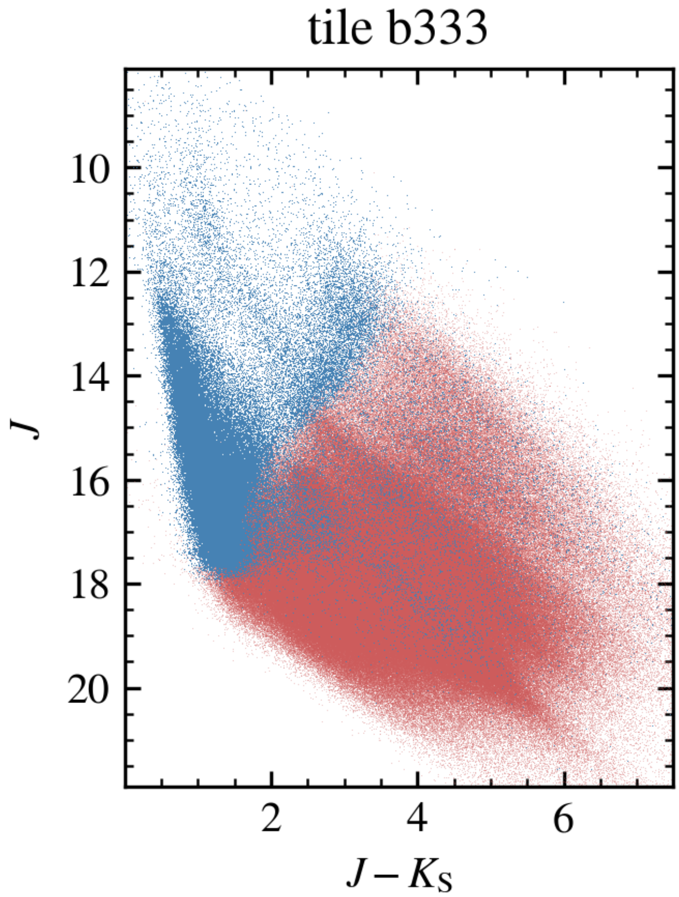

Figure 9.8: The J versus $(J - K_{\rm S})$ color-magnitude diagram of the sources in tile `b333`; blue sources are those also present in the *Gaia* catalog.

(left) and tile `b333` (right). The normalized histograms of the residuals are shown in the right panel of the plots. Dark gray points are the sources with proper-motion errors smaller than $2\,{\rm mas\,yr^{-1}}$, $K_{\rm S}$ magnitude between 12.5 and 14, *Gaia* G magnitude between 13 and 18, and measured in at least four individual images[2]. These objects represent well-measured sources in both sets. The horizontal black line represents the median residuals calculated using the dark grey sources. The standard deviation of the residual distributions are reported on the top right corner of each plot. Given the essentially negligible errors of the *Gaia* proper motions

[2]This restriction excludes sources near the tiles' borders that, as a result of the VVV dither pattern, are covered by less than four exposures. In future releases, we plan to use the data of adjacent tiles to increase the depth of coverage and measure proper motions in these regions.

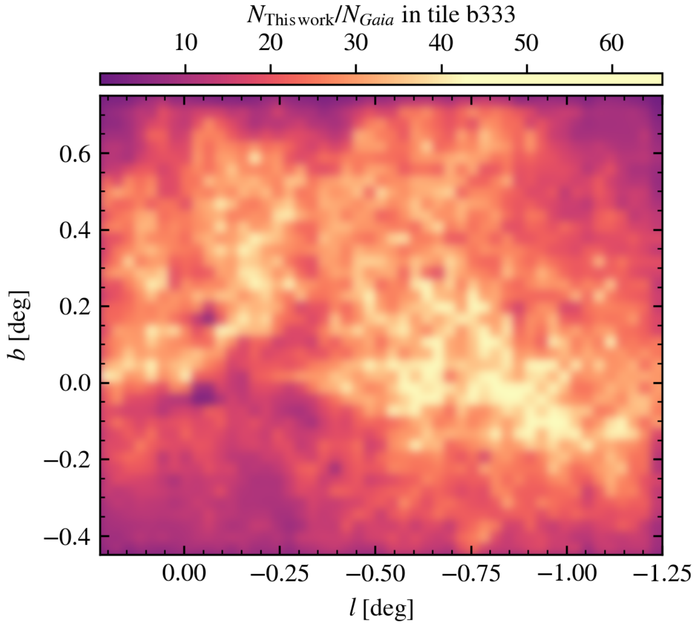

Figure 9.9: Color map of the number of sources in our catalog with respect to those in *Gaia*'s for tile `b333` in Galactic coordinates. See the text for details.

with respect to ours, the dispersion can be attributed to the random errors on our astrometry. In this regards, we notice that the dispersion is slightly larger than the proper motions errors obtained by our fit as shown in Fig. 9.5 for sources with $K_S < 14$, suggesting a possible underestimation of the proper-motion errors.

In Fig. 9.7 we show the local deviations between *Gaia*'s and our proper motions. We divided the field in $\sim$1000$\times$1000 pixel regions and, for each region, we calculated the 3σ-clipped medians $(\bar{\Delta\mu}_{\alpha^*}, \bar{\Delta\mu}_\delta)$ of the proper-motions residuals. We then computed the quantity $\bar{\Delta\mu}^2 = \bar{\Delta\mu}_{\alpha^*}{}^2 + \bar{\Delta\mu}_\delta{}^2$ using only well-measured sources, i.e. dark grey points of Fig. 9.6. From the left panel of Fig. 9.7, we can notice that the proper motions of tile `b248` are in very good agreement with *Gaia*, and, as expected, the $\bar{\Delta\mu}$ distribution across the tile is flat, with negligible local systematic deviations. The right panel for the tile `b333` instead shows hints of some spatially-dependent systematic errors. We verified that these systematics correlate with the density of *Gaia* sources in each region, with larger deviations corresponding to regions with very low density. This correlation is expected as our technique relies on a local net of *Gaia* sources to compute the boresight correction. Except for these regions with fewer *Gaia* sources, our proper motions for the tile `b333` are in good agreement with those in *Gaia*, with slightly larger residuals with respect to those exhibited by the tile `b248`, given smaller *Gaia* source density in tile `b333`.

Our independent reduction of the VVV fields allows us to extend the *Gaia* astrometry to the dense and obscured regions of the Galactic plane, providing significantly more new sources with positions and proper motions than what is available from the *Gaia* DR3 catalog in the same region. Figure 9.8 shows a J versus $(J - K_S)$ color-magnitude diagram of the sources in tile `b333`. Blue points represent stars in common with the *Gaia* DR3 catalog. All other objects are in red. It is clear that a large number of sources are not present in the *Gaia* catalog. Our catalog of tile `b333` contains more than 2 millions sources with proper motions and only $\sim$10% of them are present in *Gaia* DR3. In Fig. 9.9 we show, for the same tile, the ratio between the number of sources in our catalog and those in *Gaia*. We used all the sources in our catalog and all the sources in the *Gaia* catalog to calculate this ratio. We computed the values binning the data into $\sim$3 sq. arcmin bins and smoothing out with a Gaussian kernel. In the Galactic center we detect on average $\sim$20 times more sources than *Gaia*, with regions where this values goes up to $\sim$60.

9.5 Comparison with *VIRAC*

As a further cross-check, we compared our astrometry with the current public release of the *VIRAC* catalog (Smith et al., 2018). We cross-matched the *Gaia* and *VIRAC* catalogs together, and performed the same comparisons that we described in the previous section. First, in Fig. 9.10, we show the color-magnitude diagrams of the two tiles built using all the sources in the *VIRAC* catalog. A comparison between their color-magnitude diagrams and the ones in Fig. 9.3 shows that our photometry is less affected by saturation effects. Figure 9.11 is similar to Fig. 9.6, but for *VIRAC* sources. Dark grey points represent the sources with proper-motion error smaller than 2 mas yr^{-1} and with $12.5 < K_S < 14$, and with the flag `reliable` = 1 in the *VIRAC* catalog, which exclude bad detections and poorly measured stars. We notice that, apart from a global offset with respect to *Gaia*, the dispersions of the residuals are just slightly larger than ours. Since the formal proper motion errors given by the *VIRAC* catalog are marginally smaller than ours, we suspect that also *VIRAC* proper-motion errors might be underestimated. Finally, in Fig. 9.12, we show the distribution of the residuals across the field of view, for both tile `b248` (left) and `b333` (right). Both tiles present significantly larger scatter compared to our work (cfr. Fig. 9.7), with systematic trends that depend on position. Notice that *VIRAC*, conversely to our work, does not depend

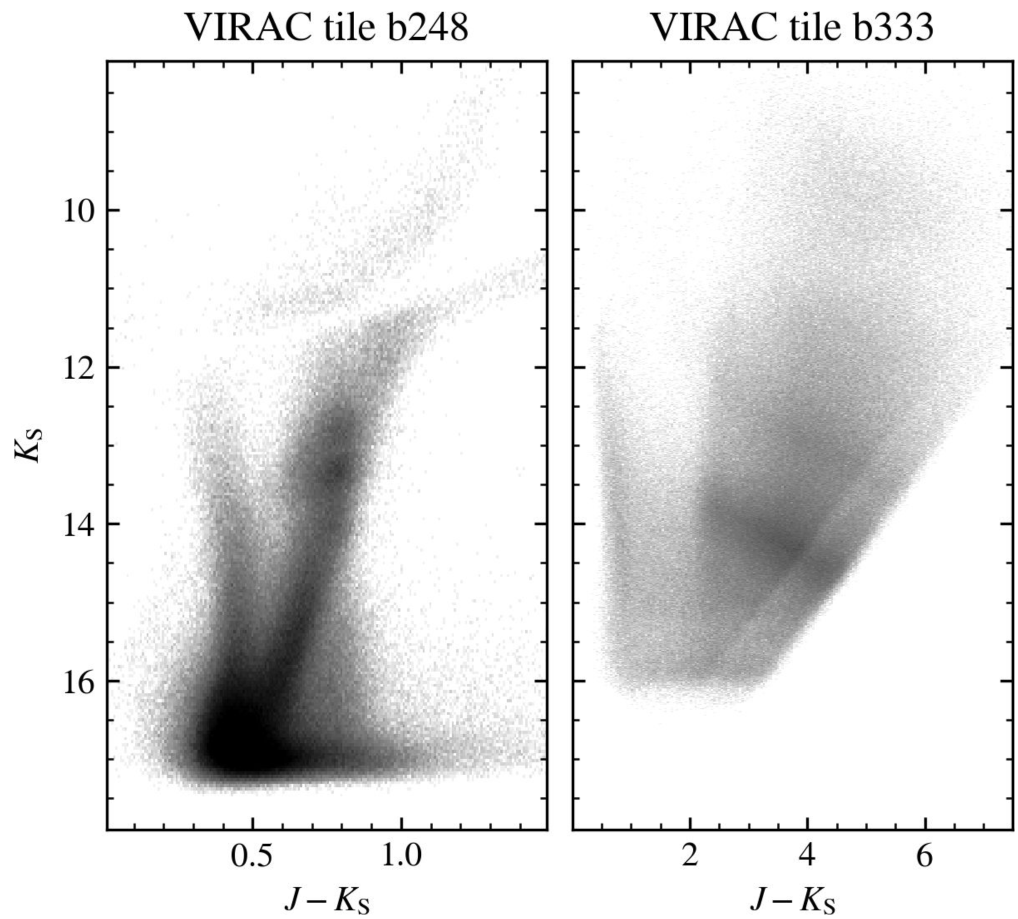

Figure 9.10: Similar to Fig. 9.3, but for *VIRAC* sources.

on *Gaia*, and as such their systematic errors cannot be attributed to the density of *Gaia* sources. As pointed out in Smith et al. (2018), *VIRAC* proper motions are relative to the average motion of sources within a few arcminutes, and in regions with large spatial variations in the extinction, the bulk motion of the reference stars can be different.

In summary, this work represents a step forward with respect to *VIRAC*, and the most notable improvements are: *(i)* a larger number of sources with proper motions, mainly thanks to second-pass photometry; *(ii)* significantly better astrometric precision (about 20-30%) thanks to improved PSFs, GD and image-motion correction, and *(iii)* improved accuracy thanks to the registration to the absolute reference system of *Gaia* DR3, which was simply not available at the time of the *VIRAC* release.

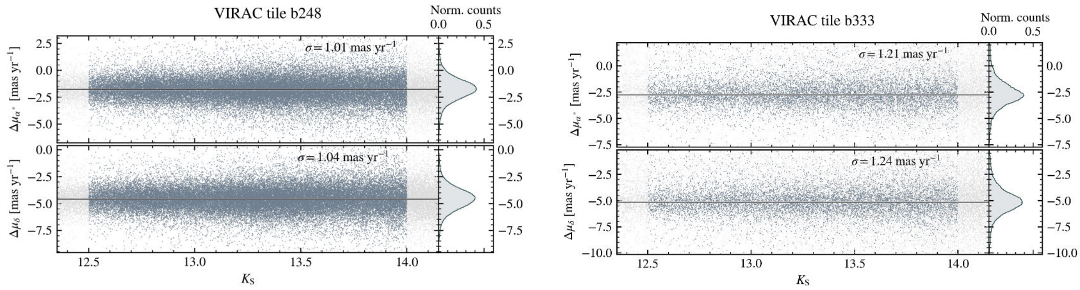

Figure 9.11: Similar to Fig. 9.6, but for *VIRAC* sources.

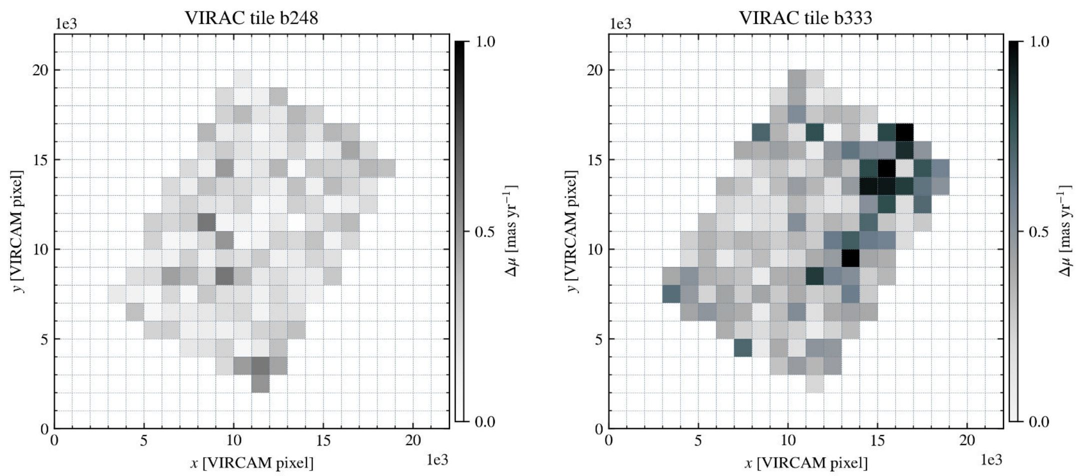

Figure 9.12: Similar to Fig. 9.7, but for *VIRAC* sources.

As a final remark, our work uses independent tools from those of *VIRAC*, and can be leveraged for potential validations/benchmarks for the upcoming *VIRAC* version 2 (Smith et al., in preparation).

9.6 Parallax fit

The relatively high cadence of observations within the VVV dataset also enables the measurement of parallaxes, at least for sources close enough to the Sun, so that the effect of the parallax on their apparent motion can be effectively disentangled from that of random positional errors. We tested our parallax fitting procedure on a sample of sources in common with *Gaia*; in particular, we selected well-measured sources with positions determined in at least 20 epochs, a time baseline of at least 3 years, a proper motion error smaller than 2 mas yr^{-1} and with *Gaia* parallax larger than 5 mas (distance $<$ 200 pc). The parallax fit was performed using the `Python NOVAS` libraries (Barron et al., 2011), adopting the same procedure as in Bedin et al. (2017). Briefly, we calculated the `NOVAS` predicted source positions at each epoch for a given $\alpha_{2000}, \delta_{2000}$, proper motion and parallax, where $\alpha_{2000}, \delta_{2000}$ are the positions at epoch 2000.0. We then computed the differences between these positions and those measured by us, and we look for the astrometric solution that minimizes these differences, using the same MCMC approach that we employed for the proper motion fit.

In Fig. 9.13, we show an example of the parallax fit, for four selected sources (two per tile). We report in the plot the fitted proper motion and parallax values, together with the values given in the *Gaia* DR3 catalog. Sources in Figs. 9.13a and 9.13c are in agreement within 2σ, while those in Figs. 9.13b and 9.13d are compatible within 1σ with the *Gaia* parallaxes.

9.7 Data reduction strategy and access

We plan to process the entire VVV dataset starting from the innermost Bulge fields. However, we will also accept requests from the astronomical community to prioritize particular VVV/VVVx tiles. The catalogs of the first two tiles presented in this work are made available at the url `https://web.oapd.inaf.it/bedin/files/PAPERs_eMaterials/VVV-VVVx/`. This repository will be constantly updated with new products once they are ready. For reasonable requests, we can also provide artificial star tests and astro-photometric time series.

9.8 Conclusion

In this paper, we exploited the VVV data to extend the *Gaia* astrometry into the Galactic plane, focusing on two pilot fields, one in the Galactic center and the other in the South-East Bulge. We were able to significantly improve astrometric precision and completeness with respect to previous efforts. These improvements are achieved through a combination of state-of-the-art techniques: (i) the use of spatially variable ePSFs for precise position and flux measurements; (ii) local transformations, which allow us to mitigate systematic errors, most notably residual geometric distortion and atmospheric effects; (iii) a combination of first- and second-pass photometry to improve the detection of faint stars in crowded fields, which allowed to detect significantly more sources than previous efforts in the literature. Our astrometry is anchored to the *Gaia* DR3 reference frame, and

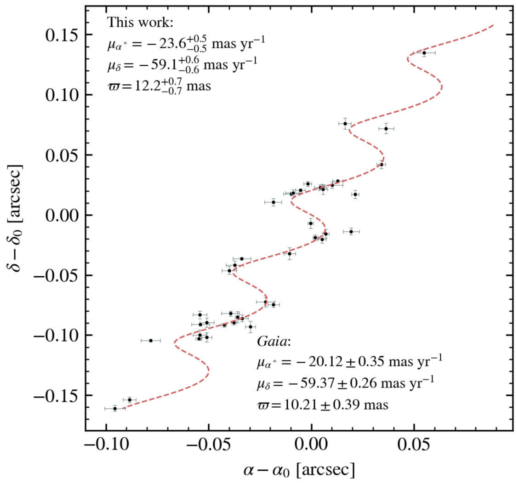

(a) *Gaia* DR3 source id `4042572202828764928`

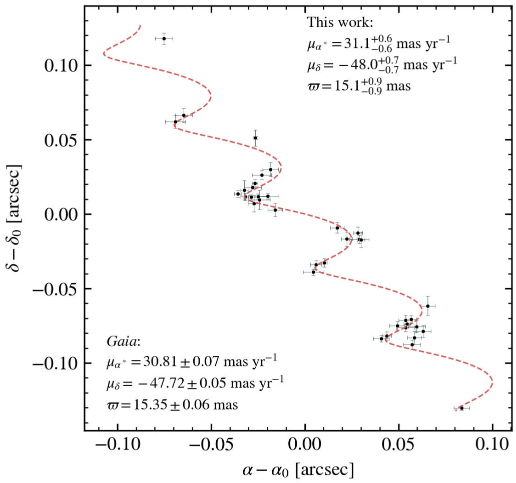

(b) *Gaia* DR3 source id `4039536902304599680`

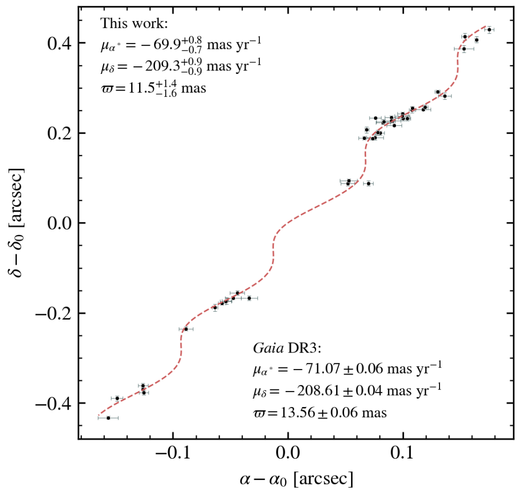

(c) *Gaia* DR3 source id `4057095072096565632`

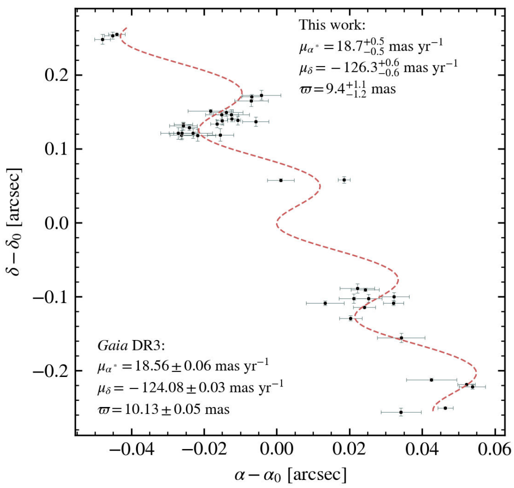

(d) *Gaia* DR3 source id `4056967490090373760`

Figure 9.13: Example of parallax fit for four sources in common with *Gaia*: panels 9.13a and 9.13b are for sources in tile `b248`, while sources in panels 9.13c and 9.13d are in tile `b333`. Coordinates are relative to (α_0, δ_0) chosen as the mean position between the first and last epochs.

represents an extension of the *Gaia* accuracy into the Galactic plane. In future releases, we plan to also include the VVVx data to increase the number of pawprints and extend the temporal baseline available for each tile. We will also combine the information from adjacent tiles in order to measure accurate proper motions also for sources near the borders of the tiles.

10. Conclusion

This thesis represents a dedicated effort to achieve high-precision photometry and astrometry with space- and ground-based surveys collected with wide-field imagers, covering large fraction of the entire sky. We developed software routines to derive spatially variable empirical PSFs from ground-based observations and techniques to calibrate the geometric distortion of a detector by leveraging the *Gaia* absolute reference frame, without needing dedicated observations. We applied our methods to several scientific cases, demonstrating the synergies between ground- and space-based surveys.

10.1 Summary

Observations carried out with the Asiago Schmidt telescope, coupled with the *Gaia* catalogue, allowed us to study the high-mass members of the white dwarf sequence of the OC M37. To derive a list of probable cluster members and reject field sources, we also developed a new formalism to compute astrometric membership probabilities that takes into account the contribution of precise parallax data provided by *Gaia* (Griggio and Bedin, 2022). With our analysis, we discovered the presence of a very rare object among M37's probable members, which we refer to as WD1, and which was previously identified as the central star of a planetary nebula (Griggio et al., 2022a). Planetary nebulae in Galactic OCs are rare objects, and only three are currently known. They are of particular interest because their distance can be determined with high accuracy, enabling for a detailed characterization of the physical properties of the planetary nebula and its ionizing central star. For this reason, we carried out a spectroscopic follow-up of WD1 with the 10-m Gran Telescopio Canarias. This object turned out to be a very rare PG1159-type star at the center of an extraordinarily-old planetary nebula, and the spectroscopic analysis also indicates that it might be a member of M37. The results of this analysis have been published in Werner et al. (2023).

The Asiago photometry, coupled with the *Gaia* catalogue, allowed us to carry out a differential photometric investigation of the unusually broadened low main sequence of M37. Our detailed comparisons with simulated stellar populations suggest that the broadening is compatible with an initial chemical spread among the cluster's stars, which can be either a spread of metallicity or a helium abundance spread (Griggio et al., 2022b).

With the same differential technique applied to M37, we studied the OC M38, which also shows a broadened main sequence; the results indicate that, at odds with M37, unresolved binaries and differential reddening across the field are responsible for the broadened sequence, and show that the differential technique that we employed is able to distinguish between different scenarios (Griggio et al., 2023c).

Our techniques to derive high-precision photometry and astrometry with wide-field imagers have also been applied to CFHT observations of the OC M37. With this dataset, we were able to study M37's white dwarf cooling sequence down to its end, using data acquired in 1999 to derive proper motions for stars in the M37 field. The analysis of the white dwarf sequence allowed us to set constraints on the M37 age, which in turn seems to exclude the helium spread scenario among the possible culprits of the low main sequence broadening (Griggio et al., 2023b). In addition, our upper limit on the age of M37 rules out the hypothesis of an age spread as the origin of the cluster's extended main sequence turnoff. This hypothesis had been previously considered as a possible explanation of this phenomenon, which seems to be recurring in several OCs.

By combining the techniques developed in this thesis to calibrate the geometric distortion, which exploits the *Gaia* reference system and auto-calibration procedures, we derived a geometric distortion solution for the NIRCam detector on board the *JWST* (Griggio et al., 2023a). We tested the goodness of our solution on different applications: (i) field-object decontamination in the GC M92; (ii) the estimation of internal proper motions of M92; and (iii) the measurement of the internal proper motions of the Large Magellanic Cloud. In each of the three tests, we obtained results consistent with literature values, proving the high-quality of our correction. The GD solution derived in this thesis have been applied to *JWST* observations of the GC 47 Tuc: using archival *HST* data we were able to isolate a sample of the cluster's members via proper motion decontamination, unveiling for the first time the brown dwarfs sequence of a GC.

Finally, we used near-infrared, ground-based data from the *VISTA Variables in the Via Lactea* survey to indirectly extend the astrometry provided by the *Gaia* catalogue to objects in heavily-extincted regions towards the Galactic bulge and plane. To this aim, we used the techniques developed in this thesis and exported the state-of-the-art techniques employed to derive high-precision photometry and astrometry with *HST* to the VIRCAM detector. We provide astrometry linked to the *Gaia* ICRF for more than 2 millions sources in the Galactic centre, of which only $\sim 5\%$ are also present in the *Gaia* catalogue (Griggio et al., submitted).

10.1.1 Future work

Chemical spread in open clusters

The unexpected chemical spread that seems to be present among the unevolved M37 members is in contrast with the idea that OCs are a proxy of simple stellar populations and, if confirmed spectroscopically, will challenge current cluster formation models. The same analysis in the OC M38 indicates that, in this cluster, unresolved binaries and differential reddening are responsible for the low main sequence broadening. These results raise the question of whether M37 is an isolated case or if chemical spreads are also found in other OCs, and how this might be connected to the observed phenomenon of multiple populations in GCs.

In this regard, we plan to conduct a survey using the Asiago telescope for the Northern hemisphere, and other instruments for the Southern Hemisphere, to assess the presence and study the origin of this phenomenon in other OCs, e.g. M35, NGC 188, M67, NGC 1817, IC 2714 to name a few.

These clusters have been selected to span a range of ages and metallicities. Coupling ground-based observations in the *Sloan* filters with *Gaia* astrometry, we will be able to compute membership probabilities as in Griggio and Bedin (2022). This will allow us to isolate cluster members from field sources, and build the pseudo-colour diagrams required for the analysis.

Low main-sequence and white dwarf sequence of open clusters

The investigation carried out on M37 with CFHT data shows how ground-based, wide-field imaging can help to explore regions of the colour-magnitude diagram of OCs that are too faint to be studied with *Gaia*.

With the same dataset employed in Chapter 4, we are studying the mass-function of M37 down to $\sim 0.2\,\mathrm{M}_\odot$. The low-mass stars of M37 are too faint for *Gaia*. A preliminary analysis of M37 mass-function is shown in Fig. 10.1. The red points are *Gaia* sources, and they stop at masses below $\sim 0.75\,\mathrm{M}_\odot$. The dark and light blue points instead represent the mass function derived from the CFHT data, using a statistical decontamination approach – similar to that employed in Chapter 4 for the white dwarf sequence – and a proper motion decontamination, respectively. Proper motions are limited by both the smaller field of view of the

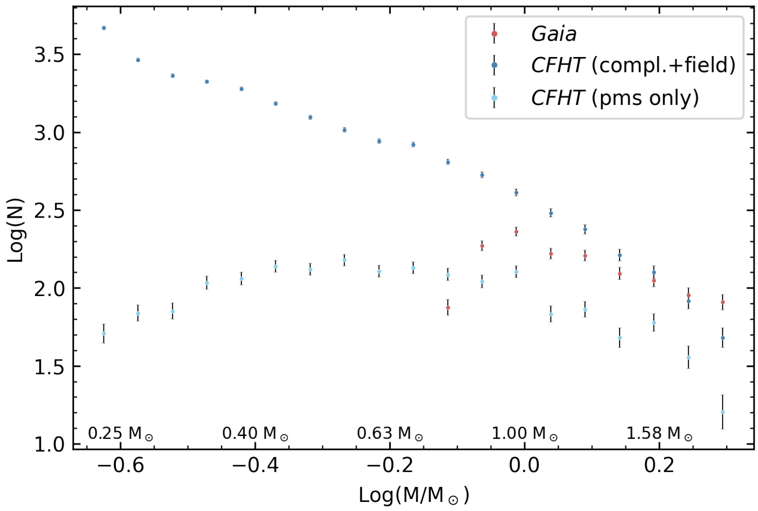

Figure 10.1: Mass function derived from the CFHT and Gaia data. See text for details.

first epoch (collected with the CFH12K detector) and its much less deep exposures. With the same dataset we also managed to derive the binary fraction of M37 in the low-mass regime unaccessible to *Gaia*.

In addition, we already collected new, deep CFHT observations of the OC M35, which also have first-epoch data collected in early 2000. This will allow us to measure proper motions for sources beyond the *Gaia*'s limit, and study its white dwarf sequence and its main sequence down to 0.1 M⊙. We will also be able to study the OC NGC 2158, which falls in the same CFHT field of view of M35.

In Fig. 10.2 we show a preliminary, quality-selected colour-magnitude diagram obtained from this new dataset, in the same *Sloan* filters g and r used in the analysis of M37 in Griggio et al. (2023b). Even if we did not perform any proper-motion selection of cluster members, M35 and NGC 2158 main sequences can be identified in the colour-magnitude. We plotted two BaSTI-IAC isochrones with age and metallicity similar to the literature estimates for these clusters. In the case of M35, the model shows that we get close to the Hydrogen burning minimum mass. Proper motions will allow to decontaminate the colour-magnitude diagram from field sources, isolating M35 and NGC 2158 members. A clean sample of members star will in turn enable precise isochrone fitting, both for the main-sequence and the white dwarf sequence, and detailed comparisons with theory.

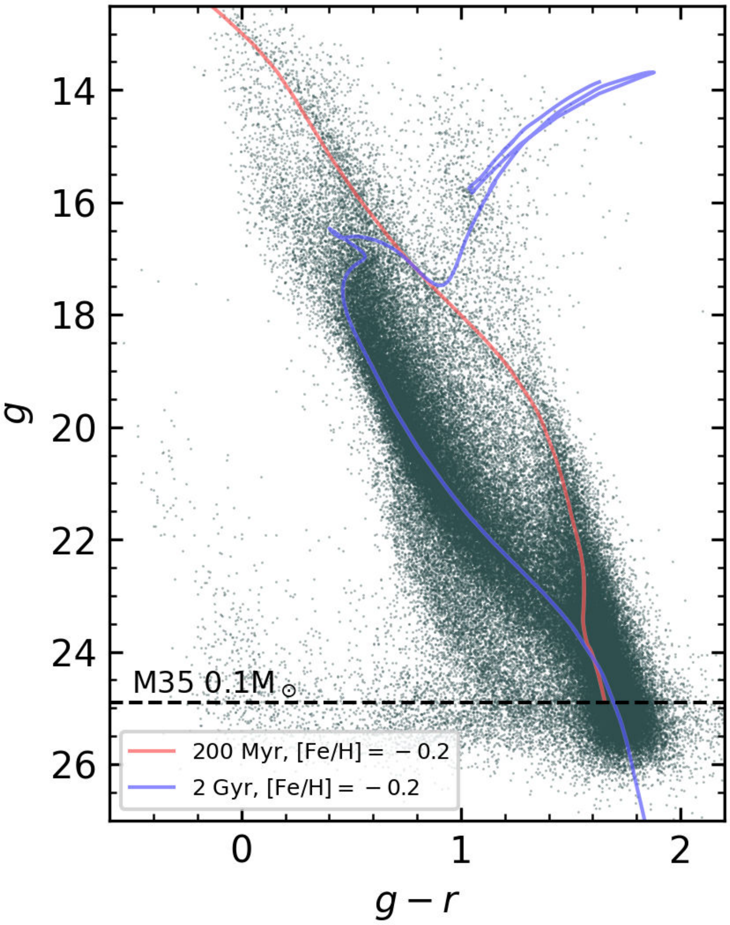

Figure 10.2: Preliminary g vs $g - r$ colour-magnitude diagrams of M35 and NGC 2158 from our new CFHT observations.

Extending *Gaia* to the Galactic plane

The pilot work on VVV in the last chapter of this thesis yielded promising results. In addition to the improvements already described in the chapter's conclusion, a further, significant increase in precision and size is possible by extending the work to all the VVV/VVVx tiles. We already started the data reduction of other tiles, and we plan to automatize most of the data-reduction routines in order to re-process the entire VVV/VVVx dataset with minimal user intervention.

This very large astro-photometric dataset of the Galactic bulge and plane will allow us to carry out several investigations. The Galactic bulge serves as an invaluable laboratory for investigating stellar interactions within high-density environments on galactic scales, offering insights into the early history of the Milky Way (e.g., Fragkoudi et al., 2020). Our high-precision proper motions will enable the separation of Bulge and Disk stars and the identification of gravitationally-bound systems such as comoving groups, star clusters, and stellar streams (e.g., Garro et al., 2022a), and the search for very-wide binaries, which can set tight constraints on the nature of dark matter in the Milky Way (Ramirez and Buckley, 2023). Additionally, the bulge hosts a significant portion of the detected microlensing events due to its high source density, and precise astrometry can help to determining the event's geometry (Mróz et al., 2019). Proper motion measurements are also instrumental in the study of both new and ancient globular clusters in the Milky Way (Contreras Ramos et al., 2018; Garro et al., 2020; Minniti et al., 2021b) and the measurement of their orbital properties (Minniti et al., 2021a).

Space-based telescopes

The techniques developed for ground-based wide-field imagers can be easily exported to other facilities, and also to space-based telescopes. In particular, we already developed data reduction routines to extract state-of-the-art photometry and astrometry from *JWST* images, as showcased in Chapters 7 and 8, and in the works by Nardiello et al. (2022, 2023b).

The experience gained with wide-field (Asiago, CFHT, VISTA) and near-infrared instruments (*JWST*, VISTA) will allow us to make the most of the new generation of space-based wide-field imagers. We will export our techniques to derive effective PSF and geometric distortion correction to the *Euclid* telescope and in the future also to the *Roman Space Telescope* and the recently approved NASA mission *UVEX*. High-precision photometry and astrometry from these instruments will provide a unique dataset that will enable several investigations, from cosmology to stellar astrophysics.

The combination of the wide-field of view and sensitivity in the infrared of the Wide Field Imager onboard *Roman*, together with its expected astrometric precision (WFIRST Astrometry Working Group et al., 2019), will allow to study the still poorly-explored region near and beyond the Hydrogen burning limit of GCs colour-magnitude diagram. Observations of objects in this mass regime will be of fundamental importance to constrain the initial-mass function. In addition, due to the cooling nature of BDs, the expected gap between the low-mass Hydrogen burning stars and the BD sequence in the luminosity function can be used to infer the cluster age, independently from the turn-off and the white dwarf sequence.

The best region to detect BDs and low-mass stars is outside of a cluster's core, where light contamination by much brighter stars is negligible. The wide field of view of *Roman* can map these regions much more efficiently than *JWST*.

The *UVEX* mission will also provide wide-field data in the UV wavelengths. With its 12 $\deg^2$, it will be able to efficiently map large areas of the sky, providing UV counterpart data to the visible and infrared observations of *Euclid* and *Roman*.

References

Alam, Shadab et al. (July 2015). "The Eleventh and Twelfth Data Releases of the Sloan Digital Sky Survey: Final Data from SDSS-III". In: ApJS 219.1, 12, p. 12. DOI: 10.1088/0067-0049/219/1/12.

Althaus, Leandro G., Marcelo M. Miller Bertolami and Alejandro H. Córsico (Sept. 2013). "New evolutionary sequences for extremely low-mass white dwarfs. Homogeneous mass and age determinations and asteroseismic prospects". In: A&A 557, A19, A19. DOI: 10.1051/0004-6361/201321868.

Anderson, J. et al. (Aug. 2006). "Ground-based CCD astrometry with wide field imagers. I. Observations just a few years apart allow decontamination of field objects from members in two globular clusters". In: A&A 454.3, pp. 1029–1045. DOI: 10.1051/0004-6361:20065004.

Anderson, Jay (July 2022). *One-Pass HST Photometry with hst1pass*. Instrument Science Report WFC3 2022-5, 55 pages.

Anderson, Jay, Mike Fall and the Astrometry Working Group (Jan. 2021). *The JWST Calibration Field: Absolute Astrometry and Proper Motions with GAIA and a Second HST Epoch*. JWST Technical Report JWST-STScI-007716, SM-12, 36 pages.

Anderson, Jay and Ivan R. King (Oct. 2000). "Toward High-Precision Astrometry with WFPC2. I. Deriving an Accurate Point-Spread Function". In: PASP 112.776, pp. 1360–1382. DOI: 10.1086/316632.

Anderson, Jay and Ivan R. King (Jan. 2003). "An Improved Distortion Solution for the Hubble Space Telescope's WFPC2". In: PASP 115.803, pp. 113–131. DOI: 10.1086/345491.

Anderson, Jay and Roeland P. van der Marel (Feb. 2010). "New Limits on an Intermediate-Mass Black Hole in Omega Centauri. I. Hubble Space Telescope Photometry and Proper Motions". In: ApJ 710.2, pp. 1032–1062. DOI: 10.1088/0004-637X/710/2/1032.

Anderson, Jay et al. (June 2008a). "Deep Advanced Camera for Surveys Imaging in the Globular Cluster NGC 6397: Reduction Methods". In: AJ 135.6, pp. 2114–2128. DOI: 10.1088/0004-6256/135/6/2114.

Anderson, Jay et al. (June 2008b). “The Acs Survey of Globular Clusters. V. Generating a Comprehensive Star Catalog for each Cluster”. In: AJ 135.6, pp. 2055–2073. DOI: 10.1088/0004-6256/135/6/2055.

Bailer-Jones, C. A. L. et al. (Mar. 2021). “Estimating Distances from Parallaxes. V. Geometric and Photogeometric Distances to 1.47 Billion Stars in Gaia Early Data Release 3”. In: AJ 161.3, 147, p. 147. DOI: 10.3847/1538-3881/abd806.

Balaguer-Núnez, L., K. P. Tian and J. L. Zhao (Dec. 1998). “Determination of proper motions and membership of the open clusters NGC 1817 and NGC 1807”. In: A&AS 133, pp. 387–394. DOI: 10.1051/aas:1998324.

Barbuy, Beatriz, Cristina Chiappini and Ortwin Gerhard (Sept. 2018). “Chemodynamical History of the Galactic Bulge”. In: ARA&A 56, pp. 223–276. DOI: 10.1146/annurev-astro-081817-051826.

Barron, Eric G. et al. (Jan. 2011). “Naval Observatory Vector Astrometry Software (NOVAS) Version 3.1, Introducing a Python Edition”. In: *American Astronomical Society Meeting Abstracts #217*. Vol. 217. American Astronomical Society Meeting Abstracts, 344.14, p. 344.14.

Bastian, N. et al. (Nov. 2018). “Extended main sequence turnoffs in open clusters as seen by Gaia - I. NGC 2818 and the role of stellar rotation”. In: MNRAS 480.3, pp. 3739–3746. DOI: 10.1093/mnras/sty2100.

Bastian, Nate and Carmela Lardo (Sept. 2018). “Multiple Stellar Populations in Globular Clusters”. In: ARA&A 56, pp. 83–136. DOI: 10.1146/annurev-astro-081817-051839.

Bastian, Nate et al. (Oct. 2019). “Multiple populations in integrated light spectroscopy of intermediate-age clusters”. In: MNRAS 489.1, pp. L80–L85. DOI: 10.1093/mnrasl/slz130.

Baumgardt, H., C. Dettbarn and R. Wielen (Oct. 2000). “Absolute proper motions of open clusters. I. Observational data”. In: A&AS 146, pp. 251–258. DOI: 10.1051/aas:2000362.

Bedin, L. R. and C. Fontanive (Dec. 2018). “Extending Gaia DR2 with HST narrow-field astrometry: the WISE J154151.65-225024.9 test case”. In: MNRAS 481.4, pp. 5339–5349. DOI: 10.1093/mnras/sty2626.

Bedin, L. R. and C. Fontanive (May 2020). “Extending Gaia DR2 with HST narrow-field astrometry - II. Refining the method on WISE J163940.83-684738.6”. In: MNRAS 494.2, pp. 2068–2075. DOI: 10.1093/mnras/staa540.

Bedin, L. R. et al. (Mar. 2014). “Improved Hubble Space Telescope proper motions for Tycho-G and other stars in the remnant of Tycho’s Supernova 1572”. In: MNRAS 439.1, pp. 354–371. DOI: 10.1093/mnras/stt2460.

Bedin, L. R. et al. (Apr. 2015). “Hubble Space Telescope observations of the Kepler-field cluster NGC 6819 - I. The bottom of the white dwarf cooling sequence”. In: MNRAS 448.2, pp. 1779–1788. DOI: 10.1093/mnras/stv069.

Bedin, L. R. et al. (Sept. 2017). “Hubble Space Telescope astrometry of the closest brown dwarf binary system - I. Overview and improved orbit”. In: MNRAS 470.1, pp. 1140–1155. DOI: 10.1093/mnras/stx1177.

Bedin, L. R. et al. (Jan. 2023). “The HST large programme on NGC 6752 - IV. The White Dwarf sequence”. In: MNRAS 518.3, pp. 3722–3736. DOI: 10.1093/mnras/stac3219.

Bedin, Luigi R. et al. (Oct. 2001). “Color-Magnitude Diagram and Luminosity Function of M4 near the Hydrogen-burning Limit”. In: ApJ 560.1, pp. L75–L78. DOI: 10.1086/324174.

Bedin, Luigi R. et al. (July 2003). “Hubble Space Telescope Astrometry of m4 and the Galactic Constant V_0/R_0”. In: AJ 126.1, pp. 247–254. DOI: 10.1086/375646.

Bedin, Luigi R. et al. (Apr. 2004). “ω Centauri: The Population Puzzle Goes Deeper”. In: ApJ 605.2, pp. L125–L128. DOI: 10.1086/420847.

Bedin, Luigi R. et al. (May 2005). “The White Dwarf Cooling Sequence in NGC 6791”. In: ApJ 624.1, pp. L45–L48. DOI: 10.1086/430310.

Bedin, Luigi R. et al. (June 2009). “The End of the White Dwarf Cooling Sequence in M4: An Efficient Approach”. In: ApJ 697.2, pp. 965–979. DOI: 10.1088/0004-637X/697/2/965.

Bellini, A., J. Anderson and L. R. Bedin (May 2011). “Astrometry and Photometry with HST WFC3. II. Improved Geometric-Distortion Corrections for 10 Filters of the UVIS Channel”. In: PASP 123.903, p. 622. DOI: 10.1086/659878.

Bellini, A. and L. R. Bedin (Dec. 2009). “Astrometry and Photometry with HST WFC3. I. Geometric Distortion Corrections of F225W, F275W, F336W Bands of the UVIS Channel”. In: PASP 121.886, p. 1419. DOI: 10.1086/649061.

Bellini, A. et al. (Jan. 2009a). “Ground-based CCD astrometry with wide field imagers. III. WFI@2.2m proper-motion catalog of the globular cluster ωCentauri”. In: A&A 493.3, pp. 959–978. DOI: 10.1051/0004-6361:200810880.

Bellini, A. et al. (Dec. 2009b). “Radial distribution of the multiple stellar populations in ω Centauri”. In: A&A 507.3, pp. 1393–1408. DOI: 10.1051/0004-6361/200912757.

Bellini, A. et al. (Apr. 2010). “The end of the white dwarf cooling sequence in M 67”. In: A&A 513, A50, A50. DOI: 10.1051/0004-6361/200913721.

Bellini, A. et al. (June 2013). “A Double White-dwarf Cooling Sequence in ω Centauri”. In: ApJ 769.2, L32, p. L32. DOI: 10.1088/2041-8205/769/2/L32.

Bellini, A. et al. (June 2017). "The State-of-the-art HST Astro-photometric Analysis of the Core of ω Centauri. II. Differential-reddening Map". In: ApJ 842.1, 7, p. 7. DOI: 10.3847/1538-4357/aa705f.

Bellini, A. et al. (2017). "The State-of-the-art *HST* Astro-photometric Analysis of the Core of ω Centauri. I. The Catalog". In: *The Astrophysical Journal* 842.1, p. 6. DOI: 10.3847/1538-4357/aa7059. URL: https://doi.org/10.3847/1538-4357/aa7059.

Bellini, Andrea et al. (Jan. 2018). "The HST Large Programme on ω Centauri. II. Internal Kinematics". In: ApJ 853.1, 86, p. 86. DOI: 10.3847/1538-4357/aaa3ec.

Best, William M. J. et al. (Jan. 2021). "A Volume-limited Sample of Ultracool Dwarfs. I. Construction, Space Density, and a Gap in the L/T Transition". In: AJ 161.1, 42, p. 42. DOI: 10.3847/1538-3881/abc893.

Bianchi, Luciana, Bernie Shiao and David Thilker (June 2017). "Revised Catalog of GALEX Ultraviolet Sources. I. The All-Sky Survey: GUVcat_AIS". In: ApJS 230.2, 24, p. 24. DOI: 10.3847/1538-4365/aa7053.

Birky, Jessica et al. (Mar. 2020). "Temperatures and Metallicities of M Dwarfs in the APOGEE Survey". In: ApJ 892.1, 31, p. 31. DOI: 10.3847/1538-4357/ab7004.

Blouin, Simon et al. (Aug. 2020). "New Conductive Opacities for White Dwarf Envelopes". In: ApJ 899.1, 46, p. 46. DOI: 10.3847/1538-4357/ab9e75.

Bond, Howard E., Andrea Bellini and Kailash C. Sahu (June 2020). "Proper-motion Membership Tests for Four Planetary Nebulae in Galactic Globular Clusters". In: AJ 159.6, 276, p. 276. DOI: 10.3847/1538-3881/ab8f9e.

Boyer, Martha L. et al. (Oct. 2011). "Surveying the Agents of Galaxy Evolution in the Tidally Stripped, Low Metallicity Small Magellanic Cloud (SAGE-SMC). II. Cool Evolved Stars". In: AJ 142.4, 103, p. 103. DOI: 10.1088/0004-6256/142/4/103.

Bressan, Alessandro et al. (Nov. 2012). "PARSEC: stellar tracks and isochrones with the PAdova and TRieste Stellar Evolution Code". In: MNRAS 427.1, pp. 127–145. DOI: 10.1111/j.1365-2966.2012.21948.x.

Caiazzo, Ilaria et al. (Jan. 2017). "Globular cluster absolute ages from cooling brown dwarfs". In: *arXiv e-prints*, arXiv:1702.00091, arXiv:1702.00091.

Caiazzo, Ilaria et al. (May 2019). "Hunting for ancient brown dwarfs: the developing field of brown dwarfs in globular clusters". In: BAAS 51.3, 521, p. 521.

Calamida, A. et al. (Aug. 2014). "First Detection of the White Dwarf Cooling Sequence of the Galactic Bulge". In: ApJ 790.2, 164, p. 164. DOI: 10.1088/0004-637X/790/2/164.

Camisassa, M. E. et al. (Oct. 2016). "Pulsations powered by hydrogen shell burning in white dwarfs". In: A&A 595, A45, A45. DOI: 10.1051/0004-6361/201628857.

Camisassa, María E. et al. (Apr. 2017). "Updated Evolutionary Sequences for Hydrogen-deficient White Dwarfs". In: ApJ 839.1, 11, p. 11. DOI: 10.3847/1538-4357/aa6797.

Camisassa, María E. et al. (May 2019). "The evolution of ultra-massive white dwarfs". In: A&A 625, A87, A87. DOI: 10.1051/0004-6361/201833822.

Cantat-Gaudin, T. and F. Anders (Jan. 2020). "Clusters and mirages: cataloguing stellar aggregates in the Milky Way". In: A&A 633, A99, A99. DOI: 10.1051/0004-6361/201936691.

Cantat-Gaudin, T. et al. (Oct. 2018a). "A Gaia DR2 view of the open cluster population in the Milky Way". In: A&A 618, A93, A93. DOI: 10.1051/0004-6361/201833476.

Cantat-Gaudin, T. et al. (July 2018b). "Characterising open clusters in the solar neighbourhood with the Tycho-Gaia Astrometric Solution". In: A&A 615, A49, A49. DOI: 10.1051/0004-6361/201731251.

Carrera, R. et al. (2019). "Open clusters in APOGEE and GALAH - Combining Gaia and ground-based spectroscopic surveys". In: *A&A* 623, A80. DOI: 10.1051/0004-6361/201834546. URL: https://doi.org/10.1051/0004-6361/201834546.

Carretta, E. et al. (Sept. 2011). "Multiple stellar populations in the globular cluster NGC 1851". In: A&A 533, A69, A69. DOI: 10.1051/0004-6361/201117269.

Casamiquela, L. et al. (Dec. 2019). "OCCASO - III. Iron peak and α elements of 18 open clusters. Comparison with chemical evolution models and field stars". In: MNRAS 490.2, pp. 1821–1842. DOI: 10.1093/mnras/stz2595.

Cassisi, S. et al. (June 2007). "Updated Electron-Conduction Opacities: The Impact on Low-Mass Stellar Models". In: ApJ 661.2, pp. 1094–1104. DOI: 10.1086/516819.

Castro-Ginard, A. et al. (Oct. 2018). "A new method for unveiling open clusters in Gaia. New nearby open clusters confirmed by DR2". In: A&A 618, A59, A59. DOI: 10.1051/0004-6361/201833390.

Catalán, S. et al. (July 2008). "The initial-final mass relationship of white dwarfs revisited: effect on the luminosity function and mass distribution". In: MNRAS 387.4, pp. 1693–1706. DOI: 10.1111/j.1365-2966.2008.13356.x.

Chambers, K. C. et al. (Dec. 2016). "The Pan-STARRS1 Surveys". In: *arXiv e-prints*, arXiv:1612.05560, arXiv:1612.05560.

Chang, S. W., Y. I. Byun and J. D. Hartman (Nov. 2015). “Photometric Study on Stellar Magnetic Activity. I. Flare Variability of Red Dwarf Stars in the Open Cluster M37”. In: ApJ 814.1, 35, p. 35. DOI: 10.1088/0004-637X/814/1/35.

Choi, Jieun et al. (June 2016). “Mesa Isochrones and Stellar Tracks (MIST). I. Solar-scaled Models”. In: ApJ 823.2, 102, p. 102. DOI: 10.3847/0004-637X/823/2/102.

Chornay, N. and N. A. Walton (June 2020). “Searching for central stars of planetary nebulae in Gaia DR2”. In: A&A 638, A103, A103. DOI: 10.1051/0004-6361/202037554.

Chornay, N. and N. A. Walton (Dec. 2021). “One star, two star, red star, blue star: an updated planetary nebula central star distance catalogue from Gaia EDR3”. In: A&A 656, A110, A110. DOI: 10.1051/0004-6361/202142008.

Clarke, C. J., I. A. Bonnell and L. A. Hillenbrand (May 2000). “The Formation of Stellar Clusters”. In: *Protostars and Planets IV*. Ed. by V. Mannings, A. P. Boss and S. S. Russell, p. 151. DOI: 10.48550/arXiv.astro-ph/9903323.

Contreras Ramos, Rodrigo et al. (Aug. 2018). “The Orbit of the New Milky Way Globular Cluster FSR1716 = VVV-GC05”. In: ApJ 863.1, 78, p. 78. DOI: 10.3847/1538-4357/aacd09.

Cordoni, G. et al. (Dec. 2018). “Extended Main-sequence Turnoff as a Common Feature of Milky Way Open Clusters”. In: ApJ 869.2, 139, p. 139. DOI: 10.3847/1538-4357/aaedc1.

Correnti, Matteo et al. (Oct. 2014). “New Clues to the Cause of Extended Main-Sequence Turnoffs in Intermediate-age Star Clusters in the Magellanic Clouds”. In: ApJ 793.2, 121, p. 121. DOI: 10.1088/0004-637X/793/2/121.

Correnti, Matteo et al. (May 2017). “Dissecting the extended main-sequence turn-off of the young star cluster NGC 1850”. In: MNRAS 467.3, pp. 3628–3641. DOI: 10.1093/mnras/stx010.

Cox, C. and R. L. Gilliland (Jan. 2003). “The Effect of Velocity Aberration on ACS Image Processing”. In: *HST Calibration Workshop : Hubble after the Installation of the ACS and the NICMOS Cooling System*, p. 58.

Cummings, Jeffrey D. et al. (July 2015). “Initial-Final Mass Relation for 3 to 4 $M_\odot$ Progenitors of White Dwarfs from the Single Cluster NGC 2099”. In: ApJ 807.1, 90, p. 90. DOI: 10.1088/0004-637X/807/1/90.

Cummings, Jeffrey D. et al. (Mar. 2016). “An Ultramassive 1.28 $M_\odot$ White Dwarf in NGC 2099”. In: ApJ 820.1, L18, p. L18. DOI: 10.3847/2041-8205/820/1/L18.

Cummings, Jeffrey D. et al. (Oct. 2018). “The White Dwarf Initial-Final Mass Relation for Progenitor Stars from 0.85 to 7.5 $M_\odot$”. In: ApJ 866.1, 21, p. 21. DOI: 10.3847/1538-4357/aadfd6.

Currie, M. J. et al. (May 2014). "Starlink Software in 2013". In: *Astronomical Data Analysis Software and Systems XXIII*. Ed. by N. Manset and P. Forshay. Vol. 485. Astronomical Society of the Pacific Conference Series, p. 391.

D'Antona, F. et al. (Mar. 2023). "On the role of dust and mass loss in the extended main sequence turnoff of star clusters: the case of NGC 1783". In: *arXiv e-prints*, arXiv:2303.16049, arXiv:2303.16049. DOI: 10.48550/arXiv.2303.16049.

Dias, W. S. et al. (July 2002). "New catalogue of optically visible open clusters and candidates". In: A&A 389, pp. 871–873. DOI: 10.1051/0004-6361:20020668.

Dieball, A. et al. (Jan. 2016). "Deep Near-IR Observations of the Globular Cluster M4: Hunting for Brown Dwarfs". In: ApJ 817.1, 48, p. 48. DOI: 10.3847/0004-637X/817/1/48.

Dieball, A. et al. (June 2019). "Hunting for brown dwarfs in the globular cluster M4: second epoch HST NIR observations". In: MNRAS 486.2, pp. 2254–2264. DOI: 10.1093/mnras/stz996.

Doherty, Carolyn L. et al. (Nov. 2017). "Super-AGB Stars and their Role as Electron Capture Supernova Progenitors". In: PASA 34, e056, e056. DOI: 10.1017/pasa.2017.52.

Donor, John et al. (May 2020). "The Open Cluster Chemical Abundances and Mapping Survey. IV. Abundances for 128 Open Clusters Using SDSS/APOGEE DR16". In: AJ 159.5, 199, p. 199. DOI: 10.3847/1538-3881/ab77bc.

Drew, Janet E. et al. (Sept. 2005). "The INT Photometric Hα Survey of the Northern Galactic Plane (IPHAS)". In: MNRAS 362.3, pp. 753–776. DOI: 10.1111/j.1365-2966.2005.09330.x.

El-Badry, Kareem, Hans-Walter Rix and Daniel R. Weisz (June 2018). "An Empirical Measurement of the Initial-Final Mass Relation with Gaia White Dwarfs". In: ApJ 860.2, L17, p. L17. DOI: 10.3847/2041-8213/aaca9c.

Fabricius, C. et al. (May 2021). "Gaia Early Data Release 3. Catalogue validation". In: A&A 649, A5, A5. DOI: 10.1051/0004-6361/202039834.

Ferrario, Lilia et al. (Aug. 2005). "The open-cluster initial-final mass relationship and the high-mass tail of the white dwarf distribution". In: MNRAS 361.4, pp. 1131–1135. DOI: 10.1111/j.1365-2966.2005.09244.x.

Foreman-Mackey, Daniel et al. (Mar. 2013). "emcee: The MCMC Hammer". In: PASP 125.925, p. 306. DOI: 10.1086/670067.

Fragkou, V. et al. (June 2019). "A high-mass planetary nebula in a Galactic open cluster". In: *Nature Astronomy* 3, pp. 851–857. DOI: 10.1038/s41550-019-0796-x.

Fragkoudi, F. et al. (Mar. 2020). "What the Milky Way bulge reveals about the initial metallicity gradients in the disc". In: *IAU General Assembly*, pp. 282–283. DOI: 10.1017/S174392131900440X.

Frebel, Anna and John E. Norris (Aug. 2015). "Near-Field Cosmology with Extremely Metal-Poor Stars". In: ARA&A 53, pp. 631–688. DOI: 10.1146/annurev-astro-082214-122423.

Freeman, Ken and Joss Bland-Hawthorn (Jan. 2002). "The New Galaxy: Signatures of Its Formation". In: ARA&A 40, pp. 487–537. DOI: 10.1146/annurev.astro.40.060401.093840.

Frinchaboy, P. M. et al. (Nov. 2008). "Tombaugh 2: the first open cluster with a significant abundance spread or embedded in a cold stellar stream?" In: MNRAS 391.1, pp. 39–51. DOI: 10.1111/j.1365-2966.2008.13875.x.

Frinchaboy, Peter M. et al. (Nov. 2013). "The Open Cluster Chemical Analysis and Mapping Survey: Local Galactic Metallicity Gradient with APOGEE Using SDSS DR10". In: ApJ 777.1, L1, p. L1. DOI: 10.1088/2041-8205/777/1/L1.

Frœschlé, Michel, François Mignard and Frédéric Arenou (1997). "Determination of the PPN Parameter gamma with the HIPPARCOS Data". In: *Proceedings of the ESA Symposium Hipparcos-Venice 1997, 13-16 May, Venice, Italy, ESA SP-402 (July 1997), p. 49-52* 402, pp. 49–52.

Gagné, Jonathan et al. (Mar. 2018). "BANYAN. XI. The BANYAN Σ Multivariate Bayesian Algorithm to Identify Members of Young Associations with 150 pc". In: ApJ 856.1, 23, p. 23. DOI: 10.3847/1538-4357/aaae09.

Gaia Collaboration et al. (Nov. 2016a). "The Gaia mission". In: A&A 595, A1, A1. DOI: 10.1051/0004-6361/201629272.

Gaia Collaboration et al. (Nov. 2016b). "The Gaia mission". In: A&A 595, A1, A1. DOI: 10.1051/0004-6361/201629272.

Gaia Collaboration et al. (Aug. 2018). "Gaia Data Release 2. Summary of the contents and survey properties". In: A&A 616, A1, A1. DOI: 10.1051/0004-6361/201833051.

Gaia Collaboration et al. (May 2021). "Gaia Early Data Release 3. Summary of the contents and survey properties". In: A&A 649, A1, A1. DOI: 10.1051/0004-6361/202039657.

Gaia Collaboration et al. (June 2023). "Gaia Data Release 3. Summary of the content and survey properties". In: A&A 674, A1, A1. DOI: 10.1051/0004-6361/202243940.

Garro, E. R. et al. (Oct. 2020). "VVVX-Gaia discovery of a low luminosity globular cluster in the Milky Way disk". In: A&A 642, L19, p. L19. DOI: 10.1051/0004-6361/202039233.

Garro, E. R. et al. (June 2022a). “A new low-luminosity globular cluster discovered in the Milky Way with the VVVX survey”. In: A&A 662, A95, A95. DOI: 10.1051/0004-6361/202243342.

Garro, E. R. et al. (Mar. 2022b). “Unveiling the nature of 12 new low-luminosity Galactic globular cluster candidates”. In: A&A 659, A155, A155. DOI: 10.1051/0004-6361/202142248.

Georgy, C. et al. (Feb. 2019). “Disappearance of the extended main sequence turn-off in intermediate age clusters as a consequence of magnetic braking”. In: A&A 622, A66, A66. DOI: 10.1051/0004-6361/201834505.

González-Fernández, C. et al. (Mar. 2018). “The VISTA ZYJHKs photometric system: calibration from 2MASS”. In: MNRAS 474.4, pp. 5459–5478. DOI: 10.1093/mnras/stx3073.

Gossage, Seth et al. (Dec. 2019). “Combined Effects of Rotation and Age Spreads on Extended Main-Sequence Turn Offs”. In: ApJ 887.2, 199, p. 199. DOI: 10.3847/1538-4357/ab5717.

Goudfrooij, Paul, Léo Girardi and Matteo Correnti (Sept. 2017). “Extended Main-sequence Turn-offs in Intermediate-age Star Clusters: Stellar Rotation Diminishes, but Does Not Eliminate, Age Spreads”. In: ApJ 846.1, 22, p. 22. DOI: 10.3847/1538-4357/aa7fb7.

Goudfrooij, Paul et al. (Dec. 2014). “Extended Main Sequence Turnoffs in Intermediate-age Star Clusters: A Correlation between Turnoff Width and Early Escape Velocity”. In: ApJ 797.1, 35, p. 35. DOI: 10.1088/0004-637X/797/1/35.

Gratton, Raffaele G., Eugenio Carretta and Angela Bragaglia (Feb. 2012). “Multiple populations in globular clusters. Lessons learned from the Milky Way globular clusters”. In: A&A Rev. 20, 50, p. 50. DOI: 10.1007/s00159-012-0050-3.

Griggio, M. and L. R. Bedin (Apr. 2022). “Astrometric star-cluster membership probability: application to the case of M 37 with Gaia EDR3”. In: MNRAS 511.4, pp. 4702–4709. DOI: 10.1093/mnras/stac391.

Griggio, M., D. Nardiello and L. R. Bedin (Mar. 2023a). “Photometry and astrometry with JWST-II: NIRCam distortion correction”. In: *Astronomische Nachrichten* 344.3, e20230006, e20230006. DOI: 10.1002/asna.20230006.

Griggio, M. et al. (Sept. 2022a). “Astro-photometric study of M37 with Gaia and wide-field ugi-imaging”. In: MNRAS 515.2, pp. 1841–1853. DOI: 10.1093/mnras/stac1920.

Griggio, M. et al. (Nov. 2022b). “Signature of a chemical spread in the open cluster M37”. In: MNRAS 516.3, pp. 3631–3640. DOI: 10.1093/mnras/stac2512.

Griggio, M. et al. (Sept. 2023b). "Exploring the origin of the extended main-sequence turn-off in M37 through the white dwarf cooling sequence". In: MNRAS 524.1, pp. 108–117. DOI: 10.1093/mnras/stad1843.

Griggio, M. et al. (Aug. 2023c). "The broadening of the main sequence in the open cluster M38". In: MNRAS 523.4, pp. 5148–5154. DOI: 10.1093/mnras/stad1754.

Groot, Paul J. et al. (Oct. 2009). "The UV-Excess survey of the northern Galactic plane". In: MNRAS 399.1, pp. 323–339. DOI: 10.1111/j.1365-2966.2009.15273.x.

Häberle, Maximilian et al. (May 2021). "Hunting for intermediate-mass black holes in globular clusters: an astrometric study of NGC 6441". In: MNRAS 503.1, pp. 1490–1506. DOI: 10.1093/mnras/stab474.

Hajdu, Gergely et al. (June 2020). "On the optimal calibration of VVV photometry". In: *Experimental Astronomy* 49.3, pp. 217–238. DOI: 10.1007/s10686-020-09661-0.

Harris, William E. (Oct. 1996). "A Catalog of Parameters for Globular Clusters in the Milky Way". In: AJ 112, p. 1487. DOI: 10.1086/118116.

Hartman, J. D. et al. (Mar. 2008). "Deep MMT Transit Survey of the Open Cluster M37. I. Observations and Cluster Parameters". In: ApJ 675.2, pp. 1233–1253. DOI: 10.1086/527465.

Hayashi, C. and T. Nakano (Oct. 1963). "Evolution of Stars of Small Masses in the Pre-Main-Sequence Stages". In: *Progress of Theoretical Physics* 30.4, pp. 460–474. DOI: 10.1143/PTP.30.460.

Heiter, U. et al. (Jan. 2014). "On the metallicity of open clusters. II. Spectroscopy". In: A&A 561, A93, A93. DOI: 10.1051/0004-6361/201322559.

Helmi, Amina et al. (Oct. 2018). "The merger that led to the formation of the Milky Way's inner stellar halo and thick disk". In: Nature 563.7729, pp. 85–88. DOI: 10.1038/s41586-018-0625-x.

Hidalgo, Sebastian L. et al. (Apr. 2018). "The Updated BaSTI Stellar Evolution Models and Isochrones. I. Solar-scaled Calculations". In: ApJ 856.2, 125, p. 125. DOI: 10.3847/1538-4357/aab158.

Hogg, David W. et al. (Dec. 2016). "Chemical Tagging Can Work: Identification of Stellar Phase-space Structures Purely by Chemical-abundance Similarity". In: ApJ 833.2, 262, p. 262. DOI: 10.3847/1538-4357/833/2/262.

Irwin, Mike J. et al. (Sept. 2004). "VISTA data flow system: pipeline processing for WFCAM and VISTA". In: *Optimizing Scientific Return for Astronomy through Information Technologies*. Ed. by Peter J. Quinn and Alan Bridger. Vol. 5493. Society of Photo-Optical Instrumentation Engineers (SPIE) Conference Series, pp. 411–422. DOI: 10.1117/12.551449.

Joshi, Gireesh C. and R. K. Tyagi (Jan. 2016). “Identification of cluster MS stars and their implication - I. NGC 2099 and NGC 6866”. In: MNRAS 455.1, pp. 785–805. DOI: 10.1093/mnras/stv2353.

Kader, Justin A. et al. (Nov. 2022). “Blanco DECam Bulge Survey (BDBS). VII. Multiple Populations in Globular Clusters of the Galactic Bulge”. In: ApJ 940.1, 76, p. 76. DOI: 10.3847/1538-4357/ac94c5.

Kalirai, Jason S. et al. (Jan. 2012). “A Deep, Wide-field, and Panchromatic View of 47 Tuc and the SMC with HST: Observations and Data Analysis Methods”. In: AJ 143.1, 11, p. 11. DOI: 10.1088/0004-6256/143/1/11.

Kalirai, Jasonjot Singh et al. (July 2001a). “The CFHT Open Star Cluster Survey. I. Cluster Selection and Data Reduction”. In: AJ 122.1, pp. 257–265. DOI: 10.1086/321140.

Kalirai, Jasonjot Singh et al. (Dec. 2001b). “The CFHT Open Star Cluster Survey. III. The White Dwarf Cooling Age of the Rich Open Star Cluster NGC 2099 (M37)”. In: AJ 122.6, pp. 3239–3257. DOI: 10.1086/324463.

Kalirai, Jasonjot Singh et al. (Jan. 2005). “The Initial-Final Mass Relationship: Spectroscopy of White Dwarfs in NGC 2099 (M37)”. In: ApJ 618.2, pp. L123–L127. DOI: 10.1086/427774.

Kamann, S. et al. (Oct. 2018). “Cluster kinematics and stellar rotation in NGC 419 with MUSE and adaptive optics”. In: MNRAS 480.2, pp. 1689–1695. DOI: 10.1093/mnras/sty1958.

Kamann, S. et al. (Feb. 2020). “How stellar rotation shapes the colour-magnitude diagram of the massive intermediate-age star cluster NGC 1846”. In: MNRAS 492.2, pp. 2177–2192. DOI: 10.1093/mnras/stz3583.

Kamann, S. et al. (Jan. 2023). “The effects of stellar rotation along the main sequence of the 100-Myr-old massive cluster NGC 1850”. In: MNRAS 518.1, pp. 1505–1521. DOI: 10.1093/mnras/stac3170.

Kang, Y. B. et al. (Mar. 2007). “Variable Stars in the Open Cluster NGC 2099 (M37)”. In: PASP 119.853, pp. 239–250. DOI: 10.1086/513883.

Kerber, L. O. et al. (Apr. 2019). “A deep view of a fossil relic in the Galactic bulge: the Globular Cluster HP 1”. In: MNRAS 484.4, pp. 5530–5550. DOI: 10.1093/mnras/stz003.

Kharchenko, N. V. et al. (Aug. 2005). “Astrophysical parameters of Galactic open clusters”. In: A&A 438.3, pp. 1163–1173. DOI: 10.1051/0004-6361:20042523.

King, Ivan R. et al. (Jan. 1998). “The Luminosity Function of the Globular Cluster NGC 6397 near the Limit of Hydrogen Burning”. In: ApJ 492.1, pp. L37–L40. DOI: 10.1086/311082.

Kirkpatrick, J. Davy et al. (Feb. 2019). “Preliminary Trigonometric Parallaxes of 184 Late-T and Y Dwarfs and an Analysis of the Field Substellar Mass

Function into the "Planetary" Mass Regime". In: ApJS 240.2, 19, p. 19. DOI: 10.3847/1538-4365/aaf6af.
Kiss, L. L. et al. (Sept. 2001). "A variable star survey of the open cluster M 37". In: A&A 376, pp. 561–567. DOI: 10.1051/0004-6361:20010980.
Koester, D. (Jan. 2010). "White dwarf spectra and atmosphere models". In: *Mem. Soc. Astron. Italiana* 81, pp. 921–931.
Koester, D. and S. O. Kepler (Nov. 2015). "DB white dwarfs in the Sloan Digital Sky Survey data release 10 and 12". In: A&A 583, A86, A86. DOI: 10.1051/0004-6361/201527169.
Kozhurina-Platais, Vera et al. (Feb. 1995). "A Proper-Motion Study of the Open Cluster NGC 3680". In: AJ 109, p. 672. DOI: 10.1086/117310.
Kumar, Shiv S. (May 1963). "The Structure of Stars of Very Low Mass." In: ApJ 137, p. 1121. DOI: 10.1086/147589.
Lardo, Carmela et al. (June 2022). "Confirmation of a metallicity spread amongst first population stars in globular clusters". In: A&A 662, A117, A117. DOI: 10.1051/0004-6361/202243843.
Legnardi, M. V. et al. (June 2022). "Constraining the original composition of the gas forming first-generation stars in globular clusters". In: MNRAS 513.1, pp. 735–751. DOI: 10.1093/mnras/stac734.
Lewis, J. R., M. Irwin and P. Bunclark (Dec. 2010). "Pipeline Processing for VISTA". In: *Astronomical Data Analysis Software and Systems XIX*. Ed. by Y. Mizumoto, K. I. Morita and M. Ohishi. Vol. 434. Astronomical Society of the Pacific Conference Series, p. 91.
Li, Chengyuan et al. (Aug. 2017). "Discovery of Extended Main-sequence Turnoffs in Four Young Massive Clusters in the Magellanic Clouds". In: ApJ 844.2, 119, p. 119. DOI: 10.3847/1538-4357/aa7b36.
Li, Chun-Yan et al. (Apr. 2021). "Investigating variable stars in the open cluster NGC 1912 and its surrounding field". In: *Research in Astronomy and Astrophysics* 21.3, 068, p. 068. DOI: 10.1088/1674-4527/21/3/068.
Libralato, M. et al. (Mar. 2014). "Ground-based astrometry with wide field imagers. V. Application to near-infrared detectors: HAWK-I@VLT/ESO". In: A&A 563, A80, A80. DOI: 10.1051/0004-6361/201322059.
Libralato, M. et al. (June 2015). "High-precision astrometry with VVV - I. An independent reduction pipeline for VIRCAM@VISTA". In: MNRAS 450.2, pp. 1664–1673. DOI: 10.1093/mnras/stv674.
Libralato, Mattia et al. (Jan. 2021). "2D kinematics of massive stars near the Galactic Centre". In: MNRAS 500.3, pp. 3213–3239. DOI: 10.1093/mnras/staa3329.

Libralato, Mattia et al. (June 2023). “JWST-TST Proper Motions. I. High-precision NIRISS Calibration and Large Magellanic Cloud Kinematics”. In: ApJ 950.2, 101, p. 101. DOI: 10.3847/1538-4357/acd04f.

Lindegren, L. et al. (May 2021a). “Gaia Early Data Release 3. Parallax bias versus magnitude, colour, and position”. In: A&A 649, A4, A4. DOI: 10.1051/0004-6361/202039653.

Lindegren, L. et al. (May 2021b). “Gaia Early Data Release 3. The astrometric solution”. In: A&A 649, A2, A2. DOI: 10.1051/0004-6361/202039709.

Mackey, A. D. and P. Broby Nielsen (July 2007). “A double main-sequence turn-off in the rich star cluster NGC 1846 in the Large Magellanic Cloud”. In: MNRAS 379.1, pp. 151–158. DOI: 10.1111/j.1365-2966.2007.11915.x.

Mackey, A. D. et al. (July 2008). “Multiple Stellar Populations in Three Rich Large Magellanic Cloud Star Clusters”. In: ApJ 681.1, p. L17. DOI: 10.1086/590343.

Majaess, Daniel J., David G. Turner and David J. Lane (Dec. 2007). “In Search of Possible Associations between Planetary Nebulae and Open Clusters”. In: PASP 119.862, pp. 1349–1360. DOI: 10.1086/524414.

Malofeeva, Alina A., Anton F. Seleznev and Giovanni Carraro (Mar. 2022). “Unresolved Binaries in the Intermediate Mass Range in the Pleiades Star Cluster”. In: AJ 163.3, 113, p. 113. DOI: 10.3847/1538-3881/ac47a3.

Marino, A. F. et al. (Sept. 2018a). “Different Stellar Rotations in the Two Main Sequences of the Young Globular Cluster NGC 1818: The First Direct Spectroscopic Evidence”. In: AJ 156.3, 116, p. 116. DOI: 10.3847/1538-3881/aad3cd.

Marino, A. F. et al. (Aug. 2018b). “Discovery of Extended Main Sequence Turnoffs in Galactic Open Clusters”. In: ApJ 863.2, L33, p. L33. DOI: 10.3847/2041-8213/aad868.

Marino, A. F. et al. (Dec. 2019). “Chemical Abundances along the 1G Sequence of the Chromosome Maps: The Globular Cluster NGC 3201”. In: ApJ 887.1, 91, p. 91. DOI: 10.3847/1538-4357/ab53d9.

Marsh, Thomas R. (June 2014). *PAMELA: Optimal extraction code for long-slit CCD spectroscopy.*

Marsh, Tom (July 2019). *molly: 1D astronomical spectra analyzer.*

Marshall, J. L. et al. (Oct. 2005). “Survey for Transiting Extrasolar Planets in Stellar Systems. II. Spectrophotometry and Metallicities of Open Clusters”. In: AJ 130.4, pp. 1916–1928. DOI: 10.1086/432685.

Martocchia, S. et al. (Aug. 2019). “The search for multiple populations in Magellanic Clouds clusters - V. Correlation between cluster age and abundance spreads”. In: MNRAS 487.4, pp. 5324–5334. DOI: 10.1093/mnras/stz1596.

Mermilliod, J. C. et al. (Mar. 1996). “Red giants in open clusters. V. NGC 2099”. In: A&A 307, p. 80.

Messina, S. et al. (May 2008). “RACE-OC project: rotation and variability in the open cluster NGC 2099 (M 37)”. In: A&A 483.1, pp. 253–262. DOI: 10.1051/0004-6361:20079216.

Milone, A. P. et al. (Apr. 2012). “The ACS survey of Galactic globular clusters. XII. Photometric binaries along the main sequence”. In: A&A 540, A16, A16. DOI: 10.1051/0004-6361/201016384.

Minniti, D. et al. (July 2010). “VISTA Variables in the Via Lactea (VVV): The public ESO near-IR variability survey of the Milky Way”. In: New Astronomy 15.5, pp. 433–443. DOI: 10.1016/j.newast.2009.12.002.

Minniti, D. et al. (Apr. 2021a). “Survival in an extreme environment: Which is the closest globular cluster to the Galactic centre?” In: A&A 648, A86, A86. DOI: 10.1051/0004-6361/202039820.

Minniti, D. et al. (Dec. 2023). “The globular cluster VVV CL002 falling down to the hazardous Galactic centre”. In: *arXiv e-prints*, arXiv:2312.16028. DOI: 10.48550/arXiv.2312.16028.

Minniti, Dante (Jan. 2018). “Mapping the Milky Way in the Near-IR: The Future of the VVV Survey”. In: *The Vatican Observatory, Castel Gandolfo: 80th Anniversary Celebration*. Ed. by Gabriele Gionti and Jean-Baptiste Kikwaya Eluo. Vol. 51. Astrophysics and Space Science Proceedings, p. 63. DOI: 10.1007/978-3-319-67205-2_4.

Minniti, Dante et al. (Nov. 2017). “New VVV Survey Globular Cluster Candidates in the Milky Way Bulge”. In: ApJ 849.2, L24, p. L24. DOI: 10.3847/2041-8213/aa95b8.

Minniti, Dante et al. (June 2021b). “Discovery of a new nearby globular cluster with extreme kinematics located in the extension of a halo stream”. In: A&A 650, L11, p. L11. DOI: 10.1051/0004-6361/202141129.

Monguió, M. et al. (June 2020). “IGAPS: the merged IPHAS and UVEX optical surveys of the northern Galactic plane”. In: A&A 638, A18, A18. DOI: 10.1051/0004-6361/201937333.

Moni Bidin, C. et al. (Jan. 2014). “Investigating potential planetary nebula/cluster pairs”. In: A&A 561, A119, A119. DOI: 10.1051/0004-6361/201220802.

Monteiro, H. et al. (Dec. 2020). “Fundamental parameters for 45 open clusters with Gaia DR2, an improved extinction correction and a metallicity gradient prior”. In: MNRAS 499.2, pp. 1874–1889. DOI: 10.1093/mnras/staa2983.

Mróz, Przemek et al. (Oct. 2019). “Microlensing Optical Depth and Event Rate toward the Galactic Bulge from 8 yr of OGLE-IV Observations”. In: ApJS 244.2, 29, p. 29. DOI: 10.3847/1538-4365/ab426b.

Nardiello, D., M. Griggio and L. R. Bedin (May 2023a). "JWST unveils the brown dwarf sequence of 47 Tucanæ". In: MNRAS 521.1, pp. L39–L43. DOI: 10.1093/mnrasl/slad021.

Nardiello, D. et al. (July 2015). "The Hubble Space Telescope UV Legacy Survey of Galactic Globular Clusters - IV. Helium content and relative age of multiple stellar populations within NGC 6352". In: MNRAS 451.1, pp. 312–322. DOI: 10.1093/mnras/stv971.

Nardiello, D. et al. (June 2018a). "The Hubble Space Telescope UV Legacy Survey of Galactic globular clusters - XIV. Multiple stellar populations within M 15 and their radial distribution". In: MNRAS 477.2, pp. 2004–2019. DOI: 10.1093/mnras/sty71910.48550/arXiv.1803.05979.

Nardiello, D. et al. (Dec. 2018b). "The Hubble Space Telescope UV Legacy Survey of Galactic Globular Clusters - XVII. Public Catalogue Release". In: MNRAS 481.3, pp. 3382–3393. DOI: 10.1093/mnras/sty2515.

Nardiello, D. et al. (May 2019). "Hubble Space Telescope analysis of stellar populations within the globular cluster G1 (Mayall II) in M 31". In: MNRAS 485.3, pp. 3076–3087. DOI: 10.1093/mnras/stz629.

Nardiello, D. et al. (Nov. 2022). "Photometry and astrometry with JWST - I. NIRCam point spread functions and the first JWST colour-magnitude diagrams of a globular cluster". In: MNRAS 517.1, pp. 484–497. DOI: 10.1093/mnras/stac2659.

Nardiello, D. et al. (Oct. 2023b). "Photometry and astrometry with JWST - III. A NIRCam-Gaia DR3 analysis of the open cluster NGC 2506". In: MNRAS 525.2, pp. 2585–2604. DOI: 10.1093/mnras/stad2445.

Netopil, M. et al. (Jan. 2016). "On the metallicity of open clusters. III. Homogenised sample". In: A&A 585, A150, A150. DOI: 10.1051/0004-6361/201526370.

Nilakshi and R. Sagar (Jan. 2002). "A comprehensive study of the rich open star cluster NGC 2099 based on deep BVI CCD observations". In: A&A 381, pp. 65–76. DOI: 10.1051/0004-6361:20011492.

Pancino, E. et al. (Feb. 2010). "Chemical abundance analysis of the open clusters Cr 110, NGC 2099 (M 37), NGC 2420, NGC 7789, and M 67 (NGC 2682)". In: A&A 511, A56, A56. DOI: 10.1051/0004-6361/200912965.

Parker, Quentin A., Ivan S. Bojičić and David J. Frew (July 2016). "HASH: the Hong Kong/AAO/Strasbourg Hα planetary nebula database". In: *Journal of Physics Conference Series*. Vol. 728. Journal of Physics Conference Series, 032008, p. 032008. DOI: 10.1088/1742-6596/728/3/032008.

Paunzen, E., O. I. Pintado and H. M. Maitzen (Dec. 2003). "CCD photometric search for peculiar stars in open clusters. V. NGC 2099, NGC 3114, NGC 6204, NGC 6705 and NGC 6756". In: A&A 412, pp. 721–725. DOI: 10.1051/0004-6361:20031065.

Phillips, M. W. et al. (May 2020). "A new set of atmosphere and evolution models for cool T-Y brown dwarfs and giant exoplanets". In: A&A 637, A38, A38. DOI: 10.1051/0004-6361/201937381.

Piatti, Andrés E. and Nate Bastian (May 2016). "Extended main sequence turn-offs in low mass intermediate-age clusters". In: A&A 590, A50, A50. DOI: 10.1051/0004-6361/201628339.

Piatti, Andres E., Juan J. Claria and Mario G. Abadi (Dec. 1995). "Chemical Evolution of the Galactic Disk: Evidence for a Gradient Perpendicular to the Galactic Plane". In: AJ 110, p. 2813. DOI: 10.1086/117731.

Pietrinferni, Adriano et al. (Feb. 2021). "Updated BaSTI Stellar Evolution Models and Isochrones. II. α-enhanced Calculations". In: ApJ 908.1, 102, p. 102. DOI: 10.3847/1538-4357/abd4d5.

Piotto, G. et al. (May 2007). "A Triple Main Sequence in the Globular Cluster NGC 2808". In: ApJ 661.1, pp. L53–L56. DOI: 10.1086/51850310.48550/arXiv.astro-ph/0703767.

Piotto, G. et al. (Nov. 2012). "Hubble Space Telescope Reveals Multiple Sub-giant Branch in Eight Globular Clusters". In: ApJ 760.1, 39, p. 39. DOI: 10.1088/0004-637X/760/1/39.

Piotto, G. et al. (Mar. 2015). "The Hubble Space Telescope UV Legacy Survey of Galactic Globular Clusters. I. Overview of the Project and Detection of Multiple Stellar Populations". In: AJ 149.3, 91, p. 91. DOI: 10.1088/0004-6256/149/3/91.

Piskunov, A. E. et al. (2008). "Tidal radii and masses of open clusters*". In: *A&A* 477.1, pp. 165–172. DOI: 10.1051/0004-6361:20078525. URL: https://doi.org/10.1051/0004-6361:20078525.

Platais, Imants, Rosemary F. G. Wyse and Norbert Zacharias (Jan. 2006). "Deep Astrometric Standards and Galactic Structure". In: PASP 118.839, pp. 107–123. DOI: 10.1086/498072.

Platais, Imants et al. (July 2002). "WIYN Open Cluster Study. VIII. The Geometry and Stability of the NOAO CCD Mosaic Imager". In: AJ 124.1, pp. 601–611. DOI: 10.1086/340953.

Poelarends, A. J. T. et al. (Mar. 2008). "The Supernova Channel of Super-AGB Stars". In: ApJ 675.1, pp. 614–625. DOI: 10.1086/520872.

Ramirez, Edward D. and Matthew R. Buckley (Nov. 2023). "Constraining dark matter substructure with Gaia wide binaries". In: MNRAS 525.4, pp. 5813–5830. DOI: 10.1093/mnras/stad2583.

Rebolo, R., M. R. Zapatero Osorio and E. L. Martín (Sept. 1995). “Discovery of a brown dwarf in the Pleiades star cluster”. In: Nature 377.6545, pp. 129–131. DOI: 10.1038/377129a0.

Reindl, N. et al. (Dec. 2014). “Analysis of cool DO-type white dwarfs from the Sloan Digital Sky Survey data release 10”. In: A&A 572, A117, A117. DOI: 10.1051/0004-6361/201424861.

Renzini, A. et al. (Dec. 2015). “The Hubble Space Telescope UV Legacy Survey of Galactic Globular Clusters - V. Constraints on formation scenarios”. In: MNRAS 454.4, pp. 4197–4207. DOI: 10.1093/mnras/stv2268.

Renzini, Alvio and Alberto Buzzoni (Jan. 1986). “Global properties of stellar populations and the spectral evolution of galaxies.” In: *Spectral Evolution of Galaxies*. Ed. by Cesare Chiosi and Alvio Renzini. Vol. 122. Astrophysics and Space Science Library, pp. 195–231. DOI: 10.1007/978-94-009-4598-2_19.

Richer, Harvey B. et al. (June 2008). “Deep Advanced Camera for Surveys Imaging in the Globular Cluster NGC 6397: the Cluster Color-Magnitude Diagram and Luminosity Function”. In: AJ 135.6, pp. 2141–2154. DOI: 10.1088/0004-6256/135/6/2141.

Richer, Harvey B. et al. (May 2021). “Massive White Dwarfs in Young Star Clusters”. In: ApJ 912.2, 165, p. 165. DOI: 10.3847/1538-4357/abdeb7.

Robichon, N. et al. (May 1999). “Open clusters with Hipparcos. I. Mean astrometric parameters”. In: A&A 345, pp. 471–484.

Salaris, Maurizio et al. (Feb. 2009). “Semi-empirical White Dwarf Initial-Final Mass Relationships: A Thorough Analysis of Systematic Uncertainties Due to Stellar Evolution Models”. In: ApJ 692.2, pp. 1013–1032. DOI: 10.1088/0004-637X/692/2/1013.

Salaris, Maurizio et al. (Feb. 2022). “The updated BASTI stellar evolution models and isochrones - III. White dwarfs”. In: MNRAS 509.4, pp. 5197–5208. DOI: 10.1093/mnras/stab3359.

Sanders, W. L. (Sept. 1971). “An improved method for computing membership probabilities in open clusters.” In: A&A 14, pp. 226–232.

Saracino, S. et al. (June 2018). “On the Use of the Main-sequence Knee (Saddle) to Measure Globular Cluster Ages”. In: ApJ 860.2, 95, p. 95. DOI: 10.3847/1538-4357/aac2c2.

Sarajedini, Ata et al. (Feb. 2004). “WIYN Open Cluster Study. XIX. Main-Sequence-Fitting Distances to Open Clusters Using V-K Color-Magnitude Diagrams”. In: AJ 127.2, pp. 991–999. DOI: 10.1086/381072.

Sarajedini, Ata et al. (Apr. 2007). “The ACS Survey of Galactic Globular Clusters. I. Overview and Clusters without Previous Hubble Space Telescope Photometry”. In: AJ 133.4, pp. 1658–1672. DOI: 10.1086/511979.

Saumon, D. et al. (Mar. 1994). “Cool Zero-Metallicity Stellar Atmospheres”. In: ApJ 424, p. 333. DOI: 10.1086/173892.

Scalco, M. et al. (Aug. 2021). “The HST large programme on ω Centauri - IV. Catalogue of two external fields”. In: MNRAS 505.3, pp. 3549–3561. DOI: 10.1093/mnras/stab1476.

Siegel, Michael H. et al. (Sept. 2007). “The ACS Survey of Galactic Globular Clusters: M54 and Young Populations in the Sagittarius Dwarf Spheroidal Galaxy”. In: ApJ 667.1, pp. L57–L60. DOI: 10.1086/52200310.48550/arXiv.0708.0027.

Siess, L. (Mar. 2006). “Evolution of massive AGB stars. I. Carbon burning phase”. In: A&A 448.2, pp. 717–729. DOI: 10.1051/0004-6361:20053043.

Skrutskie, M. F. et al. (Feb. 2006). “The Two Micron All Sky Survey (2MASS)”. In: AJ 131.2, pp. 1163–1183. DOI: 10.1086/498708.

Smith, L. C. et al. (Feb. 2018). “VIRAC: the VVV Infrared Astrometric Catalogue”. In: MNRAS 474.2, pp. 1826–1849. DOI: 10.1093/mnras/stx2789.

Soltis, John, Stefano Casertano and Adam G. Riess (Feb. 2021). “The Parallax of ω Centauri Measured from Gaia EDR3 and a Direct, Geometric Calibration of the Tip of the Red Giant Branch and the Hubble Constant”. In: ApJ 908.1, L5, p. L5. DOI: 10.3847/2041-8213/abdbad.

Subramaniam, Annapurni and Ram Sagar (Feb. 1999). “Multicolor CCD Photometry and Stellar Evolutionary Analysis of NGC 1907, NGC 1912, NGC 2383, NGC 2384, and NGC 6709 Using Synthetic Color-Magnitude Diagrams”. In: AJ 117.2, pp. 937–961. DOI: 10.1086/300716.

Tarricq, Y. et al. (Mar. 2021). “3D kinematics and age distribution of the open cluster population”. In: A&A 647, A19, A19. DOI: 10.1051/0004-6361/202039388.

Tian, Hai-Jun et al. (Jan. 2014). “Exploring the total Galactic extinction with SDSS BHB stars”. In: A&A 561, A142, A142. DOI: 10.1051/0004-6361/201322381.

Tian, K. P. et al. (Sept. 1998). “VizieR Online Data Catalog: NGC 1750 + NGC 1758 proper motions (Tian+ 1998)”. In: *VizieR Online Data Catalog*, J/A+AS/131/89, J/A+AS/131/89.

Tody, Doug (Jan. 1986). “The IRAF Data Reduction and Analysis System”. In: *Instrumentation in astronomy VI*. Ed. by David L. Crawford. Vol. 627. Society of Photo-Optical Instrumentation Engineers (SPIE) Conference Series, p. 733. DOI: 10.1117/12.968154.

van Leeuwen, Floor (Aug. 1997). “The HIPPARCOS Mission”. In: Space Sci. Rev. 81, pp. 201–409. DOI: 10.1023/A:1005081918325.

Vasilevskis, S., A. Klemola and G. Preston (Jan. 1958). “Relative proper motions of stars in the region of the open cluster NGC 6633.” In: AJ 63, pp. 387–395. DOI: 10.1086/107787.

Vasiliev, Eugene (Apr. 2019). “Proper motions and dynamics of the Milky Way globular cluster system from Gaia DR2”. In: MNRAS 484.2, pp. 2832–2850. DOI: 10.1093/mnras/stz171.

Vasiliev, Eugene and Holger Baumgardt (Aug. 2021). “Gaia EDR3 view on galactic globular clusters”. In: MNRAS 505.4, pp. 5978–6002. DOI: 10.1093/mnras/stab1475.

Villanova, S. et al. (Jan. 2010). “The metallicity of the open cluster Tombaugh 2”. In: A&A 509, A102, A102. DOI: 10.1051/0004-6361/200913258.

Werner, Klaus and Falk Herwig (Feb. 2006). “The Elemental Abundances in Bare Planetary Nebula Central Stars and the Shell Burning in AGB Stars”. In: PASP 118.840, pp. 183–204. DOI: 10.1086/500443.

Werner, Klaus et al. (Oct. 2023). “The unusual planetary nebula nucleus in the Galactic open cluster M37 and six further hot white dwarf candidates”. In: A&A 678, A89, A89. DOI: 10.1051/0004-6361/202347217.

WFIRST Astrometry Working Group et al. (Oct. 2019). “Astrometry with the Wide-Field Infrared Space Telescope”. In: *Journal of Astronomical Telescopes, Instruments, and Systems* 5, 044005, p. 044005. DOI: 10.1117/1.JATIS.5.4.044005.

Yadav, R. K. S. et al. (June 2008). “Ground-based CCD astrometry with wide-field imagers. II. A star catalog for M 67: WFI@2.2 m MPG/ESO astrometry, FLAMES@VLT radial velocities”. In: A&A 484.2, pp. 609–620. DOI: 10.1051/0004-6361:20079245.

Yuan, H. B., X. W. Liu and M. S. Xiang (Apr. 2013). “Empirical extinction coefficients for the GALEX, SDSS, 2MASS and WISE passbands”. In: MNRAS 430.3, pp. 2188–2199. DOI: 10.1093/mnras/stt039.

Zacharias, N. et al. (Oct. 2000). “The First US Naval Observatory CCD Astrograph Catalog”. In: AJ 120.4, pp. 2131–2147. DOI: 10.1086/301563.

Zhang, Ruoyi and Haibo Yuan (Jan. 2023). “Empirical Temperature- and Extinction-dependent Extinction Coefficients for the GALEX, Pan-STARRS 1, Gaia, SDSS, 2MASS, and WISE Passbands”. In: ApJS 264.1, 14, p. 14. DOI: 10.3847/1538-4365/ac9dfa.

Zhong, Jing et al. (Aug. 2020). “Exploring open cluster properties with Gaia and LAMOST”. In: A&A 640, A127, A127. DOI: 10.1051/0004-6361/201937131.

Zivick, Paul et al. (Sept. 2018). “The Proper Motion Field of the Small Magellanic Cloud: Kinematic Evidence for Its Tidal Disruption”. In: ApJ 864.1, 55, p. 55. DOI: 10.3847/1538-4357/aad4b0.

Zoccali, M. (Aug. 2019). "The Stellar Population, 3D structure, and kinematics of the Galactic bulge". In: *Boletin de la Asociacion Argentina de Astronomia La Plata Argentina* 61, pp. 137–144.

Il tuo indirizzo e-mail

massimo.griggio@unife.it

Oggetto:

Dichiarazione di conformità della tesi di Dottorato

Io sottoscritto Dott. (Cognome e Nome)

Griggio Massimo

Nato a:

Camposampiero

Provincia:

Padova

Il giorno:

21/12/1991

Avendo frequentato il Dottorato di Ricerca in:

Fisica

Ciclo di Dottorato

36

Titolo della tesi:

Photometry and astrometry with wide-field imagers

Titolo della tesi (traduzione):

Fotometria ed astrometria con imager a grande-campo

Tutore: Prof. (Cognome e Nome)

Rosati Piero

Settore Scientifico Disciplinare (S.S.D.)

FIS/05

Parole chiave della tesi (max 10):

photometry, astrometry, star clusters

Consapevole, dichiara

CONSAPEVOLE: (1) del fatto che in caso di dichiarazioni mendaci, oltre alle sanzioni previste dal codice penale e dalle Leggi speciali per l'ipotesi di falsità in atti ed uso di atti falsi, decade fin dall'inizio e senza necessità di alcuna formalità dai benefici conseguenti al provvedimento emanato sulla base di tali dichiarazioni; (2) dell'obbligo per l'Università di provvedere al deposito di legge delle tesi di dottorato al fine di assicurarne la conservazione e la consultabilità da parte di terzi; (3) della procedura adottata dall'Università di Ferrara ove si richiede che la tesi sia consegnata dal dottorando in 1 originale cartaceo e 1 in formato PDF/A caricata sulla procedura informatica Esse3 secondo le istruzioni pubblicate sul sito: http://www.unife.it/studenti/dottorato alla voce ESAME FINALE – disposizioni e modulistica; (4) del fatto che l'Università, sulla base dei dati forniti, archivierà e renderà consultabile in rete il testo completo della tesi di dottorato di cui alla presente dichiarazione attraverso la pubblicazione ad accesso aperto nell'Archivio Istituzionale dei Prodotti della Ricerca IRIS-UNIFE (www.iris.unife.it) oltre che attraverso i Cataloghi delle Biblioteche Nazionali Centrali di Roma e Firenze; DICHIARO SOTTO LA MIA RESPONSABILITA': (1) che la copia della tesi depositata presso l'Università di Ferrara in formato cartaceo è del tutto identica a quella caricata in formato PDF/A sulla procedura informatica Esse3, a quelle da inviare ai Commissari di esame finale e alla copia che produrrò in seduta d'esame finale. Di conseguenza va esclusa qualsiasi responsabilità dell'Ateneo stesso per quanto riguarda eventuali errori, imprecisioni o omissioni nei contenuti della tesi; (2) di prendere atto che la tesi in formato cartaceo è l'unica alla quale farà riferimento l'Università per rilasciare, a mia richiesta, la dichiarazione di conformità di eventuali copie; (3) che il contenuto e l'organizzazione della tesi è opera originale da me realizzata e non compromette in alcun modo i diritti di terzi, ivi compresi quelli relativi alla sicurezza dei dati personali; che pertanto l'Università è in ogni caso esente da responsabilità di qualsivoglia natura civile, amministrativa o penale e sarà da me tenuta indenne da qualsiasi richiesta o rivendicazione da parte di terzi; (4) che la tesi di dottorato non è il risultato di attività rientranti nella normativa sulla proprietà industriale, non è stata prodotta nell'ambito di progetti finanziati da soggetti pubblici o privati con vincoli alla divulgazione dei risultati, non è oggetto di eventuali registrazioni di tipo brevettale o di tutela. PER ACCETTAZIONE DI QUANTO SOPRA RIPORTATO

Firma del dottorando

Ferrara, li ____________________________ (data) Firma del Dottorando ___________________________________

Firma del Tutore

Visto: Il Tutore Si approva Firma del Tutore ____